



HAL
open science

Synthesis and characterisation of luminescent complexes using the macrocycle thiacalix[4]arene and the Mn²⁺ ion

Niall O'Toole

► To cite this version:

Niall O'Toole. Synthesis and characterisation of luminescent complexes using the macrocycle thiacalix[4]arene and the Mn²⁺ ion. Coordination chemistry. Université de Lyon, 2017. English. NNT : 2017LYSE1028 . tel-01526851

HAL Id: tel-01526851

<https://theses.hal.science/tel-01526851>

Submitted on 23 May 2017

HAL is a multi-disciplinary open access archive for the deposit and dissemination of scientific research documents, whether they are published or not. The documents may come from teaching and research institutions in France or abroad, or from public or private research centers.

L'archive ouverte pluridisciplinaire **HAL**, est destinée au dépôt et à la diffusion de documents scientifiques de niveau recherche, publiés ou non, émanant des établissements d'enseignement et de recherche français ou étrangers, des laboratoires publics ou privés.



N°d'ordre NNT : xxx

THESE de DOCTORAT DE L'UNIVERSITE DE LYON
opérée au sein de
l'Université Claude Bernard Lyon 1

Ecole Doctorale N° 206
Ecole Doctorale de Chimie de l'Université de Lyon

Spécialité de doctorat : Chimie

Soutenue publiquement le 21/02/2017, par :
Niall O'TOOLE

**Synthèses et caractérisations de
complexes luminescents préparés à
partir du macrocycle thiacalix[4]arène
et l'ion Mn^{2+}**

Devant le jury composé de :

DANIELE, Stéphane	PU,	Université de Lyon 1	Président
FROCHOT, Céline	DR CNRS,	Université de Lorraine	Rapporteuse
FERLAY, Sylvie	PU,	Université de Strasbourg	Rapporteuse
DUBOC, Carole	DR CNRS	Université de Grenoble 1	Examinatrice
BRIOUDE, Arnaud	PU,	Université de Lyon 1	Directeur de thèse
DESROCHES, Cédric	MCF,	Université de Lyon 1	Co-directeur de thèse

UNIVERSITE CLAUDE BERNARD - LYON 1

Président de l'Université

Président du Conseil Académique

Vice-président du Conseil d'Administration

Vice-président du Conseil Formation et Vie Universitaire

Vice-président de la Commission Recherche

Directrice Générale des Services

M. le Professeur Frédéric FLEURY

M. le Professeur Hamda BEN HADID

M. le Professeur Didier REVEL

M. le Professeur Philippe CHEVALIER

M. Fabrice VALLÉE

Mme Dominique MARCHAND

COMPOSANTES SANTE

Faculté de Médecine Lyon Est – Claude Bernard

Faculté de Médecine et de Maïeutique Lyon Sud – Charles Mérieux

Faculté d'Odontologie

Institut des Sciences Pharmaceutiques et Biologiques

Institut des Sciences et Techniques de la Réadaptation

Département de formation et Centre de Recherche en Biologie Humaine

Directeur : M. le Professeur G.RODE

Directeur : Mme la Professeure C. BURILLON

Directeur : M. le Professeur D. BOURGEOIS

Directeur : Mme la Professeure C. VINCIGUERRA

Directeur : M. X. PERROT

Directeur : Mme la Professeure A-M. SCHOTT

COMPOSANTES ET DEPARTEMENTS DE SCIENCES ET TECHNOLOGIE

Faculté des Sciences et Technologies

Département Biologie

Département Chimie Biochimie

Département GEP

Département Informatique

Département Mathématiques

Département Mécanique

Département Physique

UFR Sciences et Techniques des Activités Physiques et Sportives

Observatoire des Sciences de l'Univers de Lyon

Polytech Lyon

Ecole Supérieure de Chimie Physique Electronique

Institut Universitaire de Technologie de Lyon 1

Ecole Supérieure du Professorat et de l'Education

Institut de Science Financière et d'Assurances

Directeur : M. F. DE MARCHI

Directeur : M. le Professeur F. THEVENARD

Directeur : Mme C. FELIX

Directeur : M. Hassan HAMMOURI

Directeur : M. le Professeur S. AKKOUCHE

Directeur : M. le Professeur G. TOMANOV

Directeur : M. le Professeur H. BEN HADID

Directeur : M. le Professeur J-C PLENET

Directeur : M. Y. VANPOULLE

Directeur : M. B. GUIDERDONI

Directeur : M. le Professeur E.PERRIN

Directeur : M. G. PIGNAULT

Directeur : M. le Professeur C. VITON

Directeur : M. le Professeur A. MOUGNIOTTE

Directeur : M. N. LEBOISNE

RÉSUMÉ EN FRANCAIS

Ce document présente les travaux de ma thèse intitulée « Synthèses et caractérisations de complexes luminescents préparés à partir du macrocycle thiacalix[4]arène et l'ion Mn^{2+} ». Ces travaux ont été réalisés au sein du Laboratoire des Multimatériaux et Interfaces (LMI, UMR 5615) à l'Université Claude Bernard Lyon 1.

La thèse est dédiée à l'étude des propriétés photophysiques et photochimiques de systèmes contenant le macrocycle sulfonylcalix[4]arène, membre de la famille des thiacalixarènes, et l'ion métallique Mn^{2+} . Les travaux entrepris se sont focalisés sur les propriétés inattendues de luminescence de ce type de système moléculaire.

Les thiacalix[4]arènes sont des macrocycles composés de quatre unités phénoliques reliées entre elles par des atomes de soufre. Ces molécules, composées de plusieurs sites chélatants, sont connues pour être de très bons ligands conduisant souvent à de complexes métalliques polynucléaires. Précédemment, une série d'études dans notre laboratoire a permis de révéler, qu'un complexe formé de quatre ions de manganèse(II) pris en sandwich entre deux macrocycles *para-tert*-butylsulfonylcalix[4]arène ($thiaSO_2$) présente une forte émission rouge sous l'action de lumière bleue ou ultra-violette. Cette découverte est à l'origine de cette étude doctorale qui a été initiée dans le but de comprendre, d'améliorer et d'utiliser ce type de système moléculaire dans des dispositifs intégrant des phénomènes de conversion énergétique.

Le premier chapitre est une revue de la littérature concernant les thiacalixarènes et leurs complexes métalliques. La synthèse et les modifications de ces molécules seront décrites. Puis, les propriétés fondamentales des thiacalixarènes liées au grand pouvoir complexant de cette famille, tels que la flexibilité, la stabilité, l'acidité, et la facilité de modification, seront discutées afin d'éclairer cette caractéristique importante. Des exemples représentatifs de la grande variété de complexes métalliques formés avec ces ligands seront donnés et groupés soit par le mode de coordination présent dans le complexe, soit par les applications pratiques auxquelles ils sont typiquement mis en jeu. De plus, une description de la méthode solvothermale de synthèse et ces

implications importantes pour la manipulation des thiacalixarènes seront présentés dans cette partie.

La deuxième partie se concentre sur la luminescence. Afin de proposer une explication mécanistique de ce phénomène, la réponse de l'émission provenant du complexe (K)[Mn₄(thiaSO₂)₂F] (**2**) a été étudié sous des conditions variables en pression, température et atmosphère (N₂, O₂). L'influence de la modification chimique du système sur la luminescence sera aussi présentée. Spécifiquement, ces complexes sont le [K(18-couronne-6)][Mn₄(thiaSO₂)₂F] (**3**), le (K)[Mn₄(Br₄thiaSO₂)₂F] (**4**), et le [Mn₂(thiaSO₂)(DMF)₄(H₂O)₂] (**5**). L'analyse de résultats obtenus pour l'ensemble de cette étude, avec notamment le quench de luminescence engendré par la production d'oxygène singulet, conduira à une étude plus approfondie concernant l'excitation de ces systèmes moléculaires en solution qui sera présenté dans le chapitre suivant.

Le troisième chapitre s'intéresse à la photo-réaction de ces systèmes en solution. La photo-réaction des clusters tétranucléaires de Mn²⁺, nous permettra de mettre en évidence la formation d'un complexe mononucléaire stable de Mn³⁺/para-*tert*-butylsulfonylcalix[4]arène. Cette réaction de photo-oxydation sera la base de l'ensemble des études présentées dans ce chapitre. La photo-réactivité de ce système sera étudiée à travers la modification du système thiaSO₂/Mn²⁺ de départ, l'étude de la photo-réactivité du macrocycle thiaSO₂ non complexé, ainsi que l'impact de la modification de paramètres tels que le pH et l'atmosphère de réaction. Les résultats expérimentaux et théoriques obtenus, nous permettrons d'éclaircir le phénomène de photo-oxydation de ces systèmes conduisant à la préparation de complexes d'ions Mn³⁺ mais aussi à la production d'ion superoxyde ou d'oxygène singulet.

La dernière partie s'intéressera à l'insertion des agrégats [Mn₄(thiaSO₂)₂F]⁻ dans des matériaux minéraux lamellaires de type LDH (« Hydroxyde Double Lamellaires »). Ces matériaux seront réalisés par des méthodes de co-précipitation en solution. Les études préliminaires sur la structure, la luminescence, et la photo-réactivité des produits seront présentées et discutées.

La conclusion générale rappellera les objectifs de ce travail, les résultats obtenus et les perspectives envisagées pour le poursuivre.

THANKS AND ACKNOWLEDGEMENTS

I have many people to whom I must extend my gratitude for their invaluable help in the creation of this doctoral thesis.

Firstly, many thanks to Madames Céline Frochot, Sylvie Ferlay, and Carole Duboc, and Monsieur Stephane Daniele, for kindly agreeing to act as reporter or examiner and attend my thesis defence. It is greatly appreciated.

Furthermore, I am deeply grateful to M. Arnaud Brioude for accepting me into the laboratory group, and for his wisdom and guidance throughout the duration of my project. To Cédric Desroches, the co-director of my thesis, I would like to say it has been a great pleasure to carry out this work with your leadership. Thank you for the patience you have shown me, and for all the knowledge you have imparted.

My colleagues in the LMI, and in particular the coworkers in the Bâtiment Chevreul, have always made me feel welcome, which has been a great help to me when I was feeling far from home. Thank you all, it has been a true privilege to get to know you over the past years.

To all the collaborators from Lyon or otherwise, too numerous to list here, who have so kindly provided their expertise in the experiments and ideas described herein, thank you. Without you this thesis would absolutely not have been possible.

For the friends I have made during my time in France, I sincerely hope that this friendship can continue now past the point where my stay here ends. It's been great!

Cheers to all my family wherever you all may be, for your support and interest, and for all the craic.

Finally, naturally, and always, thanks to Lydi. For putting up with me, for your strength, smartness, support, and smiles, I will be forever grateful. I am proud that we did this together!

My most sincere and humble thanks to you all.

LIST OF ABBREVIATIONS

Abbreviation	Meaning
λ	Wavelength
$\nu, \bar{\nu}$	Wavenumber
Å	Angström(s)
A, abs	Absorption / Absorbance
amb	Ambient
atm	Atmosphere(s)
a.u.	Arbitrary units
bipy	Bipyridyl
mbar	millibar
cp	Cyclopentadiene
° C	Degree(s) Celsius (Centigrade)
C ⁺	Cation (when used in molecular formulae of aggregate complexes)
D	Anisotropy (magnetic)
DAC	Diamond Anvil Cell
DCM	Dichloromethane
DFT	Density Functional Theory
DMA	9,10-dimethylanthracene
DMF	N, N'-dimethylformamide
DMPO (DMPO-OH, DMPO-OOH)	5,5-dimethyl-1-pyrroline-N-oxide (OH and OOH adducts of same)
DMSO	Dimethylsulfoxide
DNA	Deoxyribonucleic Acid
DPEPO	Bis[2-(diphenylphosphino)-phenyl] ether oxide
emi	emission
(CW-)EPR	(Continuous Wave-)Electron Paramagnetic Resonance
Eq.	Equivalent(s)
Et	Ethyl
exc	excitation
eV	Electron Volts
FWHM	Full Width at Half Maximum height
g	grams
h / hr	hours
HMT	Hexamethylenetetramine
Hz (MHz)	Hertz (Megahertz)
IR	Infra-Red
irr	irradiation
k	Rate constant
K, or	Equilibrium constant
K	Degrees Kelvin (dependent on context)
L, μ -L	Ligand, bridging ligand
LDH	Layered Double Hydroxide

LDO	Calcined LDH
LMCT	Ligand to Metal Charge Transfer
Ln	Lanthanide
m (nm, mm, cm, dm)	Metre(s) (nanometre, millimetre, centimetre, decimetre)
M, or	Metal
M	Mol dm ⁻³ (dependent on context)
Me	Methyl
min	Minutes
MOF	Metal Organic Framework
mol (mmol, μmol)	Mole(s) (millimole, micromole)
MOSC	Metal-Organic SuperContainer
NMR	Nuclear Magnetic Resonance
NOESY	Nuclear Overhauser Effect Spectroscopy
³ O ₂ , ¹ O ₂ , O ₂ ^{o-}	Ground state (triplet) oxygen, singlet oxygen, superoxide radical anion
O _h	Octahedral
Pa (MPa, GPa)	Pascal(s) (Megapascal, Gigapascal)
Ph	Phenyl
PTFE	Poly-(tetrafluoroethylene)
PXRD	Powder X-Ray Diffraction
s (ms, μs)	Second(s) (millisecond, microsecond)
S	Spin
S ₀ , S ₁ , T ₁	Singlet ground state, Singlet excited state, Triplet excited state
SEM	Scanning Electron Microscopy
SHE	Standard Hydrogen Electrode
SMM	Single Molecule Magnet
thiaS (thiaSO, thiaSO ₂ , H ₄ thiaS, H ₄ thiaSO ₂ , Br ₄ thiaS, Br ₄ thiaSO ₂)	Para- <i>tert</i> -butylthiacalix[4]arene (para- <i>tert</i> -butylsulfonylcalix[4]arene para- <i>tert</i> -butylsulfonylcalix[4]arene thiacalix[4]arene sulfonylcalix[4]arene para-bromothiacalix[4]arene para-bromosulfonylcalix[4]arene)
TPP	Triphenylphosphine
TPO	Triphenylphosphine oxide
UV (-vis)	Ultra Violet (-visible)
VBT	Valence Bond Theory
XRD	X-Ray Diffraction

TABLE OF CONTENTS

RÉSUMÉ EN FRANCAIS.....	3
THANKS AND ACKNOWLEDGEMENTS.....	7
LIST OF ABBREVIATIONS.....	9
TABLE OF CONTENTS.....	13
GENERAL INTRODUCTION.....	19
References.....	24
CHAPTER 1: BIBLIOGRAPHIC REVIEW OF THICALIXARENES AND THEIR COMPLEXES.....	27
1.A: Thiacalixarenes.....	28
1.A1: General Introduction.....	28
1.A2: Syntheses.....	29
1.A3: Conformations.....	31
1.A4: Modifications.....	32
1.A4.1: Upper rim modification.....	32
1.A4.2: Meta substitution.....	33
1.A4.3: Functionalisation on the sulfur atoms.....	35
1.A4.4: Lower rim substitution.....	37
1.A5: Conclusion.....	42
1.B: Metal Complexes of Thiacalixarenes.....	42
1.B1: General.....	42
1.B2: Aggregates and Binding Modes.....	43
1.B2.1: Complexing power of the ligands.....	44
1.B2.2: Octadentate binding.....	44
1.B2.3: Heptadentate binding.....	46
1.B2.4: Hexadentate binding.....	47
1.B2.5: Pentadentate binding.....	48
1.B2.6: Tetradentate binding.....	49
1.B2.7: Tridentate binding.....	50
1.B3: Synthesis of complexes and aggregates.....	51
1.B3.1: Metal salt.....	52
1.B3.2: Base.....	52
1.B3.3: Solvent.....	53
1.B3.4: Pressure and temperature conditions.....	53
1.B4: Properties of aggregates.....	54

1.B4.1: Magnetism (Single Molecule Magnets)	54
1.B4.2: Porous materials (“Metal-Organic Supercontainers”)	56
1.B4.3: Catalysis.....	56
1.B5: Luminescence.....	57
1.B5.1: Chemical sensors involving thiacalixarenes.	58
1.B5.2: Thiacalixarenes as antenna ligands in luminescent complexes	59
1.B6: General Conclusion	60
References.....	61
CHAPTER 2: LUMINESCENCE CHARACTERISATION OF SYSTEMS CONTAINING SULFONYLCALIXARENE LIGANDS AND Mn²⁺ IONS	
2.0 Table of cluster complexes studied in this chapter.....	68
2.1: General introduction	70
2.2: Syntheses.....	78
2.3: Solid state luminescence characterisation of complex 2	79
2.3.1: Response to pressure	81
2.3.2: Response to temperature	84
2.3.3: Response to O ₂ pressure	86
2.4: The significance of the K-O=S interaction: solid state luminescence of complex 3	87
2.4.1: Response to pressure	91
2.4.2: Response to temperature	93
2.4.3: Response to O ₂ pressure	94
2.4.4: Summary of the cation effect.....	95
2.5: Chemical and conformational modification of the macrocycle	96
2.5.1: Complex 4; substitution at the para-position	97
2.5.2: Complex 5; effect of macrocycle conformation and Mn environment.....	100
2.5.3: Summary of modifications to the ligand system.....	104
2.6: Solution state luminescence	105
2.7: Conclusion	107
2.8 Summary of photophysical properties	110
References.....	111
CHAPTER 3 : PHOTOREACTIVITY OF ThiaSO₂ / Mn²⁺ SYSTEMS.....	
3.0 List of systems studied in this chapter	114
3.1 General introduction	115
3.2: Photo-oxidation of tetranuclear and dinuclear manganese(II) clusters in solution	120

3.2.1: The end product derived from $^3\text{O}_2$	121
3.2.2: Investigation of $^1\text{O}_2$	123
3.2.3: Alternative oxidants	126
3.2.4: The role of solvent, of excitation wavelength, and of accompanying cation (for complex 2)	129
3.2.5: Summary of the photo-oxidation of polynuclear manganese clusters.....	130
3.3: Photo-oxidation of solutions containing free thiaSO ₂ and manganese(II) ions.	131
3.3.1: Effect of stoichiometric ratio of thiaSO ₂ : Mn(NO ₃) ₂	131
3.3.2: Effect of Mn ²⁺ salt: MnCl ₂	136
3.3.3: Effect of addition of Et ₃ N.....	140
3.3.4: Luminescence behaviour of ThiaSO ₂ / Mn ²⁺ in solution.....	145
3.3.5: Summary of the photoreactivity of solution state reagent mixtures	146
3.4: Photoreactivity of the pure compound thiaSO ₂	146
3.5: Conclusion	152
References.....	154
CHAPTER 4: INORGANIC – ORGANIC HYBRID MATERIALS OBTAINED BY INTERCALATION OF CLUSTER COMPLEXES INTO INORGANIC HOST MATRICES.....	157
4.1 General Introduction.....	158
4.2 Syntheses.....	163
4.2.1 Synthetic routes to LDH starting materials	163
4.2.2 Intercalation routes to hybrid materials	166
4.3 Characterisation	168
4.3.1 X-ray Diffraction Characterisation.....	168
4.3.2: Scanning Electron Microscopy	176
4.3.3: IR spectroscopy characterisation	177
4.3.4 Luminescence spectroscopy characterisation.....	180
4.4 Oxygenation catalysis tests	186
4.5 Conclusion	188
References.....	190
GENERAL CONCLUSION	193
EXPERIMENTAL SECTION.....	199
6.1: Materials	200
6.2: Syntheses.....	203
6.2.1: Ligand syntheses	203
6.2.2 Manganese complex syntheses.....	206

6.2.3: LDHs and intercalate material syntheses	209
References.....	211
ANNEXE 1: CRYSTALLOGRAPHIC DATA.....	213
[Mn ₄ (Br ₄ thiaS) ₂ (DMF) ₂ (H ₂ O) ₂]	214
ANNEXE 2: CALCULATIONS OF REACTION KINETICS	251
ANNEXE 3: LUMINESCENCE LIFETIME DECAY CURVES.....	263
ANNEXE 4: LIST OF FIGURES	269
ANNEXE 5: PUBLICATIONS.....	275

GENERAL INTRODUCTION

This doctoral thesis involves a coordination chemistry investigation of molecular cluster compounds of transition metals with focus on their optical behaviour.

The term “cluster” may mean many things, depending on context. In the field of coordination chemistry the term refers to a metal complex with more than one metal centre, usually linked by multidentate ligands.¹ These materials may contain direct metal-metal bonding, but not necessarily. A vast number of species meet this criterion in this context, including bulk metals, metal nanoparticles, discrete molecular species, and supramolecular network macrostructures. There has therefore been a large number of studies on these materials and the methods by which they are synthesised.²⁻⁵

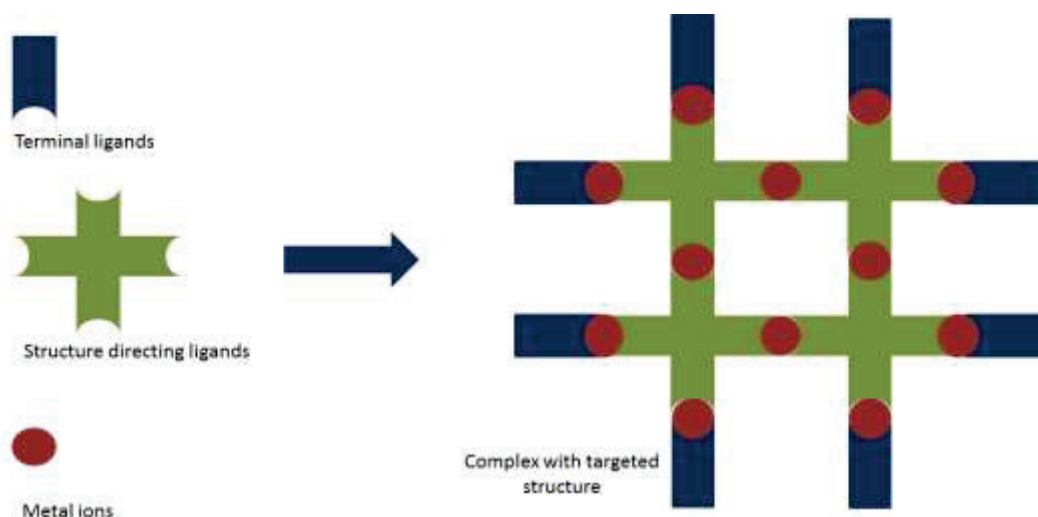


Figure I: Illustration of the molecular panelling approach to synthesise metal cluster complexes.

Two conceptually related methods for the synthesis of molecular clusters are ‘molecular panelling’ and ‘serendipitous assembly’.^{6, 7} Molecular panelling takes its inspiration from supramolecular templating methods employed in organic synthesis; directing ligands are chosen or designed to act as directing organic ‘bricks’ to connect metal centres in a targeted architecture.⁸ Figure I shows a representation of this method. Though this method has been well established and shown to be successful for the synthesis of discrete molecular architectures as well as extended macrostructures, it has its drawbacks and limitations.^{9, 10} Specifically, it remains difficult to target

architectures with a dense concentration of the metal centres.¹¹ The larger directing ligands are easier to control and predict but lead to greater space between metal atoms, whereas smaller coordinating species such as halides, oxide and hydroxide tend to be unreliable and unpredictable.

The alternative approach, serendipitous assembly, does not seek to target a specific final product structure; rather, a selection of criteria are chosen in the hopes of favouring a natural assembly of a polymetallic compound in the product with appropriate characteristics. Polyfunctional, polydentate ligands are a highly useful tool for these synthetic methods and can be extremely versatile, in that a single ligand type can give rise to very different products with relatively insignificant tweaking of the reaction conditions.^{12, 13} The most important factors to consider when making a choice from the huge library of available polyfunctional compounds are:

- **Accessibility / Price.** The serendipitous assembly method often involves trial and error, leading to considerable consumption of the reactants in the name of optimising the conditions to give the desired outcome.
- **Capacity for modification.** Once a certain ligand has proven potential for a desired type of metal cluster product, the possibility of further modification (using it as a platform molecule towards more sophisticated structures) becomes highly desirable for the fine control of the useful properties of the resultant product compounds.
- **Solubility.** The solvent of reaction can play a very important role in defining the structure and crystallinity of the product and more. Therefore, simply put, solubility in a wider variety of different solvents offers greater scope for modification of the system and thereby the products.

The primary objective of this work was to elaborate and analyse a series of metal clusters of the general formula $[M_x(\mu-L)_yL'_z]^n$; wherein M is a transition metal, $(\mu-L)$ is a bridging ligand, L' is a terminal ligand, and n is the overall charge of the aggregate. The ligands chosen for this purpose were selected from the family of thiacalixarenes, which are macrocyclic sulfur-linked oligomers of

phenol.¹⁴ In addition to their strong properties in the three fields mentioned above, these compounds display several other very interesting properties which make them highly suited to act as ligands in the creation of metal cluster complexes.

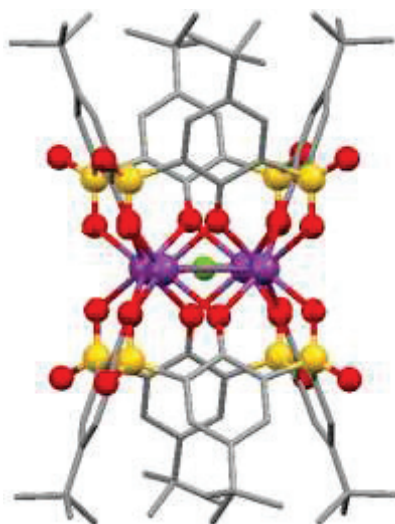


Figure II: Structure of an example cluster of four manganese ions with two thiaSO₂ ligands. Colour key: C = grey, S = yellow, O = red, Mn = purple, F = green. H atoms omitted for clarity.

Previous work within our laboratory has offered up as an attractive object of study the clusters formed by reaction of the ligand *para-tert*-butylsulfonylcalix[4]arene (referred to in this work as thiaSO₂) with ions of the transition metal manganese.¹⁵ Manganese has found well documented use in a variety of catalytic and magnetic applications for example; for our purposes its demonstrated optical properties are of particular interest.¹⁶⁻¹⁸ Manganese in the +2 or +4 oxidation state is often employed as a dopant to form optical centres in inorganic materials.^{19, 20} For various reasons (mainly its inherently weak absorption properties) such luminescent activity is not often observed from manganese when in molecular complex form; however neither is it totally unheard of.²¹ Clusters of manganese involving the ligand thiaSO₂ such as the example shown in figure II, appear to demonstrate a strong synergistic relationship between the metal ions and the ligands which exalts the optical behaviour of the complex. In addition to the standard physical and chemical characterisation, the photophysical and photochemical properties of this family of compounds has been investigated in depth in this work.

Following a bibliographic review of the state of the art in these fields, the second chapter will present a study of the UV-induced red luminescence observed for clusters of the formula $[\text{Mn}_4(\text{thiaSO}_2)_2(\mu_4\text{-F})]^-$. This section will attempt to prove the provenance of the intense luminescence is from a d-d transition of the manganese ions, via an antenna effect mechanism. Then the structural aspects of the system will be considered, including the effect of the cation upon the system and the potential for modification of the ligand to offer control of the luminescence properties. The interaction with oxygen of these compounds both in the solid state and in solution is discussed.

This leads then to the next chapter which deals with the photo-oxidation reaction which these systems were observed to undergo in solution under certain conditions. The influence of each of the relevant components of this reaction will be considered in turn, before a quantitative study on their effects on the reaction kinetics. Like photoluminescence, photo-oxidation is an important example of a substance's capability to capture and convert incident light energy in a useful way; possible useful applications of this capability will be discussed.

The fourth chapter is concerned with taking a step towards such tangible applications by the creation of hybrid materials involving manganese-sulfonylcalixarene complexes and inorganic compounds with a layered structure. By so doing we hope to ameliorate the processibility of the complex whilst also potentially adding new functionalities inherent to the layered hydroxide host material, such as protection from oxidative degradation, magnetic arrangement and catalytic sites. The synthetic routes for these hybrid materials will be discussed, followed by detailed analysis of their photophysical and photochemical characteristics.

Finally, a general conclusion of the work then seeks to bind together the presented work in view of the stated aims, and to offer insight into potential avenues for further study of this fascinating system.

References

1. Huheey, J. E.; Keiter, E. A.; Keiter, R. L.; Medhi, O. K., *Inorganic Chemistry: Principles of Structure and Reactivity*. Pearson Education: 2006.
2. Richmond, M. G., Annual survey of organometallic metal cluster chemistry for the year 2000. *Coordination Chemistry Reviews* **2002**, *228* (1), 19-41.
3. Belyakova, O. A.; Slovokhotov, Y. L., Structures of large transition metal clusters. *Russian Chemical Bulletin* **2003**, *52* (11), 2299-2327.
4. Ebert, H.; Bornemann, S.; Minar, J.; Kosuth, M.; Sipr, O.; Dederichs, P. H.; Zeller, R.; Cabria, I., Electronic and magnetic properties of free and supported transition metal clusters. *Phase Transitions* **2005**, *78* (1-3), 71-83.
5. Brait, S.; Deabate, S.; Knox, S. A. R.; Sappa, E., The coordination and transformation of arene rings by transition metal carbonyl cluster complexes. *Journal of Cluster Science* **2001**, *12* (1), 139-173.
6. Lehn, J.-M., Supramolecular Chemistry. In *Supramolecular Chemistry*, Wiley-VCH Verlag GmbH & Co. KGaA: 2006.
7. Winpenny, R. E. P., Serendipitous assembly of polynuclear cage compounds. *Journal of the Chemical Society-Dalton Transactions* **2002**, (1), 1-10.
8. Umemoto, K.; Yamaguchi, K.; Fujita, M., Molecular paneling via coordination: Guest-controlled assembly of open cone and tetrahedron structures from eight metals and four ligands. *Journal of the American Chemical Society* **2000**, *122* (29), 7150-7151.
9. Cholewa, P. P.; Beavers, C. M.; Teat, S. J.; Dalgarno, S. J., Molecular Paneling in the Rational Design of Calixarene Coordination Polymers. *Crystal Growth & Design* **2013**, *13* (7), 2703-2706.
10. Al-Rasbi, N. K.; Tidmarsh, I. S.; Argent, S. P.; Adams, H.; Harding, L. P.; Ward, M. D., Mixed-ligand molecular paneling: Dodecanuclear cuboctahedral coordination cages based on a combination of edge-bridging and face-capping ligands. *Journal of the American Chemical Society* **2008**, *130* (35), 11641-11649.
11. Fujita, M.; Umemoto, K.; Yoshizawa, M.; Fujita, N.; Kusukawa, T.; Biradha, K., Molecular paneling via coordination. *Chemical Communications* **2001**, (6), 509-518.
12. Mukherjee, S.; Mukherjee, P. S., Versatility of Azide in Serendipitous Assembly of Copper(II) Magnetic Polyclusters. *Accounts of Chemical Research* **2013**, *46* (11), 2556-2566.
13. Ledezma-Gairaud, M.; Grangel, L.; Aromi, G.; Fujisawa, T.; Yamaguchi, A.; Sumiyama, A.; Sanudo, E. C., From Serendipitous Assembly to Controlled Synthesis of 3d-4f Single-Molecule Magnets. *Inorganic Chemistry* **2014**, *53* (12), 5878-5880.
14. Iki, N.; Miyano, S., Can thiacalixarene surpass calixarene? *Journal of Inclusion Phenomena and Macrocyclic Chemistry* **2001**, *41* (1-4), 99-105.
15. Lamouchi, M.; Jeanneau, E.; Pillonnet, A.; Brioude, A.; Martini, M.; Stephan, O.; Meganem, F.; Novitchi, G.; Luneau, D.; Desroches, C., Tetranuclear manganese(II) complexes of sulfonylcalix 4 arene macrocycles: synthesis, structure, spectroscopic and magnetic properties. *Dalton Transactions* **2012**, *41* (9), 2707-2713.
16. Sessoli, R.; Gatteschi, D.; Caneschi, A.; Novak, M. A., MAGNETIC BISTABILITY IN A METAL-ION CLUSTER. *Nature* **1993**, *365* (6442), 141-143.
17. Wagloehner, S.; Nitzer-Noski, M.; Kureti, S., Oxidation of soot on manganese oxide catalysts. *Chemical Engineering Journal* **2015**, *259*, 492-504.
18. Schoenfeldt, N. J.; Ni, Z. J.; Korinda, A. W.; Meyer, R. J.; Notestein, J. M., Manganese Triazacyclononane Oxidation Catalysts Grafted under Reaction Conditions on Solid Cocatalytic Supports. *Journal of the American Chemical Society* **2011**, *133* (46), 18684-18695.
19. Diaz, H.; Lahoz, F.; Villacampa, B.; Cases, R.; Sobolev, B.; Alcala, R., Optical properties of Mn²⁺ ions in solid solutions of fluorite-type crystals. *Journal of Luminescence* **1999**, *81* (1), 53-60.
20. Ming, C. G.; Liu, H. X.; Song, F.; Ren, X. B.; An, L. Q.; Hao, Y. M.; Wang, G. Z., Adjustable wavelength and lifetime in Mn⁴⁺ ion doped phosphate glasses. *Current Applied Physics* **2013**, *13* (6), 1109-1111.

21. Hausmann, D.; Kuzmanoski, A.; Feldmann, C., MnBr₂/18-crown-6 coordination complexes showing high room temperature luminescence and quantum yield. *Dalton Transactions* **2016**, 45 (15), 6541-6547.

CHAPTER 1: BIBLIOGRAPHIC REVIEW OF THICALIXARENES
AND THEIR COMPLEXES

This work concerns cluster complexes with ligands of the thiacalixarene family, principally tetranuclear manganese(II) clusters of sulfonylcalixarene. The goal of the study was to produce variations of these tetramanganese structures, and analyse their photophysical and photochemical properties in detail. This introductory chapter provides a literature review, firstly of the thiacalixarene family of molecules themselves and then of their metal complexes, with an emphasis on the optical properties of these species in each case.

1.A: Thiacalixarenes

1.A1: General Introduction

Macrocyclic compounds have been of interest in the field of coordination chemistry for quite some time now. These species often come with interesting properties, such as structural rigidity and numerous potential metal bonding sites, that render them extremely versatile in the creation of functional metal complex materials.¹ One subgroup of macrocycles, the thiacalixarene* family, is of particular interest to us. (*The term thiacalixarene has also been used to signify sulfur linked cyclic polythiophenes.⁴ In this work only the polyphenol meaning is observed). Standard calixarenes (the name was coined by Gutsche,² and derives from the Greek word for chalice or bowl, *calix*, referring to the cup shape of the molecule) are polyphenol macrocycles wherein each phenol moiety is connected to two others at the *ortho*- positions by a connecting 'bridge' unit of methylene. The suffix -arene denotes the aromatic nature of the monomer subunits. Modification and functionalisation is possible at each point of the calixarene molecule (§1.A.4). Thiacalixarene and its derivatives share this basic structure, but the bridging function consists of sulfur atoms rather than methylene.³ The number of individual phenol units is indicated in brackets in the molecule's name; for instance a thiacalixarene with four phenol rings and *para-tert*-butyl functions on each would have the nomenclature *para-tert*-butylthiacalix[4]arene (figure 1). This molecule is referred to as "thiaS" throughout this work.

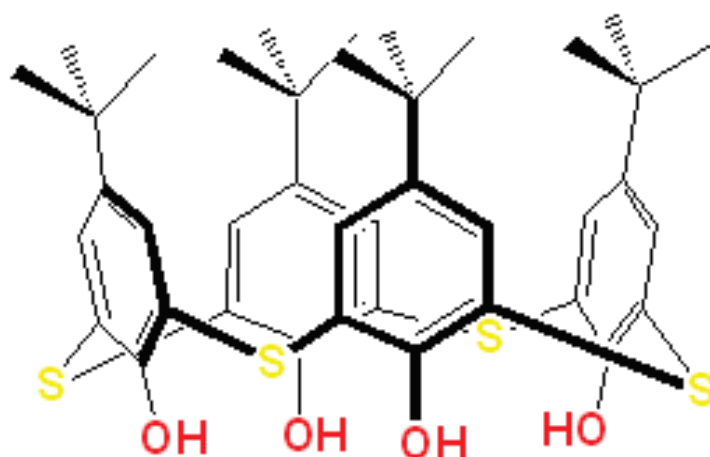


Figure 1: Structure of *para-tert-butylthiacalix[4]arene* (thiaS).

1.A2: Syntheses

The origin of thiacalixarenes arose when Rawlings *et al* reacted phenol with elemental sulfur in the presence of sodium hydroxide base.⁵ The result was a mixture of oligomeric forms of phenol linked by sulfur atoms. A reaction of *para-nonylphenol* with sulfur in the presence of a calcium salt was found to give some macrocyclic product as well as the open oligomers.⁶ In 1997 Kumagai *et al.* reported a one-step synthesis of *para-tert-butylthiacalix[4]arene* by the reaction of *para-tert-butylphenol* with sulfur at 230° C using sodium hydroxide catalyst in tetraethyleneglycol dimethylether solvent, with the loss of hydrogen sulphide, shown below in figure 2.³ In that same year, Sone *et al.* demonstrated a synthesis by progressive reactions of *para-tert-butylphenol* with sulfur dichloride, however this route provided untenably small yields (approximately 4%).⁷

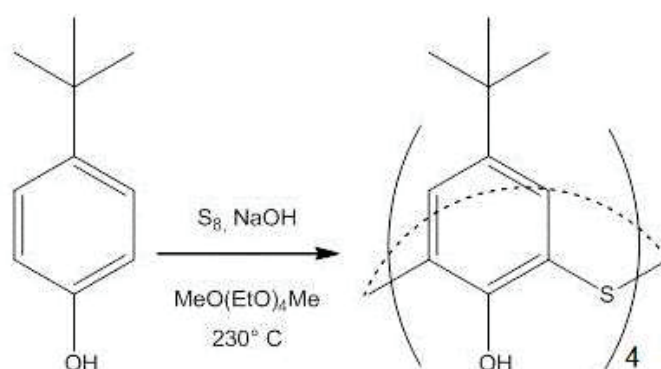


Figure 2: One step synthesis of *para-tert-butylthiacalix[4]arene*.

The modest yield of this one-step synthesis can be ameliorated by both the use of diphenylether as solvent, and by changing the starting material to a sulfur-linked dimeric form of *para-tert*-butylphenol.⁸ Figure 3 shows the dimeric starting compound obtained by reaction of *para-tert*-butylphenol with sulfur dichloride. The principal product is the four membered *para-tert*-butylthiacalix[4]arene, although small amounts of six- and eight-membered ring products were also obtained (obviously, only products with an even number of phenol residues are possible by this method).

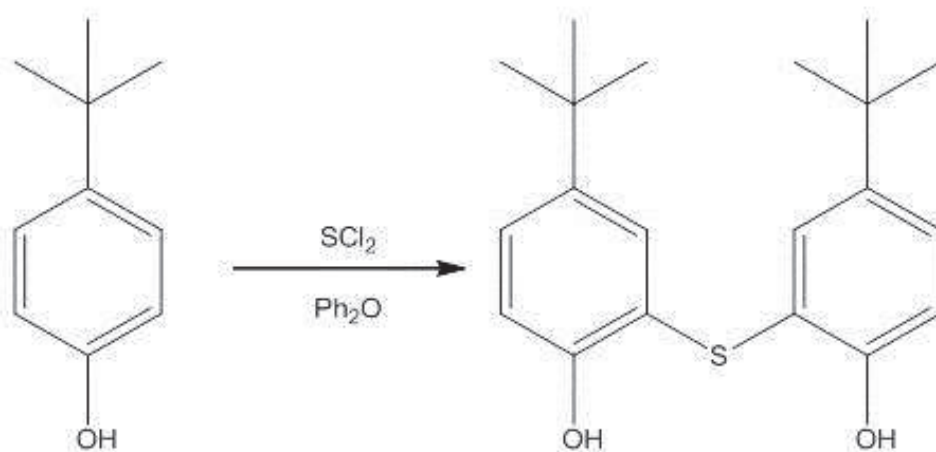


Figure 3: Synthesis of the *para-tert*-butylphenol thioether dimer.³

The four membered thiacalixarenes are significantly easier to synthesise than any other size, and therefore dominate the literature concerning these types of compound. The same (or similar) synthetic route using phenols with various functional groups in place of the *tert*-butyl (e.g. *para*-pentylphenol,⁹ *para*-octylphenol,¹⁰ biphenyl-4-ol,¹¹ ...) has been demonstrated to be viable for the synthesis of thiacalixarenes with other functional groups than butyl in this position. In some cases, the use of microwave irradiation in tetraethyleneglycol dimethylether solvent has been shown to increase the rate and the yield of the synthetic reaction.^{12, 13}

1.A3: Conformations

In the case of *para-tert*-butylthiacalix[4]arene, there are four possible molecular conformations depending on the relative orientations of each phenol moiety; specifically the cone, 1,2-alternate, 1,3-alternate, and partial cone conformations, which are shown in figure 4.¹⁴

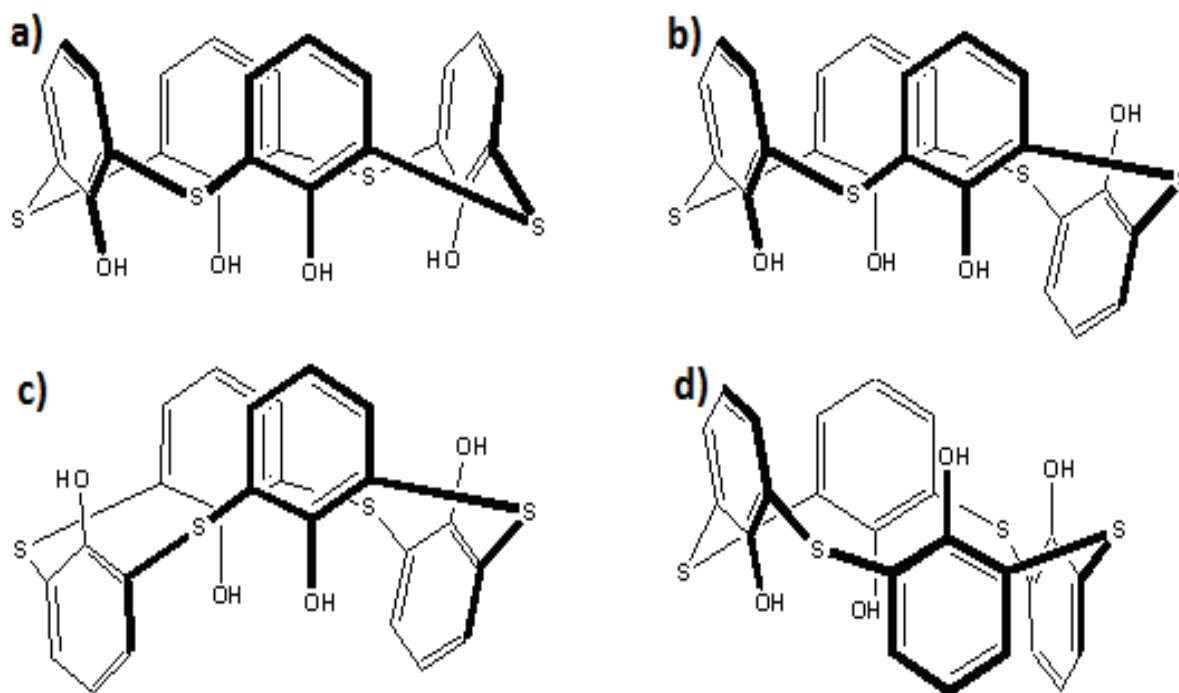


Figure 4: Possible conformations of thiacalix[4]arene: a) Cone, b) Partial Cone, c) 1,3-alternate, d) 1,2-alternate.

One significant difference of the thiacalixarenes as compared to equivalent methylene bridged calixarenes is the increased size of the macrocyclic ring. This larger size allows for total rotation of each phenol moiety around the C-S bonds.¹⁵ As such, the conformations can interconvert in solution, rendering conformational analysis by solution-state NMR difficult due to ‘averaging out’ of the signals. However, Nuclear Overhauser Effect Spectroscopy (NOESY) can differentiate between conformations to some extent.^{16, 17}

Differential Functional Theory (DFT) measurements and structures obtained by single crystal X-ray diffraction have demonstrated that the preferred conformation of *para-tert*-butylthiacalix[4]arene when crystallised is the cone conformation (C_{4v}), wherein the hydroxyl groups can benefit from hydrogen bonding to each other.¹⁸ There appears to be little energetic difference

between the three alternative conformations. The favoured conformation may change depending on certain factors such as binding to metal ions, or H-bonding interactions with solvent molecules.

As will be seen in the next section (**§1.A4.3**) the sulfur bridges of the thiacalixarene macrocycle may be oxidised, to varying degrees. In the case of one of these oxidation products, singly oxidised sulfinylcalix[4]arene (thiaSO herein), the conformational situation is more complex, as each oxygen atom may be positioned axially or equatorially on the sulfur atom.¹⁹ Thus, there are many possible conformations when considering every permutation of combinations of sulfur-oxygen stereochemistry and phenol moiety orientation. These stereoisomers can be 'locked' and isolated by etherification at the lower rim.

1.A4: Modifications

The basic thiacalixarene structure can be easily modified at the para-position (upper rim modification), on the hydroxyl groups (lower rim modification), and on the bridging sulfur atoms. Modification at the meta-position of the aromatic rings is also possible, but is less effective (and therefore less present in the literature) than these three main routes. Each type of functionalisation will be considered in turn in this section.

1.A4.1: Upper rim modification

Modification at this position has proven useful in terms of influence and control over the electronic properties of the molecule (delocalisation of electron density), its conformational preferences, and the range of solvents capable of solubilising it.^{9, 20-22} As mentioned above, some alternative parasubstitution, such as pentyl, phenyl, or adamantyl,²³ can be obtained by using the appropriate parasubstituted phenol in the calixarene ring-closing reaction. Direct *ipso* sulfonation and nitration of *para-tert*-butylthiacalixarene are both possible, and in the case of sulfonation the thiacalixarene tetrasulfonate product is water soluble.^{20, 24} Via Friedel-Craft type reaction using aluminium chloride the butyl group may be removed and replaced by hydrogen.²⁵ The resulting

thiacalix[4]arene is a suitable platform material for further substitution, some examples of which are illustrated in figure 5.

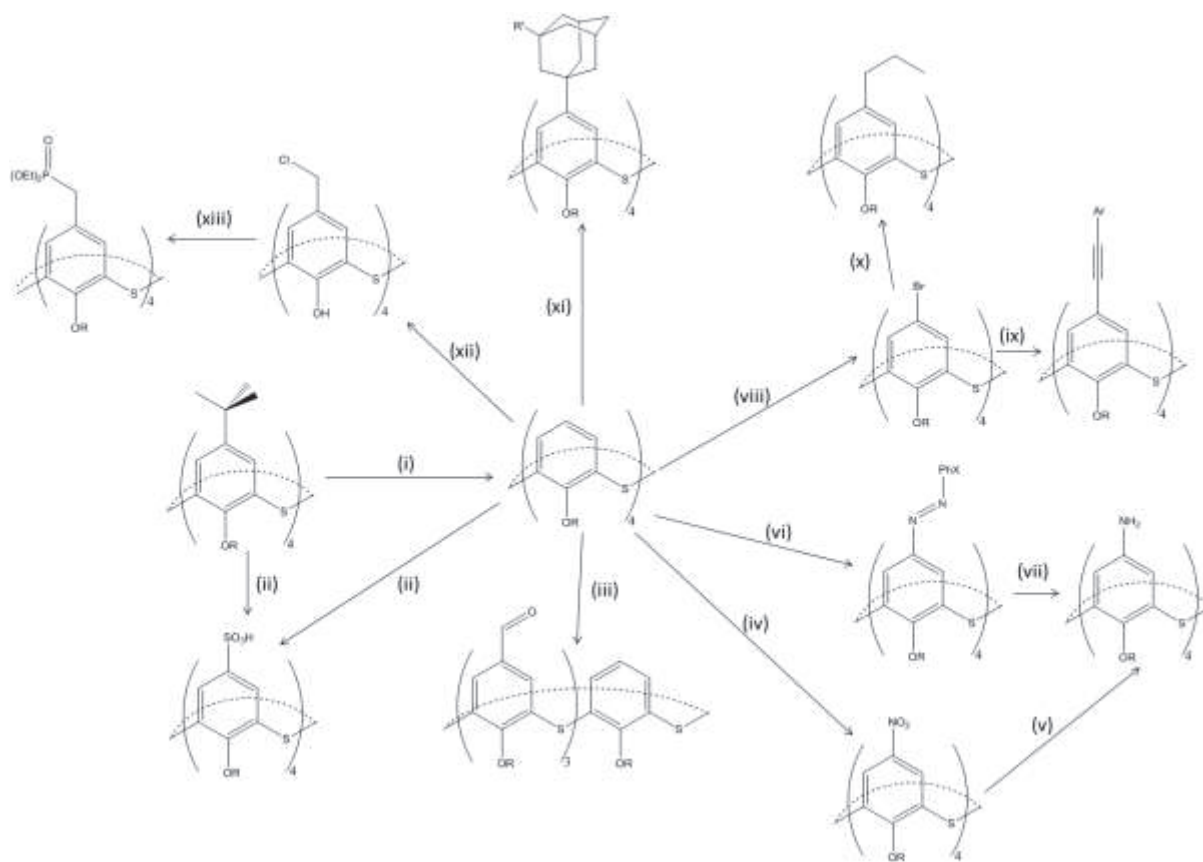


Figure 5: Summary of some of the modifications which are possible at the upper rim of thiacalix[4]arene. (i) phenol, AlCl_3 ,¹⁴; (ii) H_2SO_4 (conc.); (iii) HMT, TFA;²⁶ (iv) HNO_3 , AcOH;²⁷ (v) SnCl_2 , alcohol, HCl;²⁷ (vi) $\text{XPhN}_2+(\text{BF}_4)^-$;²⁸ (vii) NaOH, $\text{Na}_2\text{S}_2\text{O}_4$, H_2O ;²⁸

The modification of the upper rim of thiacalixarenes is thus shown to offer extreme versatility for the introduction of new functionality to these ligands.

1.A4.2: Meta substitution

Functionalisation at the meta position is much rarer than at the other possible positions, most likely due to various steric and electronic effects. Meta substitution has only been observed for thiacalixarenes which have a protecting propyl group at the lower rim. Functional groups which have been successively added at this position include chloromethyl,³² formyl,^{33, 34} halide (Cl, Br and I)³⁵ and nitro (which can then be reduced to an amino group).³⁶ A maximum of two phenol moieties in any

one calixarene molecule may be meta-substituted. Figure 6 shows the preference of thiacalixarene and calixarene for formylation under Gross conditions.

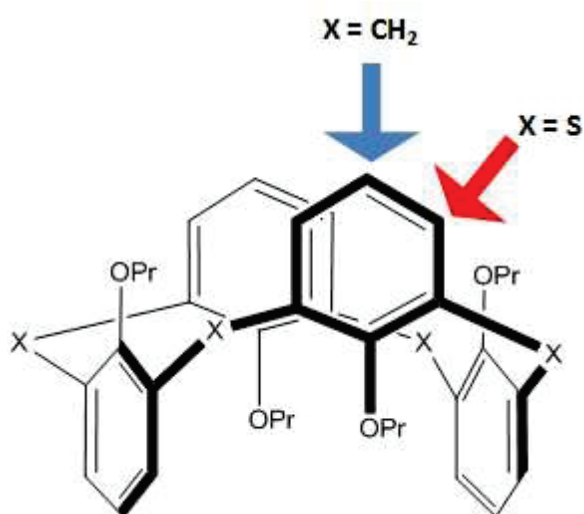


Figure 6: Stereoselectivity of Gross formylation for tetrapropylcalix[4]arene (blue arrow) and tetrapropylthiacalix[4]arene (red arrow).³³

Mercuration of tetrapropoxythiacalix[4]arene, as illustrated in figure 6, results in a mixture of upper rim and meta substituted derivatives.³⁷ Figure 7 shows how the mercurated compounds can undergo carbon – carbon bond forming reactions; however, only the upper rim isomer can form direct bonds to another thiacalixarene molecule (dimerisation, figure 8).³⁸

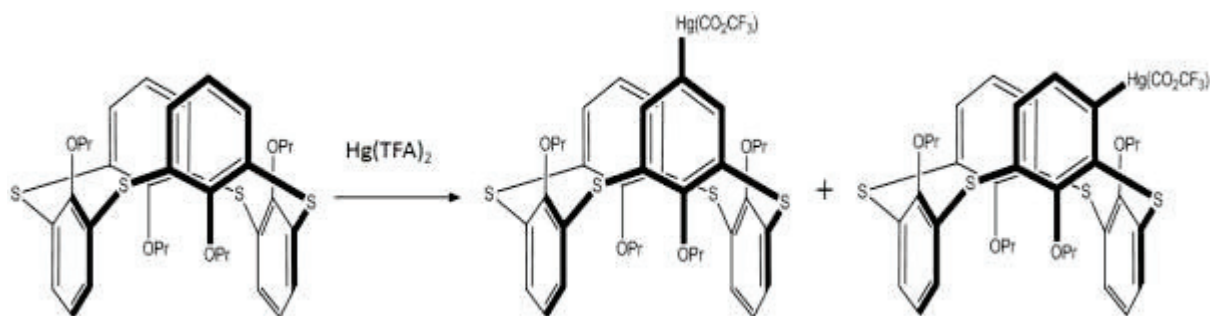


Figure 7: Mercuration of tetrapropylthiacalix[4]arene.³⁷

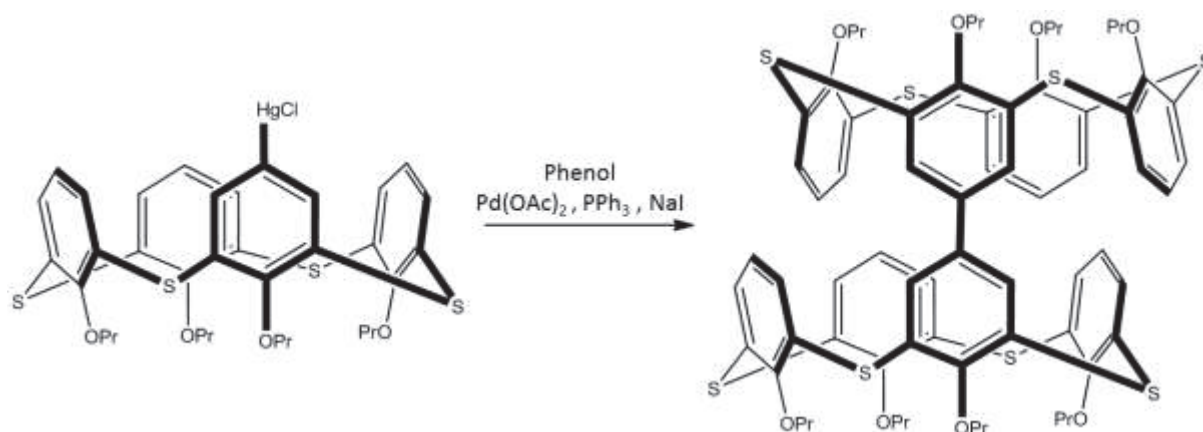


Figure 8: Dimerisation of tetrapropylthiacalix[4]arene.³⁸

1.A4.3: Functionalisation on the sulfur atoms

The most important functionalisation at this point is oxidation, either mono-oxidation (resulting in a sulfinylcalixarene), or di-oxidation (giving the sulfonylcalixarene); figure 9 shows the structure of these products.³⁹

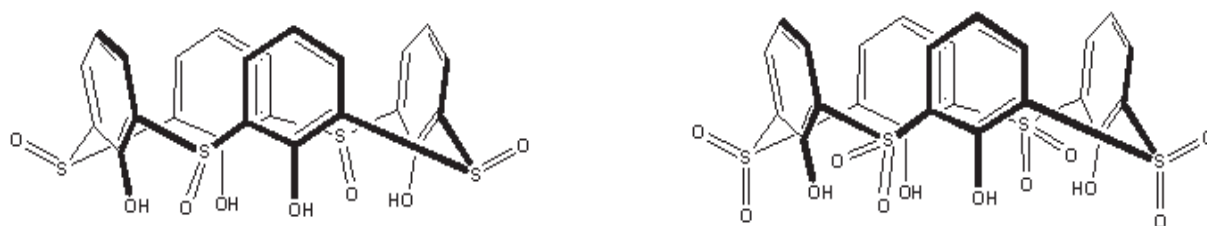


Figure 9: Structure of sulfinylcalix[4]arene and sulfonylcalix[4]arene.

For sulfinylcalixarenes, the many permutations of orientation of the oxygen atoms and the phenol moieties with respect to each other results in a large number of stereoisomers, two of which are illustrated in figure 10.¹⁹ These stereoisomers may display different reactivity and solubility from each other. Oxidation is carried out using sodium perborate, hydrogen peroxide and acetic acid; by varying the quantity of perborate the reaction can be tuned towards a certain oxidation product. An alternative oxidation reaction is possible using only trifluoroacetic acid with hydrogen peroxide, thereby using no inorganic reagents.²⁴

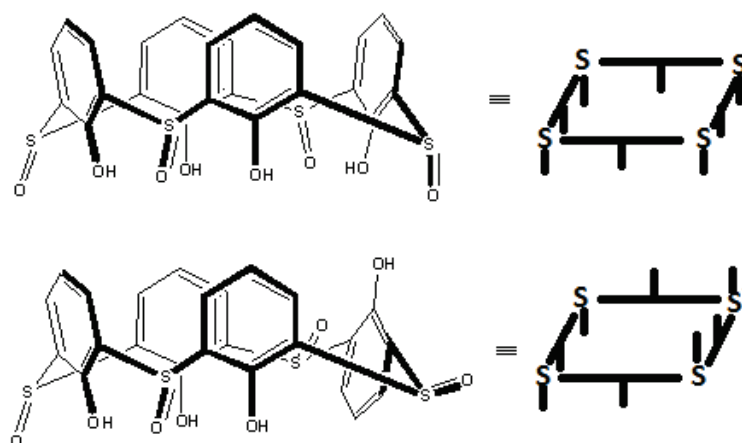


Figure 10: A representation of some stereoisomers of sulfinylicalex[4]arene.

The main alternative functionalisation to oxidation on the sulfur bridges is (mono- or di-) alkylation to give a sulfonium salt.^{40,41} The alkylating agent is either alkoxytriflate or a trialkyloxonium salt, and the phenol groups must be protected with an ether functionalisation prior to reaction. In the case of dialkylated thiacalixarenes, the alkylated sulfur atoms are always found at distal positions on the ring. When the hydroxyl groups are unprotected, it is possible by a Mitsunobu reaction to form an alkyl chain between a sulfur atom and the oxygen atom on the neighbouring phenol, as in figure 11.⁴²

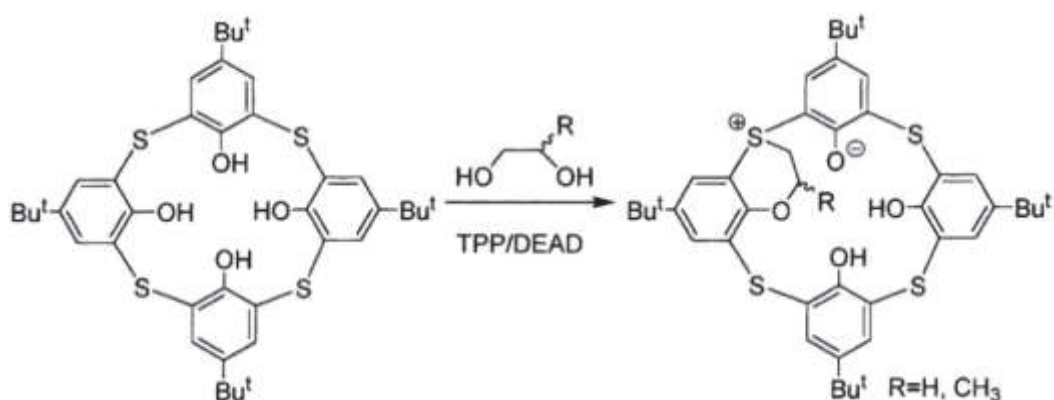


Figure 11: Sulfur – oxygen bridging by Mitsunobu reaction.⁴²

Finally a sulfilimine derivative is obtained by the reaction of methyl-protected thiacalix[4]arene with chloramine T (figure 13). As seen in figure 12, this reaction with the unprotected calixarene unexpectedly gave a monospirodienone product.⁴³

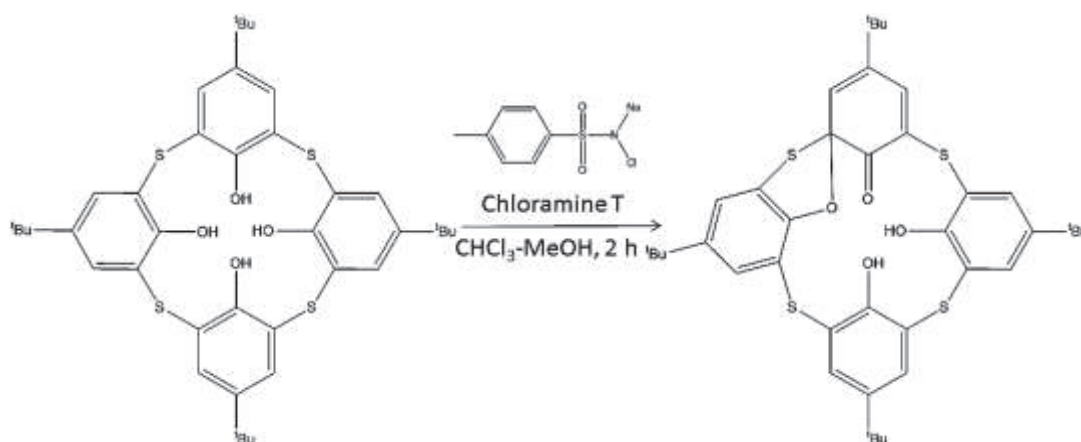


Figure 12: Synthesis of monspiropdienone derivative of para-tert-butylthialix[4]arene.⁴³

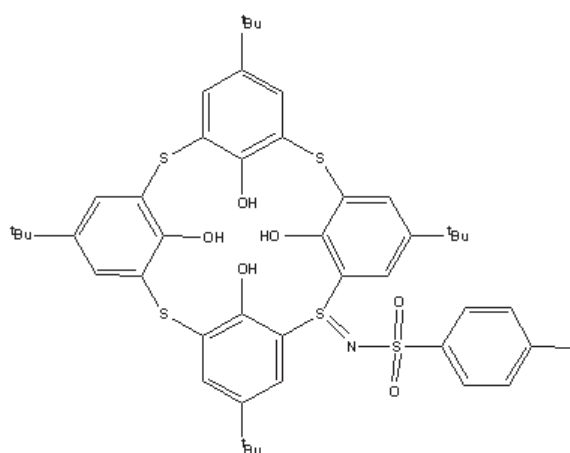


Figure 13: Mono-sulfilimine derivative of para-tert-butylthialix[4]arene.⁴³

1.A4.4: Lower rim substitution

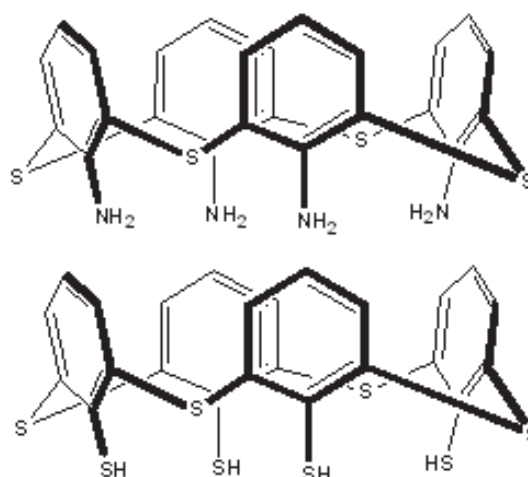


Figure 14: Structures of thialix[4]aniline and mercaptothialix[4]arene.

It is possible to replace the hydroxide of phenol with amino groups (thialixaniline) or thiol groups (mercaptothialixarene); the structures of these derivatives are shown in figure 14. The

amino derivative is obtained by substitution of hydroxyl (or methoxy) group(s) with benzylamine followed by conversion of the benzylamine into the amino variant.⁴⁴ Thiacalixanilines have been shown to demonstrate interesting specificity in metal extraction applications.⁴⁵ Conversion of NH₂ groups into diazonium salts provides a suitable starting material for the Griess reaction, which results in iodothiacalixarenes.⁴⁶

Mercaptothiacalixarenes are obtained by the Newman-Kwart rearrangement of O-bonded thiocarbamates to S-bonded thiocarbamates, which can be reduced to the corresponding thiol with lithium aluminium hydride or hydrazine hydrate.⁴⁷ Heating of the intermediate species tetra-S-bonded(N,N-dimethylthiocarbamate)thiacalix[4]arene to approximately 400° C gives rise to thiacalixanthrene compounds.⁴⁸

Etherification is an important functionalisation at this position. Typically this type of reaction is carried out to protect the hydroxyl group during further reactions, to add some further function to the calixarene molecule, or to lock the molecule in a specific conformation.⁴⁹⁻⁵² Selective substitution at one, two, three or all four phenolic oxygen atoms has been demonstrated. This section will detail each of these modifications in turn.

1.A4.4.1: Monosubstitution

Monoetherification can be carried out directly by the Williamson nucleophilic substitution reaction in the correct stoichiometric quantities.⁵³ This method involves reaction of the alcohol groups on the ligand with an alkyl halide in the presence of a base, usually an alkaline metal carbonate. It is possible to observe interesting steric effects with the choice of ether group to be substituted; figure 15 for example shows two etherification reagents which differ only by one carbon in the carbon chain, yet one reagent (with the ethyl group) favours the mono-substituted product whereas the other (with the propyl group) preferably forms the tetrasubstituted product.⁵⁴

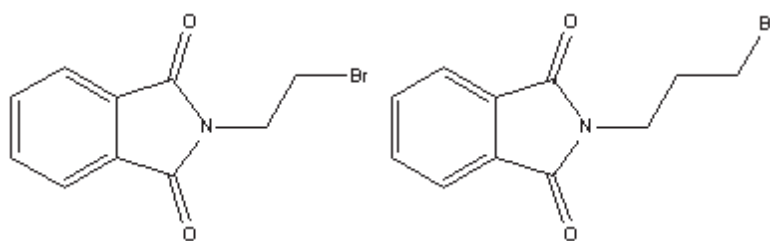


Figure 15: Structures of N-(bromoethyl)-phthalimide (left) and N-(bromopropyl)-phthalimide (right); structurally similar molecules which show different reactivity to thiacalixarene.⁵⁴

Another method is the selective cleavage of one O-C bond in a disubstituted thiacalixarene using tetrabutylammonium ions (figure 16).⁵⁵ Monoethers of thiacalixarene adopt the cone conformation.

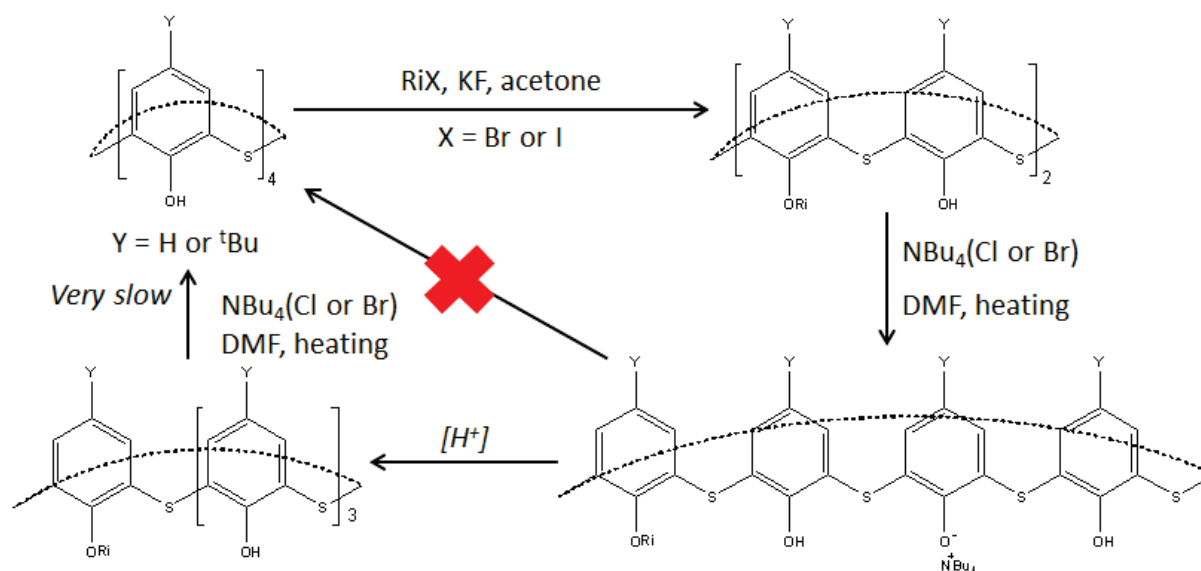


Figure 16: Route to monofunctionalised product via disubstituted transition species.⁵⁵

1.A4.4.2: Disubstitution

Substituent groups can be either adjacent (*syn*) or opposing (*distal*) to one another. Due to steric hindrance, 1,3 substitution (giving the distal product) is almost always preferred. Disubstitution is very common in the literature in comparison to mono- and tri-substitution. Tri- and tetra-substituted derivatives with mixed substituents can be obtained by further etherification on disubstituted thiacalixarene.⁵⁶ Figure 17 shows an example of a thiacalixcrown; thiacalixcrowns are compounds which contain an (ethyleneglycol)_n linking chain between two phenolic oxygen atoms, and are of great interest in the field of coordination chemistry.⁵⁷ In the example shown the crown

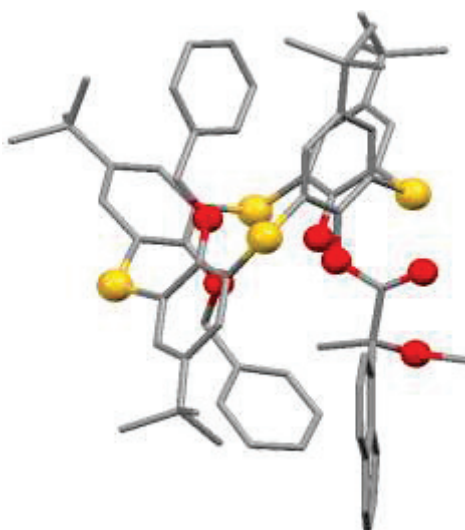


Figure 18: X-ray diffraction structure of dibenzylpara-*tert*-butylthiacalix[4]arene (methoxynaphthylpropionate). Colour key: C = grey, S = yellow, O = red. H atoms omitted for clarity.⁶¹

1.A4.4.4: Tetrasubstitution

This is the simplest of the lower rim substitution processes herein described. The standard method is Williamson nucleophilic substitution using alkyl halide and a base in polar aprotic solvent (such as acetone) and usually dry conditions. The solid state conformation of the product depends upon the starting compound used, the nature of the base, the solvent and the reaction conditions, and a conformational mixture may be produced by a single reaction, as shown in figure 19.^{19, 62} However, it may be stated that in general tetraalkylated thiacalix[4]arenes prefer to adopt the 1,3-alternate conformation, to minimise steric strain.⁶² Thiacalixarenes tetrafunctionalised with nitrile groups in this conformation have been observed to form networks when reacted with silver ions.^{63, 64} Depending on the source of silver used, the thiacalixarene backbone of these systems may link single ions (a 1:1 metal ion to ligand ratio) or they may link organised clusters of silver (in a 10:1 ratio).

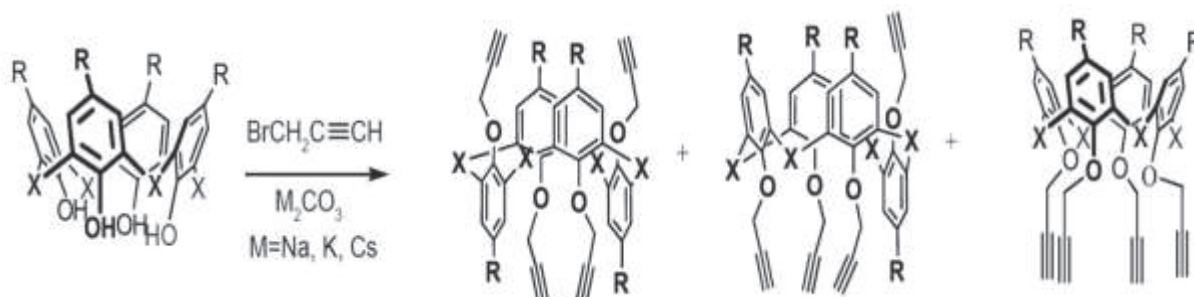


Figure 19: Synthesis of tetraacetylythiacalix[4]arene in different conformations.⁶²

1.A5: Conclusion

There are many criteria to consider when judging potential candidates for structuring ligands in the creation of metal cluster complexes. These include availability / ease of synthesis, cost, denticity and complexing power for a range of metal ions, flexibility, modifiability, stability and ease of processing (solubility *etc.*). The versatility of thiacalixarene-type molecules and their high performance with regards to these criteria, as outlined above, make them very attractive 'platform molecules' for this purpose. Furthermore, their electron rich cavity affords them strong host-guest properties which can combine in interesting ways with complex formation. For these reasons, this family of compounds has been selected for study in this doctoral work.

1.B: Metal Complexes of Thiacalixarenes

1.B1: General

The free thia-, sulfinyl-, or sulfonyl-calixarene molecules possess a stronger complexing power towards a variety of metal ions than their 'usual' calixarene analogues, rendering them viable ligands in their own right.³⁹ An alternative technique for the creation of thiacalixarene based metal complexes is to prefunctionalise some part of the molecule with a known complexing function (such as crown ether, pyridyl, ...) before reaction with the metal source material.^{65, 66} As a result of the above-mentioned versatility of this ligand family, an enormous range of types of complex have been made and analysed using them. This work, however, will primarily consider manganese complexes of sulfonylcalix[4]arene, without any added complexing functionality. Figure 20 shows a representation of these complexation reaction pathways.

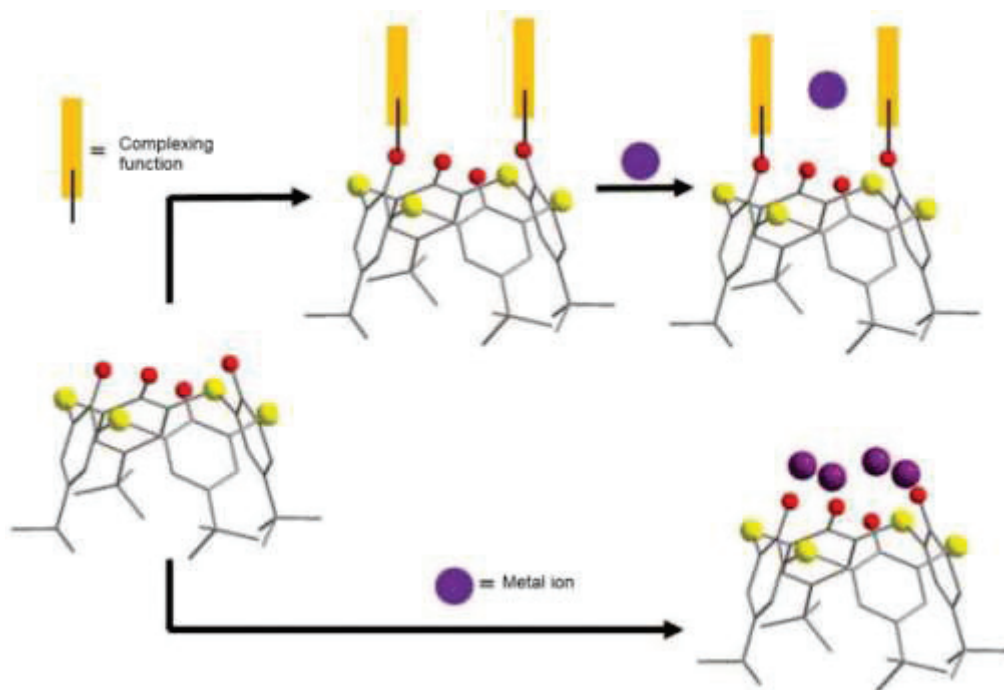


Figure 20: Representation of complexation of thiacalixarene, with direct complexation or prefunctionalisation.⁶⁷

1.B2: Aggregates and Binding Modes

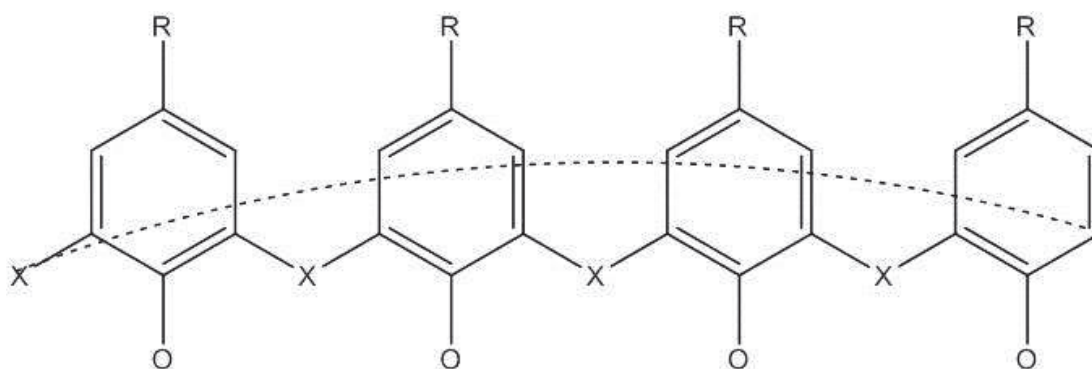


Figure 21: Representation of the binding sites on a thiacalix[4]arene ($X = S, SO$ or SO_2).

Complexes of unfunctionalised *para-tert*-butylcalix[4]arene form in the cone, or in the 1,2-alternate conformation. Most commonly the denticity of the ligand is between 3 and 8, which is the maximum number of binding atoms per ligand molecule (figure 21). The modes of binding will be considered separately in this section. The inherent layout of the molecule tends to prefer imposing a certain coordination geometry upon the complex, with two phenolic oxygen atoms and a bridging 'X' atom ($X = S, SO$ or SO_2) in a triangular formation binding. However, the flexibility of the ligand also allows it to conform to alternative geometries in many cases.

1.B2.1: Complexing power of the ligands

Extraction studies have been carried out on the ligands of the thiacalixarene family which demonstrate their superior complexing power in comparison to the standard methylene-bridged calixarenes.³⁹ Furthermore, the degree of oxidation of the ligand can be used to fine-tune the type of metal to which it will preferentially bind by virtue of the hard-soft acid-base properties, i.e. fully oxidised sulfonylcalix[4]arene binds more strongly to harder ions than thiacalix[4]arene. The intermediate sulfinylcalix[4]arene could extract metals which the other two ligands could not, such as Al^{3+} , Ru^{3+} , V^{5+} and Be^{2+} . None of the three ligands were observed to be capable of extracting the singly charged alkali metals. It has been demonstrated that this family of molecules is well suitable for the complexation of essentially all of the metallic elements of the periodic table; however this results in a lack of selectivity towards any specific metal which is detrimental to their effectiveness as extraction agents. It has also been demonstrated that a great many of these complexes are polynuclear, even including several examples of heterometallic complexes, in testament to the high multidentate complexing capacity of these compounds.

1.B2.2: Octadentate binding *Harris notation [4.22221111]*⁶⁸

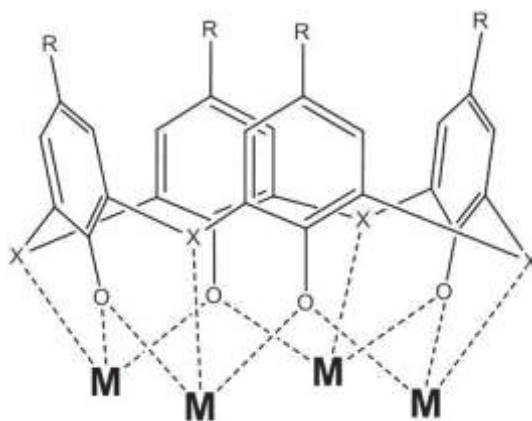


Figure 22: Octadentate binding mode.

This binding mode is only observed in the cone conformation, with transition metal ions in the +2 oxidation state or lanthanide ions in the +3 state. Each phenolic oxygen forms bonds to two metal ions, and each X atom bonds to one metal (Figure 22). Often these types of complexes form

'sandwich' type structures where two ligands bind a square planar arrangement of four ions, giving a trigonal prism coordination geometry (this geometry may be distorted, or capped by other ligands).⁶⁹ A heterometallic $[\text{ZnLn}_3]$ complex of this sandwich structure type was observed with a geometrical distortion such that one of the ligands is octadentate and the other is heptadentate.⁷⁰ In other cases, square planes of bound metal ions may form the faces of polyhedral clusters, or may be linked by polydentate ligands (e.g. bipyridyl) to form coordination polymers.⁷¹ These polyhedra can reach large dimensions (for example, this Ni_{40} coordination cage reported by Hang *et al*)⁷² and are also known as nanocages. The nanocage structure may itself contain a core cluster of metal ions; for example the simple reaction of $\text{M}(\text{DMSO})_6(\text{BF}_4)_2$ salts ($\text{M} = \text{Ni}$ or Co) with thiacalixarene in the presence of base results in an M_{32} species wherein the M_{24} nanocage encapsulates an M_8 core structure.⁷³ Figure 23 shows an example nanocage structure.

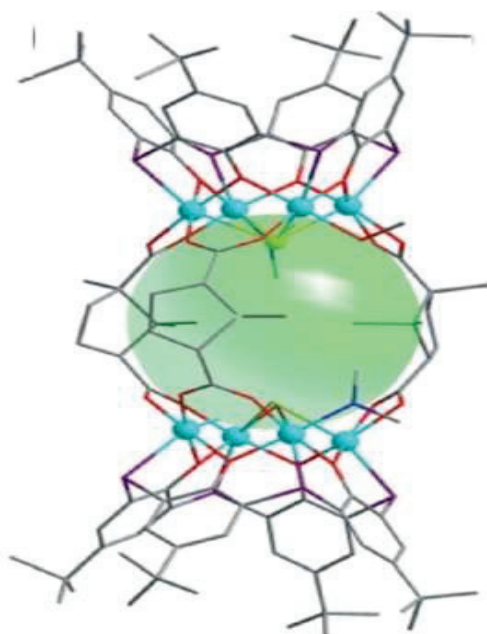


Figure 23: A Co_8 'coordination cage' with two thiacalix[4]arene ligands; the interior space is highlighted in green. Colour key: C = grey, S = purple, O = red, Co = cyan. H atoms omitted for clarity.²²

1.B2.3: Heptadentate binding [3.2211111]

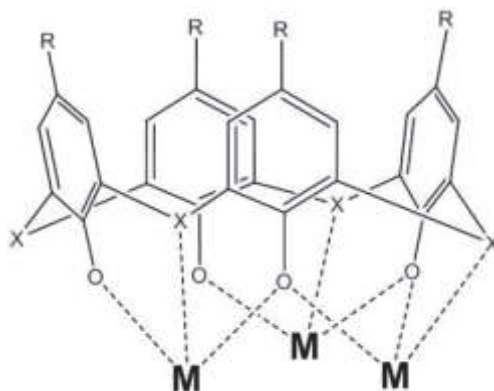


Figure 24: Heptadentate binding mode.

This binding mode is extremely uncommon. Only one publication was found which detailed a complex wherein uniquely this type of binding occurred; a trinuclear complex of zinc(II) with *para-tert*-butylthiacalix[4]arene.⁷⁴ The binding consists of two μ -2 oxygen atoms, two singly bound oxygen atoms, and three of the four available sulfur atoms form one bond each (Figure 24). Two ligands form a distorted sandwich around the Zn_3 plane, with each metal centre showing approximately octahedral coordination geometry, as illustrated in figure 25.

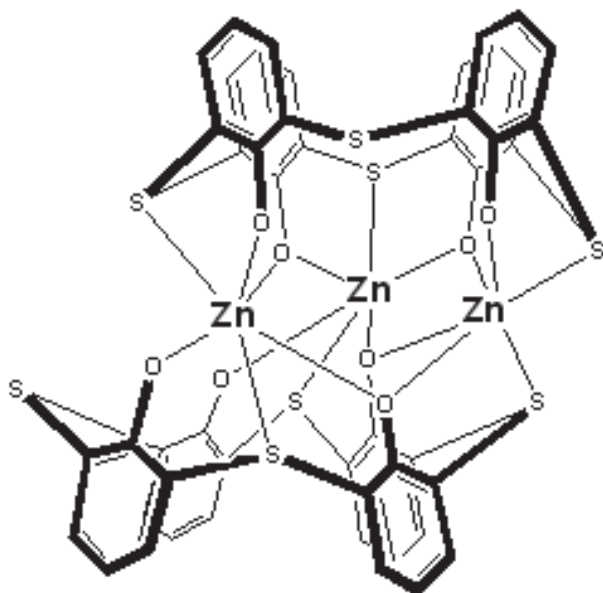


Figure 25: A trinuclear zinc complex with *para-tert*-butylthiacalix[4]arene ligands in the heptadentate binding mode. *Tert*-butyl groups and H atoms are omitted for clarity.⁷⁴

1.B2.4: Hexadentate binding [2.111111]

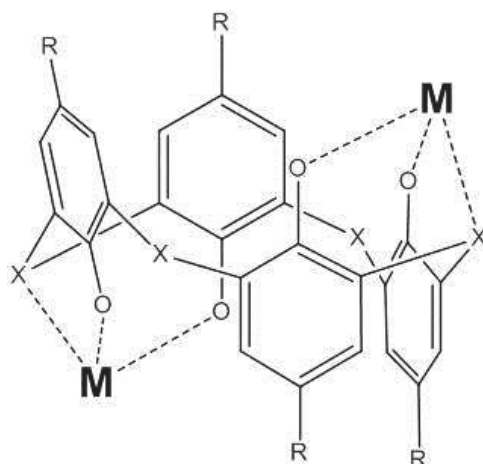


Figure 26: Hexadentate binding mode.

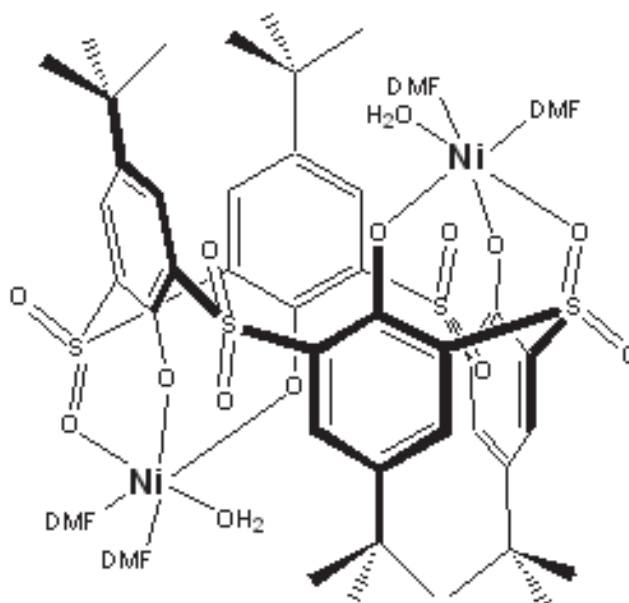


Figure 27: A dinuclear nickel cluster with *para-tert-butylthiacalixarene* demonstrating the hexadentate binding mode.⁷⁷

With the exception of two of the bridging X atoms, all of the eight available binding atoms are involved in one ligand – metal bond (Figures 26). This type of binding generally occurs for dinuclear complexes of certain metals in the +2 oxidation state with the ligand in the 1,2-alternate conformation. Both metal centres have an octahedral coordination geometry, where the empty coordination sites are filled by other ligands, such as solvent molecules. Some unusual variations on this structure include dititanium(IV) complexes, where the ligand may be 1,2-alternate or cone, and a disordered cubane containing four lanthanide ions.^{75, 76} In this latter complex, two hexadentate

sulfonylcalixarenes in the cone conformation are found in terminal positions around the Ln₄ core.

Figure 27 illustrates a dinickel complex demonstrating the hexadentate binding mode.

1.B2.5: Pentadentate binding [2.21111]

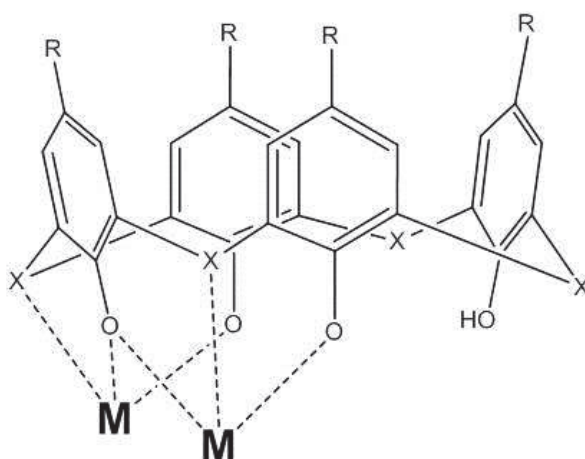


Figure 28: Pentadentate binding mode.

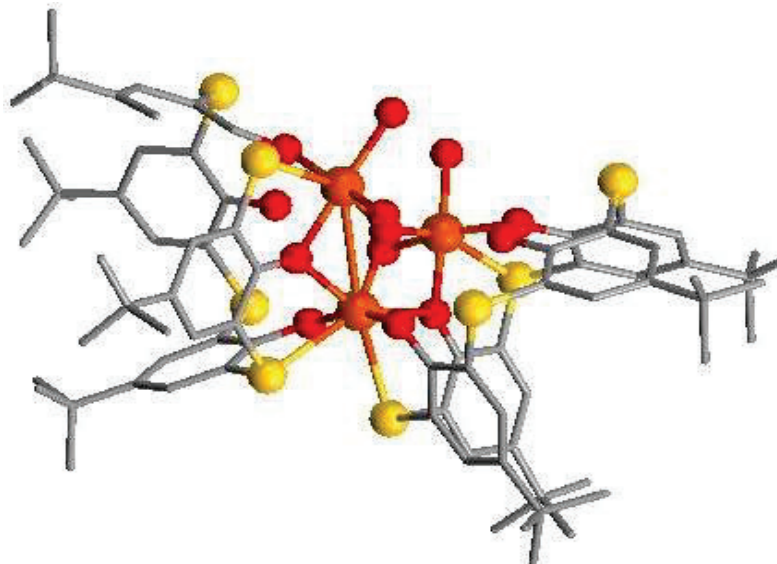


Figure 29: X-ray diffraction of complex demonstrating pentadentate binding, with Fe₃O core. Colour key: C = grey, S = yellow, O = red, Fe = orange. H atoms omitted for clarity.⁷⁸

One μ -2 phenolic oxygen, two singly bound phenolic oxygens and two bridge atoms are implicated in this binding mode (Figure 28). Most commonly this mode occurs for +3 oxidation state

metals and the cone conformation. An “asymmetric sandwich” type structure may be formed. One interesting example of this type of binding is observed in a complex of iron(III), as shown in figure 29.⁷⁸ The core structure of the complex is composed of $[\text{Fe}_3(\mu_3\text{-O})]$; this structure is well known for some transition metals for its particular magnetic properties.^{79, 80} The iron ions are not identical; two are in an octahedral coordination environment and the third is seven-coordinate.

1.B2.6: Tetradentate binding [1.1111]

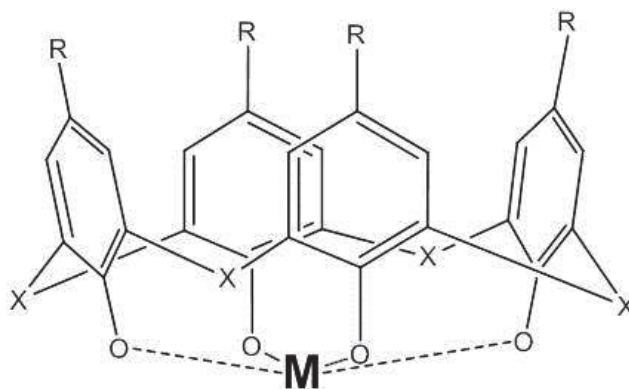


Figure 30: Tetradentate binding mode.

Figure 30 shows the tetradentate binding mode; compared to the other binding modes listed so far, this type of complex is relatively rare. The metals involved are generally alkaline earths, although it has also been observed for complexes of vanadium, tantalum, and zirconium (an example is seen in figure 31).⁸¹⁻⁸³ The macrocycle must be in the cone conformation; each phenolic oxygen atom forms one bond to a central metal ion. One of the principal complexes to be investigated in this work is a complex of Mn(III) which conforms to this type of complexation. Tetradentate binding also occurs in some polynuclear clusters of group I metals, including potassium, sodium and lithium.⁸⁴ A subverted version of this type of binding is observed in a cluster of palladium.⁸⁵ The metal centre links two ligands together by binding to two oxygen atoms from each.

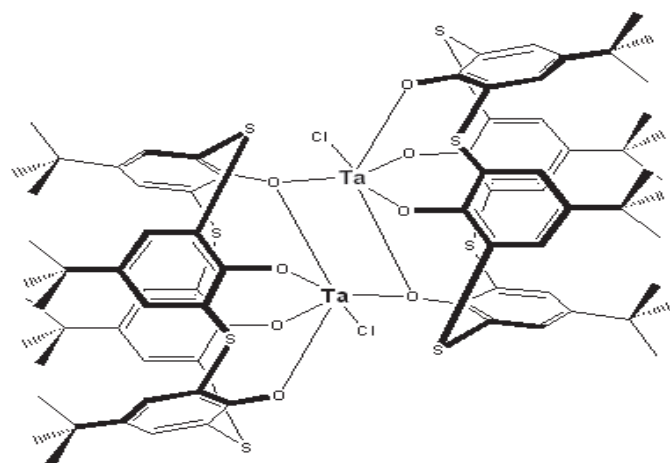


Figure 31: Dimer complex of tantalum illustrating tetradentate binding.⁸¹

1.B2.7: Tridentate binding [1.111]

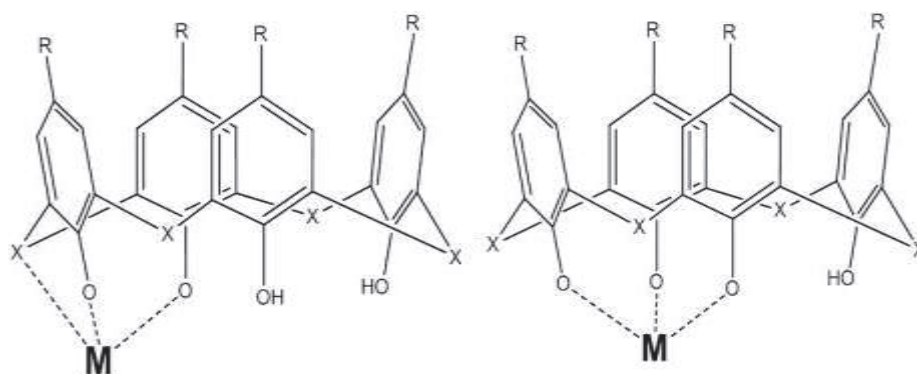


Figure 32: Tridentate binding mode.

There are two distinct possibilities for forming this binding mode: either $(2O + 1X)$ or $(3O)$ atoms form a bond to the metal centre (Figure 32). Generally this type of complex arises for the harder metal ions of the early transition series, such as Ti(IV), Mo(IV) and V(V).^{86, 87} Other possibilities include potassium and zinc.^{88, 89} NMR study of a zinc complex, shown in figure 33, with tridentate binding observed that the zinc ion was mobile upon the ligand, “gliding” between the four equivalent binding positions. The complex $[(\text{thiaS})\text{Ti}(\text{cp})]$ (cp = cyclopentadienyl) can be treated with a source of molybdenum to give the heterometallic complex $[(\text{thiaS})\text{TiMoH}(\text{PMe}_2\text{Ph})_2]$. This bimetallic complex displays pentadentate binding: the titanium ion is ligated by the four oxygen atoms, two of which bridge to the molybdenum ion which also has a bond to one of the sulfur atoms.⁸⁶ In this way the binding resembles a combination of conventional tridentate and tetradentate binding.

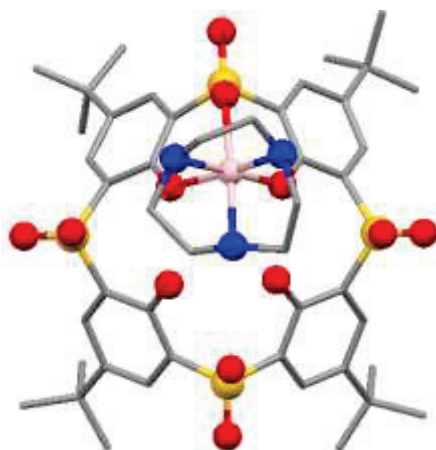


Figure 33: Representation of a 'mobile' zinc complex with tridentate binding of para-*tert*-butylsulfonylcalix[4]arene.⁸⁹ Colour key: C = grey, S = yellow, O = red, N = blue, Zn = pink. H atoms omitted for clarity

A single example of a complex demonstrating uniquely bidentate binding for a thiacalixarene ligand was found in the bibliography research: $[\text{Ru}(\text{bipy})_2(\text{thiaS})]$, shown in figure 34.⁹⁰ It was applied to the quenching of fluorescence in DNA.

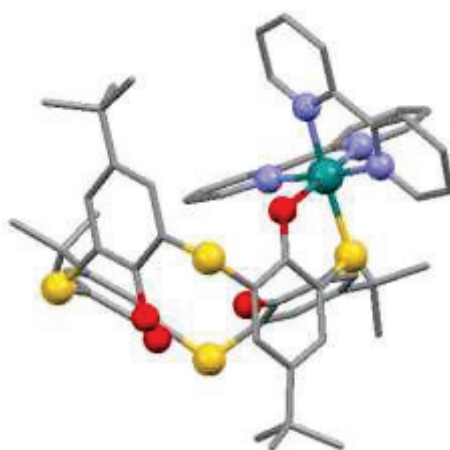


Figure 34: Structure of $[\text{Ru}(2,2'\text{-bipyridine})_2(\text{para-}i\text{tert-butylthiacalix[4]arene})]$, with one bonding oxygen atom and one bonding sulfur atom on the ligand. Colour key: C = grey, S = yellow, O = red, N = blue, Ru = teal. H atoms omitted for clarity.⁹⁰

1.B3: Synthesis of complexes and aggregates

As is logical, complexes are synthesised by introducing the ligand to a source of metal ions (i.e. a metal salt), generally in alkaline organic medium. This may be achieved via one of two reaction routes. The first (standard or conventional conditions) involves reaction under ambient pressure, either with or without heating. The second pathway is known as the solvothermal method, and requires the reaction to take place in a sealed vessel under autogenerated pressure at a temperature

higher than the boiling point of the solvent.^{91, 92} The variables under consideration will be described consecutively herein.

1.B3.1: Metal salt

If the anions involved in the metal salt are strongly complexing (for instance chloride, acetate) they may implicate themselves into the final product, and have a direct structuring influence.⁹³ In the case of less strongly coordinating ligands, such as nitrate, this influence is much less simple to define. Figure 35 shows an illustrative example; for a certain set of reaction conditions the reaction of cobalt(II) nitrate with *para-tert*-butylthiacalix[4]arene was found to produce a Co₁₂ aggregate complex. The same reaction conditions, but using cobalt(II) chloride as the cobalt source, gives rise to a Co₁₆ 'wheel' complex composed of four square planar Co₄ 'faces'.⁹⁴ In some cases a basic anion, such as acetate, can aid in the deprotonation of the ligand and therefore help solubilisation of the ligand and drive the complexation reaction.

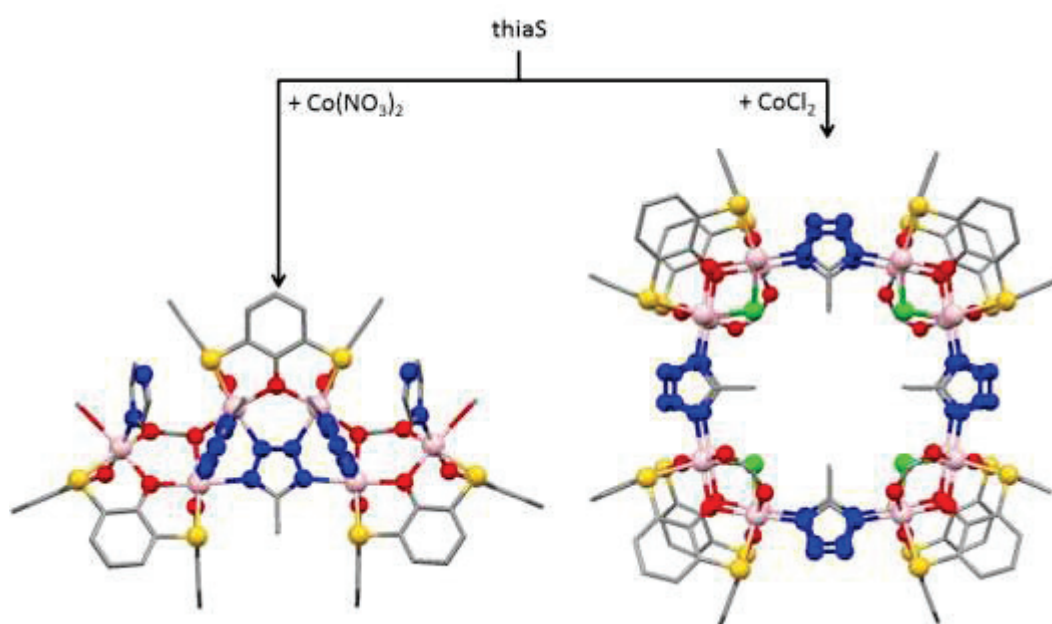


Figure 35: Effect of cobalt starting material on structure of the final complex product. Colour key: C = grey, S = yellow, O = red, N = blue, Cl = green. H atoms omitted for clarity.⁹⁴

1.B3.2: Base

Normally, the ligand forms complexes in an anionic (deprotonated) form. The pH conditions therefore play an important role in these reactions. Most commonly, amine-type bases are used. In

some cases the complex can be formed without adding base; as is the case for certain thiacalixarene complexes of iron(II), where adding base after complex formation causes oxidation to iron(III) in the presence of air.⁹⁵

1.B3.3: Solvent

There are some issues with low solubility of some thiacalixarene-based ligands, however the presence of a deprotonating agent generally improves the solubility of the compound. Organic solvents, specifically chloroform and dimethylformamide, seem to be the most used in the literature. It is possible for some solvents to decompose under solvothermal conditions into various substances, which may include complexing functions of their own right. As with metal salts, solvent molecules may incorporate themselves into the complex by coordination, or may also be a part of the crystal structure of the final product.⁹²

1.B3.4: Pressure and temperature conditions

As outlined above, these reactions may be carried out via conventional or solvothermal methods. The conventional conditions involve agitation of the reaction mixture under ambient pressure, either with or without heating. This is generally followed by a crystallisation step to obtain a pure crystalline product. Optimisation of the crystallisation step can play an important role in the quality of the product.

The alternative method, solvothermal synthesis, involves placing the reaction mixture in a sealed vessel (an autoclave), as represented in figure 36, and heating to a temperature above the boiling point of the solvent(s). Heating a fixed volume increases the pressure in the vessel, which can give greatly improved yield or crystallinity of the product compared to the standard conditions and can even give entirely different products. In particular, this allows reactions of thiacalixarenes to be carried out in alcohol / water mixtures, in which they are totally insoluble in normal circumstances.

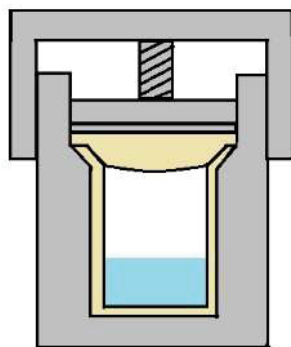


Figure 36: Cross section representation of autoclave synthesis.

There are no known hard and fast rules concerning what the outcome of either of these methods will be; they can be complementary or completely opposing. Thus it is difficult to predict before experimentation which set of conditions is more favourable for the desired product.

1.B4: Properties of aggregates

With the aim of exploiting the synergistic effect of polynuclear clusters, most studies of these aggregates are concerned with magnetic, optical or catalytic properties. Optical properties make up a large part of the central research of this work, and will be discussed in greater detail in the next section of the bibliographic chapter.

1.B4.1: Magnetism (Single Molecule Magnets)

A single molecule magnet (SMM) is a compound which behaves as a classical magnet, displaying magnetic bistability below a certain magnetic transition temperature.⁹⁶ In magnetic cluster compounds, this behaviour arises due to the interactions between magnetic metallic nuclei. The bistability gives rise to a hysteresis loop in the plot of magnetic response against increasing and decreasing external magnetic field, and represents the two magnetic orientations which are favoured due to the influence of the external field.⁹⁷ Some SMMs show incredibly long relaxation times for the magnetisation. The SMM behaviour is derived from both the overall spin S and the magnetic anisotropy D of the molecule. These two properties are antagonistic, so a compromise between them must be reached in order to optimise the magnetism.

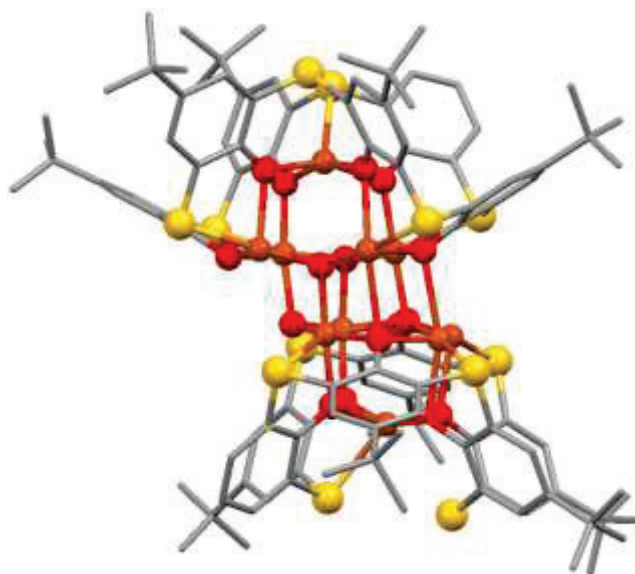


Figure 37: Structure of ferromagnetic Cu_{10} SMM complex. Colour key: C = grey, S = yellow, O = red, Cu = orange. H atoms omitted for clarity.⁹⁸

In the case of the thiacalixarene type ligands, to the best of our knowledge so far only one cluster complex demonstrates dominant ferromagnetic interactions: a decanuclear copper cluster with *para-tert*-butylthiacalix[6]arene and bridging oxo-, hydroxo- and acetate ligands shown in figure 37.⁹⁸ 6-membered thiacalixarene macrocycles remain less accessible in terms of ease of synthesis than their 4-membered counterparts. Magnetic complexes of thiacalix[4]arenes more normally feature antiferromagnetic interactions between the metal centres. Many such aggregates consist of a square planar arrangement of ions in the +2 oxidation state. This configuration with cobalt(II) or manganese(II) ions has only antiferromagnetic interactions;⁹⁹ when four nickel(II) ions are involved then the four interactions between adjacent ions are antiferromagnetic whereas the two opposing ion interactions are ferromagnetic.¹⁰⁰ This gives rise to an overall antiferromagnetic system (ferrimagnetism).

1.B4.2: Porous materials (“Metal-Organic Supercontainers”)

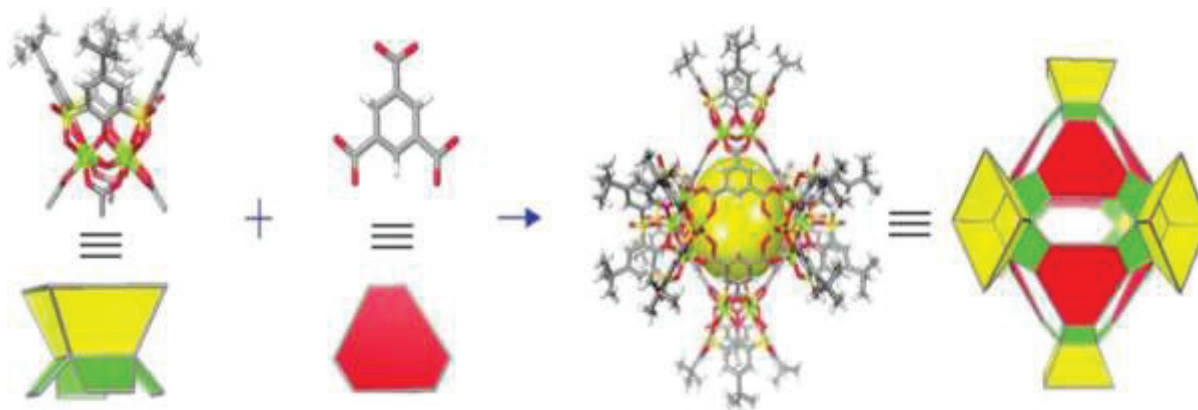


Figure 38: Formation of an MOSC material with *para-tert-butylsulfonylcalix[4]arene*. Colour key: C = grey, S = yellow, O = red, H = white, Ni = green.¹⁰¹

Certain types of macrocyclic compound are well-known to demonstrate the ability to contain other molecules within their interior space in a host-guest interaction. This property gives them use in applications such as molecular sensors and drug encapsulation / delivery systems. ‘Supercontainer’ materials consist of several such macrocycles bound together in some way, for instance via hydrogen bonding or Van der Waal’s interactions.¹⁰¹ Further, by analogy with the chemistry of metal-organic framework (MOF) materials, networks of supercontainers can be assembled by complexation to transition metals, giving rise to metal-organic supercontainers (MOSCs), such as the example shown in figure 38. Both the strength of thiacalixarene as a complexing agent, and the interior cavity within the polyaromatic macrocycle make it a highly interesting candidate for use in these types of material.

1.B4.3: Catalysis

The propensity of thiacalixarene and its derivatives to form polynuclear complexes is of great interest in the field of catalysis, especially with regard to heterometallic complexes which often have very different reactivity to their homometallic analogues. One strategy for forming such complexes is to use a structure-directing ‘template’ ligand; a description which applies to thiacalixarene with its multiple and varied coordination sites. Many studies on the complexes of thiacalixarene type ligands

as catalysts in organic synthesis have been carried out, with transition metals such as titanium, molybdenum and tungsten acting as the metal centres.^{86, 102}

1.B5: Luminescence

Thiacalixarene is known to be a chromophore (as are its derivatives) which fluoresces under the effect of UV or blue irradiation in the domain 200-350 nm approximately (absorption at $\lambda_{\text{max}} = 227$ and 297 nm, emission at $\lambda_{\text{max}} = 331$ nm in DCM solvent).¹⁰³ This proof of optical activity is taken as a foundation for the creation of thiacalixarene-based complexes for photophysical functionalities. In comparison to the methylene-bridged calixarenes, the electron density is more delocalised around the cyclic system, leading to a shift in the electronic energy levels which manifests in the $\pi \rightarrow \pi^*$ absorption energy.¹⁰⁴ The electronic energy levels are sensitive to certain factors, such as substituents on the aromatic ring, conformation of the molecule, and binding to metal ions.¹⁰⁵ In this way the electronic transitions of the molecule can be 'tuned' to meet the requirements of some applications. For example, in 2006 Kajiwara *et al* reported the synthesis of luminescent lanthanide complexes of para-*tert*-butylthiacalix[4]arene wherein the calixarene ligand adopted either the cone or the pinched cone conformation.¹⁰⁵ This relatively slight change had such a strong effect on the energy levels of the excited states of the complex that one complex shows strong luminescence whereas the other is quenched. Figure 39 shows these two configurations for the Eu^{3+} ion, one a dinuclear complex and the other a tetranuclear cubane complex.

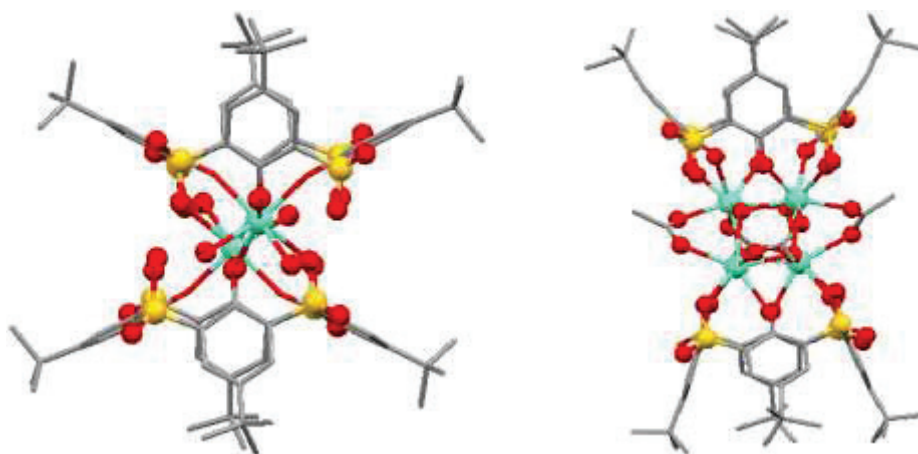


Figure 39: Europium cluster compounds with sulfonycalixarene ligands exhibiting slight conformational differences. C = grey, S = yellow, O = red, Eu³⁺ = cyan.¹⁰⁵

The two major applications for photoactive thiacalixarene compounds are in fluorescent sensors and as “antenna” ligands to enhance metal-based luminescence. These will be discussed separately below.

1.B5.1: Chemical sensors involving thiacalixarenes.

This application combines the propensity of thiacalixarene type compounds for forming non-covalent bonds to other species in a host-guest interaction, and the aforementioned strong effect of conformation on the optical properties of the material. To act as a chemical sensor the calixarene molecule is functionalised with a fluorophore, and usually with some extra binding moiety to add selectivity for the targeted substrate. In some cases the fluorophore acts as the substrate binder, making the calixarene structure a kind of flexible scaffold for the sensing site of the sensor.³⁰

The general mechanism by which these devices operate is this: in the absence of substrate the displays known luminescence characteristics which demonstrate a measurable change when bound by the targeted substrate, brought about by the change in molecular configuration induced by binding. In this way the sensor possesses definable ON and OFF states which can be easily determined by a spectral detector. A nice illustration of this principal is the molecule TCAN8QA, shown in figure 40, which is a selective sensor for the fluoride ion.¹⁰⁶ (The authors note that the thiacalixarene is superior to the standard calixarene for this application, due to its larger ring size

arising from the longer C-S bond). Binding of a fluoride anion to this sensor causes a significant change in both the intensity of emission and the form of the peaks in the emission of this fluorophore, as can be seen in the emission spectra included in figure 40.

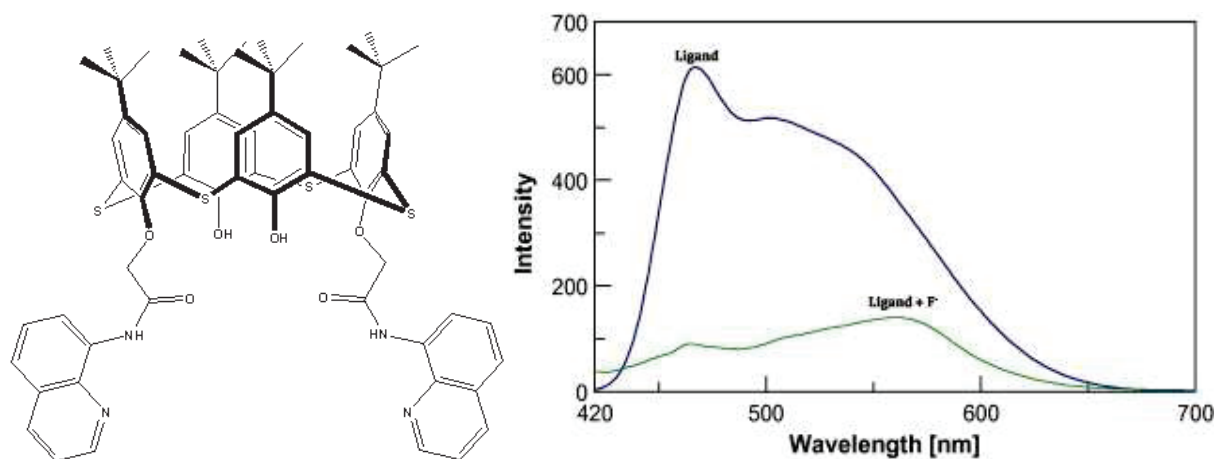


Figure 40: (Left) Chemical structure of thiacalix[4]arene-*N*-(quinolin-8-yl)-acetamide, TCAN8QA, a thiacalixarene-based fluorescent F⁻ sensor. (Right) Emission spectra of the free ligand TCAN8QA (blue curve) and the same ligand in the presence of fluoride ions (green curve).¹⁰⁶

1.B5.2: Thiacalixarenes as antenna ligands in luminescent complexes

This effect is most often noted in lanthanide complexes of thiacalixarenes. The lanthanides display multitudinous sharp optical transitions many of which fall within the visible range making them useful for applications involving visible light, such as solid state lighting, diagnostic imaging, and LASER technology for instance.¹⁰⁷⁻¹⁰⁹ However, the intrinsic light absorption properties of these ions are inherently weak, mostly due to the forbidden nature of f-f transitions. One method for circumventing this weakness is to introduce a complexing organic ligand which can strongly absorb the incident radiation before effecting a transfer of this excitation energy into the metal-based energy levels, from whence the desired metal centred emission can take place. This is known as the antenna effect; the europium complexes mentioned in the start of this section and shown in figure 39 are an example of this effect in action.

Figure 41 shows the electronic transitions involved in the photoexcitation and emission of those complexes and their terbium(III) analogues. It can be seen that the absorbed energy raises the ligand to its excited S₁ and T₁ states before transferring this energy to the lanthanide ⁵D states. Again

it is observed that the energy levels of the ligand with respect to the metal centred energy levels are of critical importance to this effect. If the correct correspondence of these levels is not present, there is no amelioration of emission.

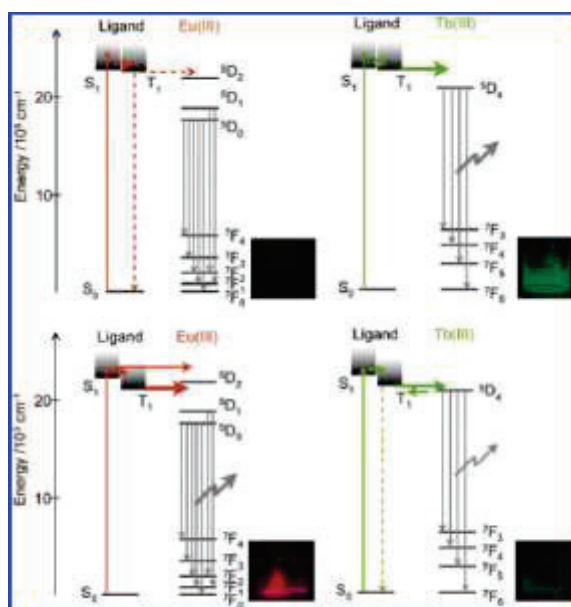


Figure 41: Energy levels and transitions involved in the antenna effect luminescence of europium, terbium, tetraeuropium and tetra terbium complexes of thiacalixarene.¹⁰⁵

1.B6: General Conclusion

With this literature review, the unique aptitude of the ligand family of thiacalixarenes for application in cluster coordination chemistry has been demonstrated and discussed. The particular physical and chemical characteristics of these species that make them so interesting for our study have been laid out, firstly considering the inherent properties of these organic compounds and their chemical transformations, and then contemplating the vast number of metal complexes that have been reported with these ligands, that have already been put to use in a plethora of applications. This doctoral thesis will now deal with the results obtained in the study of systems involving sulfonylcalix[4]arene and manganese(II).

References

1. Atkins, P. W.; Overton, T.; Rourke, J. P.; Weller, M.; Armstrong, F. A., *Shriver & Atkins' Inorganic Chemistry*. Oxford University Press: Oxford, 2010.
2. Gutsche, C. D.; Muthukrishnan, R., CALIXARENES .1. ANALYSIS OF PRODUCT MIXTURES PRODUCED BY BASE-CATALYZED CONDENSATION OF FORMALDEHYDE WITH PARA-SUBSTITUTED PHENOLS. *Journal of Organic Chemistry* **1978**, *43* (25), 4905-4906.
3. Kumagai, H.; Hasegawa, M.; Miyanari, S.; Sugawa, Y.; Sato, Y.; Hori, T.; Ueda, S.; Kamiyama, H.; Miyano, S., Facile synthesis of p-tert-butylthiacalix 4 arene by the reaction of p-tert-butylphenol with elemental sulfur in the presence of a base. *Tetrahedron Letters* **1997**, *38* (22), 3971-3972.
4. Konig, B.; Rodel, M.; Dix, I.; Jones, P. G., Synthesis of a sulfur-bridged calixarene. *Journal of Chemical Research-S* **1997**, (3), 69-&
5. Neale, A. J.; Bain, P. J. S.; Rawlings, T. J., SOME OBSERVATIONS OF REACTIONS BETWEEN PHENOL AND SULPHUR. *Tetrahedron* **1969**, *25* (18), 4593-&
6. Hori, T.; Ueda, S.; Kojima, Y.; Kugamai, H., Carboxylation of sulfurized calcium phenates. *Journal of the Japan Petroleum Institute* **1991**, *34* (5), 446-451.
7. Sone, T.; Ohba, Y.; Moriya, K.; Kumada, H.; Ito, K., Synthesis and properties of sulfur-bridged analogs of p-tert-butylcalix 4 arene. *Tetrahedron* **1997**, *53* (31), 10689-10698.
8. Kon, N.; Iki, N.; Miyano, S., Synthesis of p-tert-butylthiacalix n arenes (n=4, 6, and 8) from a sulfur-bridged acyclic dimer of p-tert-butylphenol. *Tetrahedron Letters* **2002**, *43* (12), 2231-2234.
9. Dai, F. R.; Sambasivam, U.; Hammerstrom, A. J.; Wang, Z. Q., Synthetic Supercontainers Exhibit Distinct Solution versus Solid State Guest-Binding Behavior. *Journal of the American Chemical Society* **2014**, *136* (20), 7480-7491.
10. Morohashi, N.; Iki, N.; Sugawara, A.; Miyano, S., Selective oxidation of thiacalix 4 arenes to the sulfinyl and sulfonyl counterparts and their complexation abilities toward metal ions as studied by solvent extraction. *Tetrahedron* **2001**, *57* (26), 5557-5563.
11. Lhotak, P.; Smejkal, T.; Stibor, I.; Havlicek, J.; Tkadlecova, M.; Petrickova, H., Synthesis of a deep-cavity thiacalix 4 arene. *Tetrahedron Letters* **2003**, *44* (44), 8093-8097.
12. Agrawal, Y. K.; Pancholi, J. P., Synthesis of thia-calix 4 arene hydroxamic acids by microwave irradiation. *Synthetic Communications* **2008**, *38* (14), 2446-2458.
13. Patel, M. H.; Shrivastav, P. S., Microwave assisted synthesis of Thiacalix n arenes. *Journal of Inclusion Phenomena and Macrocyclic Chemistry* **2009**, *63* (3-4), 379-382.
14. Akdas, H.; Bringel, L.; Graf, E.; Hosseini, M. W.; Mislin, G.; Pansanel, J.; De Cian, A.; Fischer, J., Thiacalixarenes: Synthesis and structural analysis of thiacalix 4 arene and of p-tert-butylthiacalix 4 arene. *Tetrahedron Letters* **1998**, *39* (16), 2311-2314.
15. Iki, N.; Morohashi, N.; Narumi, F.; Fujimoto, T.; Suzuki, T.; Miyano, S., Novel molecular receptors based on a thiacalix 4 arene platform. Preparations of the di- and tetracarboxylic acid derivatives and their binding properties towards transition metal ions. *Tetrahedron Letters* **1999**, *40* (41), 7337-7341.
16. Cajan, M.; Lhotak, P.; Lang, J.; Dvorakova, H.; Stibor, I.; Koca, J., The conformational behaviour of thiacalix 4 arenes: the pinched cone-pinched cone transition. *Journal of the Chemical Society-Perkin Transactions 2* **2002**, (11), 1922-1929.
17. Dvorakova, H.; Lang, J.; Vlach, J.; Sykora, J.; Cajan, M.; Himl, M.; Pojarova, M.; Stibor, I.; Lhotak, P., Partially O-Alkylated thiacalix 4 arenes: Synthesis, molecular and crystal structures, conformational behavior. *Journal of Organic Chemistry* **2007**, *72* (19), 7157-7166.
18. Kostin, G. A.; Kryuchkova, N. A.; Mazalov, L. N.; Torgov, V. G.; Drapaylo, A. B., Influence of conformation on the electronic structure of thiacalixarenes according to DFT calculations and X-ray emission spectroscopy. *Journal of Molecular Structure* **2011**, *1006* (1-3), 502-507.
19. Morohashi, N.; Katagiri, H.; Iki, N.; Yamane, Y.; Kabuto, C.; Hattori, T.; Miyano, S., Synthesis of all stereoisomers of sulfinylcalix 4 arenes. *Journal of Organic Chemistry* **2003**, *68* (6), 2324-2333.
20. Iki, N.; Fujimoto, T.; Miyano, S., A new water-soluble host molecule derived from thiacalixarene. *Chemistry Letters* **1998**, (7), 625-626.

21. Mackova, M.; Miksatko, J.; Budka, J.; Eigner, V.; Curinova, P.; Lhotak, P., Chiral anion recognition by a ureido-thiacalix 4 arene ligand immobilized in the 1,3-alternate conformation. *New Journal of Chemistry* **2015**, *39* (2), 1382-1389.
22. Su, K. Z.; Jiang, F. L.; Qian, J. J.; Pang, J. D.; Hu, F. L.; Bawaked, S. M.; Mokhtar, M.; Al-Thabaiti, S. A.; Hong, M. C., Bridging different Co-4-calix 4 arene building blocks into grids, cages and 2D polymers with chiral camphoric acid. *Crystengcomm* **2015**, *17* (8), 1750-1753.
23. Shokova, E.; Tafeenko, V.; Kovalev, V., First synthesis of adamantylated thiacalix 4 arenes. *Tetrahedron Letters* **2002**, *43* (29), 5153-5156.
24. Lhotak, P.; Svoboda, J.; Stibor, I., Anion receptors based on ureido-thiacalix 4 arenes. *Tetrahedron* **2006**, *62* (6), 1253-1257.
25. Kasyan, O.; Swierczynski, D.; Drapailo, A.; Suwinska, K.; Lipkowski, J.; Kalchenko, V., Upper rim substituted thiacalix 4 arenes. *Tetrahedron Letters* **2003**, *44* (38), 7167-7170.
26. Yang, W. P.; Wang, W.; Guo, R.; Gong, L. B.; Gong, S. L., Convenient Direct Syntheses of Selectively para-Substituted Di-, Tri- and Tetra-Formylated Thiacalix 4 arenes. *European Journal of Organic Chemistry* **2012**, (17), 3326-3330.
27. Hu, X. J.; Xia, N.; Ye, F.; Ren, J.; Shi, X. F., Synthesis of tetraamino derivative of thiacalix 4 arene and its acid-base property studied by UV spectroscopy. *Spectrochimica Acta Part a-Molecular and Biomolecular Spectroscopy* **2004**, *60* (7), 1427-1430.
28. Lhotak, P.; Moravek, J.; Stibor, I., Diazo coupling: an alternative method for the upper rim amination of thiacalix 4 arenes. *Tetrahedron Letters* **2002**, *43* (20), 3665-3668.
29. Desroches, C.; Lopes, C.; Kessler, V.; Parola, S., Design and synthesis of multifunctional thiacalixarenes and related metal derivatives for the preparation of sol-gel hybrid materials with non-linear optical properties. *Dalton Transactions* **2003**, (10), 2085-2092.
30. Kundrat, O.; Kas, M.; Tkadlecova, M.; Lang, K.; Cvacka, J.; Stibor, I.; Lhotak, P., Thiacalix 4 arene-porphyrin conjugates with high selectivity towards fullerene C-70. *Tetrahedron Letters* **2007**, *48* (38), 6620-6623.
31. Drapailo, A. B.; Kharchenko, S. G.; Shishkina, S. V.; Shishkin, O. V.; Kalchenko, V. I., PHOSPHORYLATED THICALIX 4 ARENES. *Phosphorus Sulfur and Silicon and the Related Elements* **2011**, *186* (4), 896-897.
32. Desroches, C.; Kessler, V. G.; Parola, S., The formylation of the upper-rims of thiacalixarenes: synthesis of the first tetra-formylated and the first meta-substituted thiacalix 4 arenes. *Tetrahedron Letters* **2004**, *45* (33), 6329-6331.
33. Kundrat, O.; Cisarova, I.; Bohm, S.; Pojarova, M.; Lhotak, P., Uncommon Regioselectivity in Thiacalix 4 arene Formylation. *Journal of Organic Chemistry* **2009**, *74* (12), 4592-4596.
34. Kundrat, O.; Dvorakova, H.; Cisarova, I.; Pojarova, M.; Lhotak, P., Unusual Intramolecular Bridging Reaction in Thiacalix 4 arene Series. *Organic Letters* **2009**, *11* (18), 4188-4191.
35. Lukasek, J.; Bohm, S.; Dvorakova, H.; Eigner, V.; Lhotak, P., Regioselective Halogenation of Thiacalix 4 arenes in the Cone and 1,3-Alternate Conformations. *Organic Letters* **2014**, *16* (19), 5100-5103.
36. Kundrat, O.; Kroupa, J.; Bohm, S.; Budka, J.; Eigner, V.; Lhotak, P., Meta Nitration of Thiacalixarenes. *Journal of Organic Chemistry* **2010**, *75* (24), 8372-8375.
37. Botha, F.; Bohm, S.; Dvorakova, H.; Eigner, V.; Lhotak, P., Mercuration of thiacalix 4 arenes in the cone and 1,3-alternate conformations. *Organic & Biomolecular Chemistry* **2014**, *12* (28), 5136-5143.
38. Botha, F.; Eigner, V.; Dvorakova, H.; Lhotak, P., Arylation of thiacalix 4 arenes using organomercurial intermediates. *New Journal of Chemistry* **2016**, *40* (2), 1104-1110.
39. Iki, N.; Kumagai, H.; Morohashi, N.; Ejima, K.; Hasegawa, M.; Miyanari, S.; Miyano, S., Selective oxidation of thiacalix 4 arenes to the sulfinyl- and sulfonylcalix 4 arenes and their coordination ability to metal ions. *Tetrahedron Letters* **1998**, *39* (41), 7559-7562.
40. Kundrat, O.; Eigner, V.; Dvorakova, H.; Lhotak, P., S-Alkylation of Thiacalixarenes: A Long-Neglected Possibility in the Calixarene Family. *Organic Letters* **2011**, *13* (15), 4032-4035.

41. Kundrat, O.; Dvorakova, H.; Bohm, S.; Eigner, V.; Lhotak, P., S-Alkylation of Thiacalixarenes: How the Regio- and Stereoselectivities Depend on the Starting Conformation. *Journal of Organic Chemistry* **2012**, *77* (5), 2272-2278.
42. Csokai, V.; Grun, A.; Balazs, B.; Toth, G.; Horvath, G.; Bitter, I., Unprecedented cyclizations of calix 4 arenes with glycols under the Mitsunobu protocol, Part 2. O,O- and O,S-bridged calixarenes. *Organic Letters* **2004**, *6* (4), 477-480.
43. Morohashi, N.; Kojima, M.; Suzuki, A.; Ohba, Y., Conversion of mono- and tetra-thiacalix 4 arenes to sulfilimine derivatives and unexpected formation of monospirodienone derivatives. *Heterocyclic Communications* **2005**, *11* (3-4), 249-254.
44. Katagiri, H.; Iki, N.; Hattori, T.; Kabuto, C.; Miyano, S., Calix 4 arenes comprised of aniline units. *Journal of the American Chemical Society* **2001**, *123* (4), 779-780.
45. Katagiri, H.; Iki, N.; Matsunaga, Y.; Kabuto, C.; Miyano, S., 'Thiacalix 4 aniline' as a highly specific extractant for Au(III) and Pd(II) ions. *Chemical Communications* **2002**, (18), 2080-2081.
46. Tanaka, S.; Katagiri, H.; Morohashi, N.; Hattori, T.; Miyano, S., Synthesis and X-ray structures of iodothiacalix 4 arenes. *Tetrahedron Letters* **2007**, *48* (30), 5293-5296.
47. Akdas, H.; Graf, E.; Hosseini, M. W.; Rao, P.; De Cian, A., Tetramercaptotetrathiacalix[4]arene the Most Sulfur Enriched Ligand: Synthesis and Structural Analysis. *Journal of Supramolecular Chemistry* **2002**, *2*, 21 - 28.
48. Zieba, R.; Desroches, C.; Chaput, F.; Sigala, C.; Jeanneau, E.; Parola, S., The first approach to a new family of macrocycles: synthesis and characterization of thiacalix 2 thianthrenes. *Tetrahedron Letters* **2007**, *48* (31), 5401-5405.
49. Kasyan, O.; Rudzevich, V.; Bolte, M.; Bohmer, V., Tetraallyl Ethers of Thiacalix 4 arenes in the 1,3-Alternate Conformation. *Journal of Chemical Crystallography* **2011**, *41* (3), 332-337.
50. Stastny, V.; Stibor, I.; Dvorakova, H.; Lhotak, P., Synthesis of (thia)calix 4 arene oligomers: towards calixarene-based dendrimers. *Tetrahedron* **2004**, *60* (15), 3383-3391.
51. Morohashi, N.; Iki, N.; Kabuto, C.; Miyano, S., Stereocontrolled oxidation of a thiacalix 4 arene to the sulfinyl counterpart of a defined S = O configuration. *Tetrahedron Letters* **2000**, *41* (16), 2933-2937.
52. Kasyan, O.; Healey, E. R.; Drapailo, A.; Zaworotko, M.; Cecillon, S.; Coleman, A. W.; Kalchenko, V., Synthesis, structure and selective upper rim functionalization of long chained alkoxythiacalix 4 arenes. *Journal of Inclusion Phenomena and Macrocyclic Chemistry* **2007**, *58* (1-2), 127-132.
53. Omran, O. A., The Reaction of Diethyl Bromomalonate with p-tert-Butylthiacalix 4 arene: An Approach to Asymmetrical Derivatives. *Molecules* **2009**, *14* (5), 1755-1761.
54. Stoikov, I.; Galukhin, A. V.; Zaikov, E. N.; Antipin, I. S., Synthesis and complexation properties of 1,3-alternate stereoisomers of p-tert-butylthiacalix 4 arenes tetrasubstituted at the lower rim by the phthalimide group. *Mendeleev Communications* **2009**, *19* (4), 193-195.
55. Lamouchi, M.; Jeanneau, E.; Chiriac, R.; Ceroni, D.; Meganem, F.; Brioude, A.; Coleman, A. W.; Desroches, C., Monosubstituted lower rim thiacalix 4 arene derivatives. *Tetrahedron Letters* **2012**, *53* (16), 2088-2090.
56. Narumi, F.; Matsumura, N.; Sasagawa, N.; Natori, K.; Kajiwara, T.; Hattori, T., Resolution of inherently chiral anti-O,O'-dialkylthiacalix 4 arenes and determination of their absolute stereochemistries. *Tetrahedron-Asymmetry* **2008**, *19* (12), 1470-1475.
57. van Leeuwen, F. W. B.; Beijleveld, H.; Kooijman, H.; Spek, A. L.; Verboom, W.; Reinhoudt, D. N., Synthesis and conformational evaluation of p-tert-butylthiacalix 4 arene-crowns. *Journal of Organic Chemistry* **2004**, *69* (11), 3928-3936.
58. Bhalla, V.; Kumar, M.; Katagiri, H.; Hattori, T.; Miyano, S., Synthesis and binding studies of novel bithiacalix 4 arenes with diimide linkages. *Tetrahedron Letters* **2005**, *46* (1), 121-124.
59. Yang, F. F.; Yin, F. J.; Guo, H. Y.; Huang, Z. S.; Zhang, X. Y., Syntheses and cations complexation properties of novel thiacalix 4 -1,3-aza-crown and bithiacalix 4 -1,3-aza-crown. *Journal of Inclusion Phenomena and Macrocyclic Chemistry* **2010**, *67* (1-2), 49-54.

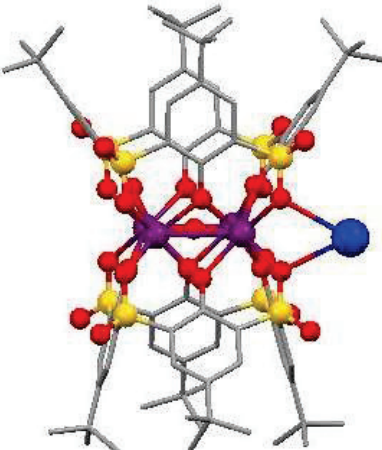
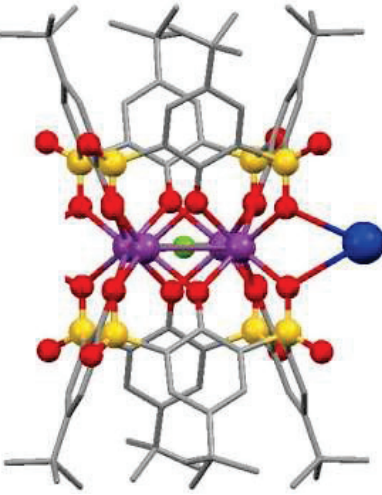
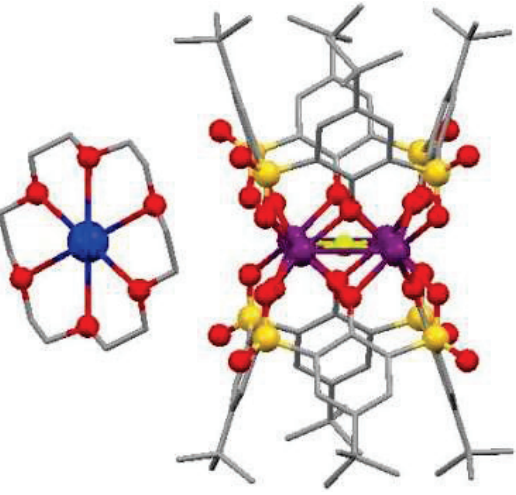
60. Narita, M.; Higuchi, Y.; Hamada, F.; Kumagai, H., Metal sensor of water soluble dansyl-modified thiacalix 4 arenes. *Tetrahedron Letters* **1998**, *39* (47), 8687-8690.
61. Narumi, F.; Hattori, T.; Matsumura, N.; Onodera, T.; Katagiri, H.; Kabuto, C.; Kameyama, H.; Miyano, S., Synthesis of an inherently chiral O,O'-bridged thiacalix 4 crown-carboxylic acid and its application to a chiral solvating agent. *Tetrahedron* **2004**, *60* (36), 7827-7833.
62. Epifanova, N. A.; Popova, E. V.; Solovieva, S. E.; Latypov, S. K.; Antipin, I. S.; Konovalov, A. I., Thiacalix 4 arenes with Triple Bonds at the Lower Rim: Synthesis and Structure. *Macroheterocycles* **2013**, *6* (1), 47-52.
63. Kozlova, M. N.; Ferlay, S.; Solovieva, S. E.; Antipin, I. S.; Konovalov, A. I.; Kyritsakas, N.; Hosseini, M. W., Molecular tectonics: on the formation of 1-D silver coordination networks by thiacalixarenes bearing nitrile groups. *Dalton Transactions* **2007**, (44), 5126-5131.
64. Kozlova, M. N.; Ferlay, S.; Kyritsakas, N.; Hosseini, M. W.; Solovieva, S. E.; Antipin, I. S.; Konovalov, A. I., Molecular tectonics: 3-D organisation of decanuclear silver nanoclusters. *Chemical Communications* **2009**, (18), 2514-2516.
65. Choe, J. I., mPW1PW91 Calculated Structures and IR Spectra of Thiacalix 4 biscrown-5 Complexed with Alkali Metal Ions. *Bulletin of the Korean Chemical Society* **2011**, *32* (5), 1685-1691.
66. Yamato, T.; Casas, C. P.; Elsegood, M. R. J.; Dale, S. H.; Redshaw, C., Synthesis and inclusion properties of a novel thiacalix 4 arene-based hard-soft receptor with 1,3-alternate conformation. *Journal of Inclusion Phenomena and Macrocyclic Chemistry* **2006**, *55* (1-2), 31-36.
67. Lamouchi, M. Matériaux moléculaires à propriétés optique et magnétique à base de complexes métalliques polynucléaires : Thiacalixarènes / métaux de transition. Université Claude Bernard Lyon 1, Lyon, 2012.
68. Winpenny, R. E. P., Serendipitous assembly of polynuclear cage compounds. *Journal of the Chemical Society-Dalton Transactions* **2002**, (1), 1-10.
69. Mislin, G.; Graf, E.; Hosseini, M. W.; Bilyk, A.; Hall, A. K.; Harrowfield, J. M.; Skelton, B. W.; White, A. H., Thiacalixarenes as cluster keepers: synthesis and structural analysis of a magnetically coupled tetracopper(II) square. *Chemical Communications* **1999**, (4), 373-374.
70. Su, K. Z.; Jiang, F. L.; Qian, J. J.; Wu, M. Y.; Xiong, K. C.; Gai, Y. L.; Hong, M. C., Thiacalix 4 arene-Supported Kite-Like Heterometallic Tetranuclear Zn(II)Ln(3)(III) (Ln = Gd, Tb, Dy, Ho) Complexes. *Inorganic Chemistry* **2013**, *52* (7), 3780-3786.
71. Liu, M.; Liao, W. P., A zigzag ladder-like metal-organic aggregate based on Co-4-TC4A subunits and aromatic tricarboxylic acids. *Journal of Molecular Structure* **2013**, *1038*, 206-210.
72. Hang, X. X.; Liu, B.; Zhu, X. F.; Wang, S. T.; Han, H. T.; Liao, W. P.; Liu, Y. L.; Hu, C. H., Discrete {Ni-40} Coordination Cage: A Calixarene-Based Johnson-Type (J(17)) Hexadecahedron. *Journal of the American Chemical Society* **2016**, *138* (9), 2969-2972.
73. Gehin, A.; Ferlay, S.; Harrowfield, J. M.; Fenske, D.; Kyritsakas, N.; Hosseini, M. W., Giant Core-Shell Nanospherical Clusters Composed of 32 Co or 32 Ni Atoms Held by 6 p-tert-Butylthiacalix 4 arene Units. *Inorganic Chemistry* **2012**, *51* (9), 5481-5486.
74. Bilyk, A.; Hall, A. K.; Harrowfield, J. M.; Hosseini, M. W.; Mislin, G.; Skelton, B. W.; Taylor, C.; White, A. H., Linear, divergent molecular receptors - Subtle effects of transition metal coordination geometry. *European Journal of Inorganic Chemistry* **2000**, (5), 823-826.
75. Morohashi, N.; Hattori, T.; Yokomakura, K.; Kabuto, C.; Miyano, S., Dinuclear titanium(IV) complex of p-tert-butylthiacalix 4 arene as a novel bidentate Lewis acid catalyst. *Tetrahedron Letters* **2002**, *43* (43), 7769-7772.
76. Liu, C. M.; Zhang, D. Q.; Hao, X.; Zhu, D. B., Syntheses, Crystal Structures, and Magnetic Properties of Two p-tert-Butylsulfonylcalix 4 arene Supported Cluster Complexes with a Totally Disordered Ln(4)(OH)(4) Cubane Core. *Crystal Growth & Design* **2012**, *12* (6), 2948-2954.
77. Kajiwara, T.; Yokozawa, S.; Ito, T.; Iki, N.; Morohashi, N.; Miyano, S., Sulfonylcalix 4 arene as a bis-tridentate facial ligand: Syntheses and structures of dinuclear complexes, M-2(L)(H₂O)(2)(dmf)(4) (M = Co(II), Ni(II); H₄L = p-tert-butylsulfonylcalix 4 arene). *Chemistry Letters* **2001**, (1), 6-7.

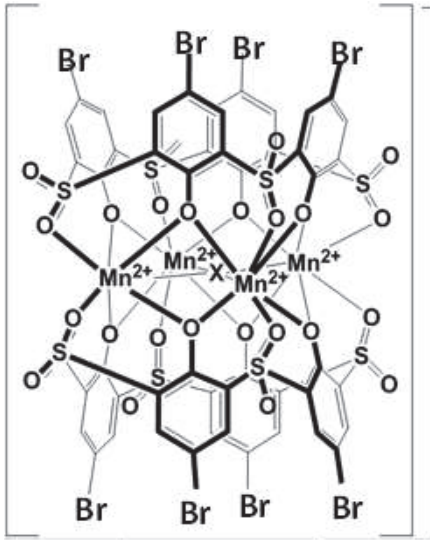
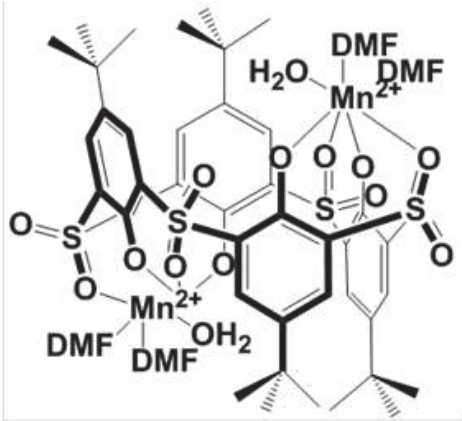
78. Fuller, R. O.; Livesey, K. L.; Woodward, R. C.; McKinley, A. J.; Skelton, B. W.; Koutsantonis, G. A., Magnetic Studies of Metal Ion Coordination Clusters Encapsulated with Thiacalixarene. *Australian Journal of Chemistry* **2014**, *67* (11), 1588-1594.
79. Sorai, M.; Kaji, K.; Hendrickson, D. N.; Oh, S. M., HEAT-CAPACITY AND PHASE-TRANSITIONS OF THE MIXED-VALENCE COMPOUND $\text{Fe}_3\text{O}(\text{O}_2\text{CCH}_3)_6(\text{PY})_3$ (PY). *Journal of the American Chemical Society* **1986**, *108* (4), 702-708.
80. Uemura, S.; Spencer, A.; Wilkinso, G., MU3-OXOTRIMETAL ACETATO-COMPLEXES OF CHROMIUM, MANGANESE, IRON, COBALT, RHODIUM, AND IRIDIUM. *Journal of the Chemical Society-Dalton Transactions* **1973**, (23), 2565-2571.
81. Morlanes, N.; Notestein, J. M., Grafted Ta-calixarenes: Tunable, selective catalysts for direct olefin epoxidation with aqueous hydrogen peroxide. *Journal of Catalysis* **2010**, *275* (2), 191-201.
82. Redshaw, C.; Elsegood, M. R. J.; Wright, J. A.; Baillie-Johnson, H.; Yamato, T.; De Giovanni, S.; Mueller, A., Cellular uptake of a fluorescent vanadyl sulfonylcalix 4 arene. *Chemical Communications* **2012**, *48* (8), 1129-1131.
83. Yuan, D. Q.; Zhu, W. X.; Xu, M. Q.; Guo, Q. L., Synthesis and structural characterization of a binuclear zirconium complex of tetraanionic p-tert-butylthiacalix 4 arene bridged by methanol. *Journal of Coordination Chemistry* **2004**, *57* (14), 1243-1249.
84. Zeller, J.; Radius, U., Alkali-metalated forms of thiacalix 4 arenes. *Inorganic Chemistry* **2006**, *45* (23), 9487-9492.
85. Morohashi, N.; Iki, N.; Miyano, S.; Kajiwara, T.; Ito, T., Synthesis and structural characterization of a Pd^{2+} complex with p-tert-butylsulfonylcalix 4 arene. *Chemistry Letters* **2001**, (1), 66-67.
86. Takemoto, S.; Tanaka, S.; Mizobe, Y.; Hidai, M., Ti-Mo heterobimetallic thiacalix 4 arene complex containing an unusual alpha-agostic $\mu(2)$ - $\eta(5)$: $\eta(2)$ -cyclopentadienyl ligand. *Chemical Communications* **2004**, (7), 838-839.
87. Redshaw, C.; Clowes, L.; Hughes, D. L.; Elsegood, M. R. J.; Yamato, T., Ethylene Polymerization Catalysis by Vanadium-Based Systems Bearing Sulfur-Bridged Calixarenes. *Organometallics* **2011**, *30* (21), 5620-5624.
88. Yamada, M.; Kondo, Y.; Iki, N.; Kabuto, C.; Hamada, F., Hydrophobic and metal coordination interacted architecture based on p-tert-butylthiacalix 4 arene-potassium complex and its vapor absorption capability. *Tetrahedron Letters* **2008**, *49* (24), 3906-3911.
89. Kajiwara, T.; Yokozawa, S.; Ito, T.; Iki, N.; Morohashi, N.; Miyano, S., Zinc(III) slides on a ligand surface: The X-ray crystal structure and dynamic behavior in solution of $\text{Zn}(\text{H}_2\text{L})(\text{tacn})$. *Angewandte Chemie-International Edition* **2002**, *41* (12), 2076-2078.
90. Hong, J.; Yang, G. S.; Duan, C. Y.; Guo, Z. J.; Zhu, L. G., Fluorescence quenching of EB-DNA complex by a novel di-bipyridyl ruthenium(II) complex of p-tert-butyltetra-thiacalix 4 arene. *Inorganic Chemistry Communications* **2005**, *8* (11), 988-991.
91. Salta, J.; Chang, Y. D.; Zubieta, J., INVESTIGATIONS OF THE V/O/RASO(3)(2-) SYSTEM - SOLVOTHERMAL SYNTHESIS AND CRYSTAL AND MOLECULAR-STRUCTURE OF $(\text{V}_2\text{O}_3)(\text{PH}(6)\text{AS}(6)\text{O}(14))$. *Journal of the Chemical Society-Chemical Communications* **1994**, (9), 1039-1040.
92. Desroches, U.; Pilet, G.; Szilagyi, P. A.; Molnar, G.; Borshch, S. A.; Bousseksou, A.; Parola, S.; Luneau, D., Tetra- and decanuclear iron(II) complexes of thiacalixarene macrocycles: Synthesis, structure, Mossbauer spectroscopy and magnetic properties. *European Journal of Inorganic Chemistry* **2006**, (2), 357-365.
93. Xiong, K. C.; Jiang, F. L.; Gai, Y. L.; Zhou, Y. F.; Yuan, D. Q.; Su, K. Z.; Wang, X. Y.; Hong, M. C., A Series of Octanuclear-Nickel(II) Complexes Supported by Thiacalix 4 arenes. *Inorganic Chemistry* **2012**, *51* (5), 3283-3288.
94. Xiong, K. C.; Jiang, F. L.; Gai, Y. L.; He, Z. Z.; Yuan, D. Q.; Chen, L.; Su, K. Z.; Hong, M. C., Self-Assembly of Thiacalix 4 arene-Supported Nickel(II)/Cobalt(II) Complexes Sustained by in Situ Generated 5-Methyltetrazolate Ligand. *Crystal Growth & Design* **2012**, *12* (6), 3335-3341.

95. Desroches, C.; Pilet, G.; Borshch, S. A.; Parola, S.; Luneau, D., Tetranuclear manganese(II) complexes of thiacalixarene macrocycles with trigonal prismatic six-coordinate geometries: Synthesis, structure, and magnetic properties. *Inorganic Chemistry* **2005**, *44* (24), 9112-9120.
96. Tamaki, H.; Zhong, Z. J.; Matsumoto, N.; Kida, S.; Koikawa, M.; Achiwa, N.; Hashimoto, Y.; Okawa, H., DESIGN OF METAL-COMPLEX MAGNETS - SYNTHESSES AND MAGNETIC-PROPERTIES OF MIXED-METAL ASSEMBLIES (NBU₄ MCR(OX)₃)_X (NBU₄⁺=TETRA(NORMAL-BUTYL)AMMONIUM ION OX(2-)= OXALATE ION M=MN²⁺,FE²⁺,CO²⁺,NI²⁺,CU²⁺,ZN²⁺). *Journal of the American Chemical Society* **1992**, *114* (18), 6974-6979.
97. Gatteschi, D.; Sessoli, R.; Villain, J., *Molecular Nanomagnets*. Oxford University Press: Oxford, 2006.
98. Kajiwarra, T.; Kon, N.; Yokozawa, S.; Ito, T.; Iki, N.; Miyano, S., Synthesis, structure, and ferromagnetic behavior of decacopper(II) cluster complex supported by hexaanionic p-tert-butylthiacalix 6 arene. *Journal of the American Chemical Society* **2002**, *124* (38), 11274-11275.
99. Lamouchi, M.; Jeanneau, E.; Pillonnet, A.; Brioude, A.; Martini, M.; Stephan, O.; Meganem, F.; Novitchi, G.; Luneau, D.; Desroches, C., Tetranuclear manganese(II) complexes of sulfonylcalix 4 arene macrocycles: synthesis, structure, spectroscopic and magnetic properties. *Dalton Transactions* **2012**, *41* (9), 2707-2713.
100. Kajiwarra, T.; Kobashi, T.; Shinagawa, R.; Ito, T.; Takaishi, S.; Yamashita, M.; Iki, N., Highly symmetrical tetranuclear cluster complexes supported by p-tert-butylsulfonylcalix 4 arene as a cluster-forming ligand. *European Journal of Inorganic Chemistry* **2006**, (9), 1765-1770.
101. Dai, F. R.; Wang, Z. Q., Modular Assembly of Metal-Organic Supercontainers Incorporating Sulfonylcalixarenes. *Journal of the American Chemical Society* **2012**, *134* (19), 8002-8005.
102. Bilyk, A.; Dunlop, J. W.; Fuller, R. O.; Hall, A. K.; Harrowfield, J. M.; Hosseini, M. W.; Koutsantonis, G. A.; Murray, I. W.; Skelton, B. W.; Stamps, R. L.; White, A. H., Systematic Structural Coordination Chemistry of p-tert-Butyltetrathiacalix 4 arene: Further Complexes of Transition-Metal Ions. *European Journal of Inorganic Chemistry* **2010**, (14), 2106-2126.
103. Fu, M. L.; Rangel, N. L.; Adams, R. D.; Seminario, J. M., Synthesis, Crystal Structure, Photophysical Properties, and DFT Calculations of a Bis(tetrathia-calix 4 arene) Tetracadmium Complex. *Journal of Cluster Science* **2010**, *21* (4), 867-878.
104. Iki, N.; Hiro-oka, S.; Tanaka, T.; Kabuto, C.; Hoshino, H., .Highly Efficient Near-Infrared-Emitting Lanthanide(III) Complexes Formed by Heterogeneous Self-Assembly of Ag-I, Ln(III), and Thiacalix 4 arene-p-tetrasulfonate in Aqueous Solution (Ln(III) = Nd-III, Yb-III). *Inorganic Chemistry* **2012**, *51* (3), 1648-1656.
105. Kajiwarra, T.; Katagiri, K.; Hasegawa, M.; Ishii, A.; Ferbinteanu, M.; Takaishi, S.; Ito, T.; Yamashita, M.; Iki, N., Conformation-controlled luminescent properties of lanthanide clusters containing p-tert-butylsulfonylcalix 4 arene. *Inorganic Chemistry* **2006**, *45* (13), 4880-4882.
106. Darjee, S. M.; Mishra, D. R.; Bhatt, K. D.; Vyas, D. J.; Modi, K. M.; Jain, V. K., A new colorimetric and fluorescent chemosensor based on thiacalix 4 arene for fluoride ions. *Tetrahedron Letters* **2014**, *55* (51), 7094-7098.
107. Hubbard, D. S.; Houlne, M. P.; Kiefer, G.; Janssen, H. F.; Hacker, C.; Bornhop, D. J., Diagnostic imaging using rare-earth chelates. *Lasers in Medical Science* **1998**, *13* (1), 14-21.
108. Gruber, J. B.; Hills, M. E.; Seltzer, M. D.; Stevens, S. B.; Morrison, C. A.; Turner, G. A.; Kokta, M. R., ENERGY-LEVELS AND CRYSTAL QUANTUM STATES OF TRIVALENT HOLMIUM IN YTTRIUM-ALUMINUM-GARNET. *Journal of Applied Physics* **1991**, *69* (12), 8183-8204.
109. Evans, R. C.; Douglas, P.; Burrow, H. D., *Applied Photochemistry*. Springer Netherlands: 2014.

CHAPTER 2: LUMINESCENCE CHARACTERISATION OF
SYSTEMS CONTAINING SULFONYLCALIXARENE LIGANDS
AND Mn²⁺ IONS

2.0 Table of cluster complexes studied in this chapter

Number	Name and Structure
1	<p>Potassium[bis-(μ_4-(<i>para-tert</i>-butylsulfonylcalixarene))(μ^4-hydroxo)tetramanganese(II)]</p>  <p>The structure shows a central tetramanganese(II) core (purple spheres) coordinated by two μ_4-(<i>para-tert</i>-butylsulfonylcalixarene) ligands (gray and yellow spheres) and one μ^4-hydroxo ligand (red sphere). A potassium ion (blue sphere) is coordinated to the complex.</p>
2	<p>Potassium[bis-(μ_4-(<i>para-tert</i>-butylsulfonylcalixarene))(μ_4-fluoro)tetramanganese(II)]</p>  <p>The structure shows a central tetramanganese(II) core (purple spheres) coordinated by two μ_4-(<i>para-tert</i>-butylsulfonylcalixarene) ligands (gray and yellow spheres) and one μ_4-fluoro ligand (green sphere). A potassium ion (blue sphere) is coordinated to the complex.</p>
3	<p>[Potassium(18crown6)][bis-(μ_4-(<i>para-tert</i>-butylsulfonylcalixarene))(μ_4-fluoro)tetramanganese(II)]</p>  <p>The structure shows a central tetramanganese(II) core (purple spheres) coordinated by two μ_4-(<i>para-tert</i>-butylsulfonylcalixarene) ligands (gray and yellow spheres) and one μ_4-fluoro ligand (green sphere). A potassium ion (blue sphere) is coordinated to the complex, and a 18-crown-6 ether ligand (gray and red spheres) is coordinated to the potassium ion.</p>

4	<p>Potassium[bis-(μ_4-(parabromosulfonylcalix[4]arene))(μ_4-fluoro)tetramanganese(II)]</p>  <p>The structure shows a central potassium atom (K) coordinated to four manganese(II) ions (Mn²⁺) in a tetrahedral arrangement. Each manganese ion is coordinated to four oxygen atoms from the sulfonate groups of a parabromosulfonylcalix[4]arene ligand. The ligand consists of four phenolic rings linked at their 1,3-positions, with a sulfonate group (-SO₂-) at the 4-position and a bromine atom at the 2-position. The four manganese ions are also bridged by a central fluoride ion (F⁻).</p>
5	<p>[(μ_2-para-<i>tert</i>-butylsulfonylcalix[4]arene)-diaqua-tetra(dimethylformamido)dimanganese(II)]</p>  <p>The structure shows two manganese(II) ions (Mn²⁺) bridged by two water molecules (H₂O). Each manganese ion is also coordinated to two dimethylformamide (DMF) molecules. The manganese ions are coordinated to the oxygen atoms of the sulfonate groups of a para-<i>tert</i>-butylsulfonylcalix[4]arene ligand. The ligand consists of four phenolic rings linked at their 1,3-positions, with a sulfonate group (-SO₂-) at the 4-position and a <i>tert</i>-butyl group at the 2-position.</p>

Colour key for all X-ray structures (1 – 3): C = grey, S = yellow, O = red, F = green, K = blue; H atoms omitted for clarity.

This chapter concerns a study of polynuclear clusters of manganese(II) with sulfonylcalixarene ligands. A series of these clusters were prepared and investigated for their novel luminescence properties, in order to ascertain the role played by structural and chemical variation upon these species in their optical properties. Based upon these observations, a fundamental mechanistic explanation of this luminescence behaviour is offered.

2.1: General introduction

The free molecule *para-tert*-butylthiacalix[4]arene (thiaS) is optically active, fluorescing in dichloromethane solution with emission between 310 nm and 350 nm under UV illumination. A computer generated excitation and emission spectrum of this molecule is shown in figure 42.¹

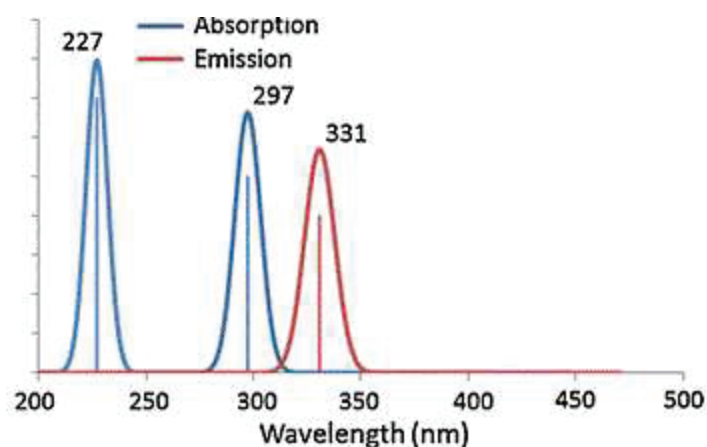


Figure 42: Simulated absorption (blue curve) and emission (red curve) spectra for free thiaS.¹

An advantage of thiacalixarene-type ligands as compared to the methylene bridged calixarenes is the greater delocalisation of the electron density afforded by the sulfur atoms. This effect is observed by the electronic energy levels of the molecule, which is to say in its UV-vis absorption profile.² The delocalisation shows significant sensitivity towards certain factors, such as the conformation or substituents of the molecule, allowing for a degree of 'tuneability' of the optical properties of the molecule and its complexes.³ Luminescence of thiacalixarene based metal complexes generally involves one of two methods:

- 1) A functionality which is intrinsically optically active is attached to the calixarene. This method is most often used to make sensors; binding to the substrate will induce or quench luminescence, or change the wavelength of emitted light, thereby providing definable ON and OFF states.⁴⁻⁶ In this way, the optical application exploits the complexing / hosting power of the thiacalixarene species.
- 2) Energy transfer from the excited ligand is used to drive emission from bound metal ions, i.e. the ligand acts as a sensitiser for the metal ion centred emission. An alternative but related process is ligand-to-metal charge transfer (LMCT), which involves the transfer of electronic density from the ligand to the metal centre directly induced by the absorption of light. By the former mechanism, the efficient absorption of the ligand is exploited. Typically the metal ions in question are lanthanides, which are known for their well-defined optical properties but poor intrinsic absorption of light due to forbidden f → f transitions.^{3, 7, 8} One particular example is a good illustration of both the strong binding capacity of this ligand family and their capacity to act as an ‘antenna’ for lanthanide ion emission: a dinuclear complex of terbium reported by Iki *et al.*⁹ Slight adjustments to the conformation of the sulfonylcalixarene ligand in this complex cause significant enough changes in the energy level of its excited triplet state with respect to the f-shell centred energy levels of the Tb³⁺ ion to have a remarkable effect on the intensity of the characteristic green luminescence.

Examples of complexes of thiacalixarene-type ligands used for optical applications include sensors as mentioned above, synergy of magnetism and luminescence,⁹ DNA binding and bio-imaging,^{10, 11} and more, illustrating the versatility of these species for a multitude of tasks. However manganese(II) ions, although quite well known as a dopant for optical properties in inorganic materials,¹²⁻¹⁴ are not so commonly employed in the form of molecular complexes for these applications. As can be derived from the Tanabe Sugano diagram for d⁵ ions, emission from the manganese(II) ion in high-spin octahedral environments is due to the ⁴T₁ to ⁶A₁ transition resulting in

red or green coloured luminescence, in a range of approximately 700 to 550 nm.¹⁵ As this transition is spin forbidden, direct excitation and emission from it is generally very weak. Despite this, a very few complexes of Mn²⁺ ions with a coordination number of 4, 7 or 8 and a mixed oxygen and halide coordination environment have demonstrated significant metal-centred photoluminescence and even triboluminescence.^{15, 16} In other cases, population of the excited state of the metal is achieved by energy transfer from the photo-excited ligand to the metal i.e. a form of the antenna effect. This effect has been observed in both a discrete molecular complex and a type of coordination polymer of manganese(II), for example.^{17, 18} The former of these is a particularly significant example of the importance of ligand design for these purposes: the manganese(II) complex MnBr₂(TPO)₂, where TPO = triphenylphosphine oxide, is almost non-luminescent entirely. Replacing the two phosphine oxide ligands with the very closely related DPEPO (bis[2-(diphenylphosphino)-phenyl]ether oxide, structure in figure 43) enhances the luminescence considerably, as the rigidity of this ligand reduces the potential for non-radiative relaxation. As a result the complex shows intense green emission between 450 nm and 575 nm ($\lambda_{\text{max}} = 502 \text{ nm}$) for excitation in the range from 250 nm to 400 nm, with an extra structured band in the excitation spectrum in the range of 400-500 nm. With a luminescence lifetime of 0.5 ms and quantum efficiency of 70 %, this optical behaviour is unusually strong for a molecular manganese(II) complex.

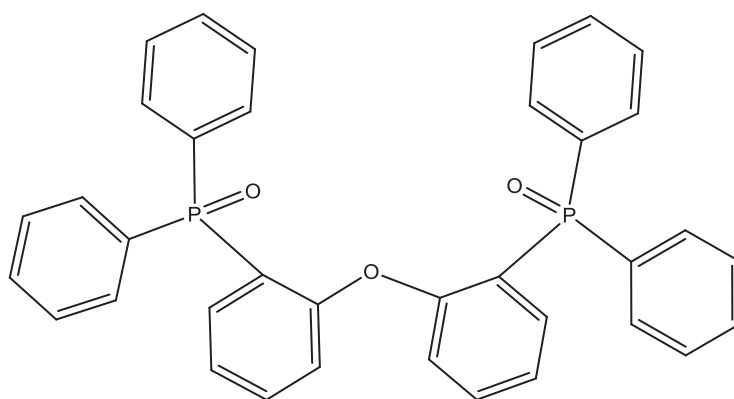


Figure 43: Structure of DPEPO.¹⁷

The principal metal complex for study in this work, a tetranuclear manganese complex, was first observed as a serendipitous outcome of a reaction intended to synthesise complexes of

manganese in higher oxidation states (+3 or +4).¹⁹ The fact that the product of solvothermal reaction between the thiacalixarene ligands and manganese always contains Mn²⁺ regardless of the starting oxidation state of manganese, the oxygenation of the ligand (thiacalixarene = thiaS, sulfinylcalixarene = thiaSO, sulfonylcalixarene = thiaSO₂), or the oxidising reaction conditions demonstrates a strong interaction between these species. The structure of the complex K[Mn₄(thiaSO₂)₂(OH)] is shown below in figure 44; this will be referred to as complex **1** for convenience throughout this work. Complex **1** is prepared by the solvothermal reaction depicted in figure 45.

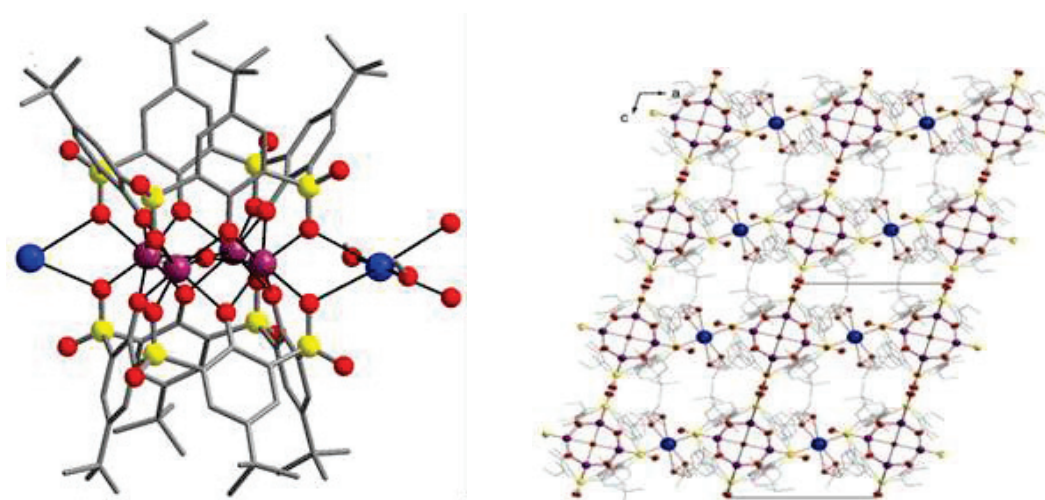


Figure 44: Structure obtained by single crystal XRD of complex **1**. Colour key: C = grey; S = yellow; O = red; Mn = purple; K = blue. H atoms omitted for clarity.²⁰

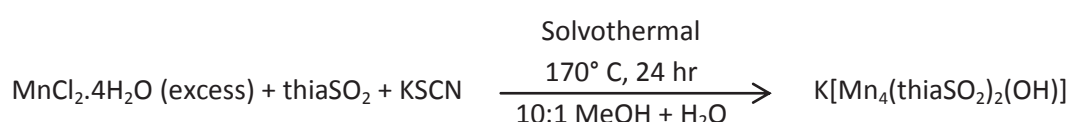


Figure 45: Solvothermal synthesis of complex **1**.

Cluster complex **1** was found to be quite unique in several interesting ways. Although the square planar arrangement of ions forming a ‘sandwich’ type cluster between two ligand molecules is well known for thiacalixarene type ligands,^{1, 21-23} in this case an OH⁻ ion (produced by the base driven deprotonation of water) was incorporated at the centre of the Mn₄ square, giving the cluster an overall negative charge (Figure 46). For hydroxide to act as a μ-4 bridging ligand is rare, and almost completely unknown in square planar geometry.¹⁹ Furthermore this arrangement of cluster components results in a fairly unusual seven-fold capped trigonal bipyramid coordination geometry

around each manganese centre. The effect of the cation must also be considered, as metal binding directly to the sulfonyl groups of the ligand could seriously affect both the ligand conformation and thus the crystal field strength.²⁴

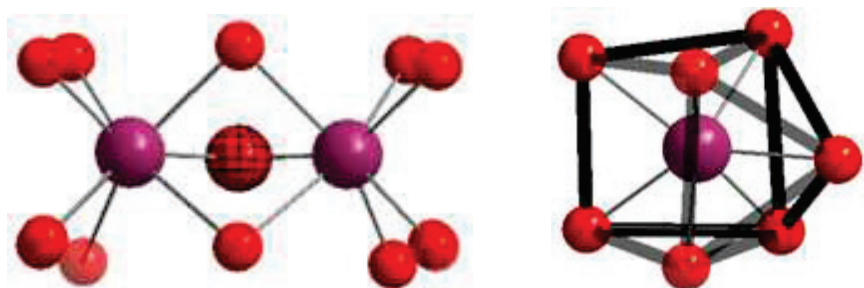


Figure 46: Side-on view representation of the $Mn_4-\mu_4(OH)$ square at the core of complex **1** (left), and the 7-coordinate C_{2v} environment of each Mn^{2+} ion (right). Colour key: Mn = purple, O = red.

Most importantly, this complex was observed to luminesce, emitting red light under UV or blue irradiation ($\lambda = 360$ nm or 400 nm). It is highly significant that this luminescence is so intense, considering that the O-H bond is known to strongly quench luminescence pathways. A previously reported 7-coordinate manganese complex with H_2O in the coordination sphere was observed to be fluorescent, but this fluorescence was so weak that it necessitated excitation by intense LASER light in order to function.²⁵ If potassium fluoride is used in place of the base in the synthesis, the hydroxide group is replaced by a fluoride ion (giving complex **2**), augmenting the absorption at 360 nm, and also the intensity and the lifetime of luminescence in the product. There is also a very slight shift of the wavelength of the maximum of the broad emission peak, from 605 nm to 585 nm. Figure 47 shows the excitation and emission spectra of complexes **1** and **2** compared. IR analysis of **1** showed an unusually fine O-H stretching peak at 3540 cm^{-1} , perhaps implying that some form of structural rigidity limits the freedom of the hydroxide in this complex to deexcite the molecule non-radiatively. This peak is not present in the IR spectrum of **2**. Figure 48 shows the IR spectra of both compounds in the relative range. The successful replacement of OH with F was also confirmed by mass spectrometry ($m/z = 1925.10$ for **1**, 1927.07 for **2**).

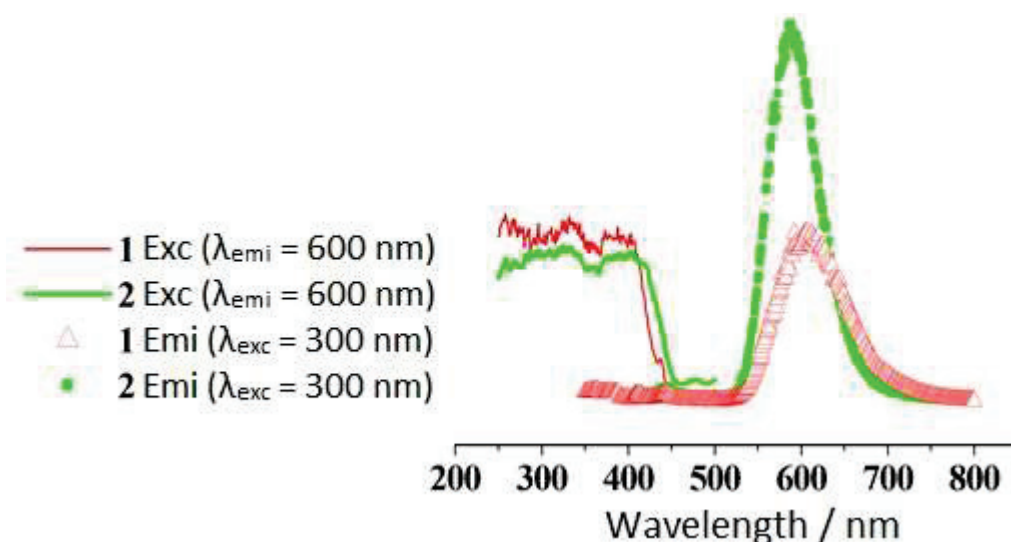


Figure 47: Solid state excitation ($\lambda_{\text{emi}} = 600 \text{ nm}$) and emission ($\lambda_{\text{exc}} = 300 \text{ nm}$) of complex 1 (red curves) and complex 2 (green curves).

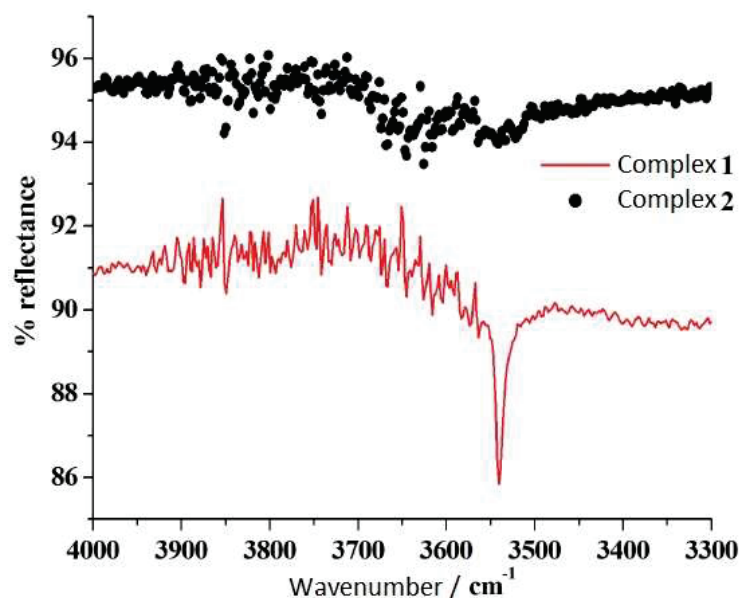


Figure 48: IR spectra of complexes 1 and 2 between $3\ 300 \text{ cm}^{-1}$ and $4\ 000 \text{ cm}^{-1}$.

The luminescence was assumed, but not proven, to be due to an antenna effect mechanism, whereby the sulfonycalixarene ligand absorbs radiation (due to its highly delocalised electron density distribution) followed by an efficient energy transfer step towards an excited electronic state on the metal ion, which then emits. One important factor influencing this hypothesis is the large Stoke's shift (greater than 200 nm) between the wavelength of absorbed and emitted light. Figure 49 shows the usual energetic basis of how a Stoke's shift comes about for emission from a singlet and triplet excited state. The very large shift implies internal relaxation to a lower energy excited state

before emission. Other factors of interest are the long lifetime of the process (implying triplet state population and energy transfer steps), the fact that complexation increases the extinction coefficient of absorption compared to that of the free ligand, and the good agreement of the wavelength of emission with the energy levels of manganese(II) ions.

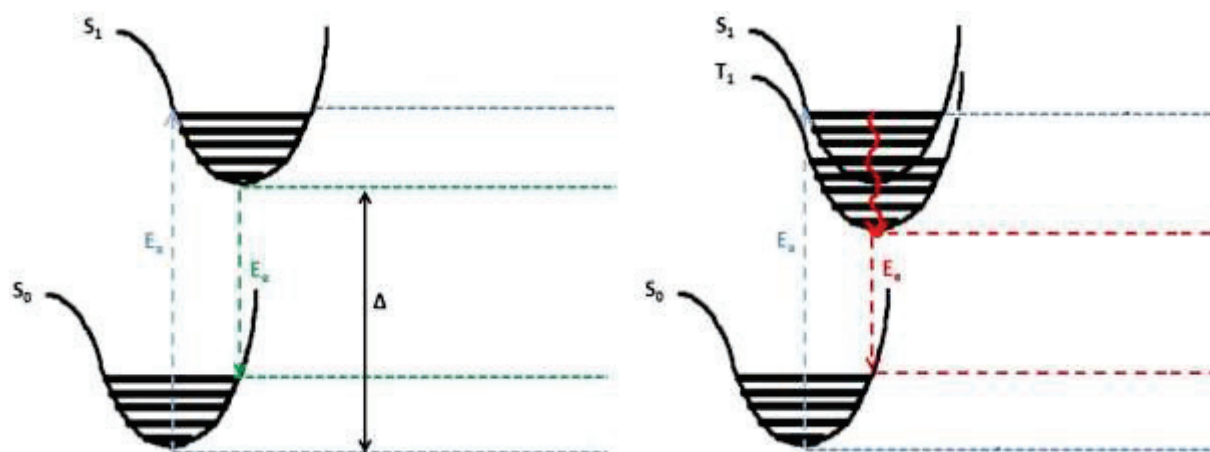


Figure 49: Energetic configurational coordinate diagrams showing the origin of the Stoke's shift in photoluminescence, where E_a is the energy of the absorbed photon and E_e is the energy of the emitted photon, for emission from a singlet state (left) and a triplet state (right).²⁶

A study was conducted on the effect of replacing the charge balancing cation, potassium, with other functions. In the cases of caesium and sodium no significant difference was observed. However, when potassium was used in conjunction with the crown ether 18-crown-6, the structure shown in figure 50 was obtained (complex **3**). Complex **3** exhibits considerably different behaviour from complexes **1** and **2**. Structurally, while the core anionic aggregate remains the same, each aggregate is now separated by a greater distance, as the cation is farther from the coordination complex, and is no longer directly bonded to the sulfonyl groups of the ligand. Its luminescence properties also change; the luminescence of **3** is strongly quenched by the presence of O_2 . This suggests some competing energy transfer reaction towards the triplet ground state of molecular dioxygen is possible for this complex.

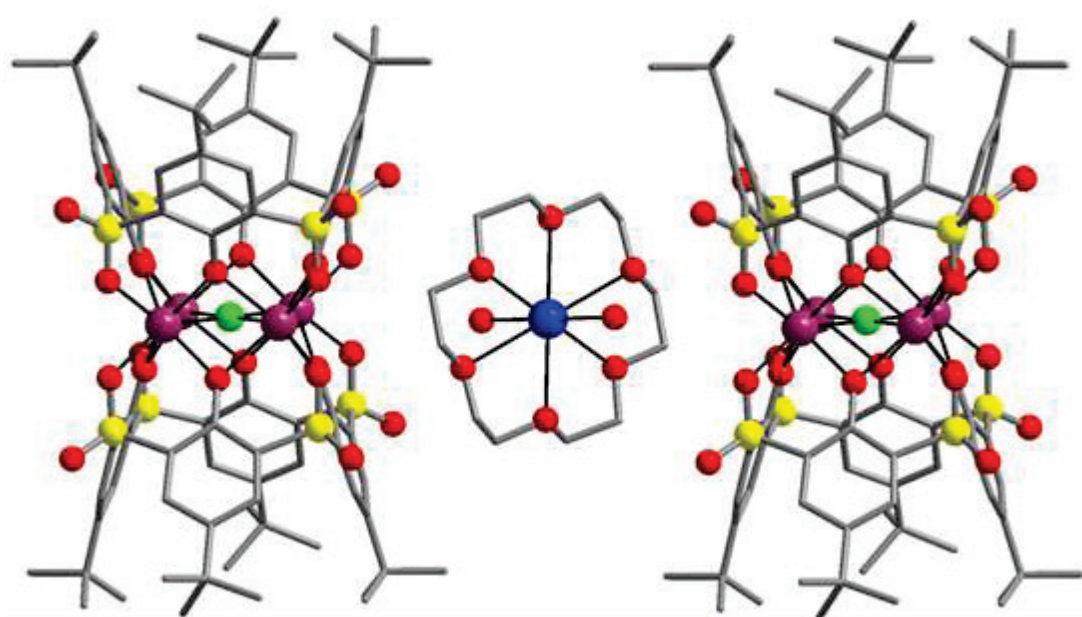


Figure 50: Structure obtained by single crystal XRD of derivative complex **3** with the cation $[K(18\text{-crown-}6)]^+$. Colour key: C = grey; S = yellow; O = red; F = green, Mn = purple; K = blue. H atoms omitted for clarity.

To further investigate the luminescence behaviour of this group of complexes, the following chapter will seek to meet the following goals:

- To characterise the luminescence process taking place in complex **2**, demonstrate that the emission arises from Mn-centred transitions and thereby prove the hypothesis that an antenna effect interaction takes place.
- To investigate and elucidate the effect of interactions with the cation, including the importance of direct bonding between the cation and the anionic aggregate and the structural changes which arise, by the characterisation of the luminescence behaviour of complex **3** and related cation-substituted structures.
- To undertake functionalisation and modification of the macrocycle, and investigate the resultant effect upon the luminescence properties of the complex.
- To investigate the luminescence of these species in solution, in particular with an eye to the response observed to the presence of molecular oxygen in the medium.

2.2: Syntheses

All synthetic methods were carried out according to procedures previously described in the literature.²⁷⁻²⁹ The ligand thiaSO₂ was obtained from the original thiaS by oxidation with sodium perborate, acetic acid and hydrogen peroxide in chloroform. The tetrabrominated form Br₄thiaSO₂ was produced by a multistep process as shown in figure 51: dealkylation with aluminium chloride and the subsequent bromination using N-bromosuccinimide were carried out to obtain the unoxidised Br₄thiaS. This was then oxidised by reaction with hydrogen peroxide and trifluoroacetic acid.

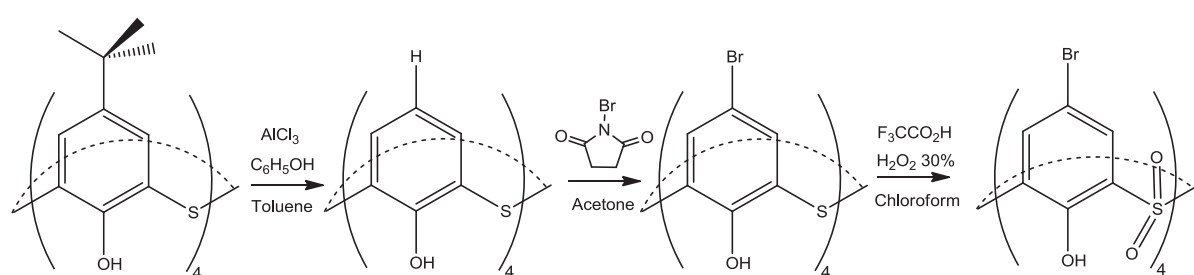


Figure 51: Synthesis of Br₄thiaSO₂ from thiaS.

Syntheses of metal complexes were all under solvothermal conditions in a 10:1 mixture of methanol and water using manganese(II) chloride tetrahydrate as the manganese salt and the appropriate combination of base and crown ether. Typically the peak temperature was 170° C, maintained for approximately 24 hours. Other materials were used 'as purchased' without further purification. The weakly luminescent dinuclear complex **5** was synthesised by a previously derived reaction of thiaSO₂ and manganese(II) chloride in the absence of oxygen as follows. To a solution of thiaSO₂ and triethylamine in chloroform solution is added an excess (2.9 : 1.18) of MnCl₂·4H₂O dissolved in the minimum amount of methanol under N₂ atmosphere. After heating to reflux under N₂ circulation for 1 hour followed by evaporation of the solvent, the product [Mn₂(thiaSO₂)(DMF)₄(H₂O)₂] was obtained by recrystallisation from DMF.¹⁹ This species is a transition complex in the photo-oxidation of the manganese(II) / thiaSO₂ system, which will be explored in greater detail in chapter 3. Hybrid materials consisting of luminescent tetranuclear aggregates [Mn₄(thiaSO₂)₂F]⁻ substituted into the interlayer space of layered double hydroxide materials were

obtained by a method of exfoliation and intercalation in formamide in the absence of oxygen. Chapter 4 will consider the synthesis of these materials and their luminescence properties in depth.

Annexe 3 contains the decay curves for all luminescence lifetime calculations carried out.

2.3: Solid state luminescence characterisation of complex 2

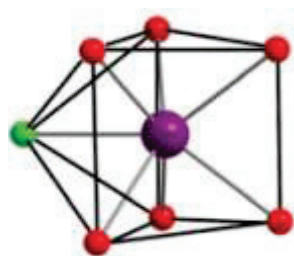
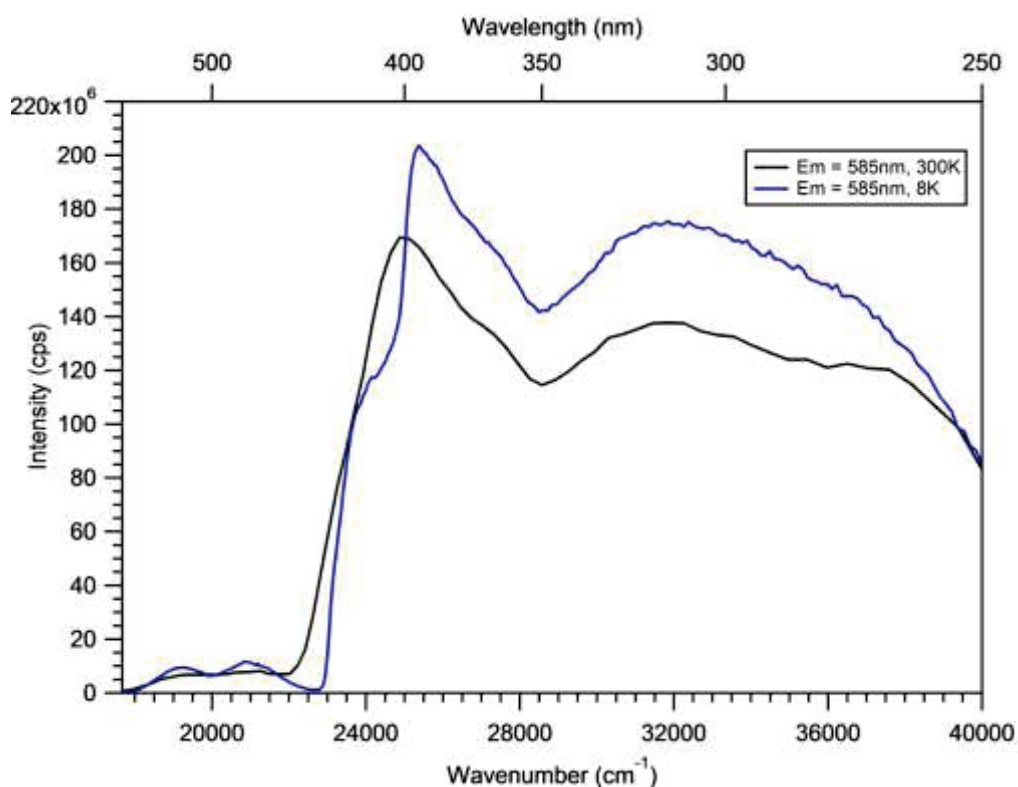


Figure 52: 7-coordinate C_{2v} manganese(II) centre found in complex 2. Colour key: Mn = purple, O = red, F = green.

In depth characterisation of the luminescence response of complex 2 to the external conditions of pressure, temperature, and O_2 pressure has been carried out. If, as it has been theorised, the luminescence arises due to an antenna effect, then the luminescence will react in a defined, predictable way to these conditions. Crucially, the effect of pressure on the coordination sphere of each manganese centre (an unusual 7-coordinate system, shown in figure 52) would show a characteristic linear shift in emission wavelength. The results of this characterisation are discussed below.

Figure 53 shows the solid state excitation spectra ($\lambda_{emi} = 585$ nm) of complex 2 at room temperature (300 K) and at low temperature (8 K), with attached the low temperature solid state excitation – emission spectrum of complex 2 in the range from $13\,500\text{ cm}^{-1}$ to $24\,000\text{ cm}^{-1}$. The room temperature excitation spectra at either temperature both show two peaks, assigned to $\pi \rightarrow \pi^*$ transitions centred upon the ligands, with a comparatively very weakly absorbing region between about 435 nm and 570 nm which is magnified in the lower part of figure 53. The principal excitation peak is centred at approximately 400 nm at room temperature, or 390 nm at low temperature, and is asymmetric in both cases between about 355 nm and 455 nm. The second peak is broader, situated between less than 250 nm and 455 nm with a maximum situated at about 310 nm in both cases.

The emission spectrum at low temperature gives an asymmetric peak with a maximum at 602 nm, ranging between 555 nm and 770 nm. The excitation spectrum has been magnified to show a very weak asymmetric double peak centred at 481 nm and 521 nm, with what seems to be a shoulder on the short-wavelength side. These absorptions are believed to correspond to direct excitation of the first electronic transition on the manganese(II) centre, i.e. ${}^6A_1 \rightarrow {}^4T_1$; this would explain both the weakness of the absorption (due to the forbidden d-d transition) and the double peak (splitting due to degeneracy in the excited 4T_1 level induced by the coordination geometry). This being the case would further implicate the manganese ion in the luminescence process, strengthening the hypothesis that the emission arises from these ions.



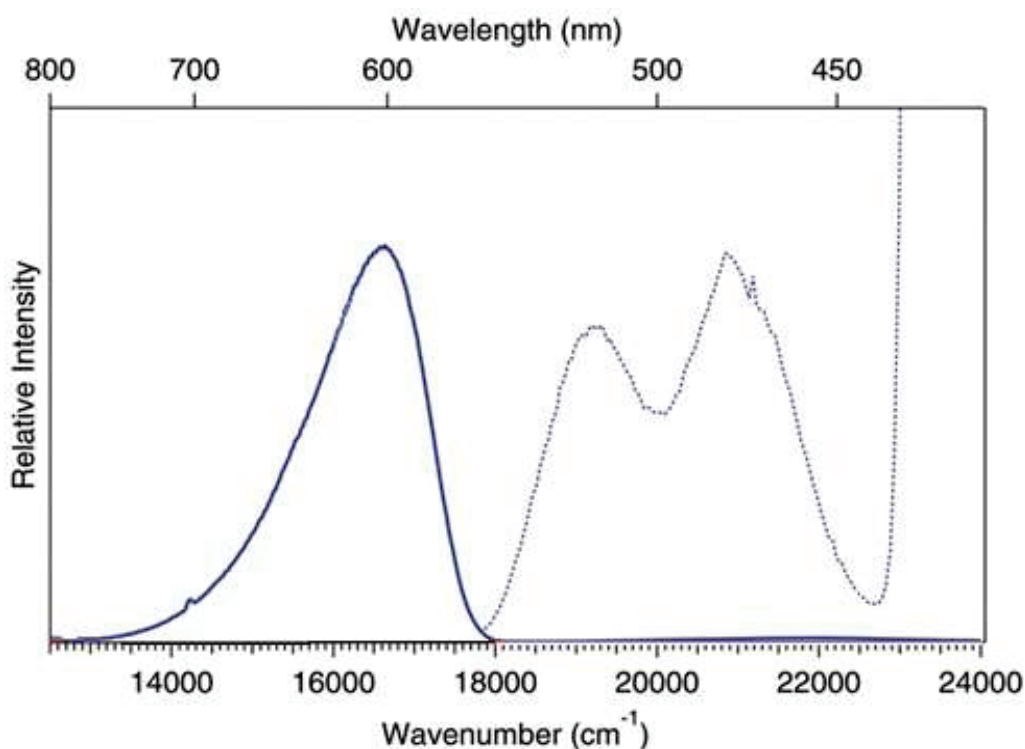


Figure 53: (Above) Solid state excitation spectra of complex 2 ($\lambda_{\text{emi}} = 585 \text{ nm}$) at both 300 K (black curve) and 8 K (blue curve). (Below) Solid state excitation spectrum (dashed line, $\lambda_{\text{emi}} = 602 \text{ nm}$) measured at 8 K magnified to highlight weak excitation peaks, and solid state emission spectrum (solid line, $\lambda_{\text{exc}} = 350 \text{ nm}$) measured at 7.5 K of complex 2.

2.3.1: Response to pressure

The response of emission to pressure in the range from ambient pressure (about 0.1 MPa) to 10 GPa was measured in a diamond anvil cell using emission of $\text{BaFCl}:\text{Sm}^{2+}$ as an internal pressure sensor.³⁰ Spectra were measured at 298 K with excitation at 405 nm. The results are plotted in figure 54 below. It can be seen that the wavelength of emission maximum redshifts with increasing pressure, at a rate of $-230 \text{ cm}^{-1} \text{ GPa}^{-1}$, and the intensity decreases. This fact confirms the hypothesis that emission is centred upon the manganese ions, and thus that an antenna effect is taking place, by the following logic.

The spin forbidden d-d transition ${}^4\text{T}_1(4\text{G}) \rightarrow {}^6\text{A}_1$ involves electron transfer from a non-bonding t_{2g} orbital to an anti-bonding e_g orbital, resulting in expansion of the coordination sphere. External pressure therefore has a destabilising effect on the ${}^6\text{A}_1$ ground state with respect to the excited state, following a work term of $P\Delta V$. Considering the rate of decrease of the luminescence, this gives an approximate value of ΔV as 5 \AA^3 for each aggregate. The basis for the redshift can be seen in the

Tanabe-Sugano diagram for d^5 ions (figure 55). An increase in the intensity of emission is observed between ambient pressure and 0.3 GPa. This effect is theorised to arise due to oxygen present within the interior space of the crystalline material, which is gradually expelled by the application of pressure until it is removed entirely by 0.3 GPa of pressure, after which point the expected response is observed. This proposition is not yet confirmed.

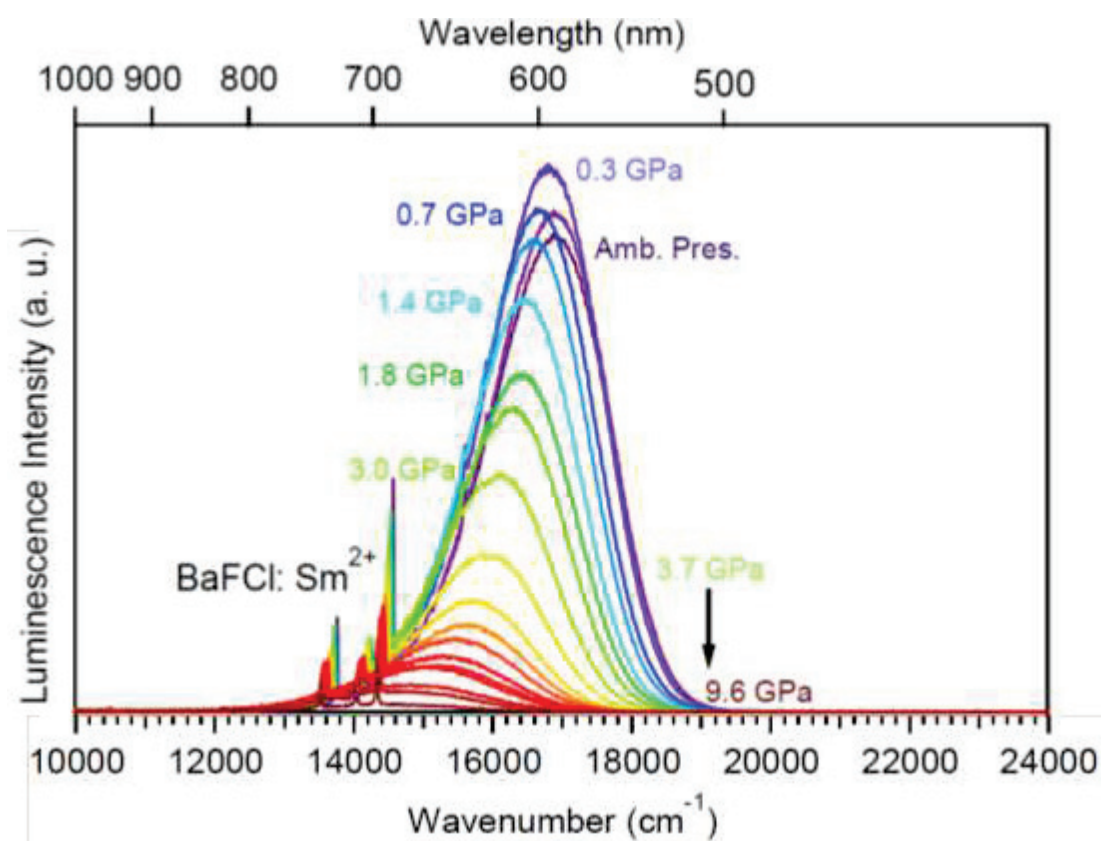


Figure 54: Evolution of emission spectrum measured at room temperature under inert atmosphere of complex 2 ($\lambda_{exc} = 405$ nm) with respect to pressure in the range from ambient pressure (purple line) to 10 GPa (maroon line). BaFCl:Sm²⁺ is employed as an internal pressure sensor.

As the pressure causes compression of the Mn-O bonds, the ligand field increases causing a simultaneous decrease in the energy gap between the $^4T_1(4G)$ and 6A_1 levels (equivalent to destabilisation of the ground state with respect to the excited state). Luminescence lifetimes were calculated for the range of pressures analysed; the value decreases steadily from 1.71 ms at ambient pressure to 0.55 ms at 10 GPa. This decrease in pressure with increasing external pressure is indicative of a decrease in luminescence quantum efficiency. The rate of non-radiative decay increases as the ground state (zero-point) energy decreases, according to the energy gap law.³¹ This

law would predict a value of 15 % at 10 GPa; however in actual fact the value at 10 GPa is less than 5 %. This discrepancy is possibly due to the splitting in the lowest excited state of Mn^{2+} , as was observed in figure 53. The individual components of this energy level may respond differently to pressure with respect to the ground state than predicted by the energy gap law.

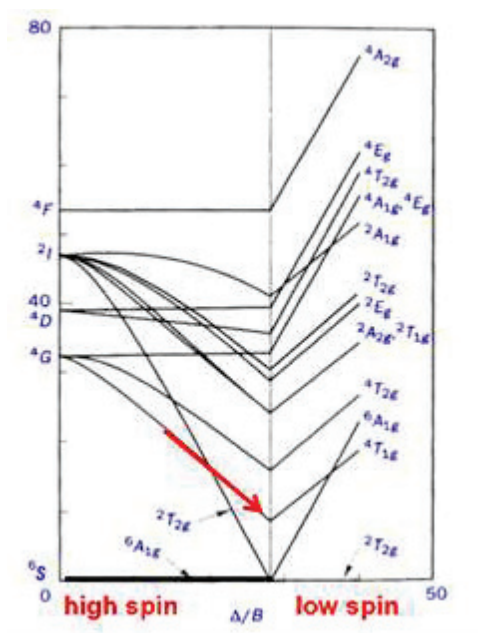


Figure 55: Tanabe-Sugano diagram for energy level of states in d^5 ions. Red arrow indicates the direction of change as pressure increases.

Figure 56 shows the proposed mechanistic pathway of luminescence following these conclusions, depicted by the bold red arrows, while figure 57 below depicts the electronic microstates involved in this mechanism. We infer that the triplet excited state of the molecule is involved in the process from the quenching effect of molecular oxygen on luminescence from the complex in the solution state. The ground state of O_2 under ambient conditions is a triplet state (§2.3.3, figure 60); therefore in order for efficient energy transfer to be taking place it stands to reason that the donor species (the photoexcited complex) is most probably also in a triplet state.

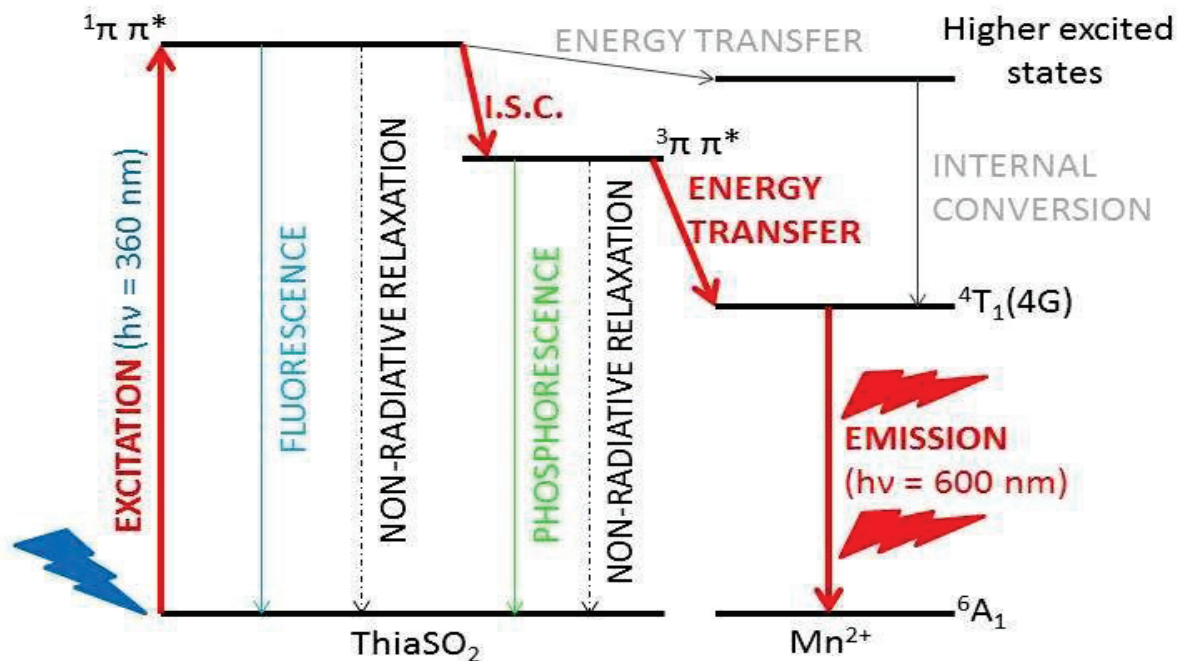


Figure 56: Proposed mechanistic scheme (bold red arrows) of antenna effect luminescence.

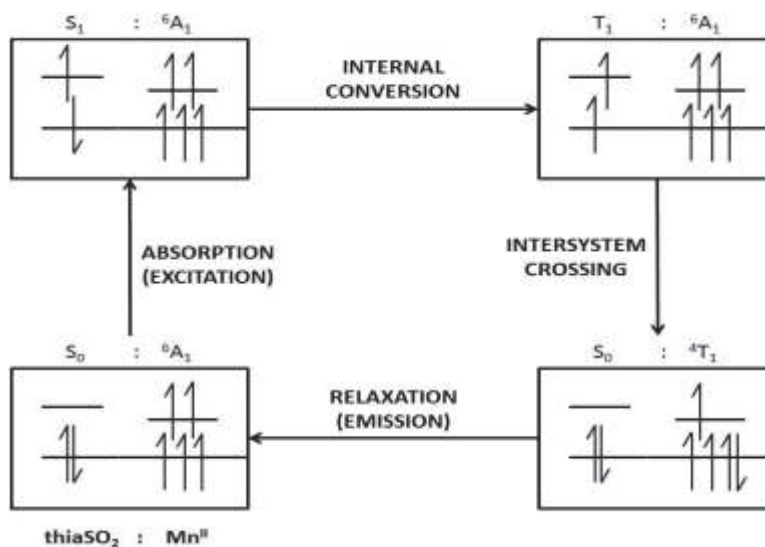


Figure 57: Electronic microstates involved in the photoluminescence of complex 2.

2.3.2: Response to temperature

Figure 58 shows how the emission peak observed for complex 2 in the solid state (centred at 602 nm and with a Full Width at Half Maximum FWHM of about $1\,700\text{ cm}^{-1}$ at 7.5 K) varies with the applied temperature.

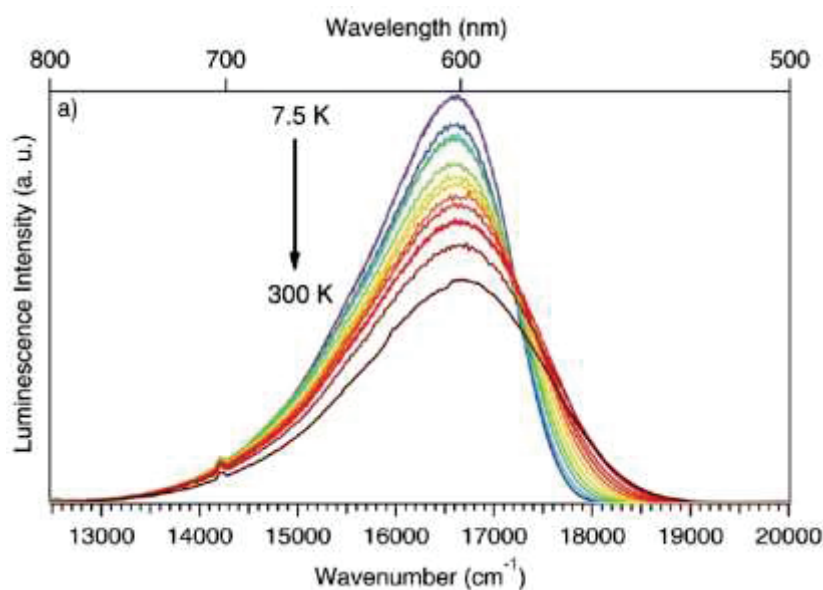


Figure 58: Evolution of solid state emission spectrum of complex 2 ($\lambda_{\text{exc}} = 350 \text{ nm}$) with increasing temperature in the range from 7.5 K (purple line) to ambient temperature 300 K (black line).

Immediately two features can be seen: firstly, with increasing temperature the intensity of emission decreases, eventually becoming about 70 % of its low temperature value at ambient temperature. This is expected behaviour for an emitting metal complex; higher temperature allows for more population of higher vibrational and rotational energy levels which increases the possibility of non-radiative relaxation of the excited molecule. The rate of decrease in intensity is fairly slow up until a temperature of 250 K, where it becomes sharper. Secondly we can observe a noticeable broadening of the emission peak, as in the FWHM increases with increasing temperature to a 300 K value of approximately $2\,200 \text{ cm}^{-1}$. Again this is related to the population of higher energy levels, as higher energy overall in the system invokes greater variation in the coordination environment around the manganese centres, corresponding to a broader peak. The beginning point of the peak remains unchanged at approximately 769 nm for all temperatures observed, whereas the end point of the domain shifts from about 555 nm at 7.5 K to about 526 nm at 300 K. This information is depicted graphically in figure 67 (§2.4.2). Finally, the luminescence lifetime initially increases with increasing temperature from its low temperature value of 2.12 ms at 3 K to a maximum value of 2.41 ms at 75 K. The value then falls gradually to an ambient temperature (300 K) value of 1.65 ms.

Considering the luminescence quantum yield at this temperature is 50 %, this gives a derived radiative lifetime of about 3 ms, which is typical of such spin forbidden d-d transitions.

2.3.3: Response to O₂ pressure

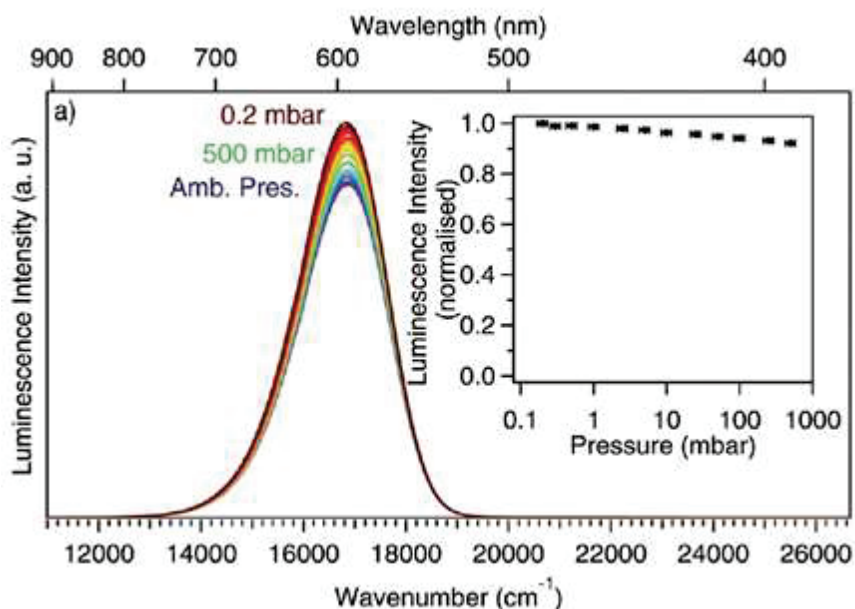


Figure 59: Evolution of the solid state emission spectrum of complex **2** ($\lambda_{\text{exc}} = 405 \text{ nm}$) at room temperature with varying oxygen pressure in the range between 0.2 mbar (maroon line) and ambient pressure (purple line).

Figure 59 shows the response of emission from complex **2** to O₂ pressure; as was noted above the presence of oxygen quenches the luminescence such that emission intensity under ambient conditions is 85% the strength of emission intensity observed in oxygen free conditions (0.1 mbar of pressure). We can conclude that the excitation energy of the photoexcited complex is transferred to molecular oxygen, resulting in non-radiative relaxation.

The ground state of the oxygen molecule is a triplet state; figure 60 depicts this ground state as well as the two lowest energy excited states along with the corresponding term symbols. This reinforces the notion that the quenching energy transfer originates from the triplet excited state of the manganese complex, meaning that significant population of this triplet level must occur during the luminescence process (see mechanism in figure 56). As seen in figure 60 both of the excited states are singlet states, one having a term symbol Δ and the other Σ . The transitions giving rise to these states are both of a lesser potential energy difference than the emitting transition of the

luminescent manganese(II) complex (600 nm is approximately 2.07 eV) indicating that excitation via energy transfer from the excited complex towards ground state oxygen is indeed possible.³²

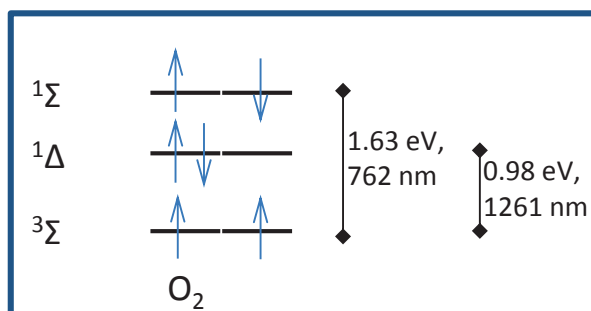


Figure 60: Occupation of the HOMO of the O₂ molecule (a π* orbital) in its ³Σ ground state and in the two nearest excited states, with the associated energy of the transitions shown.³²

2.4: The significance of the K-O=S interaction: solid state luminescence of complex 3

Complex **3** differs from complex **2** only in the cation; instead of a free potassium ion the potassium is coordinated by the crown ether 18-crown-6. It is synthesised by a solvothermal reaction shown in figure 61 between manganese(II) chloride and thiaSO₂ in the presence of potassium fluoride and 18-crown-6. A typical heating profile of this synthetic reaction would entail heating at a rate of 0.2° C min⁻¹ to 170° C, whereafter this temperature is maintained for a duration of 24 hours before slow cooling to room temperature, again at a rate of 0.2° C min⁻¹. The product is obtained in the form of pale yellow platelet crystals. Figure 62 compares the structures of complexes **2** and **3**, highlighting that the main structural change is the loss of the direct bonds between the cation K⁺ and the sulfonyl groups of the ligand.

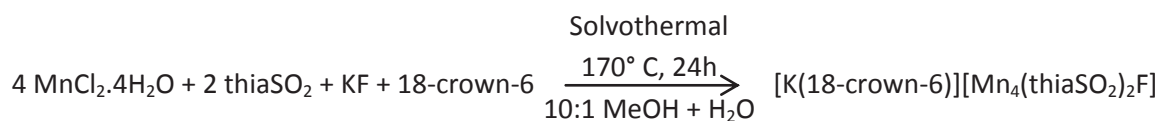


Figure 61: Solvothermal synthesis of complex 3.

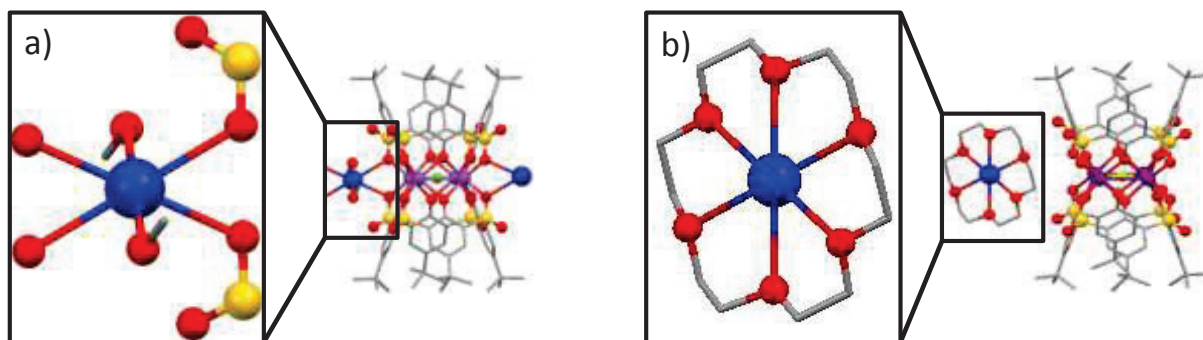
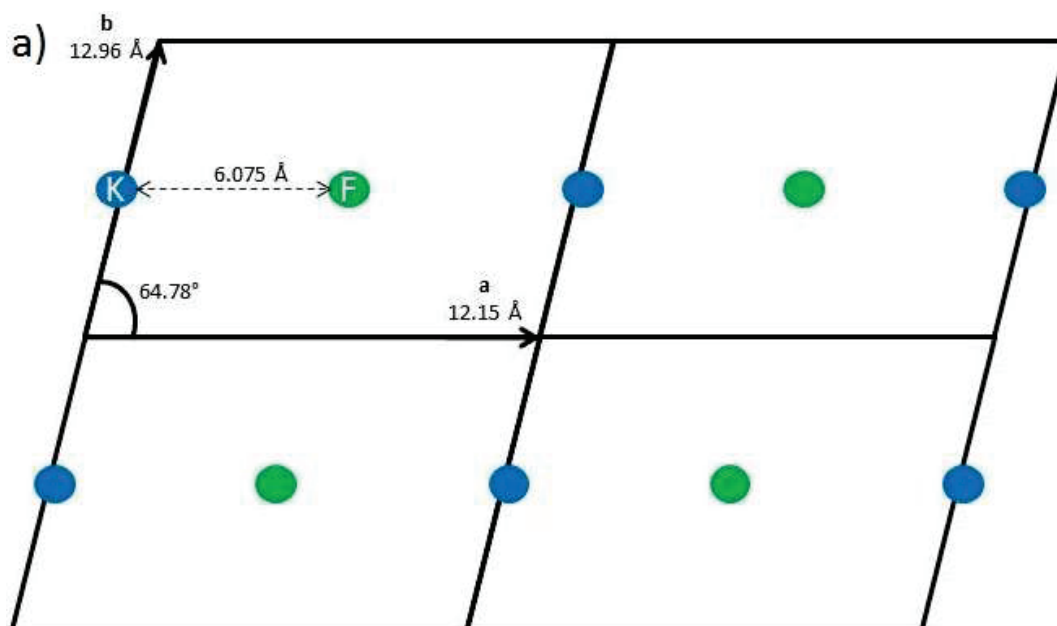


Figure 62: Zoomed in side-by-side comparison of the cation environment in a) complex 2 and b) complex 3 illustrating the direct K-(O=S) bonds which are present only in complex 2. Colour key: C = grey, S = yellow, O = red, Mn = purple, F = green, K = blue. H atoms omitted for clarity.

Discounting minor conformational changes to the ligand, the 7-coordinate, C_{2v} symmetric coordination environment of the four manganese centres in each complex is identical (figure 47). The dissociation of the cation from the luminescent aggregate observed in complex 3 can be considered as somewhat analogous to the situation in solution, where total dissociation of the cationic from the anionic components is assumed. The lack of direct bonding to the cation as well as the greater separation between luminescent centres (K-F distance = 6.075 Å in 2 and 8.539 Å in 3, although the distance between F⁻ ions at the centre of each agglomerate is very similar at 12.15 Å and 12.01 Å respectively; see figure 2.22 for a depiction of this arrangement) is believed to give rise to a more open, porous crystalline structure in this product which could play an important role in the solid state luminescence process. This section will consider in detail the luminescence behaviour of this species.



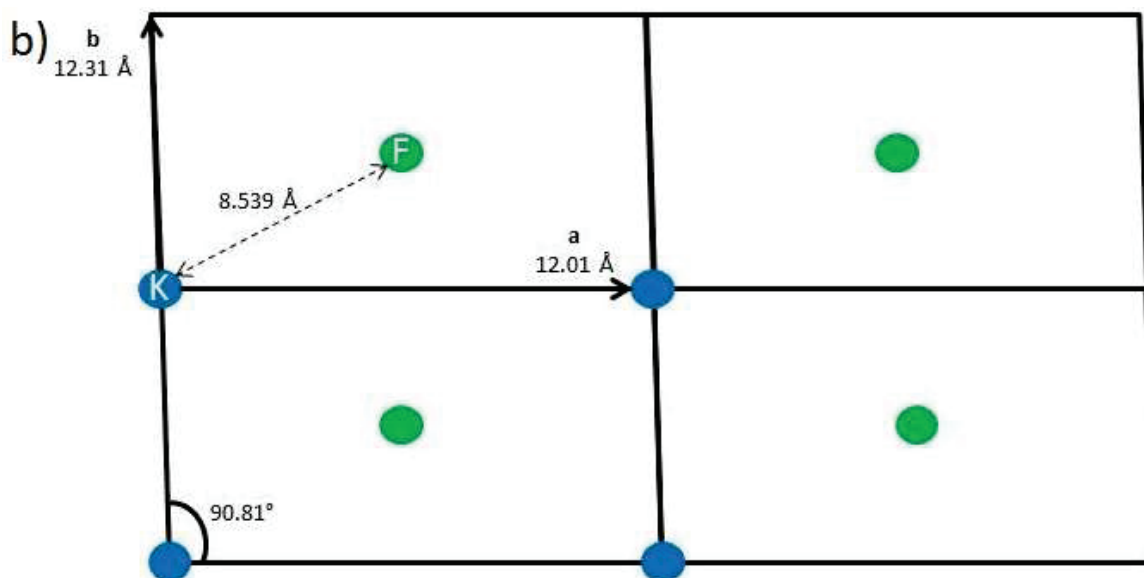
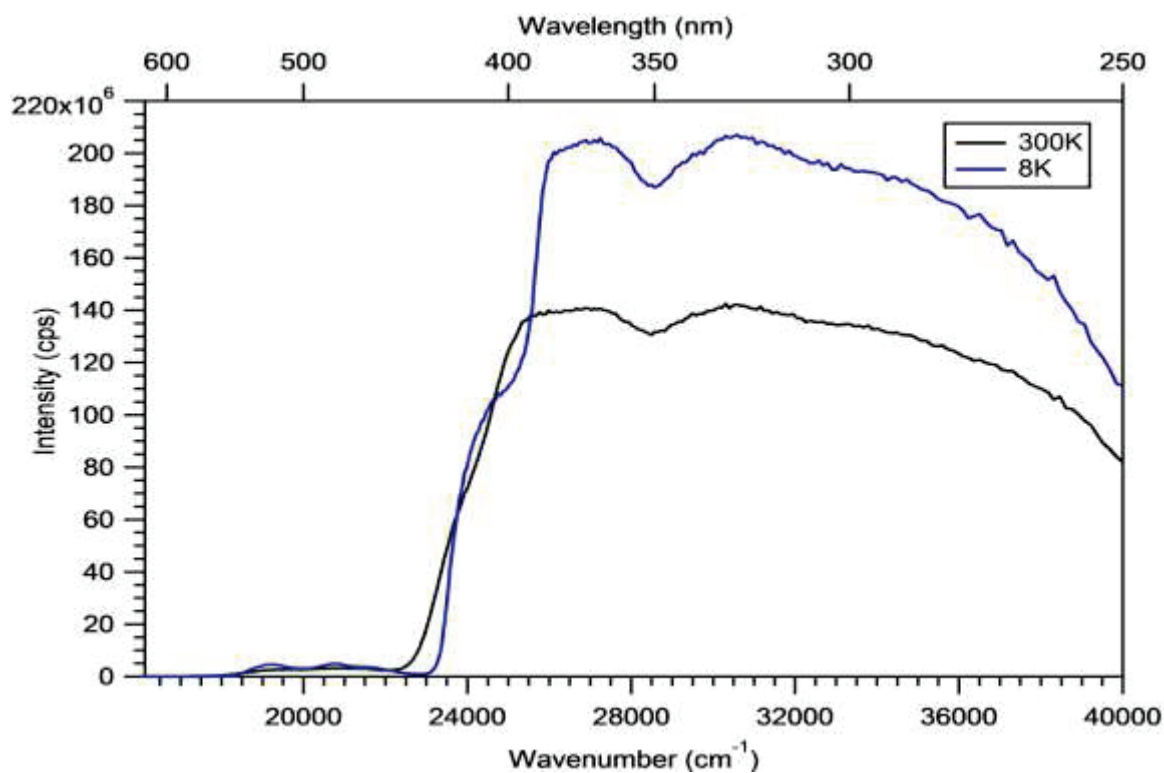


Figure 63: View of the *ab* plane of the crystallographic unit cell of a) complex **2** and b) complex **3** showing the position and spacing of the potassium cation in blue and the fluoride atom in green.

Figure 64 shows the solid state excitation spectra of complex **3** at both room temperature (300 K) and low temperature (8 K), as well as the solid state excitation (magnified) and emission spectra obtained at low temperature with the equivalent spectra of complex **2** included as a reference point. The excitation spectra at either temperature value display similarities and differences to those measured for complex **2**. The essential form of the spectra remain the same, with two large peaks arising due to $\pi \rightarrow \pi^*$ ligand-centred transitions. Again more fine detail is observed in the low temperature spectrum, with a shoulder on the low energy end of the principal excitation peak. In this case however these two peaks are broader than was observed for complex **2**, and are of approximately commensurate intensity with one another such that the excitation domain almost appears as one large plateau between about 250 nm and 400 nm. In the magnified low temperature excitation spectrum we observe the same double peak attributed to direct excitation of the ${}^6A_1 \rightarrow {}^4T_1$ transition for both complexes **2** and **3**, reinforcing the similarity of the manganese coordination environment in each. The emission peak of complex **3** takes on a different form, being both more symmetrical and broader at the half-maximum intensity point, although the emission covers the same spectral range as that of complex **2** between 555 nm and 769 nm. The position of

the emission maximum of complex **3** is redshifted with respect to that of complex **2**, occurring at about 640 nm. These differences in the form of the emission peak at this low temperature are most likely due to conformational differences in the ligand; the fact that the emission peak of complex **2** becomes similarly symmetrical at ambient temperature implies that thermal freedom equilibrates these differences by motion of the coordinating atoms.



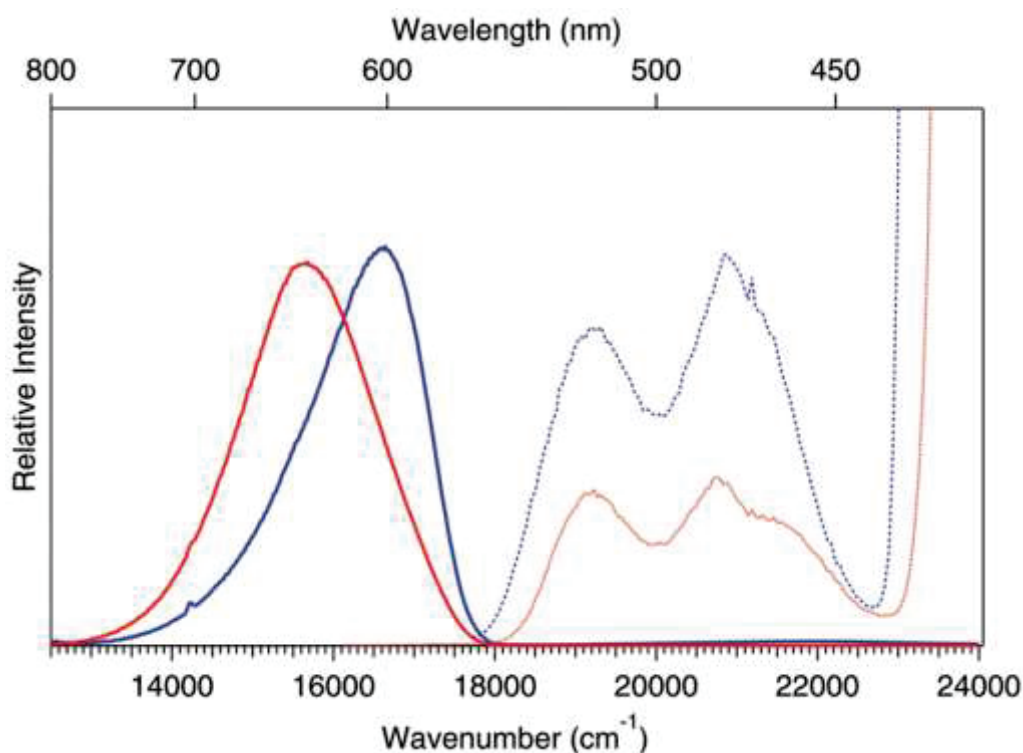


Figure 64: (Above): Solid state excitation spectra for complex **3** measured at 300 K ($\lambda_{\text{emi}} = 615$ nm, black curve) and 8 K ($\lambda_{\text{emi}} = 640$ nm, blue curve). (Below): Solid state excitation spectrum (dashed lines) measured at 8 K, and solid state emission spectrum (solid lines) measured at 7.5 K for excitation at 350 nm, of complex **2** (blue) and complex **3** (red).

2.4.1: Response to pressure

Figure 65 shows the response of the luminescence of complex **3** to pressure in the range between ambient pressure and 10 GPa; as with complex **2** measurements were carried out in a DAC using the internal standard BaFCl:Sm²⁺. The expected bathochromic shift is observed in the position of the peak maximum with a value of $-190 \text{ cm}^{-1} \text{ GPa}^{-1}$, confirming the emission arises from the same manganese-centred transition as occurs for complex **2**.

Interestingly, however, in the range between ambient pressure and 0.4 GPa there is a sharp increase in emission intensity, sharper than that observed with complex **2** between ambient pressure and 0.3 GPa; thereafter the expected decrease in intensity with increasing pressure follows. Indeed the initial emission measured in the DAC under ambient pressure is considerably less intense than that observed outside the DAC under helium atmosphere. This effect is believed to be due to the crystal structure of the material. Under ambient conditions before the experiment, oxygen from the surroundings may penetrate into any pores and channels in the structure where it would remain

once the material is placed in the oxygen free conditions of the cell. Oxygen present within the material quenches the luminescence, leading to a lower observed intensity. The application of pressure would then act to expel this adsorbed oxygen, and once it has been removed entirely the expected intensity profile is followed. The hypothesis that complexation of the potassium cation with a crown ether results in a porous crystal structure in the luminescent product is thus strengthened.

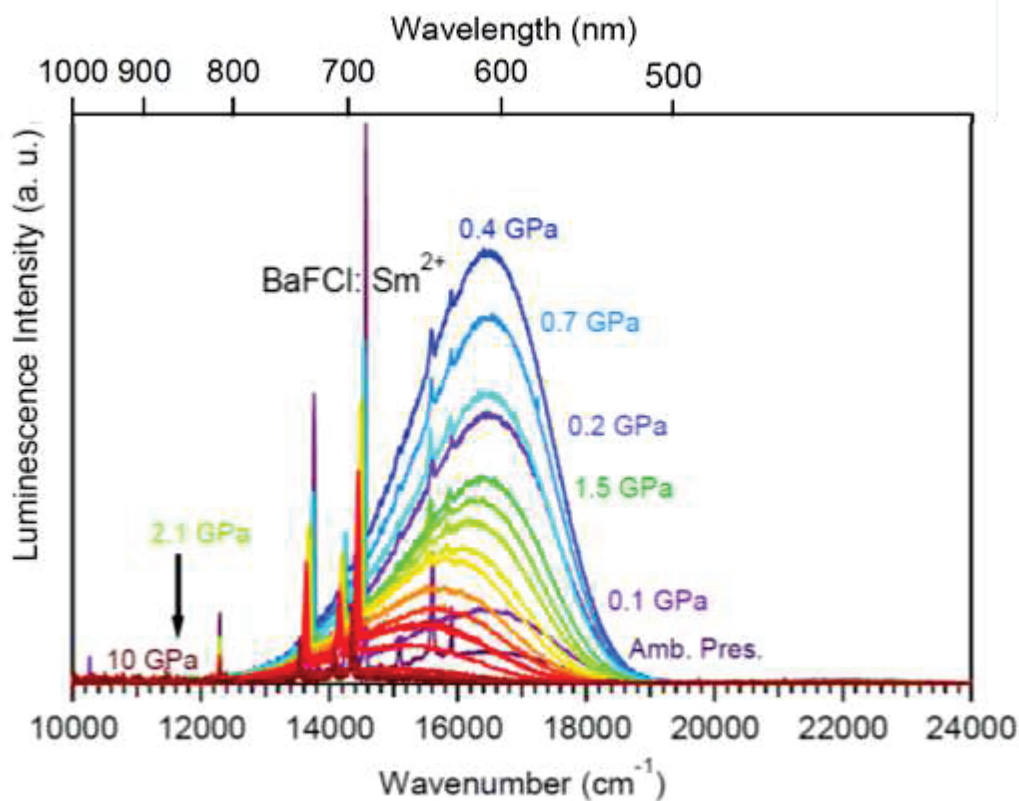


Figure 65: Evolution of emission spectrum measured at room temperature under inert atmosphere of complex **2** ($\lambda_{\text{exc}} = 405 \text{ nm}$) with respect to pressure in the range from ambient pressure (purple line) to 10 GPa (maroon line). BaFCl:Sm²⁺ is employed as an internal pressure sensor.

The luminescence lifetime of emission at ambient pressure was calculated to be 0.57 ms. This increases until a value of 1.45 ms is obtained at 0.4 GPa, then decreases in a comparable manner to **2**. The luminescence lifetime at 10 GPa is 0.59 ms. This initial increase arises for the same reasons as the initial increase in the luminescence intensity under the application of pressure, and the subsequent decrease is the expected behaviour for this type of species as was explained for complex **2** (§2.3.1). This complex also demonstrates a luminescence quantum efficiency of less than 5 % at 10 GPa of pressure, again due to the degeneracy of the lowest excited state of the Mn^{II} ion (figure 65).

2.4.2: Response to temperature

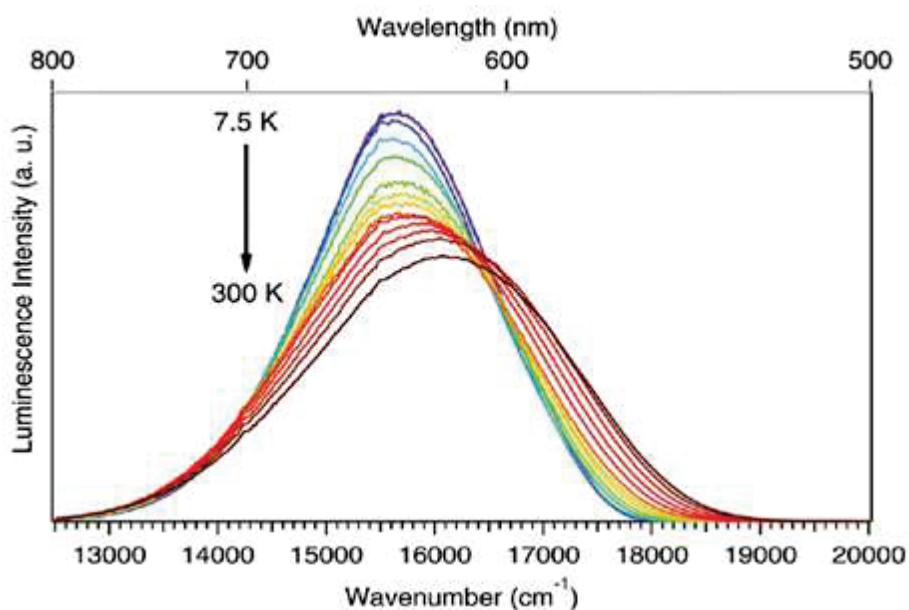


Figure 66: Evolution of solid state emission spectrum measured under inert atmosphere of complex **2** ($\lambda_{\text{exc}} = 350 \text{ nm}$) with increasing temperature in the range from 7.5 K (purple line) to ambient temperature 300 K (black line).

Figure 66 shows the effect of temperature on the observed emission for complex **3**. The intensity of emission decreases with increasing temperature as did emission of complex **2** (figure 58) such that the 300 K value is 88 % of the 7.5 K value. This decrease in intensity occurs primarily in the range between 7.5 K and 100 K, after which point it remains approximately stable. The high energy end point of the peak increases with temperature in an identical manner to complex **2** from 18 000 cm^{-1} to 19 000 cm^{-1} , and the peak width also increases with temperature in a similar manner, although at any given temperature the peak observed for complex **3** is broader than that seen in the spectrum of complex **2**. The FWHM values are 2 050 cm^{-1} and 2 800 cm^{-1} at 7.5 K and 300 K respectively. The position of the peak maximum roughly remains at around 639 nm until a temperature of 200 K, after which it increases sharply with increasing temperature (blue shift) to a 300 K value of 621 nm. This λ_{max} value is still shorter (redder) than that of complex **2**, 600 nm. The luminescence lifetimes were also measured, and found at 3 K to be 2.31 ms. The lifetime then increases to a maximum point of 2.48 ms at 100 K before gradually decreasing to an ambient temperature value and 2.00 ms respectively. The form of the plot of lifetime against temperature is similar to the analogous plot for complex **2** but the value of the lifetime is greater for complex **3** at

any given temperature. Figure 67 shows the collective data obtained from the emission spectra of complexes **2** and **3** at varying temperature.

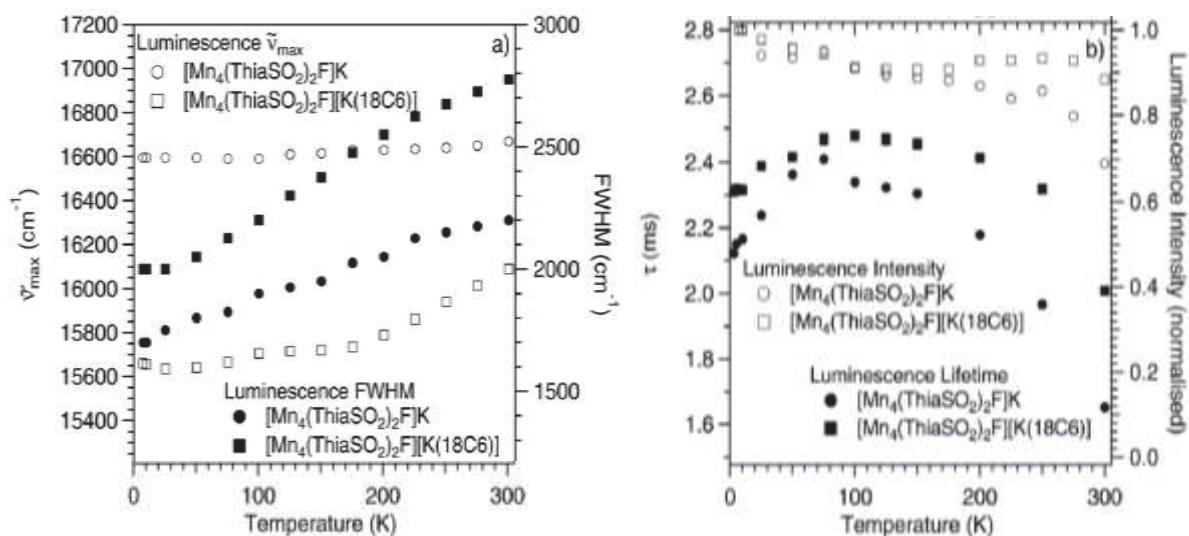


Figure 67: Comparison of temperature dependence data for the photoluminescence ($\lambda_{\text{exc}} = 350 \text{ nm}$) of complexes **2** ($[\text{Mn}_4(\text{thiaSO}_2)_2\text{F}]\text{K}$) and **3** ($[\text{Mn}_4(\text{thiaSO}_2)_2\text{F}][\text{K}(18\text{C}6)]$).

2.4.3: Response to O_2 pressure

Figure 68 shows the effect of the presence of oxygen upon the emission spectrum of complex **3**. Here again we see a quenching effect of oxygen, much stronger than was observed in the case of complex **2**. The intensity of emission under ambient pressure conditions is less than 5 % when normalised to its value under low pressure (0.1 mbar). By the assumption that the mechanism responsible for the luminescence quenching is the same energy transfer creating $^1\Sigma$ oxygen, it can be concluded that the area of contact between the luminescent species and gaseous oxygen is much greater in this material than in complex **2**. The strength of this quenching is further proof that the crystalline material **3** has a porous structure which is open to penetration by molecular oxygen.

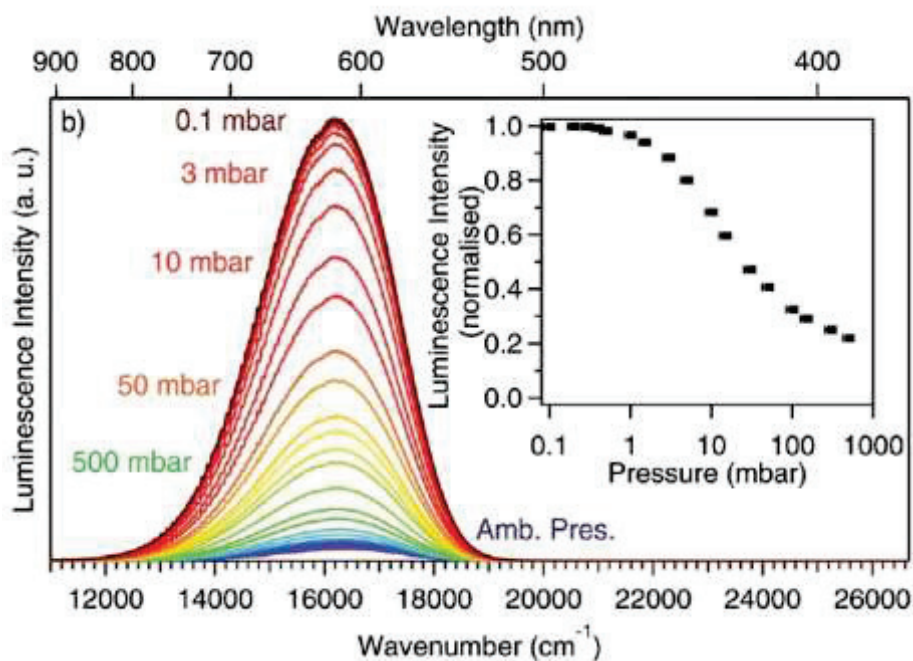


Figure 68: Evolution of the solid state emission spectrum of complex 3 ($\lambda_{\text{exc}} = 405 \text{ nm}$) at room temperature with varying oxygen pressure in the range between 0.2 mbar (maroon line) and ambient pressure (purple line), with inset plot of normalised luminescence intensity over this range of O_2 pressure.

2.4.4: Summary of the cation effect

It has been demonstrated that complexation of the potassium cation has a great influence on the luminescence behaviour of these aggregates, in terms of the form of the emission spectra, the lifetime of the emission process, and most importantly the sensitivity to the presence of oxygen in the solid state. As yet it is unclear exactly whether these changes are due to an electronic interaction present in the direct bonding of the cation to the ligand sulfonyl groups, to electronic and conformational changes induced in the ligands by removing this bonding, to the greater separation brought about between the concentration points of positive and negative charge density, or to some combination of these factors. It has, however, been possible to put forward a hypothesis on the comparative structural configurations of these species, as follows. The aggregate which contains a crown ether, while having similar crystal shape and size to the original, demonstrates a markedly higher sensitivity to the presence of oxygen via a strong quenching effect on the luminescence emission. It therefore stands to reason that this species has a microporous structure permitting the widespread interaction of the luminescent centres with gaseous oxygen all through the material.

To further extend this line of reasoning, it is interesting to envision total separation of the luminescent aggregate from the positive charge. This can be achieved by the insertion of the cluster complex into the interlayer space of positively charged layered materials, such as layered double hydroxides (LDHs). Experiments detailing the preparation of such host-guest composites and the characterisation of their luminescence are documented in the fourth chapter of this thesis.

2.5: Chemical and conformational modification of the macrocycle

The next two luminescent complexes to be considered differ considerably from those so far examined. Their structures are: complex **4** $K[Mn_4(Br_4thiaSO_2)_2F]$ where $Br_4thiaSO_2$ is the para-brominated form of the sulfonylcalix[4]arene ligand, and complex **5** $[Mn_2(thiaSO_2)(DMF)_6]$; figure 69 shows both of these structures. Complex **4** is interesting primarily as a proof of concept for the facility of modification on the ligand and how that can affect luminescence behaviour, and as a 'stepping stone' material towards more sophisticated molecular architectures; for instance the delocalised π -system could be extended via the substitution of Br with an alkyne by a Sonagashira type coupling reaction. It has been observed that, in the case of certain xanthene dyes (such as Rose Bengal, for instance), an increase in the number and atomic mass of halogen substituents on the molecular framework results in both a redshift of the peak maximum and an augmentation of the yield of intersystem crossing to the excited triplet state.³³ As the population of the triplet state is an important factor when acting as a photosensitiser for singlet oxygen generation, it would be interesting to note the effect of this substitution of Br groups upon the optical activity of the system. Thus far only preliminary characterisation has been carried out on this species. Complex **5** is a product of the reaction of complex **2** (or related complexes of that family) under certain conditions with irradiation. Worthy of particular note is that the coordination number of the Mn^{2+} ions involved has decreased from 7 to 6 with respect to the previously discussed compounds, resulting in a more normal pseudo-octahedral geometry. The comparative emission behaviour of this dinuclear complex is therefore interesting as a means to probe the effect of this change in coordination environment.

Its luminescence behaviour has been analysed in depth, and is presented in this section. We will consider these two species separately.

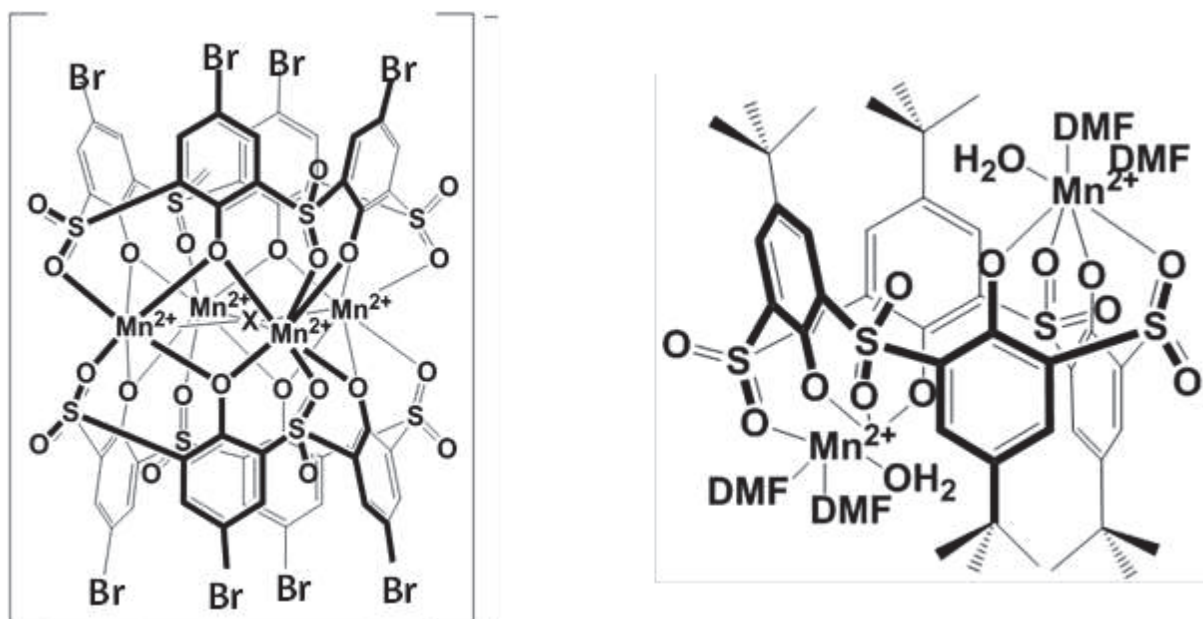


Figure 69: Chemical structures of complexes **4** (left) and **5** (right).

2.5.1: Complex **4**; substitution at the para-position

In the case of complex **4** the $C_{2v} O_6F$ coordination environment of each of the four manganese(II) atoms (the emission sites) is identical to that of complexes **2** and **3** in terms of connectivity. Also identically to those previous complexes, this species contains two sulfonylethylcalixarene ligands (the absorption site) in the cone conformation in a sandwich formation around the square plane defined by the four manganese centres. Although no crystal of sufficient quality for single crystal X-ray diffraction analysis has yet been obtained, a crystal structure of the corresponding tetramanganese complex of the unoxidised ligand Br_4 thiaS has been solved by single crystal X-ray diffraction analysis. It is shown in figure 70; the similarity of this structure to that obtained for $Mn_4(thiaS)_2$ and the comparable appearance and comporment of the luminescent complex **4** to the non-brominated analogues forms the basis of the assumption that the structure of complex **4** is related to that of complex **2**. The presence of bromine in place of butyl groups on the para position results in changes to the electron density in the conjugated system around the macrocycle; specifically, bromide is a stronger donor of electron density so the conjugated π system

in $\text{Br}_4\text{thiaSO}_2$ should have greater electron density than in the standard thiaSO_2 . Changes in electronic structure of this type have an effect on several contributing aspects of the photoluminescence process: the relevant energy levels involved (the ligand centred levels and also indirectly the manganese centred levels, via the crystal field strength), the precise conformation adopted by the ligand, and the capacity for vibrational relaxation of the molecule.

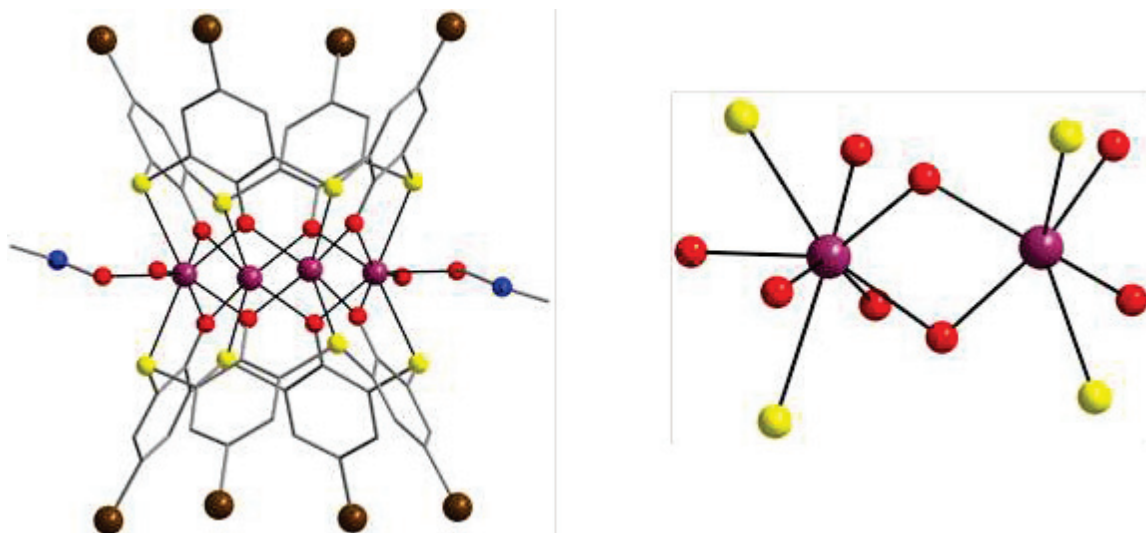


Figure 70: Structure of related complex $\text{Mn}_4(\text{Br}_4\text{thiaS})_2(\text{DMF})_2$, with magnified view showing the two distinct coordination environments of manganese (8-coordinate and 6-coordinate). Colour key: C = grey, Mn = purple, S = yellow, O = red, Br = brown, N = blue. Hydrogen atoms are omitted for clarity.

One important aspect in which the structure of this model complex $\text{Mn}_4(\text{Br}_4\text{thiaS})_2(\text{DMF})_2$ differs from that of the butylated analogue $\text{Mn}_4(\text{thiaS})_2$ is that it possesses two distinct coordination environments of manganese. One is found around the Mn^{2+} ions which have coordinated molecules of DMF; these are situated in a 8-fold coordination sphere with a distorted square anti-prism geometry (C_{2v}). The two Mn-S bonds are elongated with respect to the 6 Mn-O bonds, resulting in the distortion in the form. Note that with the oxidised analogue of the ligand, $\text{Br}_4\text{thiaSO}_2$, direct coordination of the sulfur atoms to the metal ion is impossible; the equivalent coordination sphere would contain only oxygen. The second coordination environment is 6-coordinate, with a distorted triangular prism geometry such that the point group term is also C_{2v} . Once again the distortion is caused by the greater length of the Mn-S bonds than the Mn-O bonds. Although no certain measurements have as yet been made, it would be of great interest to discover if the tetranuclear

complex of Mn^{2+} ions with $Br_4thiaSO_2$ also contains coordinated DMF molecules, and thus a variety of coordination environments of Mn^{2+} ions within the complex. In the known complexes **2** and **3**, all four of the manganese(II) ions are found in identical chemical environments.

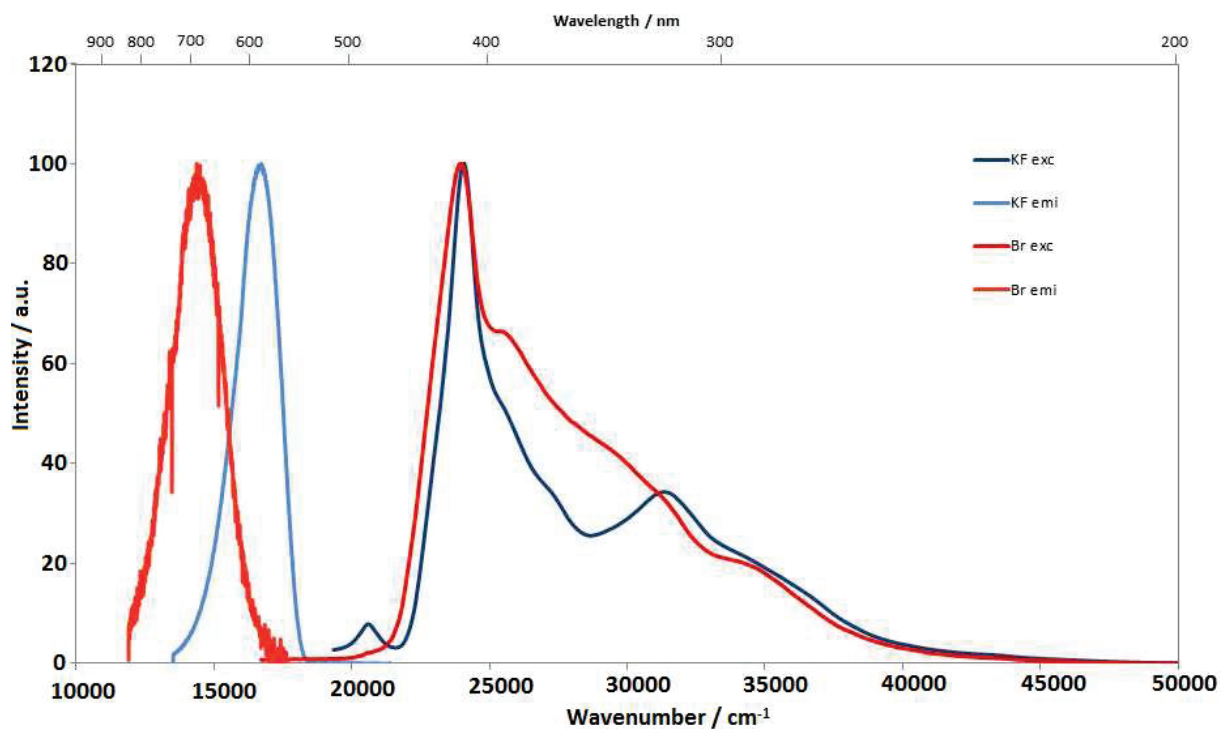


Figure 71: Excitation ($\lambda_{emi} =$ and emission spectra ($\lambda_{exc} = 320$ nm) for complex **2** (blue lines) and complex **4** (red lines) in the solid state at room temperature.

Figure 71 shows the normalised solid state excitation and emission spectra of complex **4** alongside the spectra obtained for complex **2** as a comparison. Some differences are immediately apparent, most notably in the wavelength shift of emission. The emitted light from complex **4** is redshifted by approximately 100 nm with respect to that observed in complex **2**; leading to the conclusion that the presence of bromine on the ligand lowers the energy level of the 4T_1 excited state of the manganese ion with respect to its 6A_1 ground state. Excitation of complex **4** takes place in the UV – blue range (λ_{exc} between 300 – 450 nm) similar to the previous complexes although with a slight increase in absorption over the range of 322 nm to 400 nm, with rose coloured emission between 570 nm and 800 nm centred at 714 nm. The emission peak is symmetrical in form, calling to mind the peak which is observed for complex **3** at low temperature.

2.5.2: Complex 5; effect of macrocycle conformation and Mn environment

Complex 5 is a dinuclear species featuring the ligand in the 1,2-alternate conformation; this is the preferred configuration for the sulfonylcalix[4]arene ligand under ambient conditions when forming complexes with first row transition metals. Although this complex features 6-coordinate manganese in pseudo-octahedral O_h geometry (unlike the 7-coordinate C_{2v} geometry of the previous Mn complexes), luminescence is still observed, presumably by the same antenna effect mechanism as occurs in the previously investigated manganese complexes. This luminescence is generally much less intense than that observed for the previous complexes, most likely due to the presence of water as a ligand on the manganese ions. Water is well known to quench luminescence by vibrational relaxation. Herein we consider the response of photoluminescence in this complex to various external stimuli in order to gain further understanding of the unique relationship between the sulfonylcalixarene ligand and the ion manganese(II). Figure 72 shows the structure of complex 5.

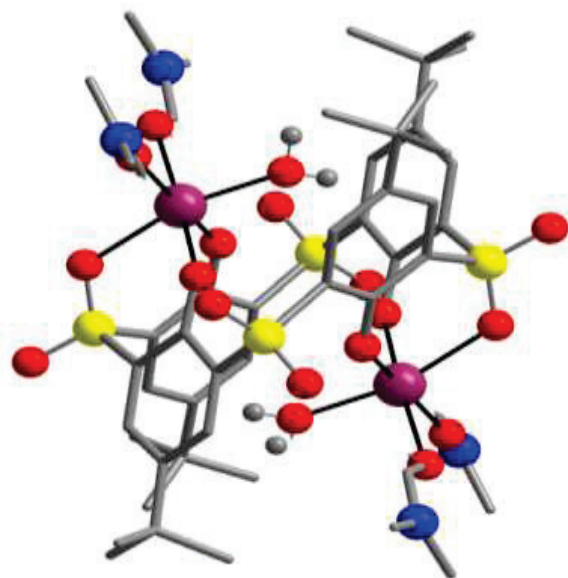


Figure 72: Structure obtained by single crystal X-ray diffraction analysis of complex 5. Colour key: C = grey capped sticks, O = red, S = yellow, Mn = purple, N = blue. H atoms omitted for clarity, except those on the H_2O ligands.

2.5.2.1: Response to temperature

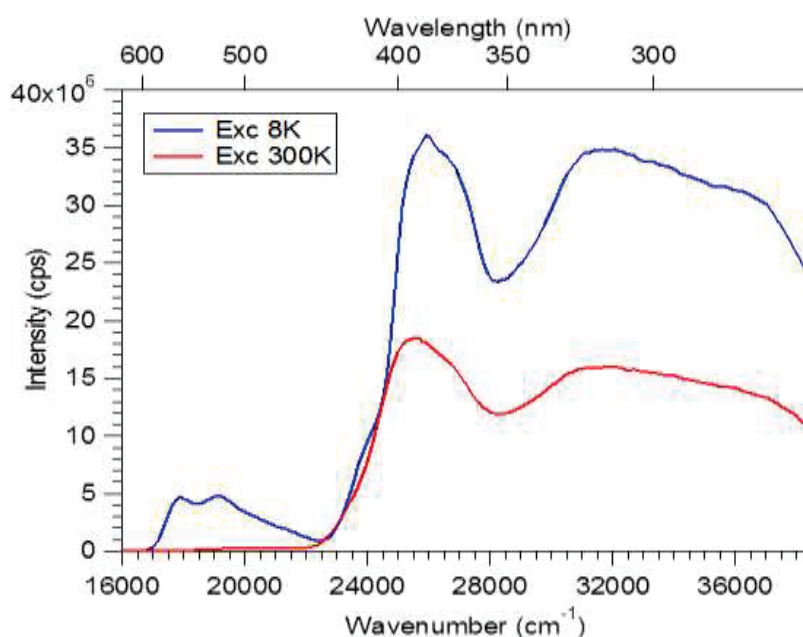


Figure 73: Excitation spectrum of complex **5** ($\lambda_{em} = 650$ nm) measured at 8 K (blue line) and 300 K (red line) under 10^{-9} mbar vacuum.

Figure 73 shows the excitation spectra of complex **5** measured at low temperature (8 K) and at ambient temperature (300 K). It is similar to that of complex **2**, with the principal absorption taking place in the range between 255 nm – 435 nm. In this range one peak is centred at 392 nm on the 300 K spectrum or 385 nm on the 8 K spectrum, with a second much broader shoulder peak centred at 299 nm appearing on both; both of these peaks are assigned to a $\pi \rightarrow \pi^*$ transition centred on the sulfonylcalix[4]arene ligand. On the low temperature plot an additional weak double peak is observed centred at 555 nm and 526 nm which is attributed to a manganese ion centred $d \rightarrow d$ transition (${}^6A_1 \rightarrow {}^4T_1$) c.f. figure 64.

Figure 74 shows the evolution of the emission spectrum of complex **5**, both under vacuum and under inert He atmosphere, with increasing temperature in the range between 3 K and 300 K. The effect of excitation wavelength was also measured, although not shown on figure 2.29 but the collected data is compared in figure 75. Emission is attributed to the same manganese-centred ${}^4T_1 - {}^6A_1$ transition which gives rise to emission in all previous complexes discussed.

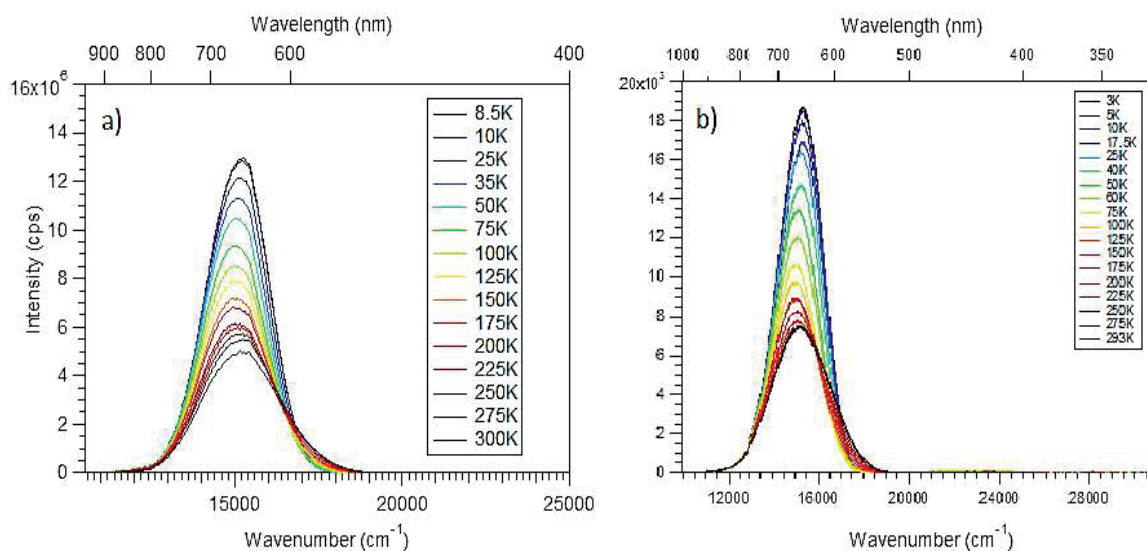


Figure 74: a) Emission spectra of complex 5 ($\lambda_{\text{exc}} = 350 \text{ nm}$) at various temperatures in the range between 8.5 K (purple line) and 300 K (maroon line) under 10^{-9} mbar vacuum. b) Emission spectra of complex 5 ($\lambda_{\text{exc}} = 350 \text{ nm}$) at various temperatures in the range between 3 K (purple line) and 293 K (maroon line) under 10^{-9} mbar vacuum.

The pertinent data related to the effect of temperature upon the luminescence of complex 5, under both vacuum conditions and under atmosphere of helium, are collated and compared in graph form in figure 2.34 below. Mostly the expected response is observed. Interestingly, however, the position of the maximum shows an unusual response; there is a redshift of the maximum for increasing temperature between 0 and 100 K, and thereafter a blueshift towards higher energy. The reason for this initial sharp redshift is not totally apparent at this moment.

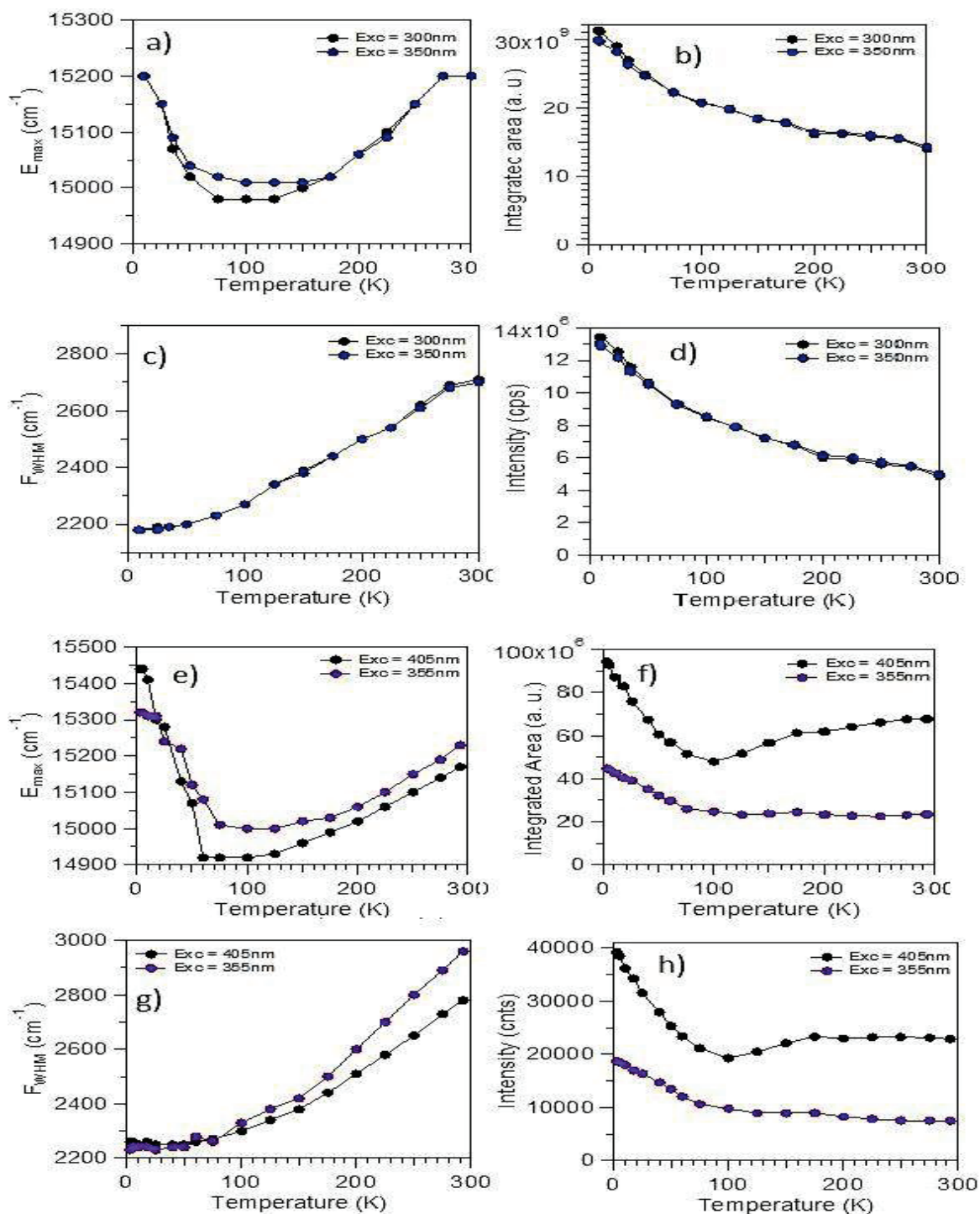


Figure 75: a)-d) Data derived from the emission spectra of complex 5 under 10^{-9} mbar vacuum at varying temperature between 8.5 K and 300 K ($\lambda_{\text{exc}} = 300$ nm black circles, 350 nm blue circles); a) position of maximum, b) peak area, c) FWHM, d) Intensity. e)-h) Data derived from the emission spectra of complex 5 measured under He atmosphere at varying temperature in the range between 3 K and 293 K ($\lambda_{\text{exc}} = 405$ nm black circles, 355 nm blue circles); e) position of maximum, f) peak area, g) FWHM, h) Intensity.

2.5.2.2: Response to O_2 Pressure

Figure 76 shows the response of emission from complex 5 in the solid state at room temperature to the presence of oxygen, with an inset describing the integrated area under the peak

for each partial pressure of O₂ between 0.1 mbar and 1010 mbar (ambient pressure). It can be seen that the oxygen once again acts to quench the luminescence, such that the intensity of emission under 1010 mbar of oxygen pressure is approximately 30 % of the emission intensity under 0.1 mbar. The order of strength of quenching effect by oxygen is therefore complex **2** (15 % decrease) < complex **5** (70 % decrease) < complex **3** (95% decrease). Following the earlier conclusion that the strength of this response is directly related to permeability of the crystalline structure (§2.4.3), we can conclude that the crystals of complex **5** are considerably porous to allow oxygen to enter into the interior space, although to a lesser extent than crystals of complex **3**.

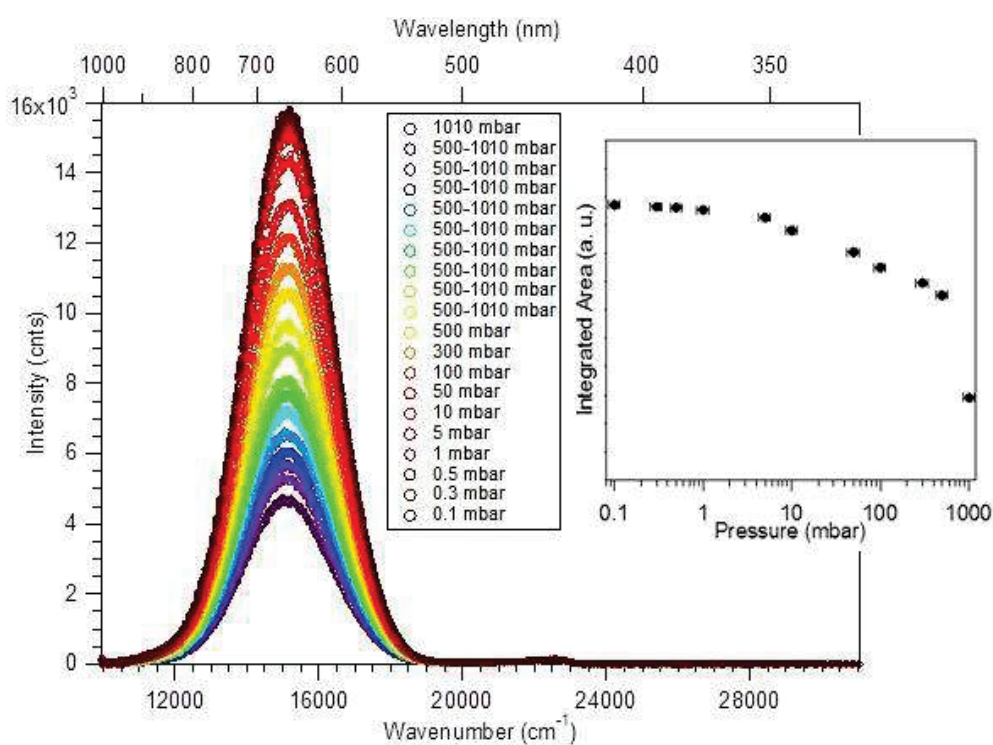


Figure 76: Solid state emission spectra ($\lambda_{exc} = 405$ nm) of complex **5** measured at 295 K for various oxygen pressure in the range between 0.1 mbar (maroon circles) to 1010 mbar (purple circles), with inset plot of integrated area under the peak at each of these oxygen pressure values.

2.5.3: Summary of modifications to the ligand system

The luminescence behaviour of two separate complexes (tetranuclear **4** and dinuclear **5**) has been observed. These complexes have demonstrated the effects upon the luminescence behaviour of the system of modification of the ligand, and of modification of the importance of the manganese(II) ions. With the bromo-substituted complex **4** a redshift in the position of emission was

observed, allowing the analogy to be drawn with xanthene dyes leading to the assumption that the yield (and therefore lifetime) of the triplet excited state upon photoexcitation of this molecule is higher than that of the analogues with no bromine present. The dinuclear system of complex **5** has also been investigated, and this complex has been observed to demonstrate the expected optical behaviour of a thiaSO₂:Mn²⁺ system. Although this compound seems to display considerable differences from the original luminescent species (i.e. coordination number, conformation of the macrocycle, nuclearity of transition metal ions, ...) it is still luminescent, albeit weakly so. This demonstrates the strong relationship present between the organic macrocycle and the metal ions.

2.6: Solution state luminescence

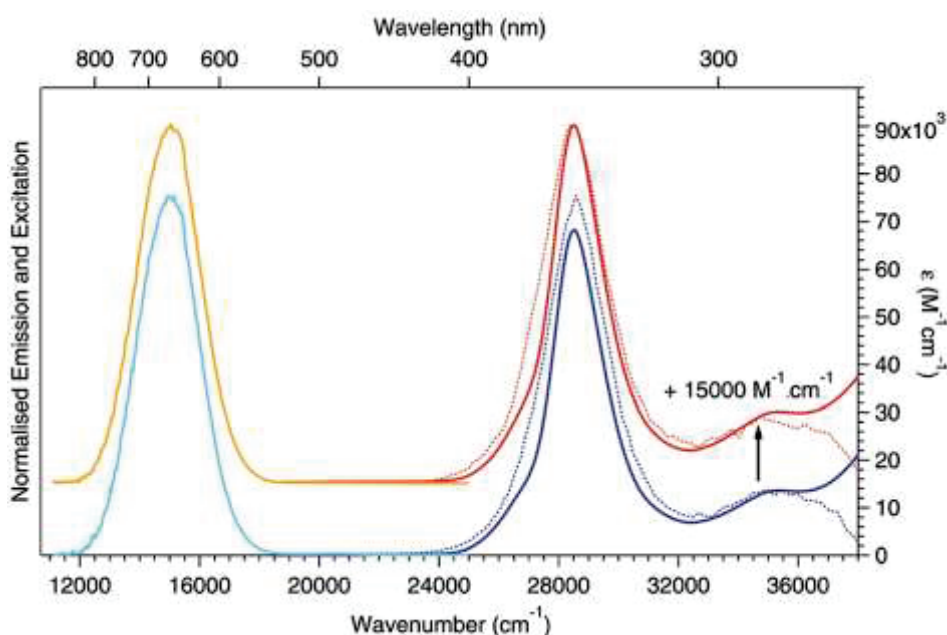


Figure 77: Normalised absorption (red and dark blue curves, $\lambda_{\text{emi}} = 650 \text{ nm}$), excitation (red and blue dotted curves, $\lambda_{\text{emi}} = 650 \text{ nm}$) and emission (orange and light blue curves, $\lambda_{\text{exc}} = 350 \text{ nm}$) spectra in DMF solution of **2** and **3** at room temperature, $c = 1.5 \times 10^{-4} \text{ M}$ for **2** and $c = 1.2 \times 10^{-4} \text{ M}$ for **3** for the absorption and emission spectra, and $c = 1.5 \times 10^{-6} \text{ M}$ for **2** and $c = 1.3 \times 10^{-6} \text{ M}$ for **3** for the excitation spectra.

Measurements of the luminescence of the complexes **2**, **3**, and **5** in DMF solution were carried out. Figure 77 shows the spectra obtained for complexes **2** and **3** (those of **3** are offset along the intensity axis for clarity) while figure 78 shows the spectra obtained for complex **5**. Dissolution is expected to bring about separation of the ionic species of the complex; we can expect any effects of the cation upon the luminescent aggregate to be absent from these spectra. Solution state

luminescence is generally expected to be less intense than the counterpart in the solid state, due to the opportunities for non-radiative relaxation via energy transfer to the solvent medium and potentially by absorption of either emitted or excitation light by solvent molecules.

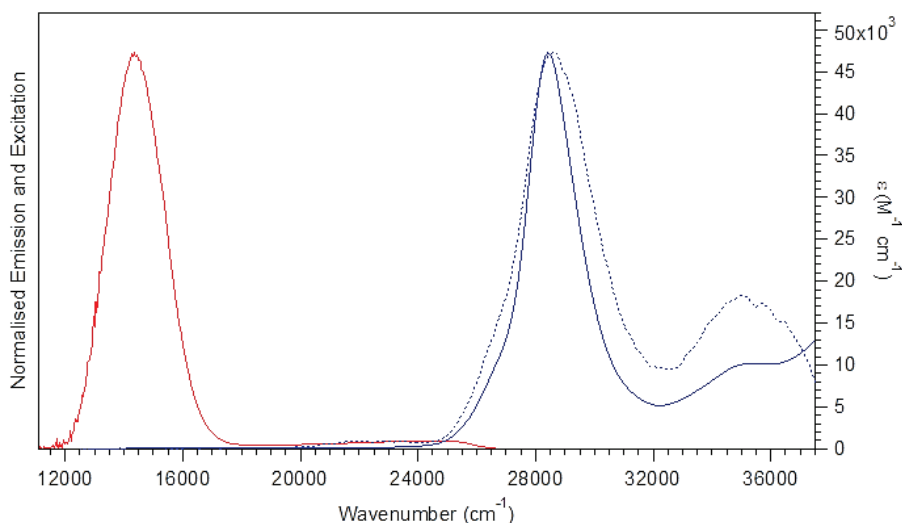


Figure 78: Normalised solution state absorption (blue curve, $\lambda_{\text{em}} = 260\text{-}800\text{ nm}$), excitation (dashed blue curve, $\lambda_{\text{em}} = 260\text{-}650\text{ nm}$) and emission (red curve, $\lambda_{\text{exc}} = 350\text{ nm}$) spectra of $1.54 \times 10^{-5}\text{ mol dm}^{-3}$ DMF solution of complex **5** at 293 K.

It can be seen that the form of all these spectra are more or less identical, demonstrating that despite the changes in ligand conformation, nuclearity, and connectivity and geometry of the manganese centres, the mechanism by which luminescence occurs in solution is the same for all of these complexes. The emission spectra obtained show an approximately symmetric peak between 555 nm and 833 nm with a maximum at 665 nm which is redshifted with comparison to the solid state emission observed at the same temperature. As is the situation in the solid state, this emission is attributed to the ${}^4T_1 \rightarrow {}^6A_1$ transition centred on the manganese ions; the shift in emission wavelength arises for similar reasons as the comparable shift which occurs under the action of pressure in the solid state. The solvent acts on the ligand in such a way as to affect the ligand field acting upon the metal centre. The principal absorption peak corresponds to the ligand $\pi - \pi^*$ transition of the ligand, found in the domain between 312 nm and 417 nm with the maximum at 350 nm where the extinction coefficient ϵ is about $70\,000\text{ M}^{-1}\text{ cm}^{-1}$ for complexes **2** and **3** and $42\,700\text{ M}^{-1}\text{ cm}^{-1}$ for complex **5**. Weaker excitation is observed in the range from 260 nm to 312 nm, also

attributed to a ligand centred transition. The luminescence lifetime was found to be 1.08 ms with a quantum efficiency of 15 %, whereas in a non-deoxygenated solution the corresponding values are 35 μ s and 0.4 %. The quenching effect of oxygen is much stronger in solution than in the solid state as dissolution allows the oxygen access to all of the luminescent aggregates.

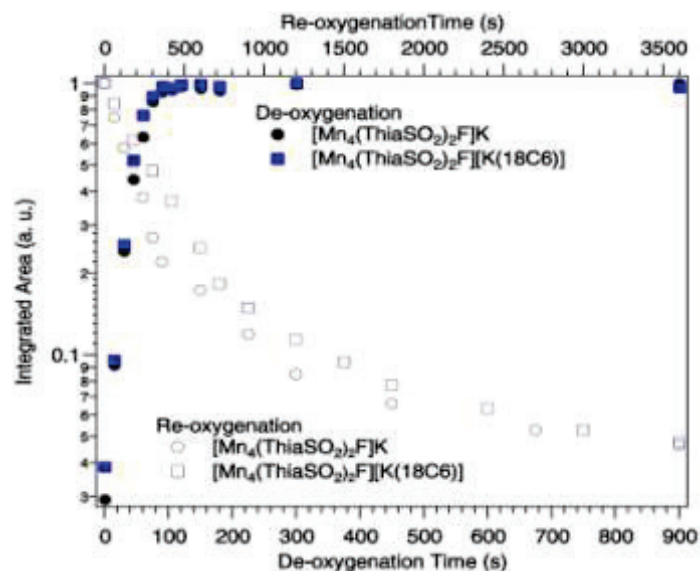


Figure 79: Normalised intensity of emission ($\lambda_{\text{exc}} = 350 \text{ nm}$) in DMF solution of complex 2 (circles) and complex 3 (squares) with time of exposure to N_2 -bubbling (filled colour shapes) or air (empty shapes).

All complexes in solution demonstrate an identical quenching effect reaction to the presence of oxygen. In each case this quenching effect is totally reversible by the action of bubbling nitrogen through the solution to purge it of oxygen. This reversibility is maintained during subsequent cycles of exposure to air and nitrogen purging. Figure 79 shows the intensity of emission for the tetranuclear complexes in DMF solution with time of exposure to nitrogen and oxygen. It can be seen that the rate of increase of luminescence intensity brought about by nitrogen purging is much sharper than the rate of intensity decrease when exposed to oxygen. With longer exposure to oxygen and irradiation an irreversible chemical change is brought about; this transformation will form the major investigation in the next chapter (§ Chapter 3).

2.7: Conclusion

Concerning the luminescent behaviour of this novel family of cluster complexes, we can conclude that there is considerable evidence for a strong synergistic relationship between the ligand

sulfonylcalixarene and the metal ion manganese(II). The energetic mechanism of the luminescence process has been derived by a variety of characterisation techniques, and comparisons have been made between modifications of the system by cation exchange and by chemical functionalisation upon the ligand itself. In this way structural and electronic effects upon the luminescent system have been elucidated, most notably the quenching effect of oxygen on the emission. The adaptability and efficacy of this system has been well established.

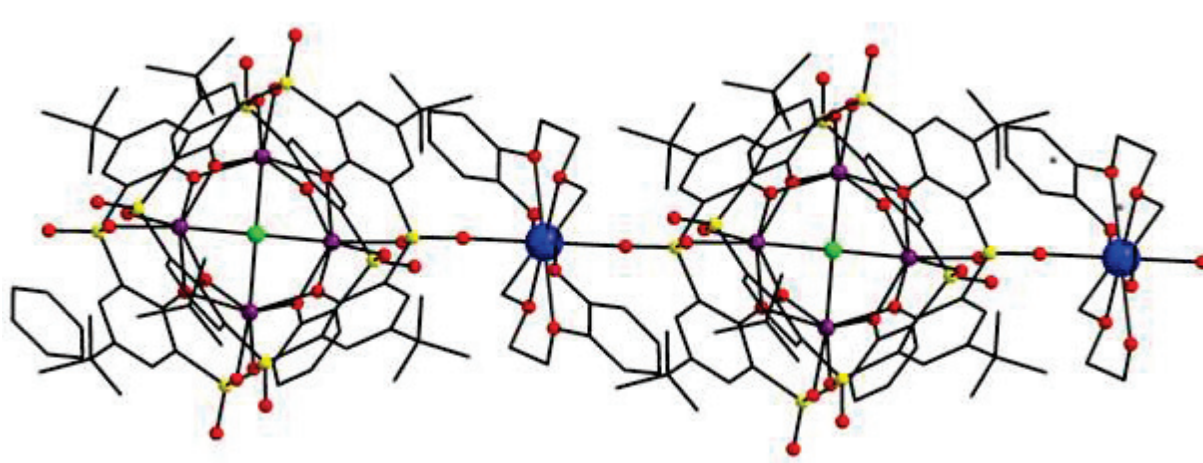


Figure 80: Crystal structure obtained by single crystal X-ray diffraction experiments of the complex $[\text{Na}(\text{dibenzo-18-crown-6})][\text{Mn}_4(\text{thiaSO}_2)_2\text{F}]$. Colour key: C = grey capped sticks, S = yellow, O = red, Mn = purple, F = green, Na = blue.

A potential avenue of further study of this system was brought about by the discovery of the structure of the complex shown in figure 80, obtained with sodium dibenzo-18-crown-6 complex as the cationic part. π -stacking interactions between the crown ether and the calixarene allow the positioning of the sodium cation such that it forms direct bonds to one of the sulfonyl groups of sulfonylcalixarene, similar to the situation of complex **2**. However, with an Na-F distance of 8.6417 Å, this complex has a slightly larger cation-anion separation than that of complex **3**. These two factors make this complex a kind of 'half-way' combination of both those previous complexes. The luminescence behaviour of this material, and in particular its response to the presence of oxygen, would be highly interesting to investigate.

There are a great many potential applications for molecular complexes of base metals which can efficiently perform photo-driven energy conversion processes. Of course one example is in the

capture of solar energy for commercial use, which is a very hot topic in current scientific research and is dominated by comparatively expensive inorganic materials. Other applications include lighting by LEDs, another field which heavily uses more expensive materials, and protection from UV damage, to name a few examples. However, the practical ramifications of application these complexes in the real world (processability, durability, etc.) have not been examined in as much detail. One prospective avenue for incorporation of the molecular system into real devices is by immobilisation upon or within an inorganic matrix material. This option will be explored in a subsequent chapter. The photoreactivity of such species, and in particular its capacity to generate singlet oxygen, is of interest for a range of applications, such as in the fields of photosensitisers for medicinal treatment and waste water treatment, and as an O₂ sensor. The following chapter is therefore concerned with the aspects of photoreactivity pertaining to these systems.

2.8 Summary of photophysical properties

Ref. no.	Formula	τ_{\max} (@T / K) / ms	λ_{\max} (@low T) / nm	λ_{\max} (@amb. T) / nm
2	$\text{K}[\text{Mn}_4(\text{thiaSO}_2)_2\text{F}]$	2.41 (75 K)	600	600
3	$[\text{K}(18\text{-crown-6})][\text{Mn}_4(\text{thiaSO}_2)_2\text{F}]$	2.48 (100 K)	640	620
4	$\text{K}[\text{Mn}_4(\text{Br}_4\text{thiaSO}_2)_2\text{F}]$	-	-	715
5	$[\text{Mn}_2(\text{thiaSO}_2)(\text{H}_2\text{O})_2(\text{DMF})_4]$	0.5 (3 K)	660	660*

*Energy value decreases to a minimum (longest wavelength) of about 667 nm at about 100 K before increasing again to the 3 K value at ambient temperature.

Ref. no.	Formula	Intensity under ambient O_2 / % of value under vacuum	
2	$\text{K}[\text{Mn}_4(\text{thiaSO}_2)_2\text{F}]$	85 %	
3	$[\text{K}(18\text{-crown-6})][\text{Mn}_4(\text{thiaSO}_2)_2\text{F}]$	< 5 %	
4	$\text{K}[\text{Mn}_4(\text{Br}_4\text{thiaSO}_2)_2\text{F}]$	-	
5	$[\text{Mn}_2(\text{thiaSO}_2)(\text{H}_2\text{O})_2(\text{DMF})_4]$	30 %	

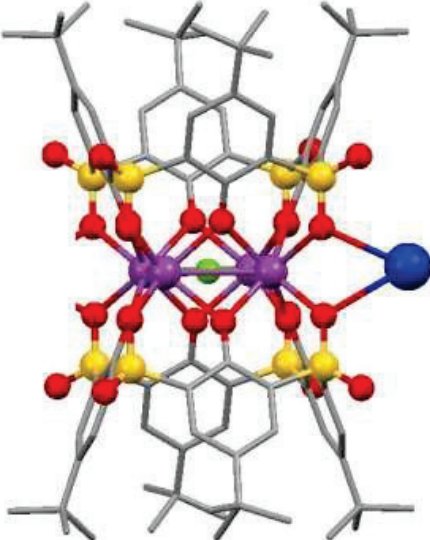
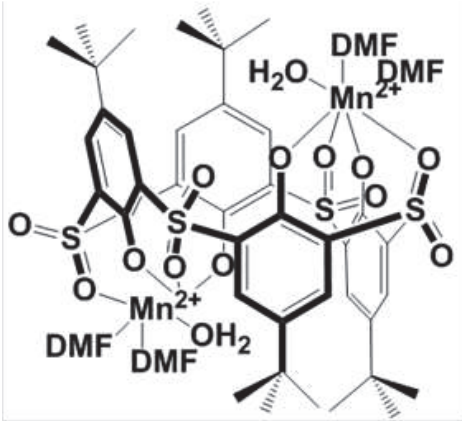
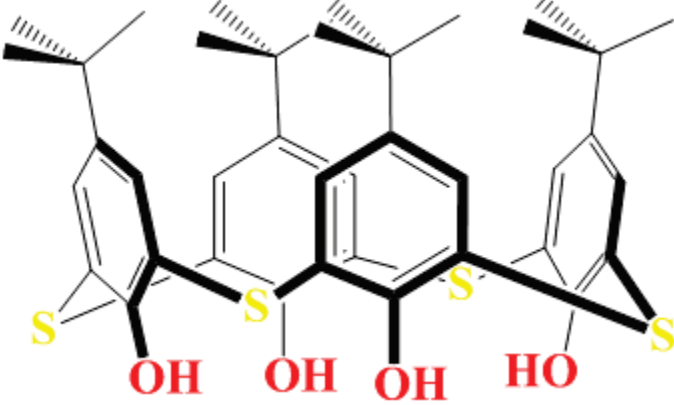
References

1. Fu, M. L.; Rangel, N. L.; Adams, R. D.; Seminario, J. M., Synthesis, Crystal Structure, Photophysical Properties, and DFT Calculations of a Bis(tetrathia-calix 4 arene) Tetracadmium Complex. *Journal of Cluster Science* **2010**, *21* (4), 867-878.
2. Iki, N.; Hiro-oka, S.; Tanaka, T.; Kabuto, C.; Hoshino, H., Highly Efficient Near-Infrared-Emitting Lanthanide(III) Complexes Formed by Heterogeneous Self-Assembly of Ag-I, Ln(III), and Thiacalix 4 arene-p-tetrasulfonate in Aqueous Solution (Ln(III) = Nd-III, Yb-III). *Inorganic Chemistry* **2012**, *51* (3), 1648-1656.
3. Kajiwarra, T.; Katagiri, K.; Hasegawa, M.; Ishii, A.; Ferbinteanu, M.; Takaishi, S.; Ito, T.; Yamashita, M.; Iki, N., Conformation-controlled luminescent properties of lanthanide clusters containing p-tert-butylsulfonylcalix 4 arene. *Inorganic Chemistry* **2006**, *45* (13), 4880-4882.
4. Darjee, S. M.; Mishra, D. R.; Bhatt, K. D.; Vyas, D. J.; Modi, K. M.; Jain, V. K., A new colorimetric and fluorescent chemosensor based on thiacalix 4 arene for fluoride ions. *Tetrahedron Letters* **2014**, *55* (51), 7094-7098.
5. Zhang, C. L.; Jin, Y.; Gong, S. L.; Zhang, X. F.; Chen, Y. Y., Syntheses and coordination properties of (thia)calix 4 arenes bearing single omega-quinolin-8-yl-oligooxyethylene pendant. *Journal of Chemical Research-S* **2006**, (9), 596-599.
6. Kumar, R.; Bhalla, V.; Kumar, M., Cu(2+) and CN(-)-selective fluorogenic sensors based on pyrene-appended thiacalix 4 arenes. *Tetrahedron* **2008**, *64* (35), 8095-8101.
7. Bi, Y. F.; Wang, X. T.; Liao, W. P.; Wang, X. W.; Deng, R. P.; Zhang, H. J.; Gao, S., Thiacalix 4 arene-Supported Planar Ln(4) (Ln = Tb-III, Dy-III) Clusters: Toward Luminescent and Magnetic Bifunctional Materials. *Inorganic Chemistry* **2009**, *48* (24), 11743-11747.
8. Iki, N.; Tanaka, T.; Hoshino, H., The role of cadmium(II) bridges in the self-assembly with lanthanide(III) and thiacalix 4 arene (TCAS) to selectively form a luminescent ternary Cd-2(II)center dot Tb-2(III)center dot TCAS(2) complex. *Inorganica Chimica Acta* **2013**, *397*, 42-47.
9. Kajiwarra, T.; Hasegawa, M.; Ishii, A.; Katagiri, K.; Baatar, M.; Takaishi, S.; Iki, N.; Yamashita, M., Highly Luminescent Superparamagnetic Diterbium(III) Complex Based on the Bifunctionality of p-tert-Butylsulfonylcalix 4 arene. *European Journal of Inorganic Chemistry* **2008**, (36), 5565-5568.
10. Hong, J.; Yang, G. S.; Duan, C. Y.; Guo, Z. J.; Zhu, L. G., Fluorescence quenching of EB-DNA complex by a novel di-bipyridyl ruthenium(II) complex of p-tert-butyltetrathiacalix 4 arene. *Inorganic Chemistry Communications* **2005**, *8* (11), 988-991.
11. Redshaw, C.; Elsegood, M. R. J.; Wright, J. A.; Baillie-Johnson, H.; Yamato, T.; De Giovanni, S.; Mueller, A., Cellular uptake of a fluorescent vanadyl sulfonylcalix 4 arene. *Chemical Communications* **2012**, *48* (8), 1129-1131.
12. Mahamuni, S.; Lad, A. D.; Patole, S., Photoluminescence properties of manganese-doped zinc selenide quantum dots. *Journal of Physical Chemistry C* **2008**, *112* (7), 2271-2277.
13. Voicu, G.; Oprea, O.; Vasile, B. S.; Andronescu, E., PHOTOLUMINESCENCE AND PHOTOCATALYTIC ACTIVITY OF Mn-DOPED ZnO NANOPARTICLES. *Digest Journal of Nanomaterials and Biostructures* **2013**, *8* (2), 667-675.
14. Margaryan, A.; Choi, J. H.; Shi, F. G., Spectroscopic properties of Mn(2+) in new bismuth and lead contained fluorophosphate glasses. *Applied Physics B-Lasers and Optics* **2004**, *78* (3-4), 409-413.
15. Reid, H. O. N.; Kahwa, I. A.; White, A. J. P.; Williams, D. J., Intense photosensitized emission from stoichiometric compounds featuring Mn²⁺ in seven- and eightfold coordination environments. *Inorganic Chemistry* **1998**, *37* (15), 3868-3873.
16. Hausmann, D.; Kuzmanoski, A.; Feldmann, C., MnBr₂/18-crown-6 coordination complexes showing high room temperature luminescence and quantum yield. *Dalton Transactions* **2016**, *45* (15), 6541-6547.
17. Chen, J.; Zhang, Q.; Zheng, F. K.; Liu, Z. F.; Wang, S. H.; Wu, A. Q.; Guo, G. C., Intense photo- and tribo-luminescence of three tetrahedral manganese(II) dihalides with chelating bidentate phosphine oxide ligand. *Dalton Transactions* **2015**, *44* (7), 3289-3294.

18. Yang, B. P.; Mao, J. G., New types of metal squarato-phosphonates: Condensation of arniodiphosphonate with squaric acid under hydrothermal conditions. *Inorganic Chemistry* **2005**, *44* (3), 566-571.
19. Lamouchi, M. Matériaux moléculaires à propriétés optique et magnétique à base de complexes métalliques polynucléaires : Thiacalixarènes / métaux de transition. Université Claude Bernard Lyon 1, Lyon, 2012.
20. Lamouchi, M.; Jeanneau, E.; Pillonnet, A.; Brioude, A.; Martini, M.; Stephan, O.; Meganem, F.; Novitchi, G.; Luneau, D.; Desroches, C., Tetranuclear manganese(II) complexes of sulfonylcalix 4 arene macrocycles: synthesis, structure, spectroscopic and magnetic properties. *Dalton Transactions* **2012**, *41* (9), 2707-2713.
21. Bilyk, A.; Hall, A. K.; Harrowfield, J. M.; Hosseini, M. W.; Skelton, B. W.; White, A. H., A unique rare-earth cluster within a calixarene sandwich: Parallels in the chemistry of cyclosiloxanes and calixarenes. *Australian Journal of Chemistry* **2000**, *53* (11-12), 895-898.
22. Desroches, U.; Pilet, G.; Szilagy, P. A.; Molnar, G.; Borshch, S. A.; Bousseksou, A.; Parola, S.; Luneau, D., Tetra- and decanuclear iron(II) complexes of thiacalixarene macrocycles: Synthesis, structure, Mossbauer spectroscopy and magnetic properties. *European Journal of Inorganic Chemistry* **2006**, (2), 357-365.
23. Mislin, G.; Graf, E.; Hosseini, M. W.; Bilyk, A.; Hall, A. K.; Harrowfield, J. M.; Skelton, B. W.; White, A. H., Thiacalixarenes as cluster keepers: synthesis and structural analysis of a magnetically coupled tetracopper(II) square. *Chemical Communications* **1999**, (4), 373-374.
24. Eisenberg, R.; Ibers, J. A., TRIGONAL PRISMATIC COORDINATION . CRYSTAL AND MOLECULAR STRUCTURE OF TRIS(CIS-1,2-DIPHENYLETHENE-1,2-DITHIOLATO)(RHENIUM). *Inorganic Chemistry* **1966**, *5* (3), 411-&.
25. Reid, H. O. N.; Kahwa, I. A.; White, A. J. P.; Williams, D. J., Seven-coordinate Mn²⁺ ions in Mn(15-crown-5)(H₂O)₂ (2+) as luminescent probes for dynamic supramolecular events. *Chemical Communications* **1999**, (16), 1565-1566.
26. Duggal, A.; Jüstel, T.; Ronda, C.; Srivastava, A. M.; Suijver, J. F.; Vergeer, P., *Luminescence From Theory to Applications*. 1 ed.; WILEY-VCH: Germany, 2008.
27. Kasyan, O.; Swierczynski, D.; Drapailo, A.; Suwinska, K.; Lipkowski, J.; Kalchenko, V., Upper rim substituted thiacalix 4 arenes. *Tetrahedron Letters* **2003**, *44* (38), 7167-7170.
28. Lhotak, P.; Svoboda, J.; Stibor, I., Anion receptors based on ureido-thiacalix 4 arenes. *Tetrahedron* **2006**, *62* (6), 1253-1257.
29. Iki, N.; Kumagai, H.; Morohashi, N.; Ejima, K.; Hasegawa, M.; Miyanari, S.; Miyano, S., Selective oxidation of thiacalix 4 arenes to the sulfinyl- and sulfonylcalix 4 arenes and their coordination ability to metal ions. *Tetrahedron Letters* **1998**, *39* (41), 7559-7562.
30. Suffren, Y.; O'Toole, N.; Hauser, A.; Jeanneau, E.; Brioude, A.; Desroches, C., Discrete polynuclear manganese(II) complexes with thiacalixarene ligands: synthesis, structures and photophysical properties. *Dalton Transactions* **2015**, *44* (17), 7991-8000.
31. Englman, R.; Jortner, J., ENERGY GAP LAW FOR RADIATIONLESS TRANSITIONS IN LARGE MOLECULES. *Molecular Physics* **1970**, *18* (2), 145-+.
32. Schweitzer, C.; Schmidt, R., Physical mechanisms of generation and deactivation of singlet oxygen. *Chemical Reviews* **2003**, *103* (5), 1685-1757.
33. DeRosa, M. C.; Crutchley, R. J., Photosensitized singlet oxygen and its applications. *Coordination Chemistry Reviews* **2002**, *233*, 351-371.

CHAPTER 3 : PHOTOREACTIVITY OF ThiaSO₂ / Mn²⁺ SYSTEMS

3.0 List of systems studied in this chapter

Ref. No. or description	Structure
Complex 2	<p>Potassium[bis-(μ_4-(para-<i>tert</i>-butylsulfonylcalixarene))(μ_4-fluoro)tetramanganese(II)]</p> 
Complex 5	<p>[(μ_2-para-<i>tert</i>-butylsulfonylcalix[4]arene)-diaqua-tetra(dimethylformamido)dimanganese(II)]</p> 
Mixed solution (free thiaSO ₂ and MnX ₂ , base)	<p>X = NO₃⁻, Cl⁻. Base = triethylamine.</p>
thiaSO ₂	<p>Para-<i>tert</i>-butylsulfonylcalix[4]arene</p> 

A great number of these systems containing sulfonylcalix[4]arene were found to undergo photo-driven chemical reactions. In this chapter, we set out to study and classify these reactions in a methodical manner. The investigation begins with the reactions of polynuclear cluster complexes of manganese, which were responsible for the initial discovery of this photoreactivity, then subsequently this system will be simplified in steps in order to provide a mechanistic explanation of the photophysical transformations which are occurring.

3.1 General introduction

The title compound, complex (**1** or **2**), when stood in DMF solution near a window, was observed to change colour from colourless / pale yellow to dark purple as is shown in figure 81.¹ The purple colour could be indicative of the presence of Mn^{n+} ions ($n>2$), or a phenoxy radical species. This serendipitous discovery of photodriven redox reactivity was taken as the basis for an in depth study of the chemical behaviour of the complex under illumination. It is noteworthy that manganese(II) is generally highly resistant to photochemical reaction.²

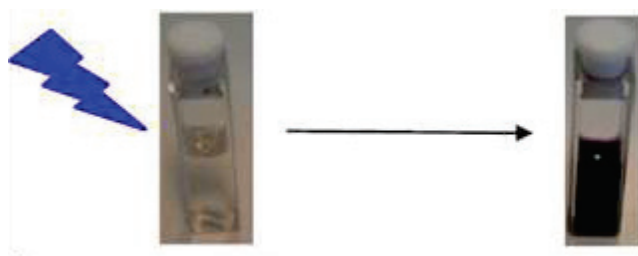


Figure 81: Transformation of complex 2 in solution under the action of sunlight.

Photodriven reactions and photocatalysis make up an important part of modern research,³⁻⁸ and materials which can absorb and process solar energy are in great demand as a reliable answer to the question of global energy needs.⁹ Conversely, the reactivity afforded by illumination, such as sunlight, are often undesirable and technological means are sought to avoid or shield from this effect.^{10, 11} Surface coatings, for example, often contain organic polymer materials and are exposed to exterior conditions. In these materials the action of sunlight over time will degrade the organic content, by means of photo-oxidation, ultimately destroying the coating. There must be a

mechanistic understanding of the degradation process in order to properly protect and adapt these systems for future use. Therefore research into photoreactions is concerned with both the constructive and the destructive aspects of these transformations.

Photon energy, as opposed to thermal energy, results in peculiarities in the reactivity of such photoreactions, which we will examine in detail here. Such reactions must involve at least one species in an electronic excited state (as UV – visible photon energies correspond to electronic transitions) which generally shows a different reactivity than the unexcited ground state. Photoreactions and photocatalysed reactions therefore involve harnessing this reactivity in some way; the excited molecule may be a direct reactant, or it may transfer the excitation energy by collision to another reactant such as molecular oxygen in the air.¹²

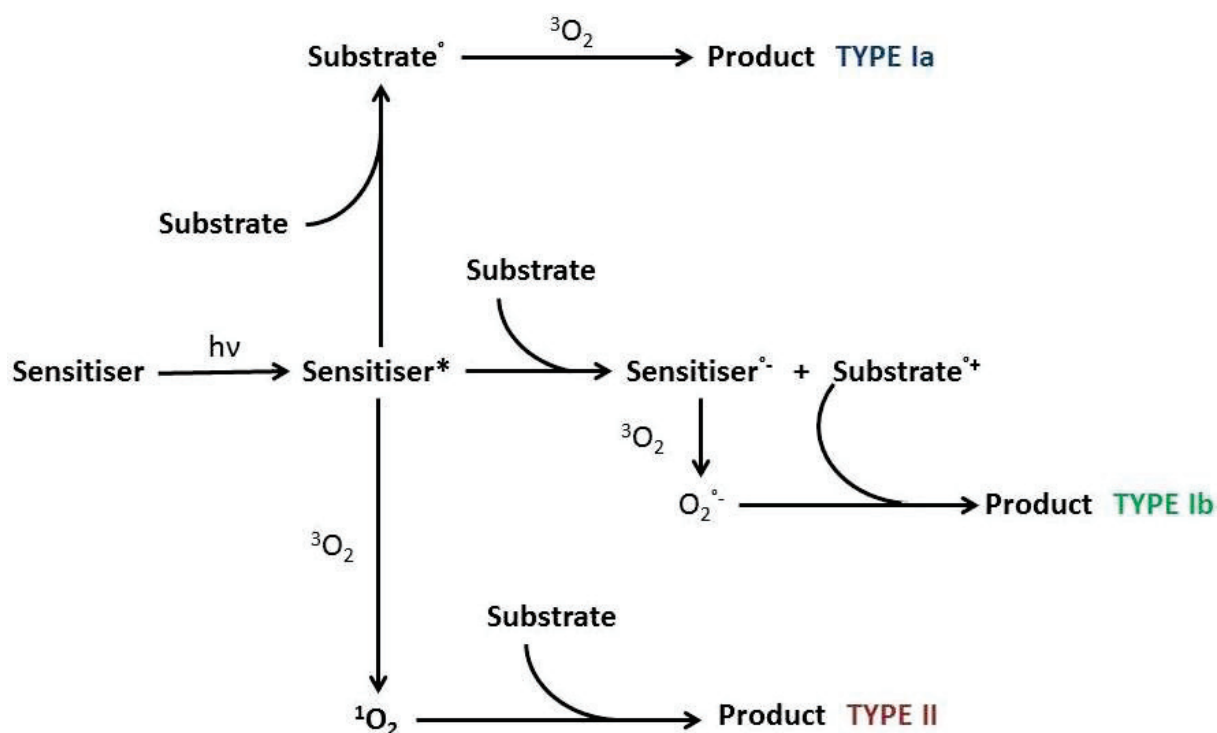


Figure 82: Types of photo-oxygenation.¹²

When characterising photo-oxidation reactions there may be difficulty in distinguishing whether the absorbing species is itself the oxidised species (a direct reaction) or if energy transfer to the oxidised species subsequent to the absorption step occurs (a photosensitised reaction). In either case, the oxidising reagent must also be identified. Photo-oxygenations are classified as either type I

for atom or electron transfer reactions, and type II if the reaction is mediated by singlet oxygen $^1\text{O}_2$, formed by energy transfer from the excited molecule (the sensitiser). Type II interactions are only possible for species where the energy gap between the excited triplet state and the singlet ground state is larger than the energy of singlet oxygen. Figure 82 illustrates these reaction types.

Oxygen presence is relevant to this case of photo-reactivity observed in complex **2**, as no reaction is observed in the absence of air. From this fact, and the necessity of light for the reaction to proceed, it can be inferred that the reaction is a photo-oxidation process. The use of photo-driven oxidation and oxygenation for synthetic reactions has been of scientific interest for almost a century.¹³ One of the most prominent examples of a photo-driven synthetic reaction is, naturally, photosynthesis which takes place within plant cells.¹⁴ Photosynthetic species are ubiquitous around the world. This naturally occurring process gives rise to organic molecules such as sugars, using only carbon dioxide, water, and sunlight as 'fuel', with the release of molecular oxygen. The catalyst of the oxygen evolving step, the enzyme known as photosystem II, contains amongst others a multivalent manganese and calcium centre.¹⁵ Much research in the field of photochemistry has sought to reproduce or emulate the action of this centre, whether for reduction of water or for adaptation to other redox type reactions.^{16, 17} Thus molecular manganese complexes often find use as catalysts for these types of transformations.

The preliminary analysis of the photo-transformation of complex **2** ascertained the following information:¹

- As stated above, an oxidant is necessary for the reaction to proceed. This affirms that it is an oxidation reaction. Furthermore, illumination is required; the reaction does not proceed in the dark.
- Either the solvent must be capable of coordinating the manganese ion or some ligand species which is capable of this must be present. The product is a manganese complex with this species as a ligand.

- The reaction proceeds via formation of a dinuclear transition species, the structure of which was shown in chapter 2 (§2.5). This species could be isolated by conventional synthesis techniques under anaerobic conditions. As was mentioned in an earlier chapter (§2.5.2) this species is also luminescent, although to a much lesser degree than occurs in the tetranuclear starting material. It has been confirmed to contain manganese(II) ions by EPR study.
- Both bond length analysis (utilising Valence Bond Theory) and EPR analysis confirm that the product is a complex of manganese(III) showing a Jahn-Teller distortion as would be expected. Its structure as found by X-ray diffraction is shown in figure 383, alongside its EPR spectrum.

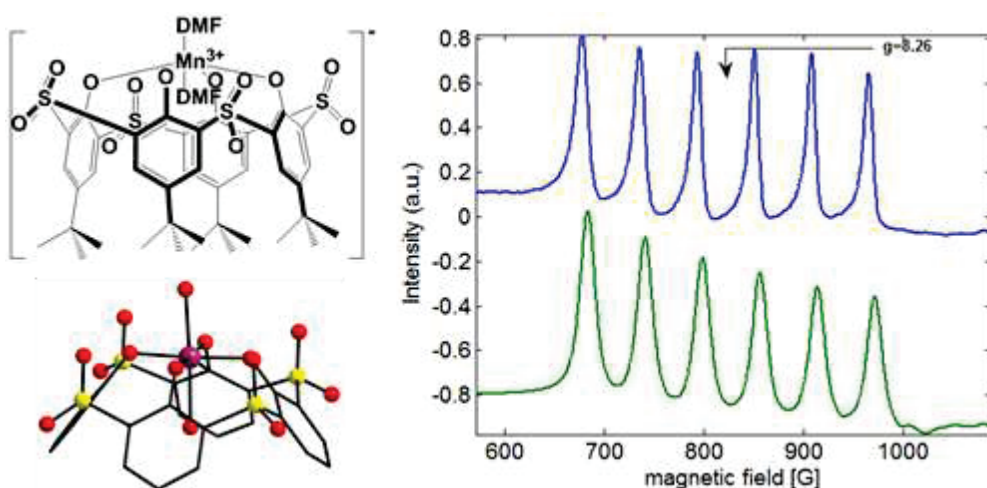


Figure 83: (Left) Structure of the manganese(III) complex obtained by photo-oxidisation of tetramanganese complex. Colour key: C = grey, S = yellow, O = red, Mn = purple. H atoms omitted for clarity. (Right) Parallel mode CW-EPR spectrum (blue curve) of this metal complex (experimental parameters are: microwave frequency 9.38 GHz, microwave power 21 mW, temperature 11 K), and derivative of the simulation (green curve) of the experimental data (simulation parameters are: $S = 2$, $g = [2.1.99\ 1.985]$, $|D| = 2.0050\text{ cm}^{-1}$, $|E| = 0.2165\text{ cm}^{-1}$, $a = [184\ 184\ 160]\text{ MHz}$, $aav = 62.86\text{ G}$).

- In order to neutralise the charge imbalance ($\text{thiaSO}_2^{4-} + \text{Mn}^{3+}$) a potassium ion is present in the product, directly coordinated to the S=O groups on the thiaSO₂ ligand. This interaction is depicted in figure 84, as is the octahedral coordination geometry of the manganese(III) ion.

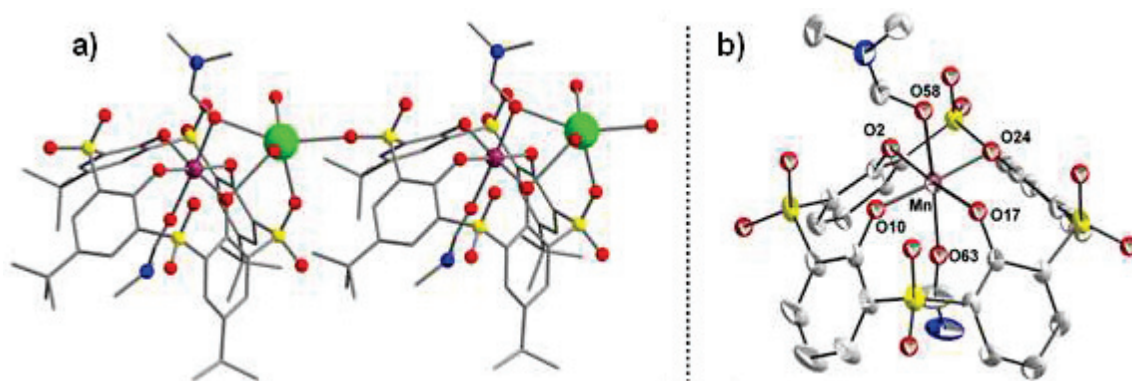


Figure 84: Structures solved by single crystal X-ray diffraction analysis of the Mn³⁺ oxidation product. a) Ball and stick representation demonstrating the connectivity to the potassium ion (green); hydrogen atoms are omitted for clarity. b) Thermal ellipsoid representation of the octahedral coordination environment of Mn³⁺; hydrogen atoms and *tert*-butyl groups are omitted for clarity.

- Brechin *et al* have previously reported structures containing Mn^{III} ions situated at the centre of the square plane formed by four phenol moieties; this arrangement is quite rare.^{18, 19} The product is identified by the growth of an LMCT peak centred at 540 nm in the UV-visible absorption spectrum, as seen in figure 85.

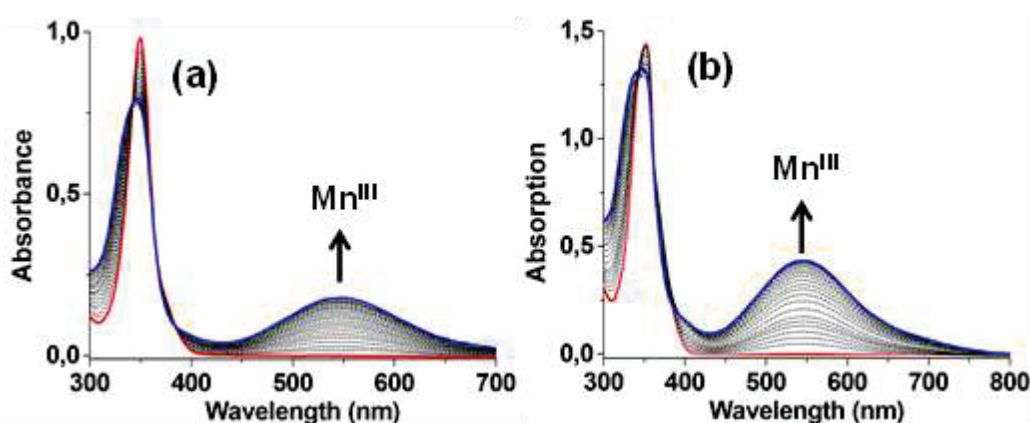


Figure 85: Time resolved UV-vis spectra obtained for irradiation at 400 nm in air of 4 cm³ DMF solutions containing a) tetramanganese cluster 2 (30 μmol dm⁻³, cuvette = 0.5 cm, 20° C) between 0 min (red curve) and 70 min (blue curve), and b) dimanganese cluster 5 (300 μmol dm⁻³, cuvette = 0.2 cm, 20° C) between 0 min (red curve) and 34 min (blue curve).

Figure 86 illustrates this transformation of these manganese(II) clusters into the resulting manganese(III) complex.

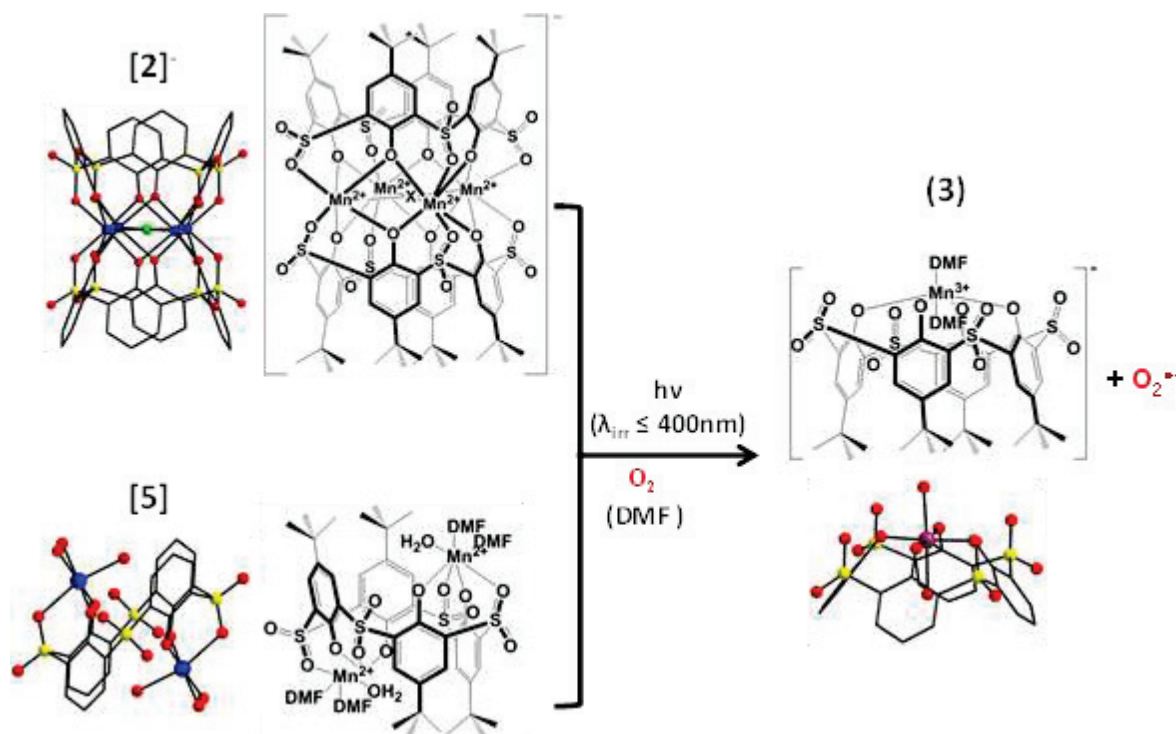


Figure 86: Structures of manganese complexes involved in the photo-oxidation reaction. Colour key: C = grey, S = yellow, O = red, F = green, Mn = blue. H atoms omitted for clarity.

In this chapter we will seek to elucidate the mechanism and scope of this transformation. The kinetics of the reaction under varying conditions will be described, as will the nature of the oxidant and its role in the overall process. To conclude, the potential for utilisation of this process in practical materials and devices will be examined.

3.2: Photo-oxidation of tetranuclear and dinuclear manganese(II) clusters in solution

In the examination of the luminescence behaviour of these species, it was noted that the quantum yield of luminescence is significantly lowered in solution, and especially in the presence of oxygen. This quenching is explained as being the result of an energy transfer from the excited state of the complex to molecular oxygen, which is in a triplet state under normal conditions. Molecular oxygen is observed to be necessary for this photo-oxidation reaction to proceed; it can be imagined therefore that this energy transfer process might play some role in the oxidation reaction of manganese(II) coordinated by thiaSO₂. There are many questions regarding the role of oxygen in this

chemical transformation which must be addressed to thoroughly clarify and characterise the mechanism of photoreaction.

3.2.1: The end product derived from $^3\text{O}_2$

The reaction is a photo-oxidation reaction between oxygen and a manganese(II) complex which is believed to generate the superoxide anion; this belief was investigated by following with EPR spectroscopy the irradiation ($\lambda = 400$ nm) of a solution of complex **2** or **5** in DMF in the presence of 5,5-dimethyl-1-pyrroline-N-oxide (DMPO), a 'spin-trap' capable of capturing transient radical species by the formation of adducts.²⁰ Figure 87 shows the resulting spectrum.

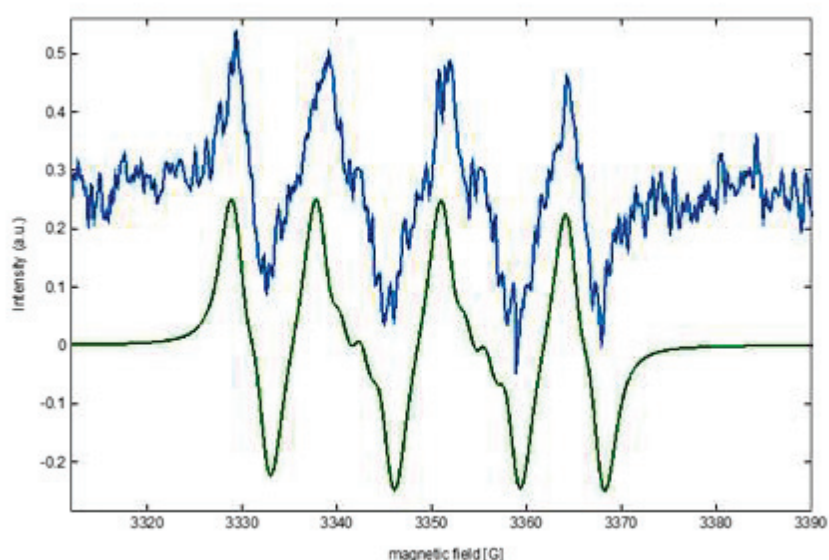
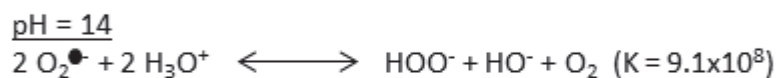
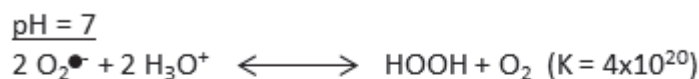


Figure 87: Experimental (blue curve) and simulated (green curve) EPR spectrum resulting from the irradiation at 400 nm (or 360 nm) of a solution of complex **2** in DMF in the presence of DMPO. Simulation parameters: DMPO-OOH, $a(\text{N}) = 12.34$ G, $a(\text{H}) = 8.34$ G, $a(\text{H}) = 2$ G, $g = 2.007$.

The measured spectrum is extremely similar to what would be expected for the hydrogen superoxide adduct of DMPO (DMPO-OOH; simulated spectrum shown in green in figure 87). When DMPO is used as a spin-trap in EPR spectroscopy of this kind, it is capable of forming both adducts DMPO-OH and DMPO-OOH, although the latter species tends to spontaneously decompose giving the former.²¹ This experiment has therefore demonstrated that there is a one-electron transfer process between the manganese complex and oxygen, generating a mononuclear manganese(III) species and the superoxide radical anion, O_2^\ominus . In 2011 Liu *et al* reported a complex containing

zwitterionic aminated calix[4]arene and the manganese(III) ion with direct coordination of superoxide to the metal centre, which is found in the centre of the square plane formed by four phenolic oxygen atoms as in our Mn³⁺ complex.²² This complex was then found to be an effective catalyst for epoxidation reactions of alkene compounds. It has been impossible to isolate (and thereby study by single crystal X-ray diffraction) any such compound showing coordination of the superoxide ion to the Mn^{III} ion with our system. The strong coordinative stabilisation of the manganese(III) ion by the four phenolate residues and two DMF molecules is believed to be responsible for this lack. What becomes of the superoxide anion after reaction has not yet been ascertained; hypotheses for its degradation are summarised in figure 88.²³

Hypothesis 1



Hypothesis 2



Hypothesis 3



Figure 88: Hypothesised routes for destruction of the superoxide anion formed during the photo-oxidation reaction.²³

Hypothesis 1 (Figure 88) is based on the fact that the superoxide anion is known to be a very strong Brønsted base, capable of deprotonating acids weaker than water (up to pK_a = 23).²³ In so doing the radical HOO is created, which reacts rapidly with itself or another superoxide anion. In a medium of pH = 7, the equilibrium of the disproportionation reaction of superoxide giving peroxide and oxygen is driven entirely to the right (K = 4 × 10²⁰); even in highly alkaline solution of pH = 14 the equilibrium is strongly driven towards the disproportionation products (K = 9.1 × 10⁸). A second possibility is that the oxidation of manganese from the +2 to +3 oxidation states by oxygen could be

reversible. The third hypothesis arises from the fact that in aprotic media the superoxide anion acts as a powerful nucleophile (in protic solvents its role as a deprotonating base takes precedence). If there is any electrophile present in the solution (for instance, the carbon of the amide moiety in DMF), it could undergo attack by this anion leading to the disappearance of superoxide from the mixture.

This redox reaction involving the generation of a mononuclear sulfonylcalixarene complex of the manganese(III) ion along with superoxide (figure 3.6) is very similar to that reported by Liu *et al* (see above); however one important differentiating factor is that in our case the reaction is photo-driven whereas their case involved a purely chemical oxidation reaction. We thus have proof of the photo-induced electron transfer reaction taking place between the photo-excited manganese(II) complex and molecular oxygen; it is plausible that this reaction necessarily proceeds via the formation of singlet oxygen ($^1\text{O}_2$) which then acts as the oxidant upon the metal complex. To verify the feasibility of this idea, and probe the role of singlet oxygen in this transformation, two routes of investigation were considered:

- The UV illumination of the manganese clusters **2** and **5** in DMF solution with the addition of triphenylphosphine (PPh_3) or 9,10-dimethylanthracene (DMA), both known to be singlet oxygen scavengers.^{24, 25}
- The illumination in the range 550 - 700 nm of a solution of manganese(II) cluster and methylene blue, a photosensitiser in this wavelength range for the production of singlet oxygen.²⁶

3.2.2: Investigation of $^1\text{O}_2$

DMA is itself photoactive; figure 89 shows the evolution of the UV-visible absorption spectrum with time upon illumination at 360 nm of a DMF solution ($0.24 \text{ mmol dm}^{-3}$) of DMA. Figure 3.11 then gives the analogous spectra for illumination at the same wavelength of mixed solutions in

DMF of DMA ($0.24 \text{ mmol dm}^{-3}$) with a) the tetranuclear manganese(II) complex **2** ($0.15 \text{ mmol dm}^{-3}$), or b) the dinuclear manganese(II) complex **2** ($0.15 \text{ mmol dm}^{-3}$).

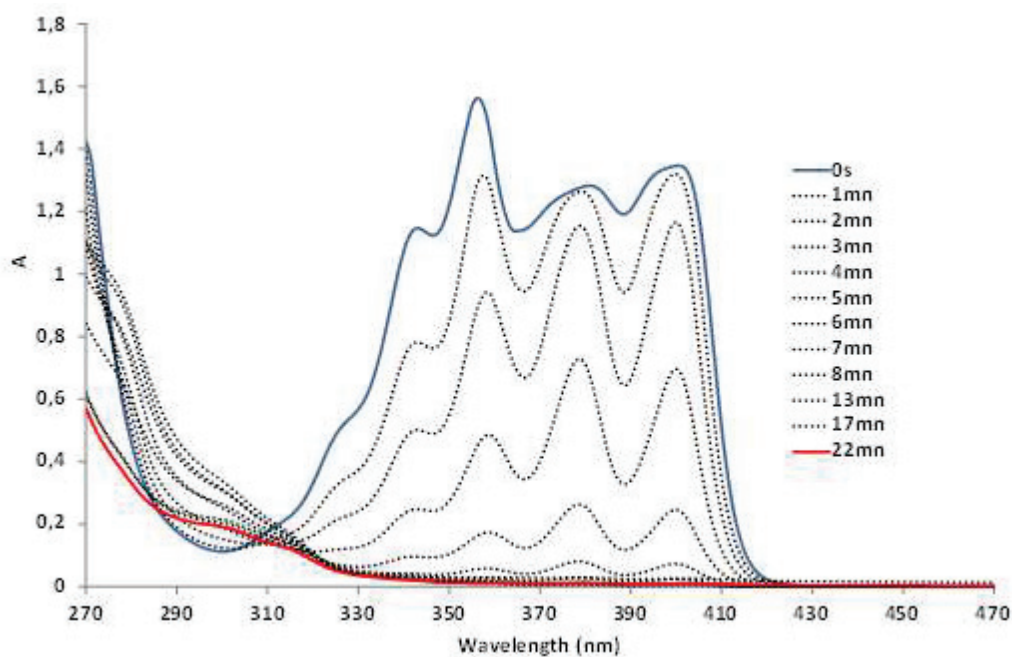


Figure 89: UV-vis absorption spectra obtained from a solution of DMA ($0.24 \text{ mmol dm}^{-3}$) in DMF with varying time of illumination ($\lambda = 360 \text{ nm}$) between 0 min (blue curve) and 22 min (red curve).

It can be seen that the characteristic absorption band in the region between 320 – 420 nm diminishes steadily with illumination, indicating the auto-degradation of the DMA forming the corresponding *endo*-peroxide, as shown in figure 90. It takes approximately 20 minutes of illumination to bring about the total disappearance of the initial DMA.

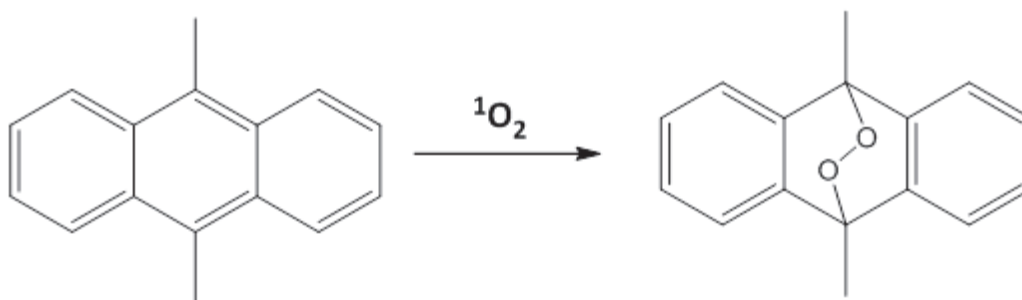


Figure 90: Oxidation by singlet oxygen of 9,10-dimethylanthracene, giving the *endo*-peroxide.

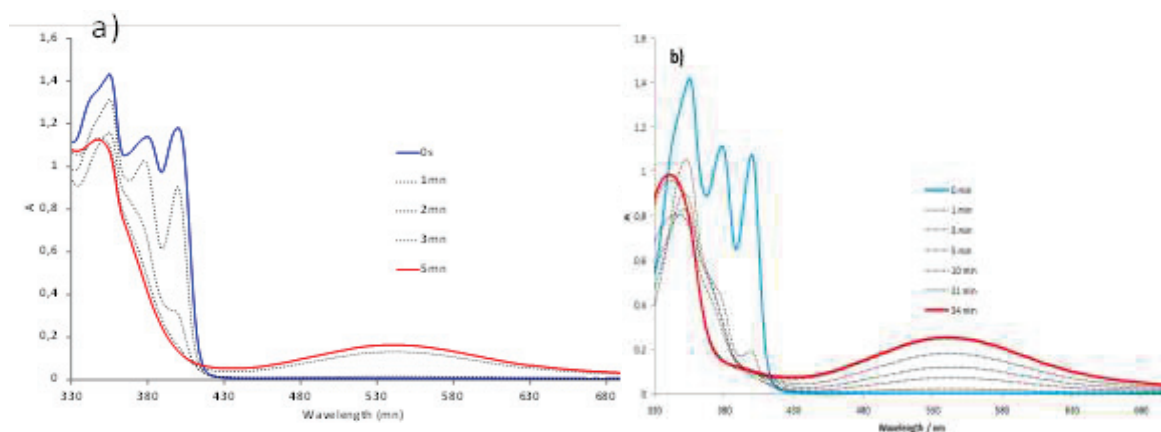
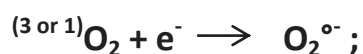


Figure 91: UV-vis absorption spectra obtained from a DMF solution of DMA ($0.24 \text{ mmol dm}^{-3}$) with varying time of illumination ($\lambda = 360 \text{ nm}$) in the presence of Mn^{II} cluster: a) complex **2** ($0.15 \text{ mmol dm}^{-3}$) between 0 min (blue curve) and 5 min (red curve); b) complex **5** ($0.15 \text{ mmol dm}^{-3}$) between 0 min (blue curve) and 34 min (red curve).

Now with the addition of manganese(II) cluster to the solution, the photodegradation of dimethylantracene occurs much more quickly. In both cases, whether with the tetranuclear complex **2** or the dinuclear complex **5**, it takes about two minutes or less before the spectral characteristics of DMA have disappeared, and the growth of peaks corresponding to the mononuclear Mn^{3+} begin to be apparent. If essentially the same experiment is carried out using a large excess concentration of PPh_3 in the place of DMA, no purple colouration is observed until such point that all of the phosphine has been converted to phosphine oxide. These results would indicate that the generation of singlet oxygen is necessary in order for the photo-oxidation reaction to take place. From a thermodynamic viewpoint this is logical, as the standard redox potential for the dioxygen – superoxide couple (with respect to the standard hydrogen electrode, SHE) is greater for singlet oxygen than for the triplet state alternative, as shown in figure 92.²⁷



$$E^\circ \text{ } {}^3\text{O}_2 / \text{O}_2^{\circ-} = -0.33 \text{ V / SHE}, E^\circ \text{ } {}^1\text{O}_2 / \text{O}_2^{\circ-} > 0.65 \text{ V / SHE}$$

Figure 92: Standard redox potentials for the single electron transfer transformation between molecular dioxygen and the superoxide anion.²⁷

Armed with this knowledge that singlet oxygen plays an essential role in the photo-oxidation reaction, experiments were then carried out to test the idea that singlet oxygen alone might act as the oxidant in the reaction, with no direct photoexcitation of the manganese species taking place. To

this end the manganese(II) clusters in DMF solution were illuminated at 650 nm in the presence of methylene blue; at this wavelength there is minimal absorption of the metal complex whereas the organic dye methylene blue shows strong absorption and generation of $^1\text{O}_2$. In no case was any photo-oxidation of the Mn^{2+} species observed; only auto-degradation of the methylene blue was seen for all experiments. This allows us to draw the conclusion that there must be photoexcitation of the manganese(II) sulfonylcalixarene complex itself in order for the reaction with oxygen, whatever its spin state, to progress. Thus, all these results taken together allow the mechanistic pathway of photo-oxidation shown in figure 93 to be posited.

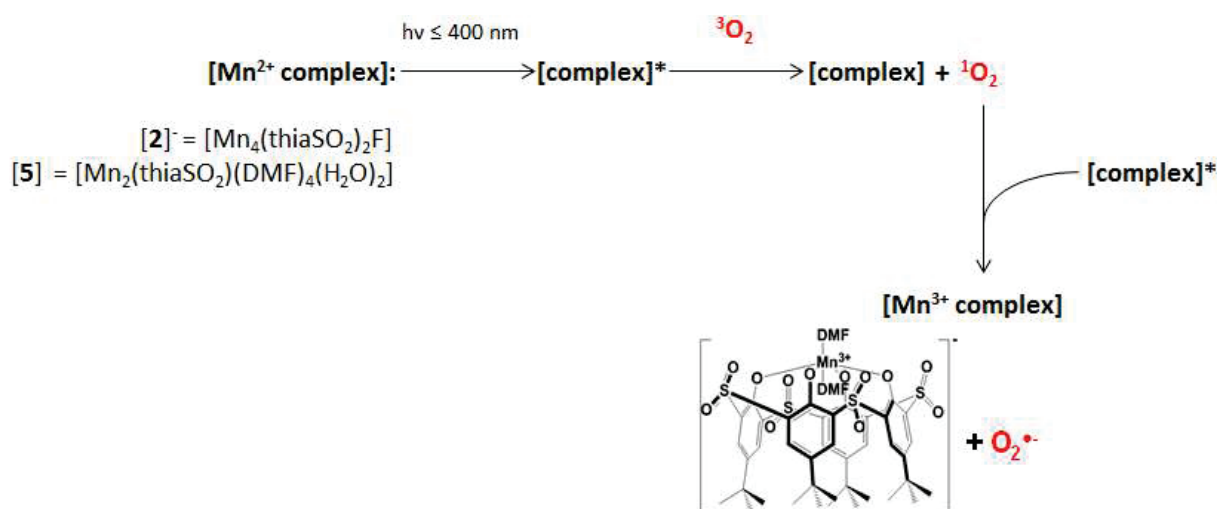


Figure 93: Route of photo-oxidation of Mn^{II} clusters derived from UV-vis absorption data.

To further round out the characterisation of this reaction, experiments were carried out to probe the roles of other parameters; namely, the nature of the oxidant (can alternatives to oxygen be utilised?), the solvent, the wavelength of the incident excitation light, and (in the case of complex 2) the nature of the accompanying cation.

3.2.3: Alternative oxidants

The group of Grätzel *et al* have reported the use of the nitrate anion, NO_3^- , to quench the triplet excited states of organic molecules (namely N-methylphenothiazine and N,N,N',N'-tetramethylbenzidine) by an irreversible redox reaction passing via NO_3^{2-} (which spontaneously degrades in aqueous media releasing hydroxide ions, leading to the irreversibility of the

transformation) ultimately giving the oxidised radical cation of the organic compound and the nitrite anion, NO_2^- .²⁸ This reaction was postulated to be suitable for the quantum storage of radiative energy by the formation of a chemical 'fuel'. The results for our system are preliminary, but it appears that when a solution of the manganese cluster (**2** or **5**) is illuminated at 360 nm or 400 nm under air-free conditions in the presence of a nitrate salt (i.e. KNO_3 , NaNO_3 , ...), the solution becomes purple, and demonstrates the characteristic UV-vis absorption profile of the mononuclear Mn^{3+} complex product of the previous aerobic oxidations, indicating that the same time of reaction may be taking place. By adapting the mechanism given in that report (and adding the possibility of disproportionation of NO_2) we can propose the following related mechanism given in figure 94 for our system.

It can be seen that the transformation of the NO_3^{2-} ion (a reductant) into NO_2 (a strong oxidant) is responsible for the irreversibility of the reaction. Balancing the equations reveals that in both cases two manganese(II) ions are oxidised for each nitrate ion consumed, with the formation of one nitrite ion and two hydroxide ions. Route (a) involves one electron transfer step per absorbed photon, whereas by route (b) two electrons are transferred for every photon absorbed. Either or both of these routes may be what occurs in the system; one method to differentiate between them would be to measure the quantum yield of photo-oxidation and compare it with the expected quantum yield of excited triplet state formation for the relevant Mn^{2+} cluster. One important feature to note, however, is that the nitrite anion is also known to be a quencher of organic triplet states, more often by an energy transfer than a charge transfer mechanism.²⁹

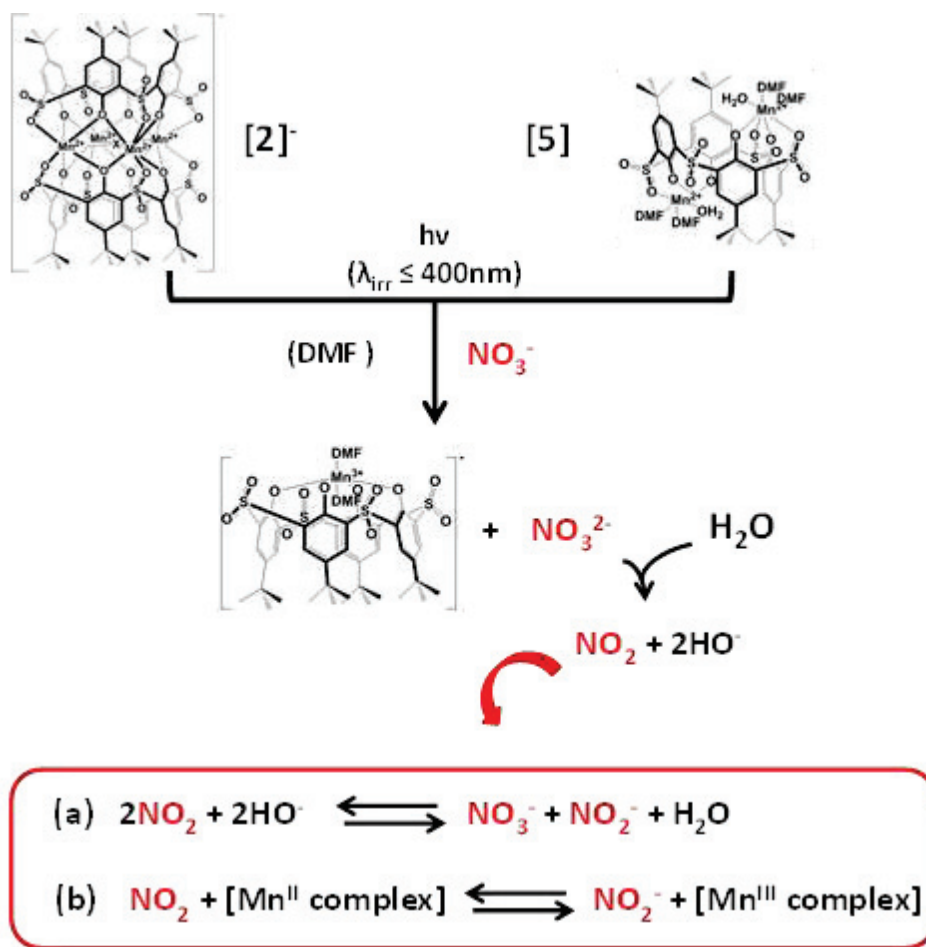


Figure 94: Mechanistic routes for the photo-oxidation of manganese(II) clusters of sulfonycalixarene using nitrate as the oxidant. Route (a) features disproportionation of the formed nitrogen dioxide, route (b) features a second oxidation of Mn^{II} species by this compound.

The photoreaction of these manganese(II) clusters with alkaline nitrite salts in air-free solution was also observed to produce the purple Mn^{3+} oxidation product, which would suggest that the inherent energy of the charge transfer complex formed between these species under the action of light is greater than that of the excited triplet state of the sensitizer complex. No oxidation product is observed when hydrogen peroxide, H_2O_2 , is used in place of the oxidant, rendering it difficult to establish a relationship between the redox potentials of these couples under these conditions. For future work upon this subject, a series of flash photolysis experiments are envisioned in order to fully identify the transient species and side products which are involved in this transformation.

3.2.4: The role of solvent, of excitation wavelength, and of accompanying cation (for complex 2)

†Calculations of the kinetics of photo-oxidation in air were made to compare the effect of the solvents DMF and DMSO (the most common solvents in which the metal complexes are easily soluble), of the excitation wavelength (360 nm and 400 nm), and of the nature of the cationic species, using **2** as the starting material. A kinetic comparison of the two manganese clusters (**2** and **5**, see figure 87) as starting material was also made. Figure 95 summarises the results obtained for complex **2**.

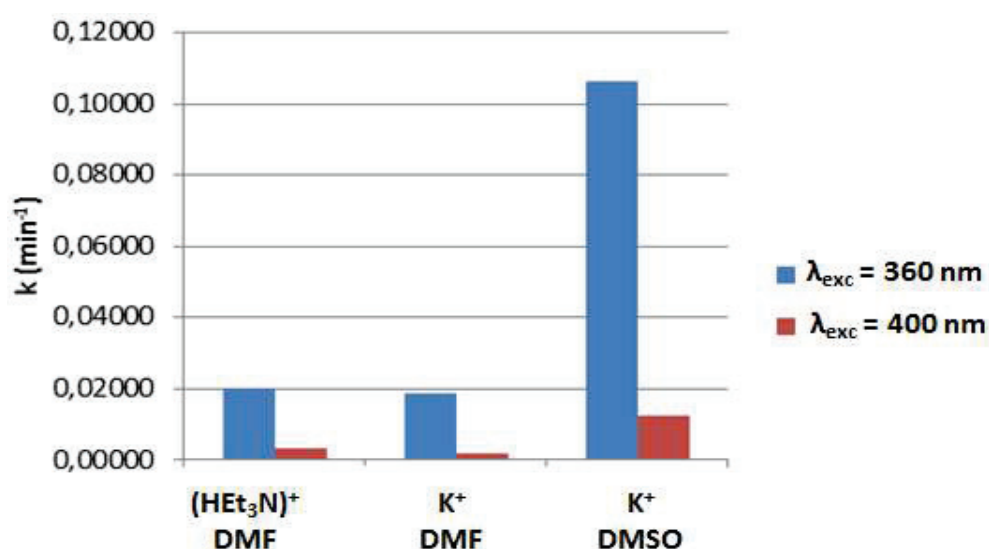


Figure 95: Rate constants k for the photo-oxidation of complex **2** under varying conditions.

The effect of the cationic species in complex **2** is seen to be negligible; there is almost no difference in the calculated rate constants when potassium or triethylammonium are used. The wavelength of excitation, on the other hand, strongly influences the rate of reaction, as would be expected. The absorption of the manganese complex is much stronger at 360 nm than at 400 nm, and as a result the rate of reaction when the former is used is approximately an order of magnitude larger than for the latter, regardless of the solvent medium. The solvent is also observed to play an important role, as the reaction proceeds much more rapidly in dimethylsulfoxide than in dimethylformamide ($k_{DMF} / k_{DMSO} < 20\%$). Franco *et al* calculated by a photochemical method the

†See annexe for details and data obtained for kinetic calculations.

is approximately 4 times more soluble in DMF than in DMSO.³⁰ The opposite effect is observed in this oxidation, so we must assume that oxygen concentration is not a factor and that oxygen is in excess in the aerated solutions with respect to the manganese-based reactant. As the product contains two molecules of solvent directly coordinated to the manganese(III) ion, it would appear, then, that DMSO is more strongly stabilising than DMF in this role. This hypothesis has yet to be confirmed; no study of the thermodynamic stability or lability with regards to exchange of the oxidised product has thus far been made.

3.2.5: Summary of the photo-oxidation of polynuclear manganese clusters

This intriguing photochemical transformation has been studied in depth, and many of the factors involved in the process have been elucidated. The reaction was qualitatively confirmed to be a photo-oxidation reaction between the manganese(II) complex and molecular dioxygen, with the reduction product of oxygen being discovered to be the superoxide anion by paramagnetic resonance spectroscopy utilising a nitron spin-trap to observe transient radical species. The necessary generation of oxygen in its singlet state as a transition species has been verified by a series of photochemical reactions followed by UV-visible absorption spectroscopy, although it was observed that the species $^1\text{O}_2$ cannot act alone as an oxidant for these manganese complexes without photoexcitation of the metal species. The nitrogen-based anions NO_2^- and NO_3^- were observed to also function as oxidants in the absence of elemental oxygen, conforming to their known behaviour as oxidative quenchers of triplet state excited molecules. Finally, the kinetic behaviour of the reaction has been determined for varying conditions of solvent, incident radiation wavelength, and cationic accompaniment to the photoactive aggregate anion $[\text{Mn}_4(\text{thiaSO}_2)_2\text{F}]^-$, and attempts have been made to explain this behaviour in a photophysical sense. To continue, we will now consider the reaction which occurs when the reagents (thiaSO₂ and Mn²⁺ ions) are uncomplexed before illumination; as in, the effect of irradiation upon a mixed solution of protonated sulfonylcalix[4]arene and a salt of manganese(II).

3.3: Photo-oxidation of solutions containing free thiaSO₂ and manganese(II) ions.

In addition to studying the photoreactivity of pre-isolated coordination compounds of thiaSO₂ and Mn²⁺ ions, we were interested in the photo-oxidation of these separate components when mixed in solution and immediately illuminated. This system offers not only the benefit of a broader range of solvents in which it is soluble, but also removes the necessity of the initial metal complex synthesis step. The irradiation of such a mixture in either DMF or DMSO has been observed to give rise to the same manganese(III) complex product as for complexes **2** and **5**, above, and the production of the superoxide anion has been confirmed by EPR. Figure 96 shows the evolution of the UV-vis absorption spectrum of a mixture of thiaSO₂ and Mn(NO₃)₂·4H₂O in DMF with time of irradiation ($\lambda_{\text{exc}} = 400 \text{ nm}$).

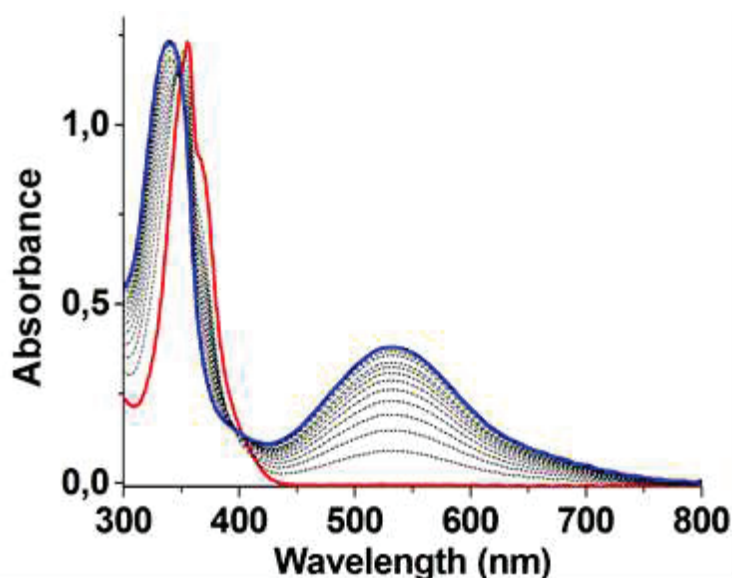


Figure 96: Time resolved spectral changes in the UV-vis absorption profile of a solution of thiaSO₂ and Mn(NO₃)₂·4H₂O (0.3 mmol dm⁻³) in DMF at 20° C upon irradiation ($\lambda = 400 \text{ nm}$) between 0 min (red curve) and 17 min (blue curve); spectroscopic path length = 0.2 cm.

3.3.1: Effect of stoichiometric ratio of thiaSO₂ : Mn(NO₃)₂

Initially we considered the photoreaction between thiaSO₂ and the salt manganese(II) nitrate tetrahydrate in DMF solvent. Under illumination at 400 nm, the colourless solutions became purple indicating the occurrence of photo-oxidation of the manganese(II) ion. The effect of the stoichiometric ratio upon the reaction was tested by carrying out the reaction using 1 and 4 molar equivalents of manganese salt with respect to calixarene ligand, and following the changes by UV-vis absorption spectroscopy. Figure 97 shows the resulting spectra of these experiments, respectively.

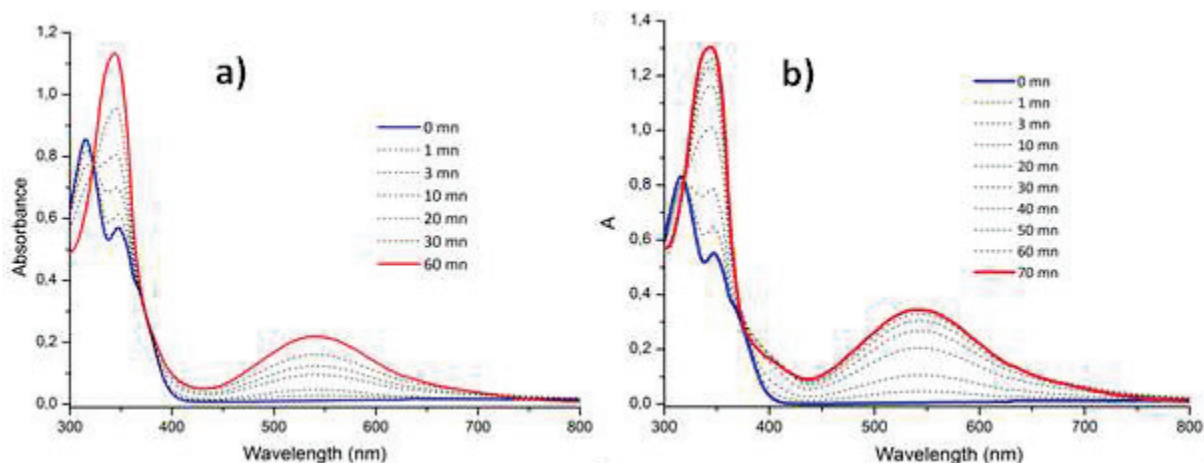


Figure 97: Evolution of the UV-vis absorption spectrum of a solution of thiaSO₂ (0.3 mmol dm⁻³) in DMF with time of irradiation ($\lambda = 400$ nm) at 20° C in air; path length = 0.2 cm. a) With 1 eq. of Mn(NO₃)₂, between 0 min (blue curve) and 40 min (red curve). b) With 4 eq. of Mn(NO₃)₂, between 0 min (blue curve) and 70 min (red curve).

The initial spectra of both mixtures show absorption peaks at 280 nm and 350 nm, which are assigned to the sulfonylcalixarene-centred π - π^* levels. With illumination at 400 nm in the presence of manganese(II) ions there is a diminution of the higher energy peak at 280 nm but an augmentation of the 350 nm peak. In both cases irradiation causes the characteristic broad band centred at 540 nm to appear, attributed to a ligand-to-metal charge transfer (LMCT) in the mononuclear product [Mn^{III}(thiaSO₂)(DMF)₂]⁻. This peak appears to reach its maximum after approximately 40 minutes of illumination for both metal ion concentrations. For reaction with 1 molar equivalent of Mn(NO₃)₂, this maximum ($\lambda_{\text{max}} = 537$ nm) occurs at an absorption intensity of 0,1905 (a.u.) whereas in the case of reaction with 4 molar equivalents of metal salt this maximum value at the same wavelength is 0.3443. This difference implies that a dynamic equilibrium is established between the components of this reaction.

To test the effect of using a great excess of Mn²⁺ ions, spectroscopy experiments were carried out on the same reaction with 20 molar equivalents of manganese(II) nitrate tetrahydrate. The resulting UV-vis absorption spectra are shown in figure 98.

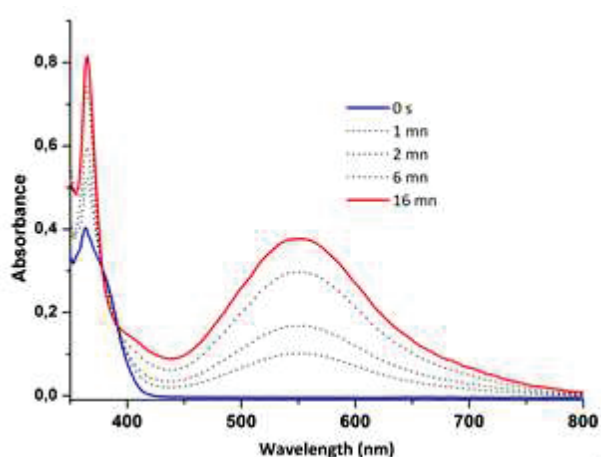


Figure 98: Evolution with time of irradiation ($\lambda = 400 \text{ nm}$) of a solution of thiaSO₂ (0.3 mmol dm^{-3}) and 20 eq. of Mn(NO₃)₂ in DMF at 20° C in air between 0 min (blue curve) and 16 min (red curve); path length = 0.2 cm.

All of these peaks grow with illumination at 400 nm, and the peak at 320 nm is either redshifted to or replaced by a peak at 340 nm. The growth of the expected LMCT peak centred at 540 nm is observed, taking approximately 16 minutes of illumination to reach its maximum value of 0.3773. The assumption is made that this represents total reaction of the ligands thiaSO₂ to form the Mn³⁺ complex, due to the excess of metal present. With that assumption, considering that thiaSO₂ is the limiting reagent, the final concentration of oxidised product is assumed to be equal to its initial concentration of 0.3 mmol dm^{-3} (i.e. full complexation of all thiaSO₂ molecules). From this value a molar extinction coefficient, ϵ , for the product complex at its maximum point 540 nm ($A_{540} = 0.3773$) is calculated to be $6288 \text{ M}^{-1} \text{ cm}^{-1}$.

With this assumption, following the empirical formula of the reaction the equilibrium constant K can be calculated by the equation shown in figure 99. ThiaSO₂(H₄) is used to signify the neutral, tetraprotonated starting material, i.e. the compound thiaSO₂ in its uncomplexed state. {X} signifies the concentration of species X.

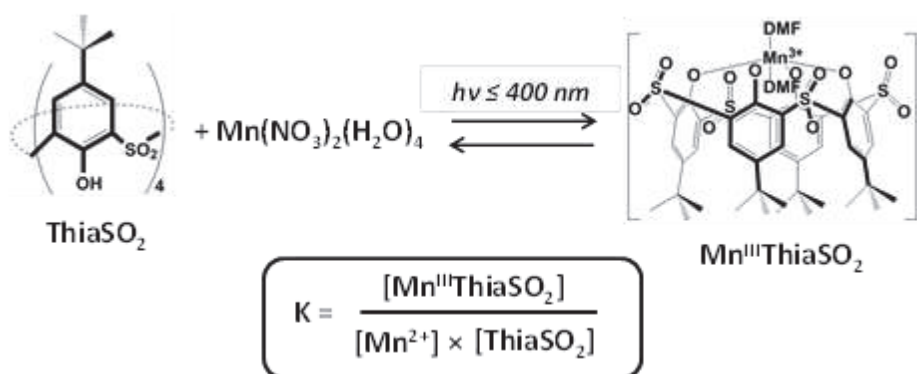


Figure 99: Hypothetical dynamic equilibrium established upon illumination of solutions of thiaSO₂ and manganese(II) nitrate, with equation for calculation of the equilibrium constant K.

The equilibrium constants for the reactions involving 1 and 4 equivalents of manganese(II) salt can now be derived using the extinction coefficient above to calculate the concentration of product formed in these cases. From these values of 0.1905 and 0.3443, the constants $K_{(1\text{eq.})}$ and $K_{(4\text{eq.})}$ are found to be 6870 M⁻¹ and 11283 M⁻¹ respectively. A few explanations for the discrepancy between these values can be postulated:

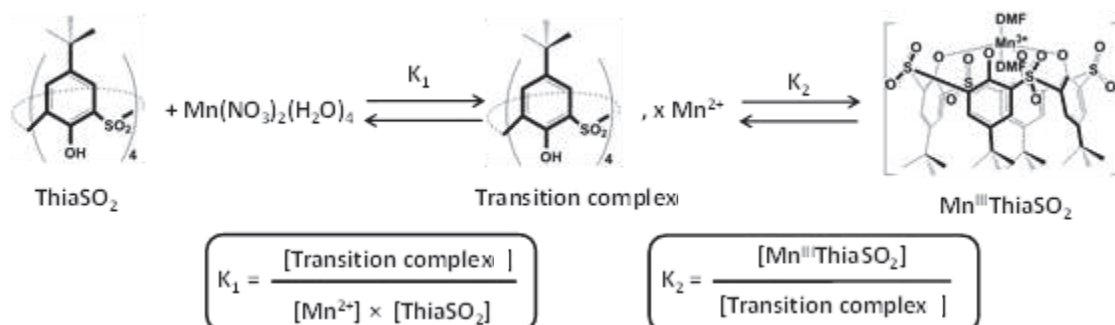


Figure 100: Modified reaction diagram for photo-oxidation reactions of sulfonylcalix[4]arene and manganese(II) nitrate taking into account a precomplexation step; below are given the revised equations used to calculate the equilibrium constants of these reaction steps.

- Even though the solution is illuminated immediately after being made, the elementary equation used to describe the reaction is wrong. This is due to an initial step whereby the liberated Mn²⁺ ions and the thiaSO₂ molecules interact, in a type of 'precomplexation'. This initial step should not have any effect on the overall equilibrium constant ($K = K_1 \times K_2$) but will affect the calculations we carry out to find the constant (see figure 100).

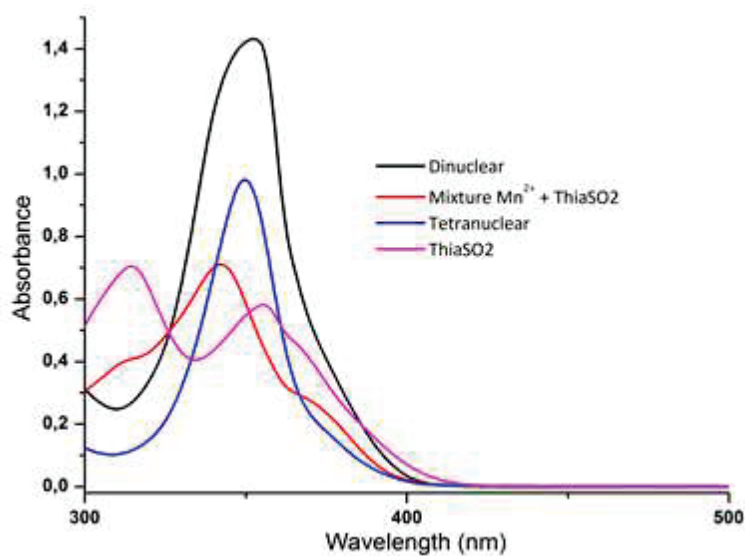


Figure 101: UV-visible absorption spectra for freshly made DMF solutions of tetranuclear manganese complex 2 (blue curve), dinuclear manganese complex 5 (black curve), a mixture of thiaSO₂ and manganese(II) nitrate tetrahydrate (red curve), and the pure compound thiaSO₂ (pink curve), at room temperature.

- This idea of an interaction occurring between the ligand and the metal ion before reaction is confirmed by the UV-visible absorption spectra shown in figure 101. The spectrum of the thiaSO₂ solution immediately after addition of manganese(II) nitrate is markedly different from that of the ligand thiaSO₂ alone; it also does not resemble neither the spectrum of the tetranuclear nor of the dinuclear complexes discussed above (**§3.2**). It can be imagined that the nitrate anion, which is not a strongly coordinating ligand, is easily displaced by the sulfonylcalixarene. Figure 102 demonstrates that spectra obtained immediately after a fresh solution is made and those obtained after the solution is agitated overnight in the absence of light (whether using 1 or 4 equivalents of manganese salt) are identical; strengthening this idea. At this point no crystalline sample of the species (there may be only one, or several) formed in solution has been isolated for X-ray diffraction analysis.
- Furthermore, the manganese(II) nitrate salt is known to hydrate rapidly upon exposure to air (Alfa Aesar provider labels it as 'hygroscopic'; <https://www.alfa.com/en/catalog/A18521>). This introduces significant error when calculating the concentration values for this compound.

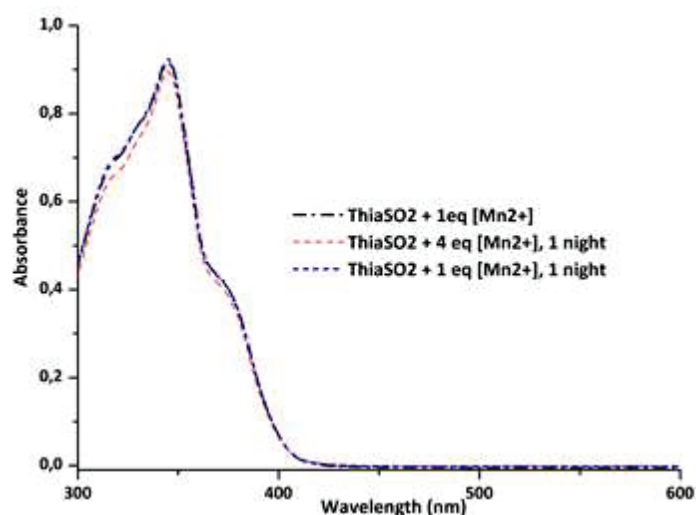


Figure 102: UV-vis absorption spectra for DMF solutions of thiaSO₂ and manganese(II) nitrate, in a 1:1 molar ration immediately after dissolution (dashed black curve), in a 1:1 ration after 1 night agitation (dashed blue curve), and in a 1:4 ratio after 1 night agitation (dashed red curve).

Thus far we have established that the photo-oxidation of manganese(II) ions in solution with sulfonylcalix[4]arene is viable, and appears to follow a dynamic equilibrium, without requiring any prior preparation of the tetranuclear or dinuclear clusters described above. The addition of a large excess of manganese(II) salt greatly accelerates the rate of the reaction. To further understand these phenomena, we next considered the use of a manganese(II) source containing a more strongly coordinating counter ion, which is also less susceptible to spontaneous hydration: MnCl₂·4H₂O.

3.3.2: Effect of Mn²⁺ salt: MnCl₂

The photoreaction of DMF solutions of manganese(II) chloride tetrahydrate were studied by UV-visible absorption spectroscopy. Figure 103 shows the spectra obtained for this reaction when an initial molar ratio of Mn²⁺:thiaSO₂ of 20:1 is used.

With the use of manganese(II) chloride, the maximum absorbance of the product is the same no matter how much of a molar excess of the manganese salt is added at the beginning. This maximum absorption occurs at $\lambda_{\text{max}} = 540 \text{ nm}$ with a value of 0.1937. Employing the value $\epsilon_{540} = 6288 \text{ M}^{-1} \text{ cm}^{-1}$ for this product, that absorbance corresponds to a concentration of 0.154 mmol dm⁻³, or 51.3 % conversion. Contrarily to the situation observed with the nitrate salt, the amount of product which is formed does not change depending on the initial concentration of manganese salt; the rate

of the reaction is however strongly affected by this parameter. With the initial mixtures containing a stoichiometric amount, a fourfold excess, and a twentyfold excess of manganese(II) chloride the reaction required a duration of 190 minutes, 110 minutes, and 87 minutes respectively to reach maximum conversion. It should be noted that all of the rates of reaction when using manganese(II) chloride are considerably slower than those observed when using manganese(II) nitrate. The oxidising power of the nitrate anion (§3.2.3) is almost surely a contributing factor in this difference of reaction rates.

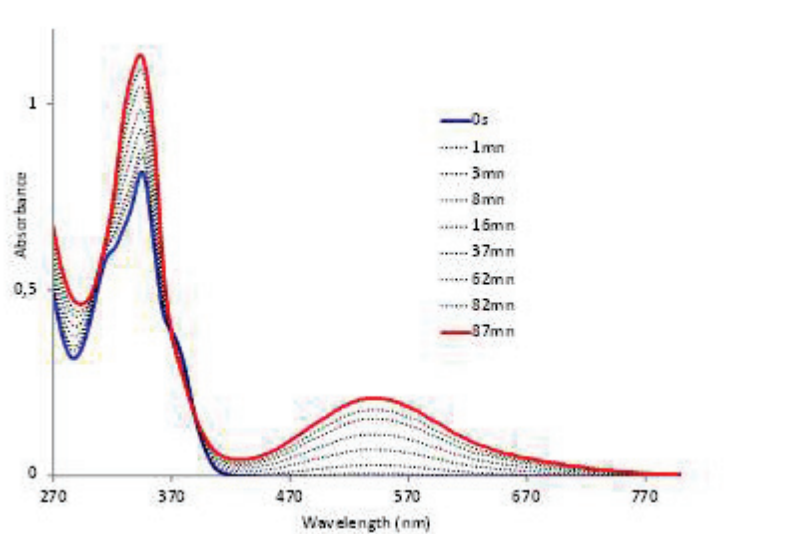


Figure 103: Evolution of the UV-vis absorption spectrum with time of irradiation ($\lambda = 400 \text{ nm}$) for DMF solutions of thiaSO₂ (0.3 mmol dm^{-3}) and manganese(II) chloride in air at room temperature, containing 20 molar equivalents of MnCl₂ with respect to thiaSO₂, between 0 min (blue curve) and 87 min (red curve); path length = 0.2 cm.

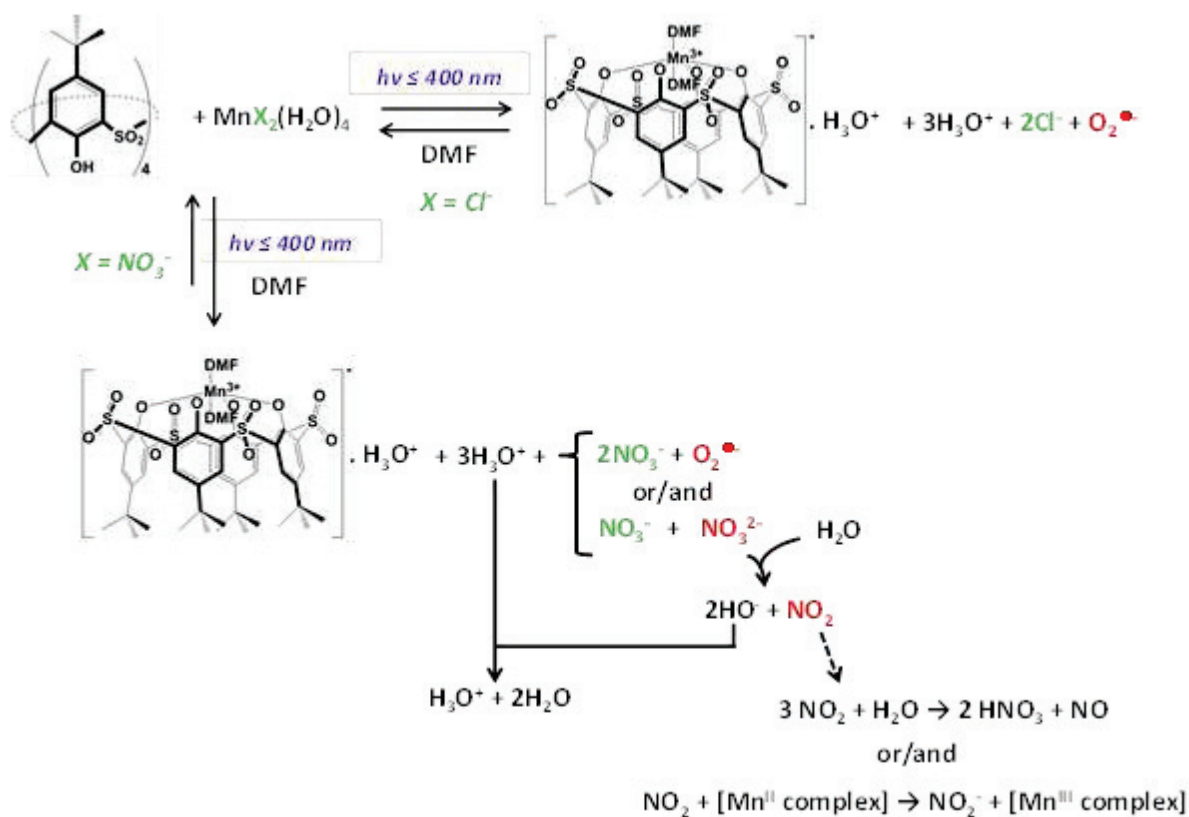


Figure 104: Proposed routes for the photoreaction ($\lambda \leq 400 \text{ nm}$) of systems containing thiaSO₂ and manganese(II) salt, highlighting the importance of further reactions of the nitrate ion.

From all of this we reach the conclusion that the initial form of the manganese species is essential in dictating the properties of the oxidative transformation. When the weakly coordinating nitrate anion is used, the comparative initial concentration of manganese salt directly influences the overall yield of the reaction; conversely, with the strongly coordinating chloride anion the initial concentration of manganese salt has no effect on the yield but strongly directs the kinetics of the reaction. As the reaction releases hydroxonium ions, as well as relying upon the deprotonation of thiaSO₂ molecules, it can be seen that the acid base properties of the components that are involved are of extreme importance to the process. Furthermore, we know that this type of system can induce the reduction of the nitrate ion, modifying its behaviour in the presence of these ions in comparison to solutions containing chloride ions. Experiments were carried out in the absence of oxygen for reaction mixtures containing one of the two manganese salts, nitrate or chloride. Purple colouration was observed solely in the case of the nitrate. We can therefore formulate the hypothesis presented in figure 104.

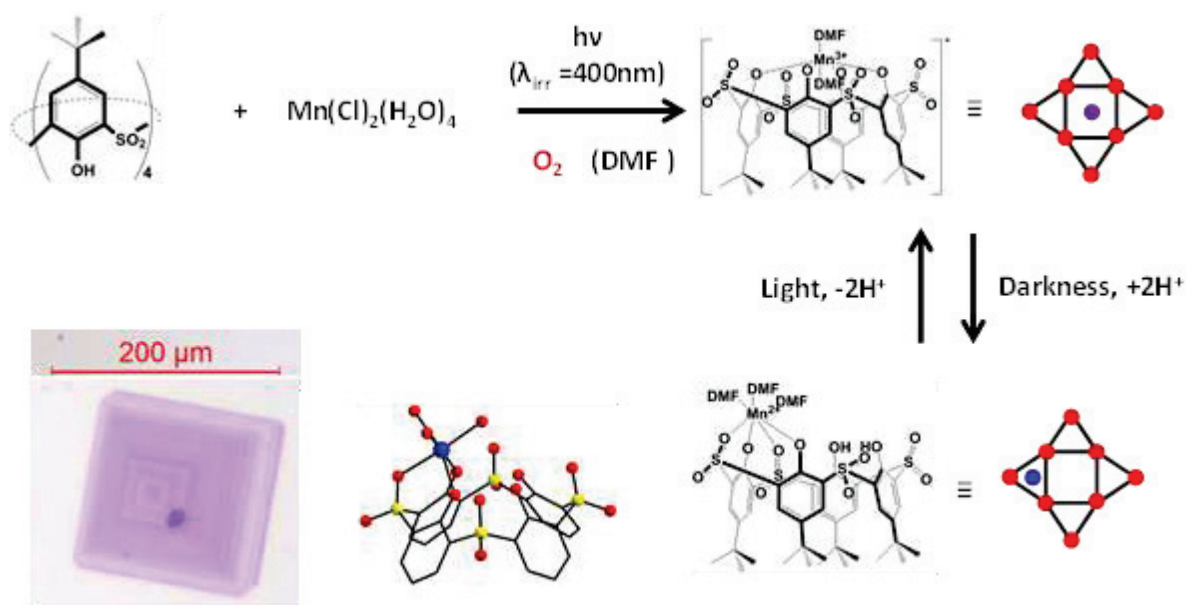


Figure 105: Hypothetical light-controlled switching mechanism between Mn^{II} and Mn^{III} systems with (right) a top-down view representation of the Mn^{II} ion (purple) and eight relevant oxygen atoms (red). Inset: a crystal of the mononuclear Mn^{II} complex showing the purple colouration.

One important factor to notice, dependent upon this pH stability, is the reversibility of the reaction. When free H^+ ions are available in solution (no base present), the reaction is reversible. The eventual product of this interaction, a mononuclear manganese(II) complex, bears a strong resemblance to the mobile zinc complex of sulfonycalix[4]arene which has been described before by Kajiwara *et al.*³¹ This mononuclear Mn^{II} species was isolated and characterised by X-ray diffraction crystallography. The paramagnetic nature of the Mn^{2+} ion makes it difficult to investigate this hypothesis by the NMR method that they demonstrated in their article; however if it is true for our system as it appears to be, it could open the door for possibilities which have so far not been envisioned for these systems, such as light-controlled molecular switches. The mononuclear Mn^{II} species was isolated and studied by single crystal XRD analysis. Obtaining a pure sample of this complex is difficult; it has only ever been obtained after the disappearance of the trivalent manganese complex brought about by illumination of a 1:1 mixture of thiaSO₂ and $\text{MnCl}_2 \cdot 4\text{H}_2\text{O}$, and each time a purple discolouration existed at the surface of the crystals. This would appear to be analogous to a kind of passivation layer upon the material surface. Figure 105 illustrates the

proposed light-based switching mechanism for these systems, with an inset showing the crystal morphology.

The reversibility of this reaction is dependent upon the pH of the reaction medium. This concept was further investigated therefore by testing the effect of the addition of base upon this system.

3.3.3: Effect of addition of Et₃N

The UV-visible spectroscopy characteristics of these systems upon illumination with the addition of base were also investigated. The base triethylamine, Et₃N, was chosen as it is not strongly coordinating, and therefore is unlikely to interfere in the creation of metal complexes. Figure 106 shows the UV-visible absorption spectra obtained for the illumination of mixtures of thiaSO₂ and manganese salt Mn(NO₃)₂ in the presence of Et₃N.

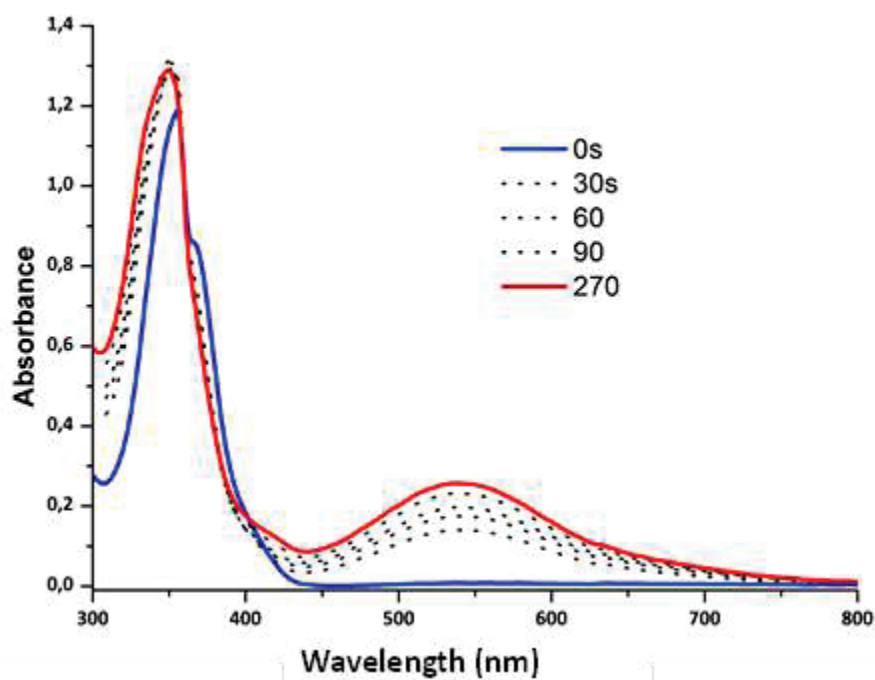


Figure 106: Time resolved UV-vis absorption spectra for illuminated ($\lambda = 400 \text{ nm}$) mixture in DMF solution of thiaSO₂ (0.3 mmol dm^{-3}) and 1 eq. of Mn(NO₃)₂·4H₂O, between 0 min (blue curve) and 4.5 min (red curve); path length = 0.2 cm.

The pH of the system evidently has strong implications upon the photo-oxidation reaction described in this chapter, mainly relating to the extent of deprotonation on the phenolic moieties of the sulfonylcalixarene ligand, and the amount of free protons H^+ in the system. The ligand is the principal absorbing part of the aggregate, and its absorption profile differs subtly depending on the ratio of different forms of thiaSO₂ (fully protonated, monoanionic, dianionic, trianionic, tetraanionic) which are present.

The addition of base causes the rate of the reaction to increase regardless of the initial manganese salt used: with the nitrate about 40 min is necessary (as expected) and with the chloride 30 minutes of illumination is necessary to reach full conversion to the product. The addition of base affects the initial absorption profile of the mixture, as shown in figure 107.

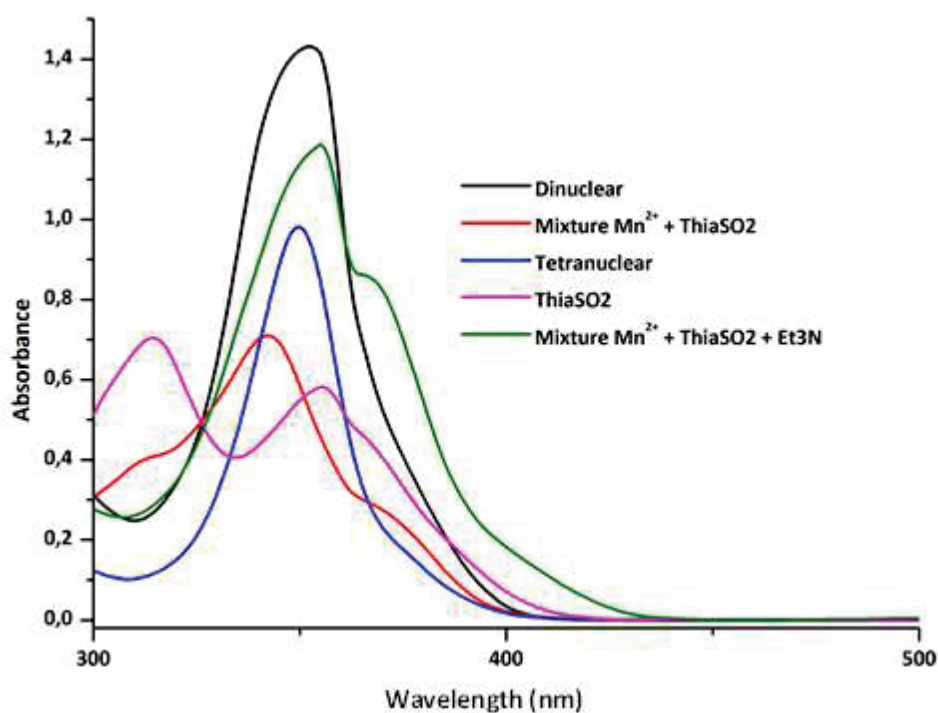


Figure 107: UV-vis absorption spectra for fresh solutions containing the tetranuclear manganese complex 2 (blue curve), the dinuclear complex 5 (black curve), a mixture of thiaSO₂ and Mn(NO₃)₂ (red curve), and the same mixture with Et₃N (green curve), and the pure compound thiaSO₂ (pink curve), at 20° C.

It can be seen that the addition of base causes the absorption profile to more closely resemble that of the manganese clusters formed with sulfonylcalixarene; this insinuates that the

base facilitates the formation of either a dinuclear or tetranuclear starting product in solution before illumination.

3.3.3.1: Effect of λ_{exc}

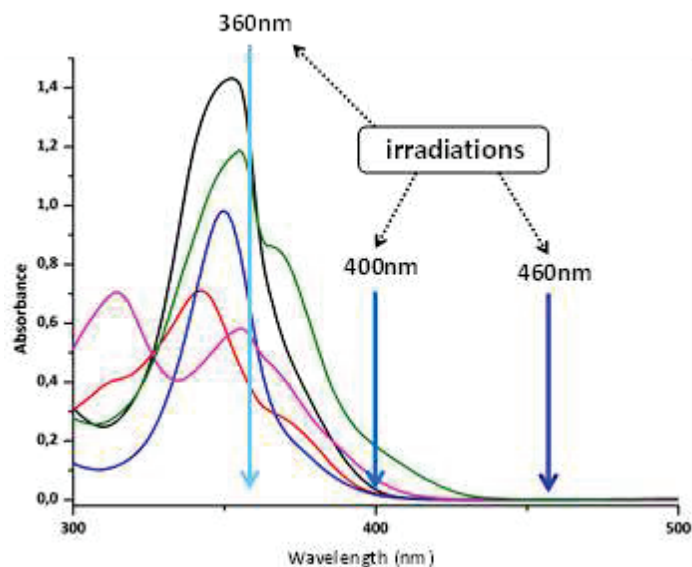


Figure 108: Adaptation of figure 107 indicating the excitation wavelengths which are available to our laboratory.

The laboratory possesses LED lamps which illuminate at wavelengths of 360 nm, 400 nm, and 465 nm, which are indicated on figure 3.28. It is worth making note of the effect of the excitation wavelength as a function of the absorption profile of the reagents; thus far all experiments listed have made use of light of 400 nm for photoexcitation of reaction experiments.

- 465 nm. At this wavelength almost no absorption is observed for any of the systems studied, and no photo-oxidation is observed with excitation at this wavelength.
- 360 nm. This wavelength is strongly absorbed by all of the systems studied, and results in extremely fast photo-oxidation of the manganese(II) ions regardless of the initial source species which is chosen.
- 400 nm. The various species examined all possess a tail on their UV absorption profiles at approximately this wavelength, rendering it the most interesting as regards the effect of illumination wavelength upon the photo-oxidation system.

One very interesting factor which was observed is that, with illumination at 360 nm using triethylamine base, photo-oxidation of the manganese ions was observed in the absence of oxygen. This phenomenon can be related to the photo-oxidation which was observed with polynuclear clusters of manganese(II) with the nitrate anion as oxidant. It is quite clear that some kind of excitation – quenching interaction occurs between the alkylamine species and the nitrate anion when illumination at this wavelength is produced.

3.3.3.2 Illumination of heterometallic systems

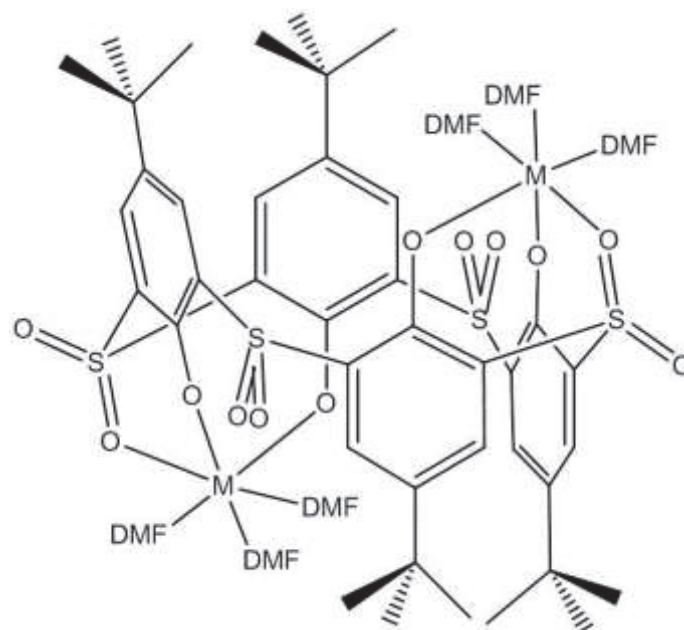


Figure 109: Generalised structure of the dinuclear complex formed in solution between nickel(II) or cobalt(II) ions and thiaSO₂, which adopts the 1,2-alternate conformation.

The observed response when the ligand sulfonylcalix[4]arene in mixed solution with salts of manganese and another transition metal (nickel or cobalt) is illuminated with light of 400 nm wavelength is worthy of note. When the reaction solution contains manganese(II) and cobalt(II), whether manganese is in excess or in a 1:1 ratio, irradiation causes immediate formation of the purple mononuclear manganese(III) species observed under normal circumstances. The solution gradually decolours again over time, and can be once again oxidised by the action of illumination. However, if the reaction mixture is stood for a sufficient length of time in the dark (approximately 36 hours) then photo-oxidation is no longer possible; the solution remains pale pink-red no matter how

long it is illuminated with UV light. When the competing metal ion is nickel(II) instead of cobalt(II), this effect is not observed. Even after a period of weeks, UV illumination of the solution still causes the purple colour change indicative of Mn^{2+} to Mn^{3+} oxidation. The reasoning for this behaviour centres on the inherent lability of each metal ion and the thermodynamic stability of the complex formed with sulfonylcalixarene. Under ambient conditions, a solution of sulfonylcalix[4]arene with solely cobalt(II) or nickel(II) ions forms a dinuclear complex such as is illustrated in figure 109.

Logically, this is the structure of the complex which forms when there is no illumination acting upon the solution, with three possible options: two manganese ions, two cobalt / nickel ions, or a heterometallic mixture with one of each. While the calixarene ligand remains uncomplexed, or at least one manganese ion is coordinated by it, then the energetic driving force provided by illumination is sufficient for the manganese oxidation reaction to occur. Cobalt ions in the solution will over time substitute into the complex preferentially over manganese, until only dicobalt complex exists in the mix. At this point, the stability of the complex overcomes the energetic impetus for manganese oxidation effectively preventing both complexation and oxidation of manganese. Nickel on the other hand does not fully replace the manganese in the complex within the time frame so far observed, due to being more inert or forming weaker complex bonds than cobalt. Therefore the oxidation of manganese can always be brought about by UV irradiation regardless of the length of time the mixture is allowed to equilibrate.

Consider the Irving-Williams series, which established a generalised order for the stability of complexes formed by the divalent cations of transition metals.³² This series states that, in general, the complexes formed by the Ni^{2+} ion are more stable than those formed by the Co^{2+} ion, and both of these cations form more stable complexes than the Mn^{2+} ion. This would seem to correlate well with the concept of displacement of bound Mn^{2+} ions by Co^{2+} ions over time in solution. The case involving the Ni^{2+} ion appears to be somewhat more complicated, however, with other factors than the stability of the complex formed with thiaSO₂ playing a role. These factors may concern the system

thermodynamics; both the solvent and other ligands present (anions from the initial metal salts) may form more stable complexes with nickel ions than does the sulfonylcalixarene molecule. Alternatively, the situation may be explained by the reaction kinetics. Complexes of nickel are not known to be particularly labile in terms of ligands exchange; it may be that with a greater length of time the reaction mixture containing Ni^{2+} ions will show total replacement of the Mn^{2+} ions in sulfonylcalixarene complexes, similarly to the observed behaviour of the solutions containing Co^{2+} ions.

3.3.4: Luminescence behaviour of ThiaSO₂/Mn²⁺ in solution

No luminescence of these mixtures in solution is observed, except for the fluorescence attributed to the sulfonylcalixarene ligand itself. Furthermore, the illumination of these systems in the presence of triphenylphosphine is observed to form the expected phosphine oxide, which could account for either the formation of singlet oxygen or of radical ions, as shown in figure 110. This process could occur by an energy transfer, as was hypothesised for the polynuclear complexes discussed in section 3.2, or via a more direct charge transfer procedure.

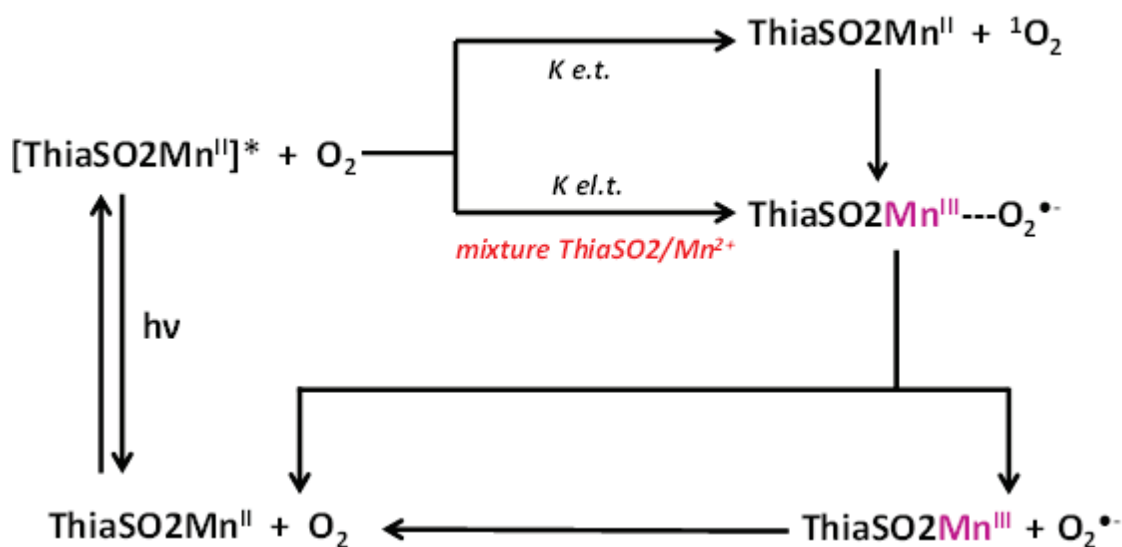


Figure 110: Summary of the hypothesised routes of photo-oxidation of solution state mixtures of the ligand thiaSO₂ and sources of the ion Mn²⁺. K e.t. = energy transfer, K el. t. = electron transfer.

3.3.5: Summary of the photoreactivity of solution state reagent mixtures

It has been established that the interaction between the sulfonylcalix[4]arene ligand and the Mn^{2+} ion is sufficient to allow photochemical oxidation of these species in mixed solution without prior complexation and arrangement. The role of the various constituents of this photoreaction has been elucidated, demonstrating that the nature of both the initial manganese(II) salt employed and the solvent medium in which the reaction takes place play a crucial part in the physical attributes of the reaction. The control of the pH of the reaction medium, and the presence of base in general, have been shown to be viable in controlling the essential aspects of the photo-oxidation, and have demonstrated the likelihood of a photophysical interaction between the excited triplet state of the base triethylamine and the accompanying nitrate anion under certain circumstances. All in all, this photo-driven creation of a metal-organic coordination complex is quite fascinating, and there remains some work to be done to fully characterise this chemical process. For the final section of this chapter, we will consider the photophysical aspects of the compound thiaSO₂ in solution without the addition of metal ions.

3.4: Photoreactivity of the pure compound thiaSO₂

Firstly, the effect of irradiation ($\lambda = 400$ nm) upon the pure compound in DMF solution was observed. Figure 111 compares the UV-vis absorption spectra of this compound in DMF solution when freshly made, and after 40 min agitation with illumination at 400 nm.

The product of this illumination was subjected to mass spectrometry; the results are shown below in figure 112. This analysis revealed the presence of several oligomeric polyphenol forms, highlighting the susceptibility of the compound thiaSO₂ to oxidative degradation under irradiation in the absence of transition metal ions. It appears as though the C-S bond is severed to create each of the oligomeric degradation products. These compounds could be of potential interest as starting material in the synthesis of thiacalixarenes of larger cycle sizes than 4 phenol units.

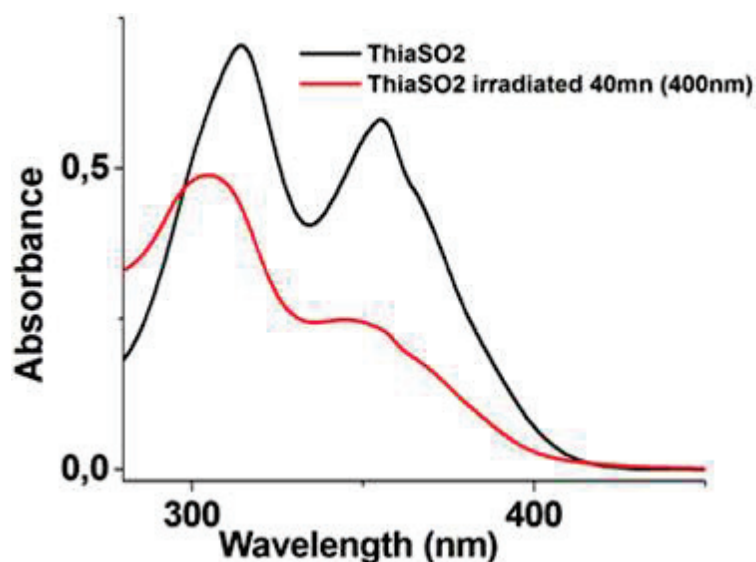


Figure 111: Comparison of the UV-vis absorption profile of a solution of thiaSO₂ in DMF immediately upon dissolution (black curve) and after 40 minutes of illumination ($\lambda = 400$ nm, red curve) in air at room temperature.

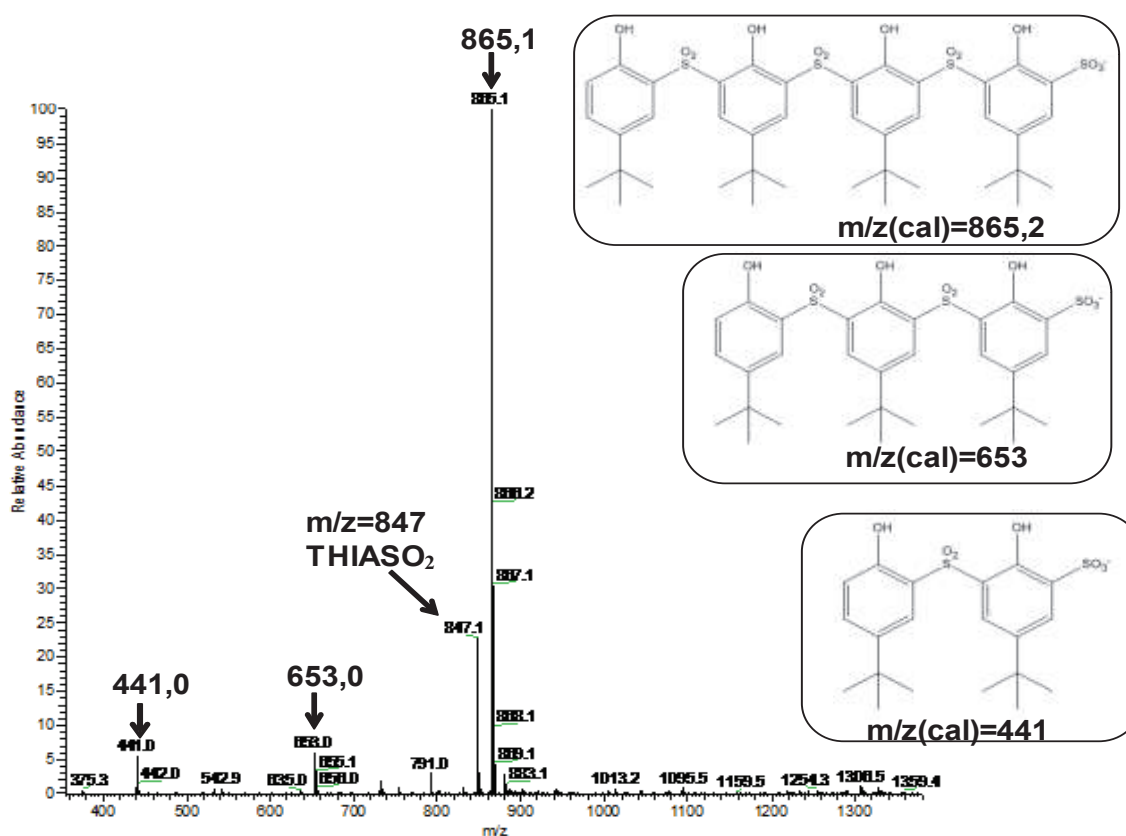


Figure 112: Mass spectrometry results from the illumination ($\lambda = 400$ nm) of thiaSO₂ in DMF solution, with hypothesised oligomeric products and their mass values inset.

This photo-reactivity in the absence of metal centres is of interest, raising the question of whether the molecule thiaSO₂ itself might be capable of acting as a photosensitiser for the generation of singlet oxygen in a similar manner to the solution state mixtures of thiaSO₂ and Mn^{II}

ions. One way to detect this would be to probe for the luminescent emission of $^1\text{O}_2$ which occurs in the IR range at approximately 1 270 nm.³³ With an appropriate detector, therefore, the yield of singlet oxygen produced by a photosensitiser may be assessed by measuring the IR emission spectrum in this region in comparison to a known standard. Rose Bengal is a xanthene dye which is found in the literature to produce singlet oxygen, and its quantum yield has been reported in a variety of different solvents, making it viable as a reference standard for this application.³⁴ Figure 113 shows the results of this test for photosensitisation by thiaSO₂. No formation of singlet oxygen was observed for excitation of the molecule at these wavelengths, in contrast to a control sample of Rose Bengal. We can conclude therefore that the presence of metal ions is a requirement for the system to act as a photosensitiser for the generation of singlet oxygen.

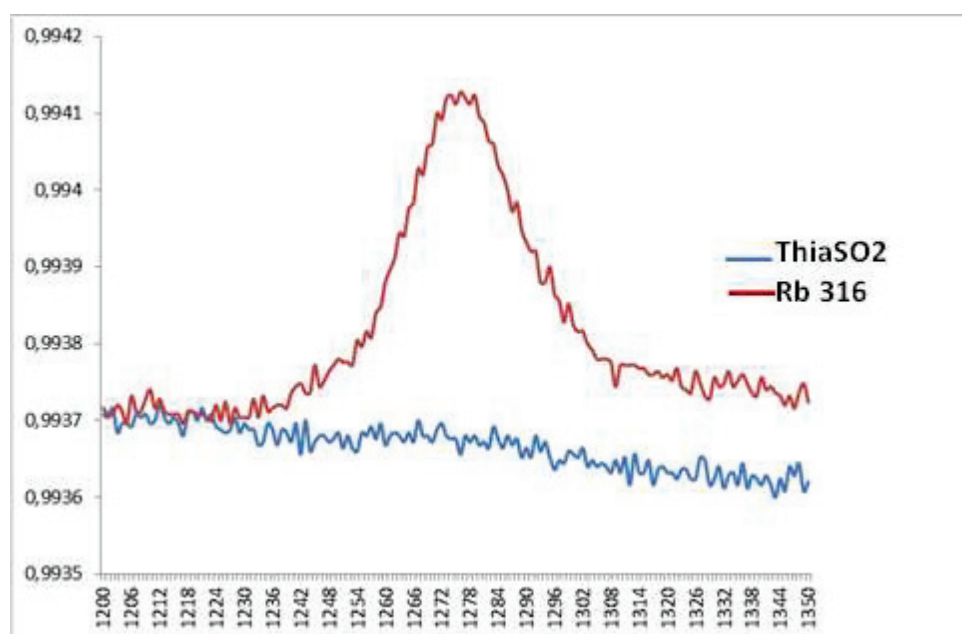


Figure 113: Emission spectra in the range from 1 200 nm to 1 350 nm for irradiated samples of thiaSO₂ (blue curve) and Rose Bengal (red curve) to test for the luminescence of singlet oxygen.

DFT experiments reveal that the primary absorptions of this molecule correspond to transitions resulting in the delocalisation of electronic charge around the molecule analogous to the formation of a phenolate radical. Figure 114 shows the DFT results for the UV-visible spectra of the neutral, monoanionic, and dianionic forms of this molecule, with a second spectrum highlighting the

transitions arising due to the singly deprotonated molecule and the form of the molecular orbitals involved.

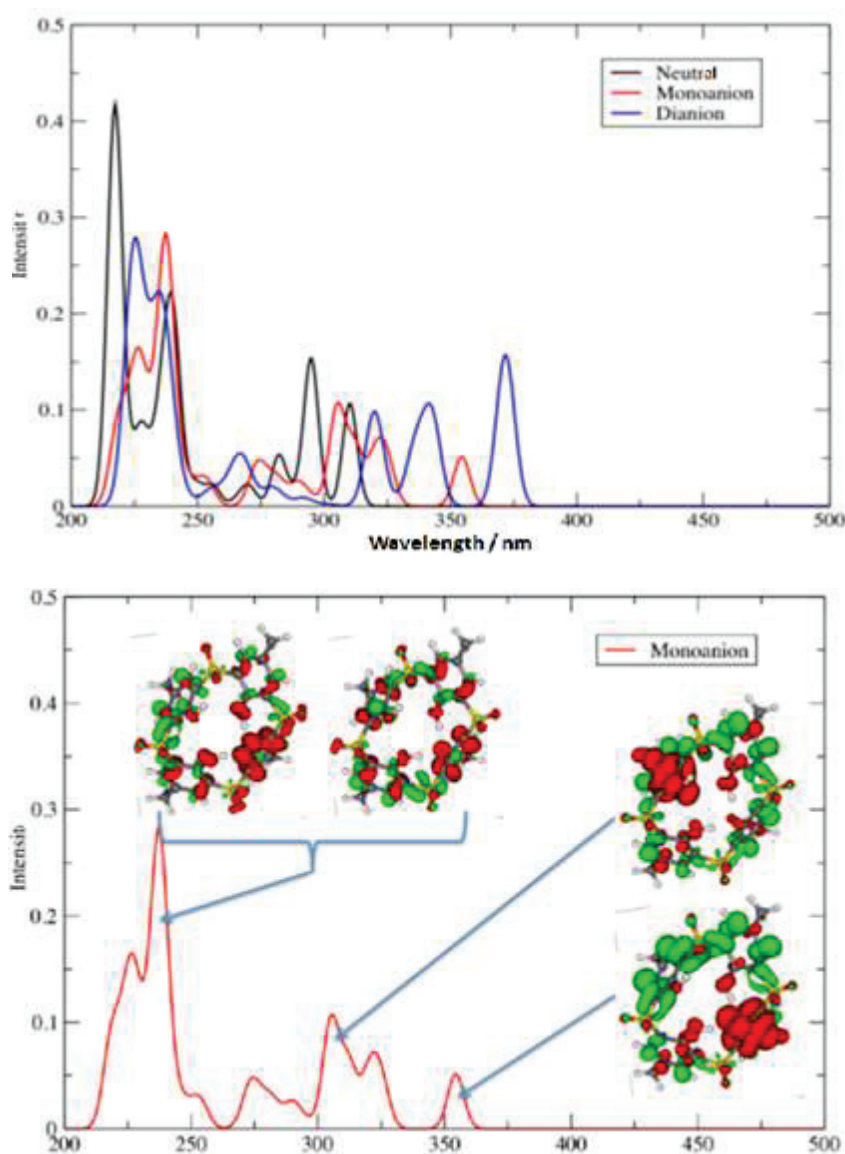


Figure 114: (Above) Theoretical UV-visible absorption spectra calculated by DFT methods for the molecule thiaSO₂ in its neutral (black curve), monoanionic (red curve), and dianionic (blue curve) forms. (Below) The calculated spectrum of the monoanion, with assigned transitions shown as electronic density / molecular orbital diagrams.

Two facts are important to note here; the calculated spectrum for the monoanionic form of thiaSO₂ shows peaks approximately in the regions where the experimentally observed peaks occur (316 and 359 nm), and the neutral, fully protonated molecule is expected to show no absorption of wavelengths longer than 320 nm. The calculations reveal that the transitions of the monoanion correspond to the (n.π*) states showing delocalisation of electronic density from being concentrated

on the phenolic oxygen atom around the conjugated structure of the molecule; these peaks are in good accord with the experimentally observed peaks. Figure 115 illustrates this transition as the formation of a phenolate radical type species.

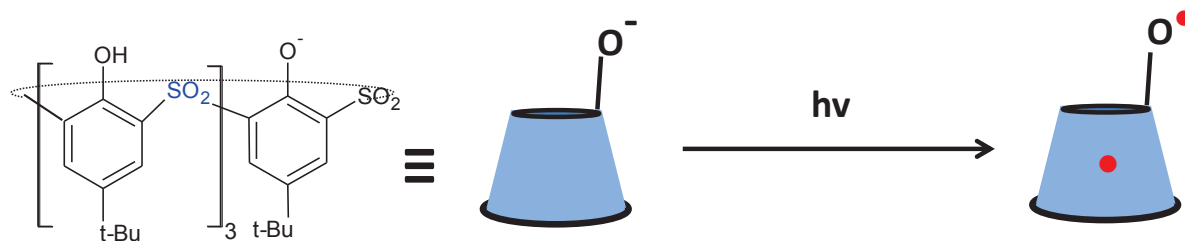


Figure 115: Illustration of the formation of biradical forms of the molecule thiaSO₂ by absorption due to the monoanion at 316 nm or 359 nm. The polyphenol macrocycle is represented by a shape depicting its cone conformation.

This hypothesis of charge separation, resulting in a phenol based radical and a delocalised radical, has an interesting implication. The phenol-based radical should act as an oxidant, whereas the delocalised unpaired electron on the calixarene cage structure is expected to be a reductant. Assuming that the lifetime of these species is long enough, this could provide very interesting functionality of the thiaSO₂ molecule. When thiaSO₂ in DMF solution is illuminated at 360 nm in the presence of triphenylphosphine PPh₃, the product triphenylphosphine oxide, Ph₃P(=O), is observed. Following the report of Ohkubo *et al* concerning the photocatalytic oxidation of PPh₃ by oxygen and radical species, the reaction mechanism given in figure 116 can be postulated.³⁵

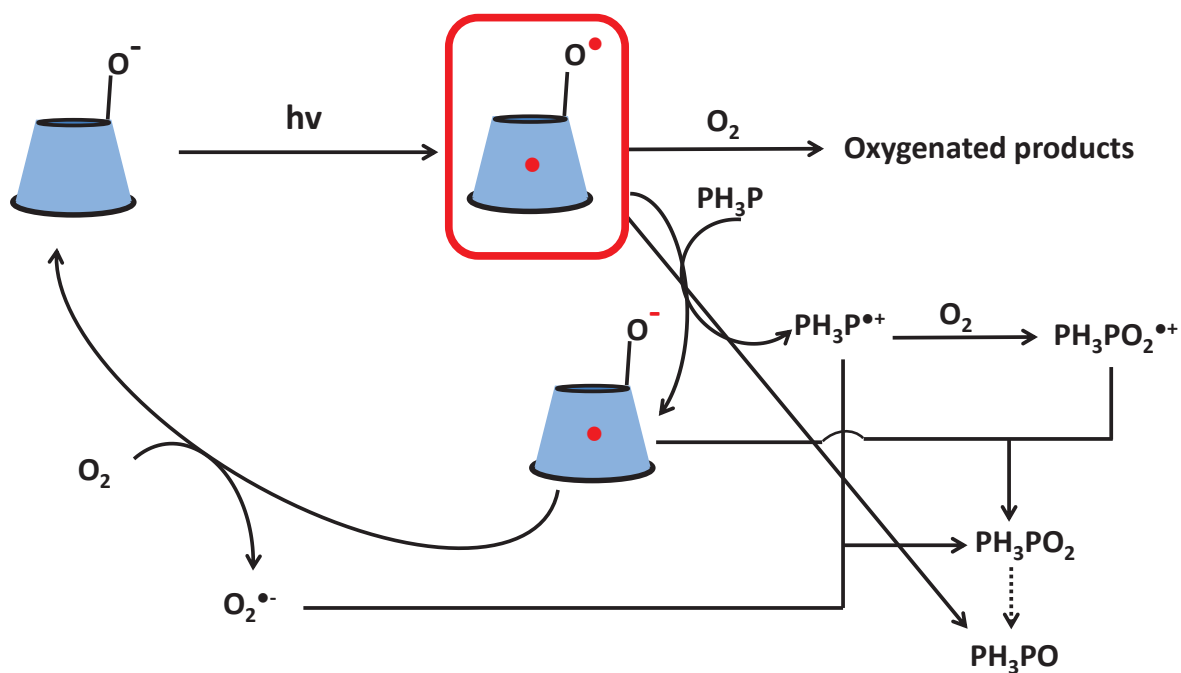


Figure 116: Hypothetical reaction mechanism for the photoreaction of thiaSO₂ with Ph₃P.³⁵

This mechanism may seem complicated; essentially it involves the action of the phenol-based radical (formed by the action of light upon the monoanion thiaSO₂⁻) as an electron acceptor from triphenylphosphine. The phosphine is then activated in terms of reactivity towards molecular oxygen, forming the radical cation Ph₃PO₂^{•+}. The remaining unpaired electron on the calixarene cage can now either interact with this phosphone radical (forming triphenylphosphine oxide, Ph₃P(=O)) or directly with a molecule of oxygen to form the superoxide anion, in both cases regenerating the monoanionic form of the thiaSO₂ molecule. The superoxide radical anion can interact with the radical phosphone cation to give rise to the stable phosphine oxide product.

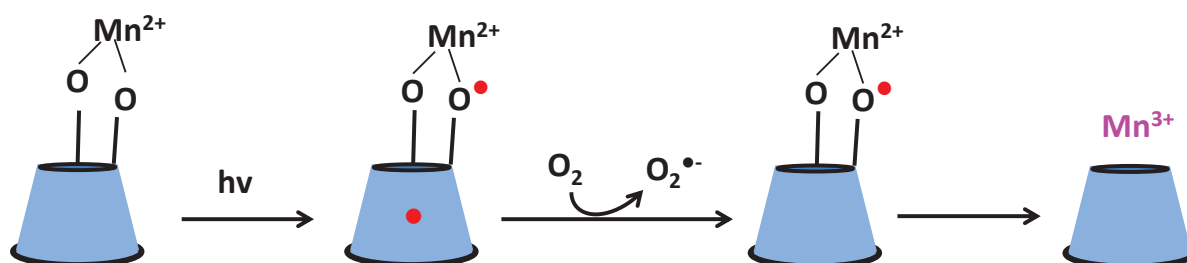


Figure 117: Illustration of the process of photo-oxidation of Mn²⁺ ions when in solution with the thiaSO₂ macrocycle via the hypothesised charge separation transition route.

This concept can be extended to include the interactions of thiaSO₂ with radiation in the presence of Mn²⁺ ions. Figure 117 illustrates this process.

The figure shows the precomplexation interaction in solution, followed by the formation of the radical species by illumination. The unpaired electron found on the macrocycle cage is donated to molecular oxygen to form the superoxide anion, and the phenol moiety receives an electron from the manganese ion to stabilise its unpaired spin. The Mn²⁺ ion is thus oxidised to its 3+ oxidation state.

In summary, the compound thiaSO₂ shows some interesting photophysical properties in its own right. Its fluorescence behaviour has been characterised and shown to be dependent upon the incident light which causes it. The photoreactivity of this species towards oxygen has been demonstrated, and theoretical calculations have been made in order to offer some explanation of this reactivity. The results of DFT calculations have also been used to try and shed some light on the strong synergy observed between the macrocycle and the manganese(II) ion under the influence of UV illumination.

3.5: Conclusion

Thorough characterisation of the various photoactive systems involving *para-tert*-sulfonylcalix[4]arene has been made, including polynuclear complexes of manganese, uncomplexed mixtures of thiaSO₂ and transition metal ions, and finally the pure compound thiaSO₂ itself. The propensity of these systems to undergo photodriven oxidation reactions has been described, and the potential mechanistic routes of these transformations have been mapped out. The systems have been shown to give rise to singlet oxygen and reactive radical ions, both of which are of interest in organic synthesis among other fields. These descriptions have taken into account the effect of the various reaction conditions upon the thermodynamic and kinetic properties of the process, demonstrating the importance of the solvent (which becomes incorporated into the oxidation

product), the nature of the oxidant (both triplet oxygen and nitrate anions are viable), and the wavelength of the incident light (UV light in the range 300 – 400 nm is necessary).

For the further characterisation of these systems, two routes of study are envisioned. The first involves flash photolysis experiments with UV-visible absorption and emission spectroscopy analysis, and *in situ* EPR spectroscopy to follow the reaction. These methods would allow a more in depth knowledge of the transitory species which are involved in the photodriven transformation, their respective lifetimes and reactivity and so on. The second route would be to perform electrochemical experiments on the systems, to elucidate the standard potentials of the electron transfer process involved and gain some insight into the stability of the relevant compounds in this respect.

It has been seen that this interaction with oxygen interferes with the luminescence behaviour of the manganese clusters described. The following chapter will discuss the immobilisation of these systems in the interior of an inorganic host matrix. This process is hoped to offer protection against oxidative degradation of the luminescent species, while also offering a potential platform for the incorporation of this material into functional materials. Other potential benefits include polarisation of emission brought about by structural ordering within the layered inorganic host.

References

1. Lamouchi, M. Matériaux moléculaires à propriétés optique et magnétique à base de complexes métalliques polynucléaires : Thiocalixarènes / métaux de transition. Université Claude Bernard Lyon 1, Lyon, 2012.
2. Harriman, A., PHOTOCHEMISTRY OF MANGANESE COMPLEXES. *Coordination Chemistry Reviews* **1979**, 28 (2-3), 147-175.
3. Noh, T. H.; Lee, H.; Kim, D.; Moon, D.; Lee, Y. A.; Jung, O. S., Photoreaction of adsorbed diiodomethane: halide effects of a series of neutral palladium(II) coordination cages. *Dalton Transactions* **2016**, 45 (23), 9574-9581.
4. Nakano, M.; Nishiyama, Y.; Tanimoto, H.; Morimoto, T.; Kakiuchi, K., Remarkable Improvement of Organic Photoreaction Efficiency in the Flow Microreactor by the Slug Flow Condition Using Water. *Organic Process Research & Development* **2016**, 20 (9), 1626-1632.
5. Li, M. K.; Qiang, Z. M.; Hou, P.; Bolton, J. R.; Qu, J. H.; Li, P.; Wang, C., VUV/UV/Chlorine as an Enhanced Advanced Oxidation Process for Organic Pollutant Removal from Water: Assessment with a Novel Mini-Fluidic VUV/UV Photoreaction System (MVPS). *Environmental Science & Technology* **2016**, 50 (11), 5849-5856.
6. Garza-Campos, B.; Brillas, E.; Hernandez-Ramirez, A.; El-Ghenymy, A.; Guzman-Mar, J. L.; Ruiz-Ruiz, E. J., Salicylic acid degradation by advanced oxidation processes. Coupling of solar photoelectro-Fenton and solar heterogeneous photocatalysis. *Journal of Hazardous Materials* **2016**, 319, 34-42.
7. Liu, W.; Sun, W. L.; Borthwick, A. G. L.; Wang, T.; Li, F.; Guan, Y. D., Simultaneous removal of Cr(VI) and 4-chlorophenol through photocatalysis by a novel anatase/titanate nanosheet composite: Synergetic promotion effect and autosynchronous doping. *Journal of Hazardous Materials* **2016**, 317, 385-393.
8. Zhu, Z.; Li, X. N.; Gu, W.; Wang, J. L.; Huang, H. L.; Peng, R. R.; Zhai, X. F.; Fu, Z. P.; Lu, Y. L., Improving photocatalysis and magnetic recyclability in Bi₅Fe_{0.95}Co_{0.05}Ti₃O₁₅ via europium doping. *Journal of Alloys and Compounds* **2016**, 686, 306-311.
9. Wegertseder, P.; Lund, P.; Mikkola, J.; Alvarado, R. G., Combining solar resource mapping and energy system integration methods for realistic valuation of urban solar energy potential. *Solar Energy* **2016**, 135, 325-336.
10. Derradji, M.; Ramdani, N.; Gong, L. D.; Wang, J.; Xu, X. D.; Lin, Z. W.; Henniche, A.; Liu, W. B., Mechanical, thermal, and UV-shielding behavior of silane surface modified ZnO-reinforced phthalonitrile nanocomposites. *Polymers for Advanced Technologies* **2016**, 27 (7), 882-888.
11. Wang, Y.; Li, T.; Ma, P. M.; Bai, H. Y.; Xie, Y.; Chen, M. Q.; Dong, W. F., Simultaneous Enhancements of UV-Shielding Properties and Photostability of Poly(vinyl alcohol) via Incorporation of Sepia Eumelanin. *Acs Sustainable Chemistry & Engineering* **2016**, 4 (4), 2252-2258.
12. Davidson, R. S.; Goodwin, D.; Pratt, J. E., Problems associated with distinguishing between singlet oxygen and electron transfer photooxygenation reactions. *Free radical research communications* **1987**, 2 (4-6), 313-20.
13. Kostenbauder, H. B.; Deluca, P. P., ENHANCED PHOTOREACTIVITY OF RIBOFLAVIN IN AQUEOUS SOLUTION IN PRESENCE OF MACROMOLECULES. *Nature* **1963**, 199 (489), 999-&.
14. Gibson, R. J. H., A photoelectric theory of photosynthesis. *Annals of Botany* **1908**, 22 (85-88), 117-120.
15. Cady, C. W.; Crabtree, R. H.; Brudvig, G. W., Functional models for the oxygen-evolving complex of photosystem II. *Coordination Chemistry Reviews* **2008**, 252 (3-4), 444-455.
16. Rivalta, I.; Brudvig, G. W.; Batista, V. S., Computational Studies of the Oxygen-Evolving Complex of Photosystem II and Biomimetic Oxomanganese Complexes for Renewable Energy Applications. *Applications of Molecular Modeling to Challenges in Clean Energy* **2013**, 1133, 203-215.

17. Kanady, J. S.; Lin, P. H.; Tsui, E. Y.; Agapie, T., Synthetic strategies towards a Mn₄CaO_n model complex of the oxygen-evolving complex of photosystem II. *Abstracts of Papers of the American Chemical Society* **2014**, *248*, 1.
18. Taylor, S. M.; Karotsis, G.; McIntosh, R. D.; Kennedy, S.; Teat, S. J.; Beavers, C. M.; Wernsdorfer, W.; Piligkos, S.; Dalgarno, S. J.; Brechin, E. K., A Family of Calix 4 arene-Supported (Mn₂Mn₂II)-Mn-III Clusters. *Chemistry-a European Journal* **2011**, *17* (27), 7521-7530.
19. Taylor, S. M.; McIntosh, R. D.; Piligkos, S.; Dalgarno, S. J.; Brechin, E. K., Calixarene-supported clusters: employment of complementary cluster ligands for the construction of a ferromagnetic Mn-5 cage. *Chemical Communications* **2012**, *48* (91), 11190-11192.
20. Harbour, J. R.; Chow, V.; Bolton, J. R., ELECTRON-SPIN RESONANCE STUDY OF SPIN ADDUCTS OF OH AND HO₂ RADICALS WITH NITRONES IN ULTRAVIOLET PHOTOLYSIS OF AQUEOUS HYDROGEN-PEROXIDE SOLUTIONS. *Canadian Journal of Chemistry-Revue Canadienne De Chimie* **1974**, *52* (20), 3549-3553.
21. Finkelstein, E.; Rosen, G. M.; Rauckman, E. J.; Paxton, J., SPIN TRAPPING OF SUPEROXIDE. *Molecular Pharmacology* **1979**, *16* (2), 676-685.
22. Liu, L. L.; Li, H. X.; Wan, L. M.; Ren, Z. G.; Wang, H. F.; Lang, J. P., A Mn(III)-superoxo complex of a zwitterionic calix 4 arene with an unprecedented linear end-on Mn(III)-O-2 arrangement and good catalytic performance for alkene epoxidation. *Chemical Communications* **2011**, *47* (39), 11146-11148.
23. Sawyer, D. T., *Oxygen Chemistry*. Oxford University Press: 1991.
24. Albitzer, E.; Alfaro, S.; Valenzuela, M. A., Photosensitized oxidation of 9,10-dimethylanthracene with singlet oxygen by using a safranin O/silica composite under visible light. *Photochemical & Photobiological Sciences* **2015**, *14* (3), 597-602.
25. Chemtob, A.; De Paz-Simon, H.; Dietlin, C.; Croutxe-Barghorn, C.; Salmi, H.; Allonas, X.; Chany, A. C.; Vidal, L.; Rigolet, S., A highly reactive photobase catalytic system for sol-gel polymerization. *Thin Solid Films* **2014**, *550*, 177-183.
26. DeRosa, M. C.; Crutchley, R. J., Photosensitized singlet oxygen and its applications. *Coordination Chemistry Reviews* **2002**, *233*, 351-371.
27. Koppenol, W. H.; Butler, J., Energetics of interconversion reactions of oxyradicals. *Advances in Free Radical Biology & Medicine* **1985**, *1* (1), 91-131.
28. Frank, A. J.; Gratzel, M., SENSITIZED PHOTO-REDUCTION OF NITRATE IN HOMOGENEOUS AND MICELLAR SOLUTIONS. *Inorganic Chemistry* **1982**, *21* (10), 3834-3837.
29. Treinin, A.; Hayon, E., QUENCHING OF TRIPLET-STATES BY INORGANIC-IONS - ENERGY-TRANSFER AND CHARGE-TRANSFER MECHANISMS. *Journal of the American Chemical Society* **1976**, *98* (13), 3884-3891.
30. Franco, C.; Olmsted, J., PHOTOCHEMICAL DETERMINATION OF THE SOLUBILITY OF OXYGEN IN VARIOUS MEDIA. *Talanta* **1990**, *37* (9), 905-909.
31. Kajiwarra, T.; Yokozawa, S.; Ito, T.; Iki, N.; Morohashi, N.; Miyano, S., Zinc(III) slides on a ligand surface: The X-ray crystal structure and dynamic behavior in solution of Zn(H₂L)(tacn). *Angewandte Chemie-International Edition* **2002**, *41* (12), 2076-2078.
32. Irving, H.; Williams, R. J. P., THE STABILITY OF TRANSITION-METAL COMPLEXES. *Journal of the Chemical Society* **1953**, (OCT), 3192-3210.
33. Boso, G.; Ke, D. M.; Korzh, B.; Bouilloux, J.; Lange, N.; Zbinden, H., Time-resolved singlet-oxygen luminescence detection with an efficient and practical semiconductor single-photon detector. *Biomedical Optics Express* **2016**, *7* (1), 211-224.
34. Redmond, R. W.; Gamlin, J. N., A compilation of singlet oxygen yields from biologically relevant molecules. *Photochemistry and Photobiology* **1999**, *70* (4), 391-475.
35. Ohkubo, K.; Nanjo, T.; Fukuzumi, S., Photocatalytic electron-transfer oxidation of triphenylphosphine and benzylamine with molecular oxygen via formation of radical cations and superoxide ion. *Bulletin of the Chemical Society of Japan* **2006**, *79* (10), 1489-1500.

CHAPTER 4: INORGANIC – ORGANIC HYBRID MATERIALS
OBTAINED BY INTERCALATION OF CLUSTER COMPLEXES
INTO INORGANIC HOST MATRICES

This chapter describes the study which was made into the incorporation of luminescent manganese clusters into an inorganic matrix. The family of Layered Double Hydroxides (LDHs) was chosen as the basis of this host matrix, for a number of reasons. These are well known, and well characterised, materials with an abundance of variety on offer. The interlayer space between positively charged inorganic layers is an ideal candidate for insertion of the negatively charged manganese aggregates. Finally, the low cost of these materials, and the increased 'processibility' which could be gained by this intercalation, would greatly increase the efficacy of such luminescent species towards eventual valorisation. The principal goals of this study were to derive a synthetic route to these hybrid materials, to characterise the resulting products, and to analyse the extent to which they retain their luminescent properties.

4.1 General Introduction

An understanding of the fundamental science behind such luminescent species as discussed herein should be well complemented by a knowledge and motivation to find real, practical application for these properties. Harnessing energy, and in particular energy of the electromagnetic spectrum, is of enormous significance in scientific research, and methods of incorporating photoactive species into commercialisable forms must be studied and optimised. There are a number of ways and means available for exploitation in the creation of these types of functional materials.

Preliminary results from the examination of the nature of the interaction between cation and anion in the $(C)^+(\text{luminescent aggregate})^-$ system led us to envision other systems to study, such as the interaction of triplet oxygen with the species $[\text{Mn}_4(\text{thiaSO}_2)_2\text{F}]^-$. In this case, the generation of singlet oxygen could prove interesting for certain oxidation reactions via a process of heterogeneous catalysis. Effective photosensitisers for the generation of $^1\text{O}_2$ are of great interest owing to their potential applications in such fields as industrial wastewater treatment, photochemical synthesis, and photodynamic therapy.¹⁻⁵ Incorporation of such a photosensitiser into a solid support material (for instance silica, or metal oxide) has shown the potential to display distinctive attributes of

heterogeneous catalysis.⁶⁻⁸ However, many of the approaches for obtaining these immobilised photosensitiser materials suffer from drawbacks including synthetic difficulties, vulnerability to leaching of the photoactive centres, or unfavourable spatial configuration in the product.

It is in this context that we envision the development of the luminescent $[\text{Mn}_4(\text{thiaSO}_2)_2\text{F}]^-$ system, with the intercalation of this photoactive centre into the interlayer space of inorganic positively charged layers of layered double hydroxide (LDH) materials.⁹ The complex $[\text{Mn}_4(\text{thiaSO}_2)_2\text{F}]^-$ with various cations is soluble in the solvents DMF and DMSO. The concept of photofunctional materials supported on host materials has gained considerable interest as a means of obtaining controllable optical properties for application in the next generation of light emitting materials and sensors.¹⁰

Benefits which intercalation between the hydroxide layers might offer include:

- The opportunity to evaluate the luminescence properties and capacity for singlet oxygen generation of our system, not only as it pertains to the inherent properties within such a matrix, but also with respect to the application of various stimuli both directly and indirectly induced by the LDH material (such as magnetic effects of appropriate metal ions e.g. cobalt or iron, inherent pressure imposed by the hydroxide layers, redox properties of the metal ions, host guest interactions ...).
- The potential for dispersion of the solid material in various media; in particular the dispersion in alcoholic or hydraulic media is useful for the elaboration and processing of hybrid materials by soft chemistry techniques such as sol-gel methods.
- One particular functionality which could be imagined for such an organised arrangement of luminescent species within regular layered material is the construction of films showing polarised photoemission. In theory it should be possible to obtain a uniform orientation of the luminescent coordination complex within the rigid LDH matrix. For our study, attention will be paid to attaining an ordered and uniform structure for the creation of LDH based thin films

showing polarised photoemission, and to the characterisation of stimulus-response behaviour, for use in sensors. Figure 118 illustrates the creation of such a potential ordered photoactive hybrid material.

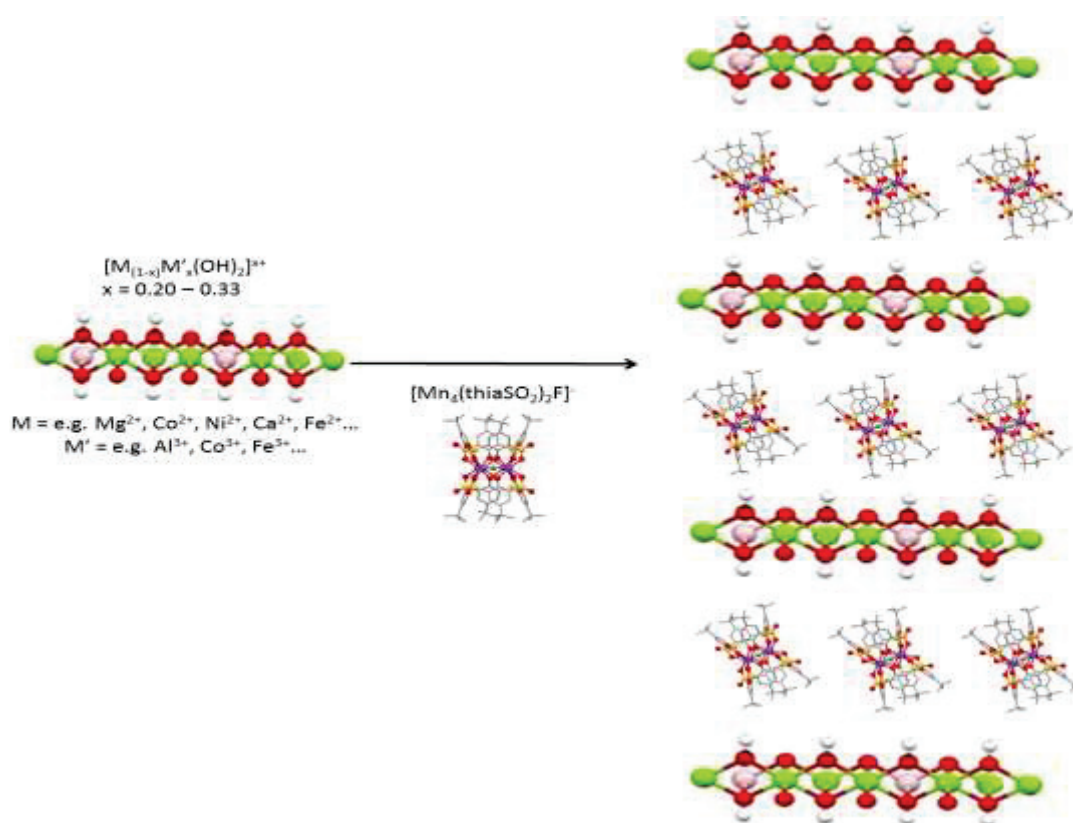


Figure 118: Hypothetical representation of the assembly of ordered hybrid materials. Ions in green represent M^{II} ions, those in pink represent M^{III} .

Other potential hybrid species containing these tetramanganese clusters, that have not been thoroughly explored in this work, include incorporation into a conducting polymer network for use in, for example, phosphorescent polymer light emitting diodes (PPLEDs), or deposition on a semiconductor film to act as a wavelength converter to optimise the absorption of incident light in solar cells (currently the system acts as a downconverter; modification of the system could be imagined to yield upconversion behaviour).^{11,12}

In any case, for effective exploitation of the luminescent species there needs to be an effective method for incorporating it into the desired device. A vast range of such methods are

available to the materials scientist, including sol-gel co-synthesis, polymerisation (as mentioned above), chemical or physical layer deposition, and more.¹³⁻¹⁶ One possibility which is of particular interest for this work is intercalation within a layered inorganic material.¹⁷ This process could offer protection from UV degradation and improve the dispersibility in various media, as well as potentially giving rise to unique material specific properties, for instance magnetic or structural.¹⁸ The specific lamellar material that we will consider in this doctoral thesis is the family of Layered Double Hydroxides (LDHs), for reasons which will be illuminated later in this section.

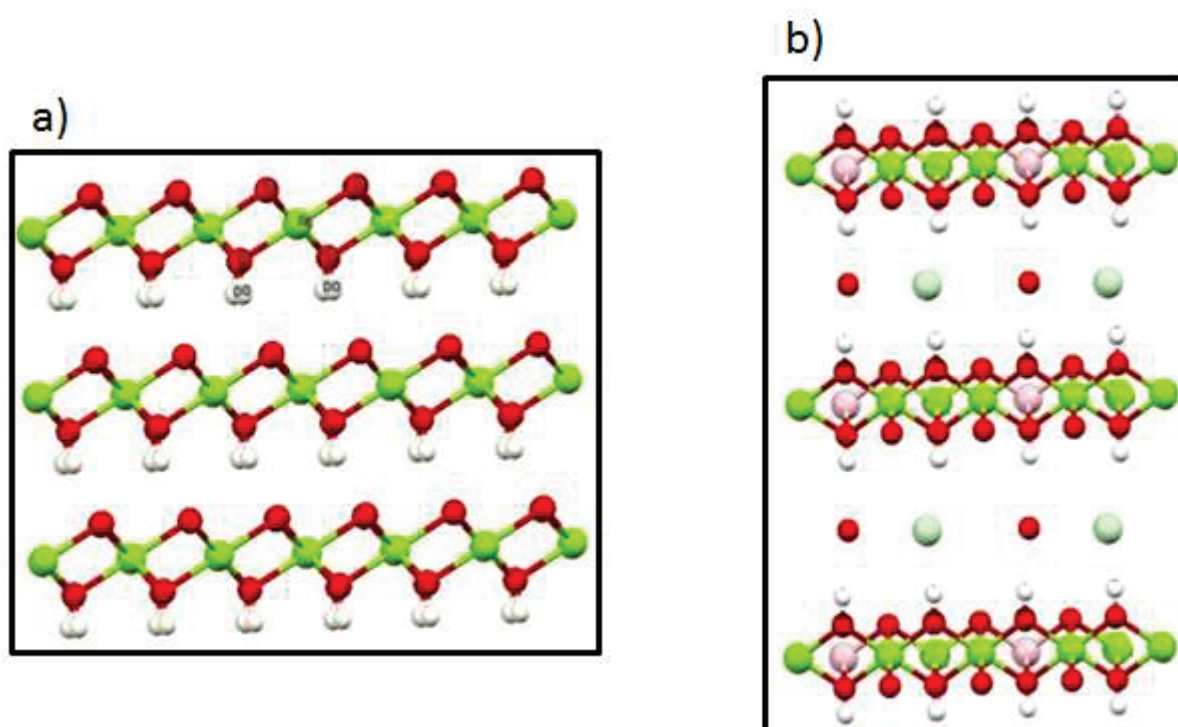
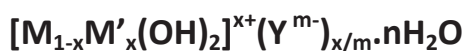


Figure 119: Representation of the structural families of a) brucite $Mg(OH)_2$ and b) hydrotalcite; in the interlayer space of hydrotalcite is a representation of highly disordered water molecules and carbonate anions.^{19, 20} Colour key: Mg = green, Al = pink, O = red, H = white, CO_3^{2-} = blue. O atoms in the interlayer space (b) represent H_2O molecules.

LDHs are a class of hydroxide materials containing two types of metal ions, a divalent and a trivalent.²¹ As is shown in figure 119, this can be considered an adaptation of the brucite type structure of divalent metal hydroxides wherein there is some proportion of trivalent metal ions in the metal hydroxide layers. This results in an overall positive formal charge on the metal hydroxide layers, thus necessitating anionic species (A) to balance the charge which can be found in the

interlayer space along with interstitial water or solvent molecules. The general formula for LDH materials is therefore:



where **M** is the divalent metal, **M'** is the trivalent metal, **x** is the degree of substitution, **Y** is an anion of charge **m**, and **n** is the number of interstitial water molecules found in the cell. LDHs are unusual in that most materials of this structural type contain negatively charged layers.⁹ The mix of metal valency can be brought about by topical oxidation of a purely divalent material, or by direct synthesis using starting materials of the appropriate valencies.

The simplest form of LDH is the naturally occurring mineral hydrotalcite, which contains magnesium and aluminium, with the formula $[Mg_{0.75}Al_{0.25}(OH)_2](CO_3)_{0.125} \cdot 0.5H_2O$ in the natural form; however a huge range of permutations of combinations of divalent metal, trivalent metal and anion (of appropriate size) can be obtained in this structural family. Furthermore LDHs may be doped with a third metal, opening more possibilities for variation.²² Carbonate is the anion with the strongest affinity for the interlayer space of hydrotalcite.²³

The efficacy and versatility of LDH materials has resulted in intense scientific interest in them, and there are many different synthetic methods to obtain materials of this structure. These methods range from the simple (for instance slow addition of base to a solution containing both metal ions, or hydrothermal amine hydrolysis releasing ammonia into the reaction mixture) to the relatively sophisticated (such as the combination of inverse microemulsions, or for LDHs with iron as the trivalent metal, steel ball milling of the reaction solution giving rise to LDH deposited within the mill).^{18, 24-26} Synthetic methods will be considered in greater detail in the next section (**§4.2.1**). In order to synthesise LDHs suitable for the preparation of candidate hybrid materials with the title luminescent species in this work, a hydrothermal route was selected. This was judged to be the most convenient; as the luminescent complex is itself synthesised by a solvothermal method the necessary

equipment was already available, and the use of amine as the base avoids the possibility of inclusion of sodium or other undesired metal ions in the final product. Carbon dioxide present in the air means that the usual product of synthesis under normal solvothermal conditions contains the carbonate anion, regardless of the anion in the original metal salts.

The practical applications of LDHs are as varied as the potential components of the material. LDHs with desirable electronic properties have been demonstrated to be viable for use in modified electrodes, supercapacitors, electrocatalysts, sensors and batteries, all by employing permutations of ions such as alkali metals, transition metals, and p-block elements in the formulation.^{17, 27-30} Doping with lanthanide ions or using intercalated organic anions with appropriate optical properties can give LDHs for use in photocatalysis, UV protection, and magnetically controlled luminescence, for example.^{27, 31, 32} Moreover, LDHs with appropriate composition have found use in magnetic, environmental and medicinal applications.³³⁻³⁵ Taking into consideration this vast scope of fields in which LDHs can be very effectively employed, they are ideal candidates for the inorganic matrix to host the luminescent manganese cluster. The anionic nature of the luminescent species allows it to act as the interlayer anion in an LDH, offering a simple route towards the creation of a hybrid material. Once the proof of concept has been achieved, this idea can be elaborated upon by envisioning variations of the LDH matrix with appropriate metal cations designed to provide optical, magnetic or catalytic properties to act in a synergistic way with the intercalated complex.

4.2 Syntheses

4.2.1 Synthetic routes to LDH starting materials

As stated in the introduction, there are many different synthetic methods towards LDHs, in part due to the incredible variation which is possible for this structural family. The following are just some of the possibilities which could be considered for this project. The simplest of these methods would be ambient pressure reaction by pH control. This may be achieved by addition of a solution of base (typically NaOH or Na₂CO₃) to a mixed solution of the appropriate metal nitrates, or by

simultaneous addition of two metal salt solutions while maintaining a constant pH (typically around 10). While this method is relatively simple, uncostly, and reliable, it requires very close control of the addition rates and the pH and often results in some sodium contamination in the final product. One interesting analogous method from this route involves creating two inverse microemulsions, one a base solution and the other a metal source solution, both suspended in organic solvent.²⁵ Combination of these emulsions followed by treatment at 75° C for 15 hours has been shown to be effective for the synthesis of luminescent Eu-doped LDH. Unfortunately one-step microemulsion synthesis of LDHs intercalated with large organic anions is not really feasible, as there are too many complications to finding a solvent system which both solubilises the separate components and forms a stable emulsion. This method offers good control of the particle size distribution of the product, which is dictated by the size of the micelles in the reaction emulsion.

In 2012, Iwasaki *et al* reported an interesting mechanochemical synthetic pathway to make LDHs.²⁴ It involves processing an acidic aqueous solution of nickel or cobalt chloride by steel ball milling. The resulting product which precipitates from the solution is an LDH of Ni²⁺ or Co²⁺ and Fe³⁺, where the iron ions originate from the steel balls. This process is unusual in a few ways; it proceeds at room temperature, with no addition of base to precipitate the product and no added 'reagent' necessary as a source of iron(III) ions. Their theory for the mechanism of LDH formation involves dissolution of iron ions from the steel balls into the reaction mixture, with the release of electrons. This would then cause hydrolysis of water, releasing hydroxide which facilitates the precipitation of the product. Evidently this method has so far only proven applicable to LDHs wherein the trivalent metal ion is iron. Another method demonstrating a noteworthy combination of chemical and physical techniques was reported by Anandan *et al* in 2014 for the synthesis of *turbostratic* (layers out of alignment) manganese – nickel hydroxide.³⁶ This synthesis involves sonification of a solution of nickel (II) nitrate, manganese(II) nitrate and urea, with a polymer stabiliser. Both of the metal ions in the product are in the +2 oxidation state, so there is no positive charge on the hydroxide layers, as in the

brucite structure, where the layers are out of alignment. Like the above mechanochemical reaction, this sonochemical process doesn't require high temperature treatment during the reaction.

Hydrothermal synthesis, the most appropriate option for this work, signifies a solvothermal reaction of aqueous solution (**§1.B3.1**). The reaction mixture consists of a salt, usually nitrate, of each metal desired and an amine compound.³⁷ The principal is that as the temperature increases, the amine is hydrolysed releasing ammonia into the solution thus raising the pH and bringing about the precipitation of the product. This method works best when the trivalent ion involved is aluminium; the amphoteric nature of the Al^{3+} ion makes it an effective centre for precipitation of the product in the fluctuating pH solution.⁹ As all the equipment is already available in the laboratory for the solvothermal synthesis of thiacalixarene complexes, this method was the one chosen for LDH inorganic matrix synthesis in this work.

Hydrotalcite was synthesised by hydrothermal reaction of magnesium nitrate hexahydrate $\text{Mg}(\text{NO}_3)_2 \cdot 6\text{H}_2\text{O}$ and aluminium nitrate nonahydrate $\text{Al}(\text{NO}_3)_3 \cdot 9\text{H}_2\text{O}$, in the presence of hexamethylenetetramine (HMT, $\text{C}_6\text{H}_{12}\text{N}_4$), maintained at a temperature of 140°C for 24 hours. The resulting precipitate was recovered by centrifugation and washed with deionised water at least three times. Powder X-ray Diffraction analysis (PXRD) was carried out and the results are shown in Figure 120 below. The lowest angle peak, at a 2θ value of 11.45° is assigned to the (003) plane (this is the first possible reflection for the space group R-3m; c.f. the general reflections conditions of R-3m N° 166), which corresponds to one interlayer distance $d_{(003)} = 7.72 \text{ \AA}$.³⁸ The corresponding (006) plane reflection is found at $2\theta = 22.90^\circ$, which gives a $d_{(006)}$ value of 3.88 \AA . This indexation corresponds perfectly to the JCPDS data form of hydrotalcite, N° 04-011-5899. The combination of carbon dioxide from the air and water is responsible for the presence of this anion. Attempts were made to directly coprecipitate the complex-intercalated product by addition of some complex **2** into the reaction mixture. However, even with presolubilisation in minimal DMF, this approach proved to be fruitless. By replacing the magnesium nitrate starting material with zinc nitrate (obtained by dissolving

metallic zinc in concentrated nitric acid) the zinc aluminium carbonate LDH was obtained. However as this product was found to be less effective in the next intercalation steps, the main focus was placed upon the magnesium-based material.

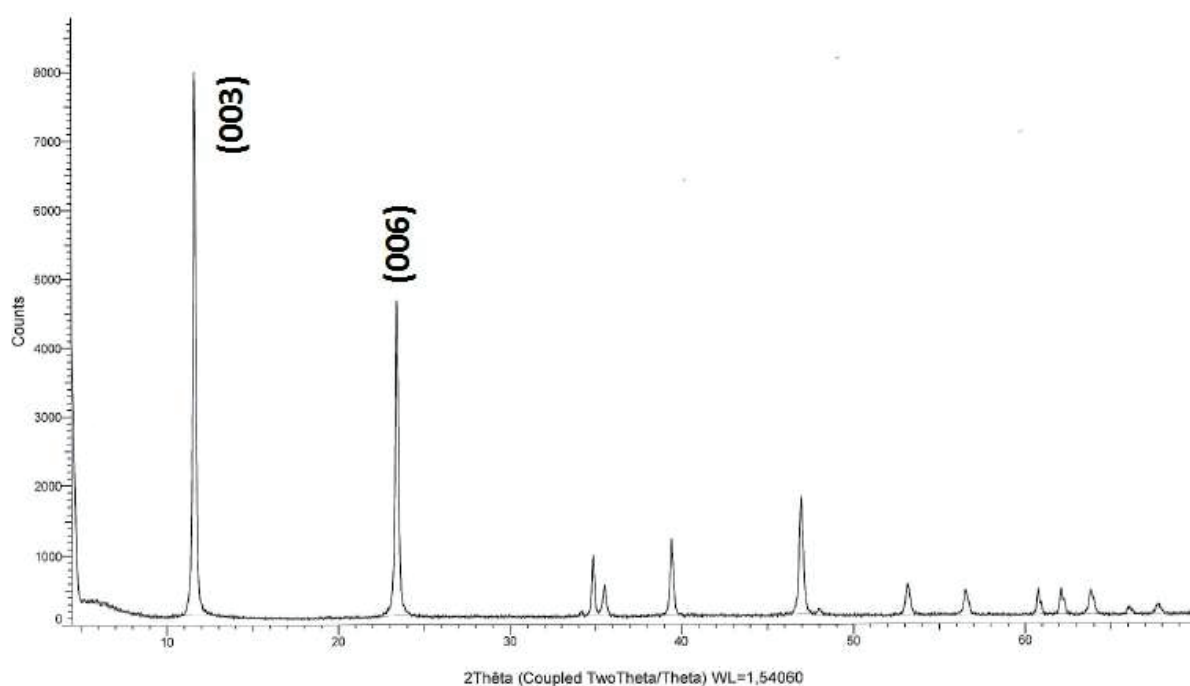


Figure 120: Powder X-Ray diffraction pattern for MgAl-CO₃ LDH obtained by hydrothermal reaction.

4.2.2 Intercalation routes to hybrid materials

The initial attempts to introduce the luminescent complex into the LDH material involved preliminary calcination of the hydroxide, forming an oxide (denoted LDO) of the spinel type.³⁹ From this LDO, the LDH can be reconstituted by simple hydration, therefore logically if this rehydration is carried out in the presence of the anionic aggregate, the layers will form around the luminescent material encapsulating them. Unfortunately this method failed in practice, due to the incompatibility of the manganese cluster with aqueous media. Therefore an alternative route was sought; direct anion exchange on the layered double hydroxide with the complex in solution.

Because of the strength of the attraction between carbonate ion and the interlayer space of the LDH, this species is substituted with a nitrate anion before the complex intercalation takes place.⁴⁰ To this end, the LDH-carbonate is suspended in an aqueous acid – salt solution of concentration 0.005 mol dm⁻³ NaNO₃ and 1 mol dm⁻³ HNO₃ under a neutral atmosphere (Ar or N₂).

After stirring for 16 hours at room temperature the product is recovered by centrifugation, and washed with degassed water. The PXRD analysis is shown below in figure 121; again the first peak corresponding to the (003) plane is the most important, corresponding to one interlayer distance. It can clearly be seen that, at a 2θ value of 9.90° giving a $d_{(003)}$ spacing of 8.93 \AA , the layers have moved apart, as the attractive force due to the nitrate anion holding the layers together is weaker than that in the carbonate. Again the (006) peak is also present, at $2\theta = 19.88^\circ$ corresponding to $d_{(006)} = 4.47 \text{ \AA}$.

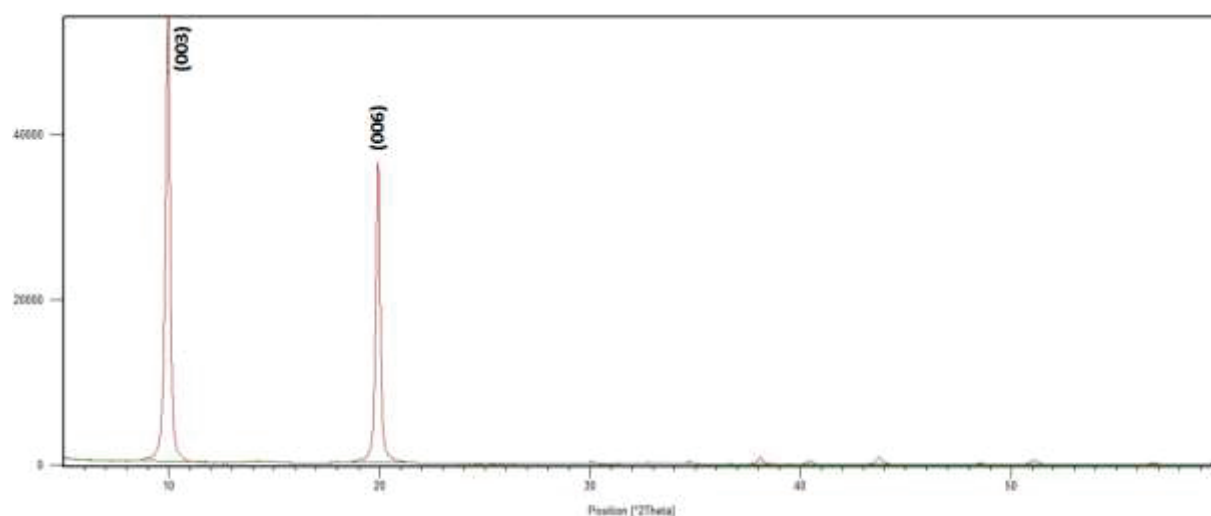


Figure 121: Powder X-Ray diffraction pattern of MgAl-NO₃ LDH obtained by anion exchange.

From the nitrate material direct anion exchange with the anionic tetramanganese cluster can be carried out. This entire process is done under Ar or N₂ atmosphere to avoid contamination with CO₂ from the surroundings, which would form carbonate anions within the LDH layers. First the LDH-nitrate is suspended in formamide. Osmotic pressure of the formamide molecules pushes apart the LDH layers causing exfoliation eventually leading to total dissociation. The resulting suspension shows a Tyndall scattering when beam of light is shone through it.⁴¹ A DMF solution of the luminescent complex **2** or **3** is filtered through PTFE (pore diameter $0.45 \mu\text{m}$) to remove any solid residue before being added to the LDH suspension, which immediately becomes cloudy as the nanosheets of hydroxides reform around the luminescent centres. The best results were obtained when this mixture was agitated with heating to 90°C for 16 hours before centrifuging to obtain the solid product. Typically not all of the complex has been intercalated, so the supernatant solution can

be removed after the centrifugation and used to repeat the intercalation process. The intercalated product, after washing with DMF and water, is an off-white micro-powder which emits red luminescence under UV or blue irradiation, identically to the neat manganese complex.

4.3 Characterisation

4.3.1 X-ray Diffraction Characterisation

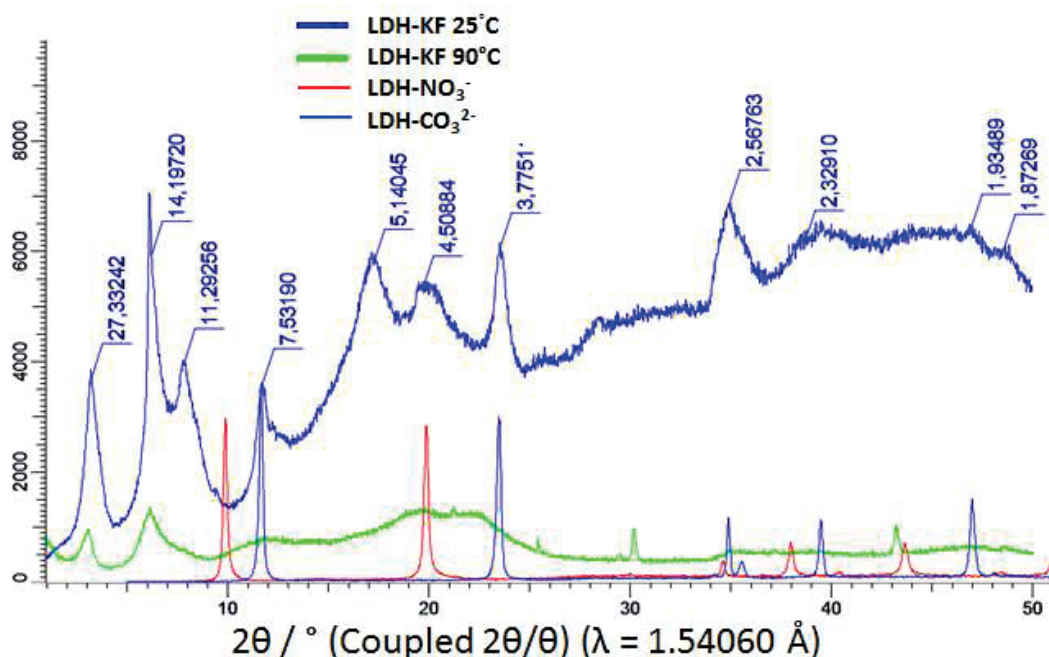


Figure 122: Overlay comparison of the X-ray diffractograms obtained with an X-ray source of $\lambda = 1.54060 \text{ \AA}$ over an angular range from 2° to 60° of the intercalated hybrid material measured after treatment at 25° C and at 90° C , with the diffractograms of the nitrate and carbonate forms for comparison.

Figure 122 shows a comparison of the X-ray diffraction data obtained for the LDH hybrid product obtained from reaction at room temperature and at 90° C , and the corresponding traces for the LDH nitrate and the LDH carbonate. It can be seen that the (dark blue) trace corresponding to the inorganic-organic hybrid material from 25° C reaction differs considerably from those of the pure inorganic nitrate and carbonate forms. It appears as though the peaks corresponding to d values of 7.53 \AA and 3.78 \AA represent the presence of the LDH carbonate in the product, highlighting the necessity of carrying out the intercalation reaction under inert atmosphere to avoid the inclusion of carbonate arising from carbon dioxide in the surroundings. However, the peaks showing a larger d

value of $d = 27.33 \text{ \AA}$, 14.20 \AA , and 11.29 \AA are taken as indicative that there has been successful intercalation into the LDH layers.

These peaks are attributed to single interlayer spaces. Making the assumption that this material forms in the same space group as the CO_3 and NO_3 starting materials (which is to say R-3m) then they must be assigned to crystal planes with Miller indices falling within this system, which includes for instance (003), (006), (101), (009), (012) *et cetera*. However, the expected numerical relationships between these d values are not appropriate to these indices; no assignment can be made following the given system that yields these values of d . For example, we would expect the largest d value to correspond to the (003) plane, which would mean that the smaller distances would be exact divisions of this; $27.33 / 2 = 13.66 \text{ \AA}$ for the (006) plane, $27.33 / 3 = 9.11 \text{ \AA}$ for the (009). This is evidently not the case. An attempt to determine the unit cell dimensions, using the Fullprof software, yielded no result. Therefore we make the hypothesis, illustrated in figure 123, that some kind of mixture of phases or domains is present in the material. These phases could arise from the positioning and orientation of the luminescent aggregate within the material, and its interaction with solvent molecules.

We will consider below the features of the most probable of these hypothesised phases and their likely probability of formation, making the assumptions that each of these three lowest angle peaks present on the diffraction diagram of the product obtained at 25° C represent a distance between hydroxide layers pertaining to a particular distinct domain of the intercalation product.

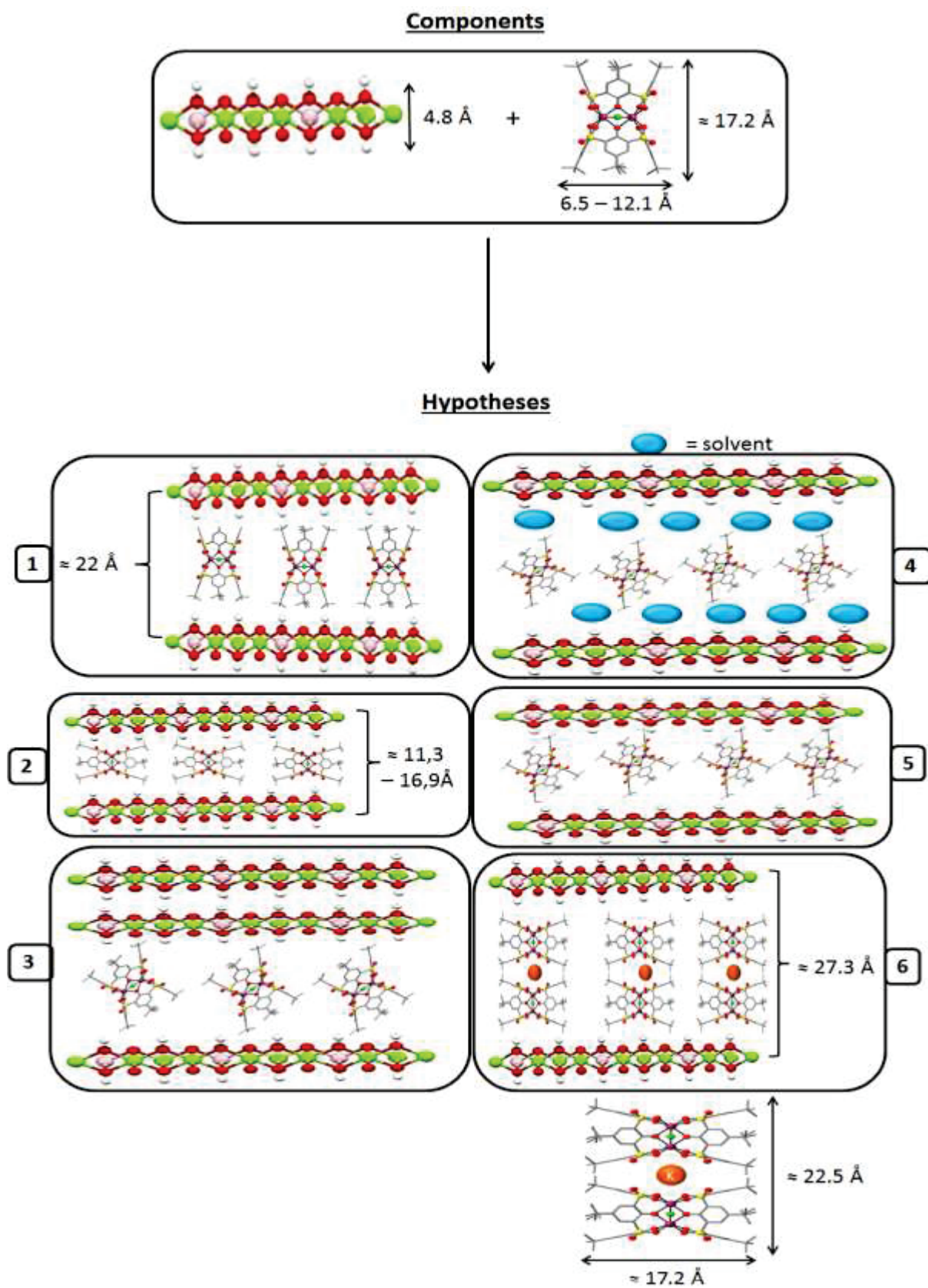


Figure 123: Schematic of hypothesised potential phases formed by the intercalation of luminescent aggregate into MgAl-LDH.

- **Hypothesis 1.** Arrangement of the complex with the long axis perpendicular to the metal hydroxide plane. The dimensions of this arrangement do not correspond to any observed peak on the diffraction diagram, and furthermore it seems to present unfavourable electrostatic interactions between the hydroxide layers and the butyl groups of the ligands. Indeed in the crystalline form of these compounds the charge balancing cation is found near the sulfonyl groups, in the plane formed by the four manganese ions, indicating that the negative charge is concentrated in this region. This hypothesis is therefore deemed unlikely.
- **Hypotheses 2 and 5.** Arrangement of the long axes parallel, or rotated, with respect to the hydroxide planes. Considering the concentration of the negative charge discussed above, a parallel arrangement of the luminescent complexes makes more logical sense as it brings this charge into closer proximity to the positive charge centres in the hydroxide material. The theoretical d values for these hypotheses cover the range between 11.3 – 16.9 Å and could likely therefore correspond to the observed peaks at 11.29 Å and 14.20 Å.
- **Hypothesis 3.** This involves the same arrangement as in hypotheses 2 and 5 as before, with the addition of an extra layer without the presence of extra complex. An extra, non-intercalated layer would result in an increase in distance of about 8 Å, which could therefore give rise to the peak of 27.33 Å. This theoretical cannot be confirmed or dismissed by XRD analysis alone, though the peak corresponding to a d value of 7.53 Å is taken to imply the presence of non-intercalated (carbonate) phases in the sample.
- **Hypothesis 4.** The intercalated layers undergo swelling induced by solvent. This hypothesis is considered highly unlikely, as the sample is subjected to extensive drying before analysis.
- **Hypothesis 6.** The luminescent clusters are intercalated in dimer form, linked by a potassium cation bonded to the sulfonyl groups as in the starting material complex **2**. The calculated interlayer distance d for this configuration was 27.3 Å, corresponding almost exactly to the lowest angle peak on the LDH-KF 25° C diagram with its d value of 27.33 Å. Hypothesis 6 is thus considered to be the most likely explanation for the origin of this peak.

In order to avoid the formation of this dimer species, intercalation experiments were made using the complex **3** as the starting material, wherein the potassium cation is fully complexed by the crown ether 18-crown-6. The results of PXRD analysis of this product are shown in figure 124.

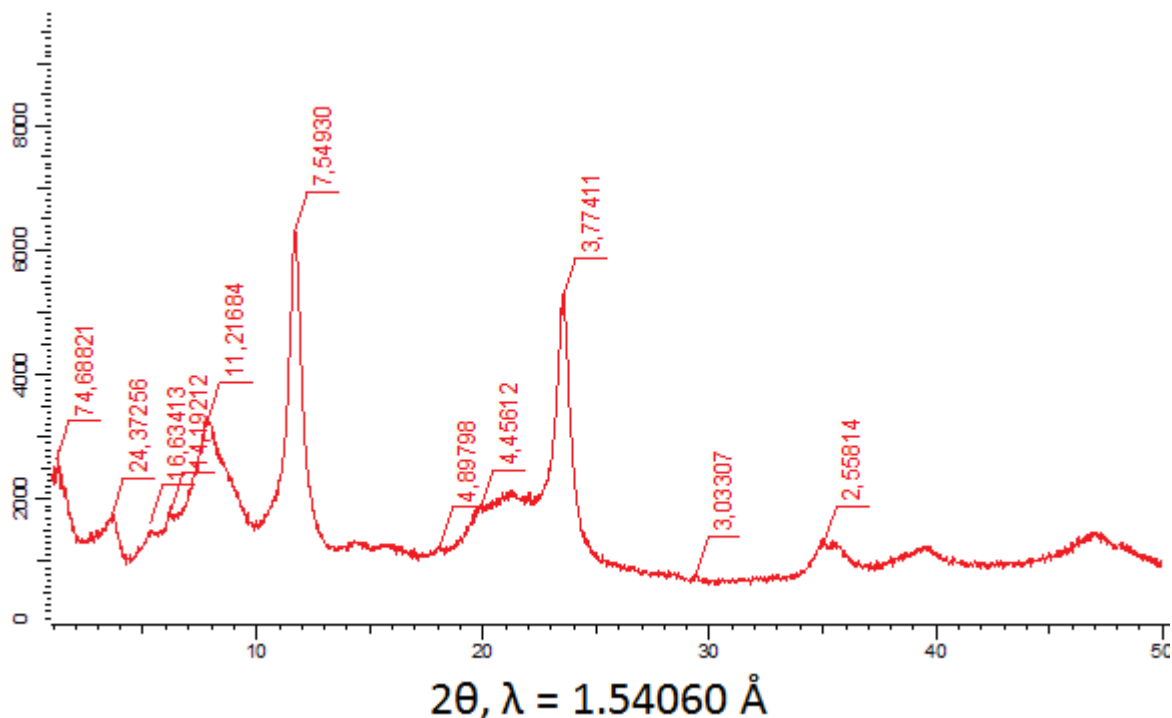


Figure 124: X-ray diffraction diagram for the intercalation product of complex **3** into MgAl layered double hydroxide over the angular range between 2° and 50°, using an X-ray source of 1.54060 Å.

It can be seen that this product is considerably contaminated with carbonated form, as indicated by the peaks corresponding to 7.55 Å and 3.77 Å. The low angle (high d) region has changed with respect to the product obtained with complex **2**. Figure 125 shows a potential explanation for the interlayer distance of 74.69 Å: a non-covalent tetramer of four anionic aggregates with three complexed potassium cations spacing between them. The peaks corresponding to distances of 11.22 Å, 14.19 Å, 16.63 Å, and 24.37 Å are presumed to arise from some combination of hypotheses 2, 5, and 6 as outlined above. Although this XRD analysis indicates that intercalation has taken place in both cases (using complex **2** or complex **3** as the intercalating agent) the results remain difficult to interpret, and seem to show the formation of oligomeric forms of the luminescent aggregate during the intercalation process. Further work to investigate this concept will include a study of the effect of concentration of tetramanganese complex in the original solution (lower

concentrations should inhibit the formation of dimers) and a conductometric titration study of the complex in DMF to investigate the ion pair formation phenomenon.

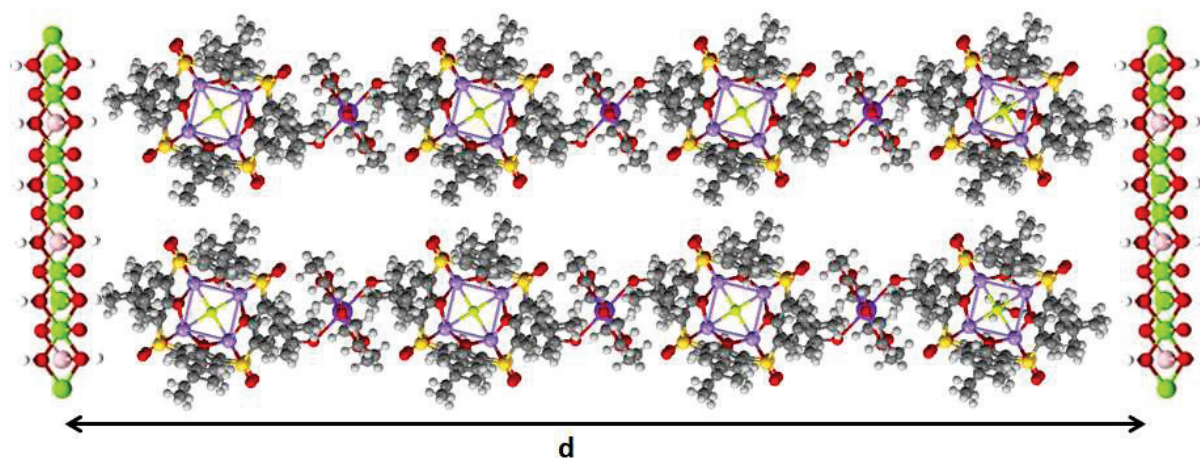


Figure 125: Representation of a hypothesised origin of the observed peak corresponding to a d value of 74.69 \AA , pertaining to four iterations of the luminescent tetramanganese aggregate with three complexes [K(18-crown-6)] between each of them.

In many cases, insertion of anions into these types of layered structures involves an aging step with heating.⁴² Therefore experiments were carried out with heating of the intercalation mixture (after initial addition at room temperature) to 90° C over a period of 16 hours. The PXRD analysis of the product of this treatment can be seen in figure 122 (green curve); figure 126 shows an enlargement of the two lowest angle peaks. The overall form of this diagram is flatter than the LDH-KF 25° C curve. The peaks representing the carbonated structure have disappeared, and the peak at 11.29 \AA is also not present. The remaining two peaks, at 28.71 \AA and 14.41 \AA , are very slightly shifted and have a larger FWHM (they are broadened) with respect to those observed in the room temperature curve. Peak broadening in X-ray diffraction arises from fundamental inconsistencies in the averaged particle (crystallite) size, resulting in an alteration of the fundamental crystallography domain. The peak at $d = 28.71 \text{ \AA}$ most likely corresponds to the structure seen in hypothesis 6, above. There are then two ways of interpreting the peak at $d = 14.41 \text{ \AA}$: being half the value of the larger d peak it could be indexed as arising from the (006) plane which would therefore mean the other peak is assigned to the (003) plane. Alternatively, it could correspond to the structure of

hypothesis 2. At this juncture it is impossible to draw any certain conclusions from these diffraction diagrams.

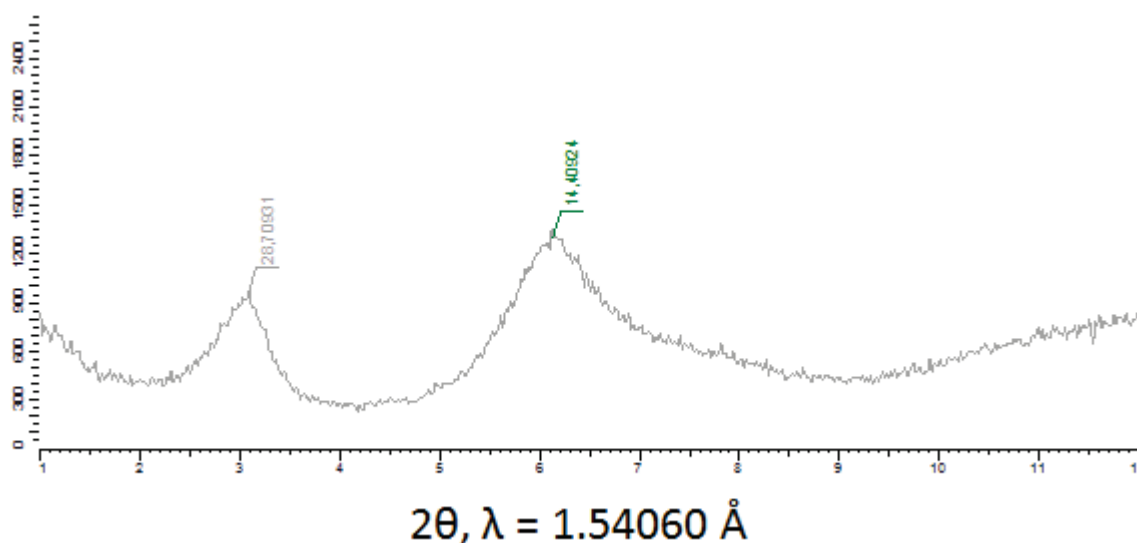


Figure 126: Magnification of the 2θ region between 1° and 12° from the PXR diagram of the intercalation product after a 90° C aging treatment.

Some diagrams obtained show peaks which by their profile cannot correspond to LDHs. Phase matching has determined that these peaks arise due to contaminants such as manganese fluoride (MnF_2) most likely formed by degradation of the manganese complex. Furthermore, the macrocycle thiaSO₂ is known to be highly coordinating towards ‘hard’ cations such as the trivalent ion Al^{3+} . It appears that under certain conditions, the ligands extricate aluminium(III) ions from the inorganic hydroxide layers, forming a tetranuclear complex as a result. This anomaly was not observed for the samples which were subjected to longer intercalation times with the elevated temperature aging step.

The reaction between thiaSO₂ and aluminium(III) nitrate nonahydrate in DMF at room temperature was studied. It yielded white rectangular block crystals, which were studied by single crystal X-ray diffraction. Figure 127 shows the structure obtained from this analysis. In it, the metal core consists of four Al^{3+} ions in an approximate square planar arrangement, linked by μ_2 -hydroxide ligands lying in this metal plane. Each metal centre shows identical pseudo-octahedral coordination geometry, with two bonds to hydroxide ligands, two bonds to phenolic oxygen from the calixarene

and one to a sulfonyl oxygen, with a molecule of DMF completing the coordination sphere. The ThiaSO₂ ligands each coordinate two aluminium ions, in a rare hexadentate pinched cone conformation fashion, such that the angle formed by O – Al – O is approximately 90° for all coordinating oxygen atoms.

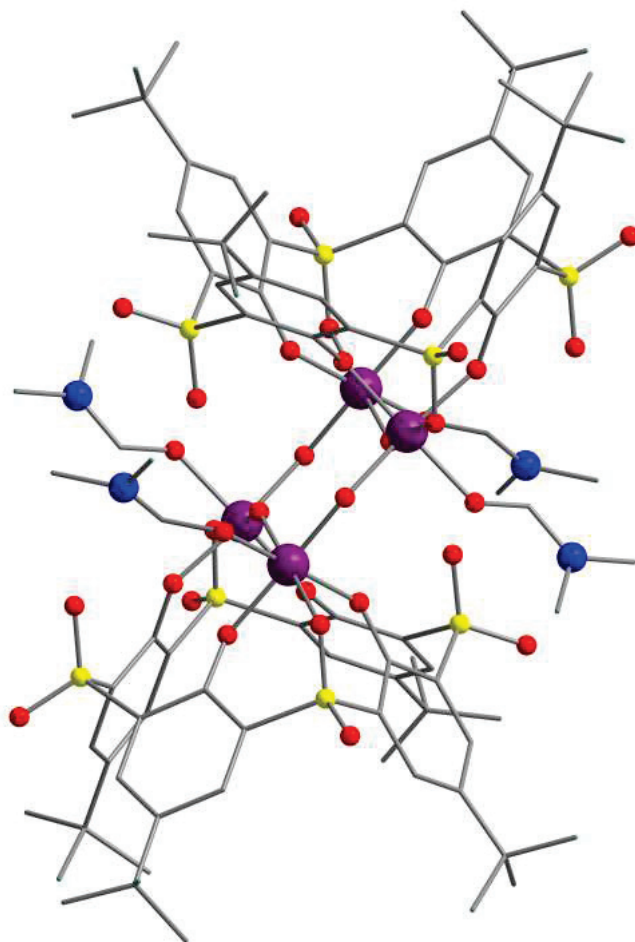


Figure 127: Structure of suspected contaminant tetraaluminium complex of thiaSO₂. Colour key: C = grey capped sticks, Al = purple, S = yellow, O = red, N = blue.

In summary, XRD analysis of these products has indicated that insertion of the luminescent material into these LDH hosts has been successful. Although the diagrams are difficult to interpret with certainty, much insight has been gained into the structural nature of these species, allowing estimations of the most probable structures to be made. The products appear to be relatively free of impurity, with the most important pollutant identified as the highly stable carbonated LDH form. Despite seeming to demonstrate a phase mixture, the PXRD experiments coupled with visual analysis of the luminescent powder material seem to indicate that the formation of ordered intercalation

structures is possible, and that the host matrix retains its form during the intercalation process. To further bolster these assertions made on the basis of diffraction analysis, the microcrystalline morphology of the products was analysed by SEM.

4.3.2: Scanning Electron Microscopy

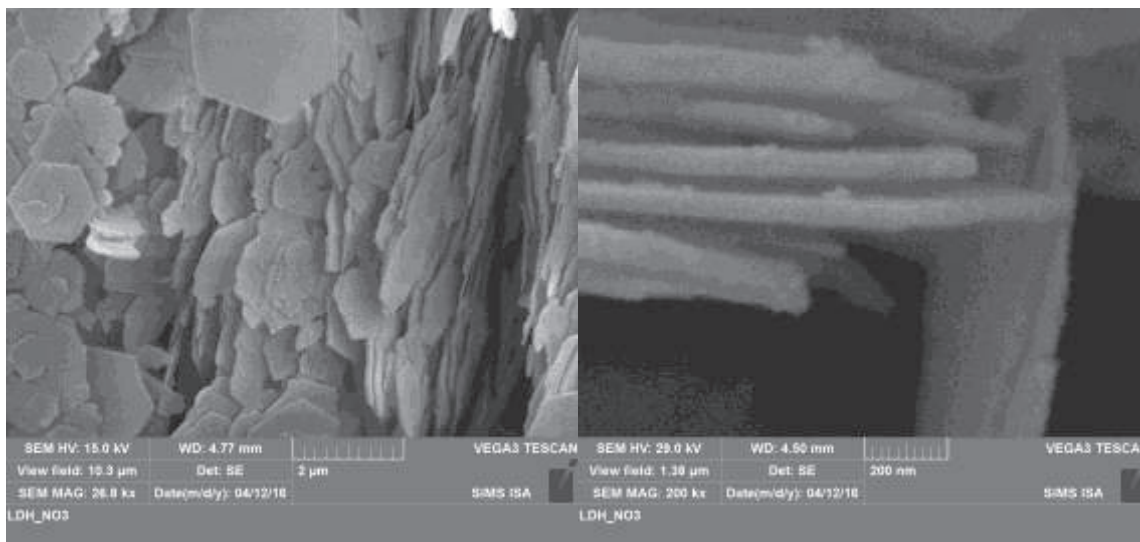


Figure 128: SEM images of MgAl-NO₃ LDH.

Hydrotalcite and its nitrate derivative both crystallise in the trigonal-rhombohedral ($R\bar{3}m$, $N^{\circ}166$) lattice system, a subset of the hexagonal crystal family.⁴¹ The symmetry arising from this crystalline class results in a hexagonal form of the particles. Figure 128 shows SEM images of the crystalline form of the nitrated material, proving that there has been no (or minimal) deformation during the acid-salt treatment. LDHs can be vulnerable to attack by strong acid. The change in the shape of the diffraction pattern of the LDH intercalated with luminescent complex may be due to a change in the space group after the intercalation process. Figure 129 shows that the hexagonal crystalline form of the intercalated LDH remains unchanged. We can therefore state that no major change of morphology has taken place during the treatment, and can hypothesise that the product therefore perhaps also does not undergo major changes in terms of the symmetry class.

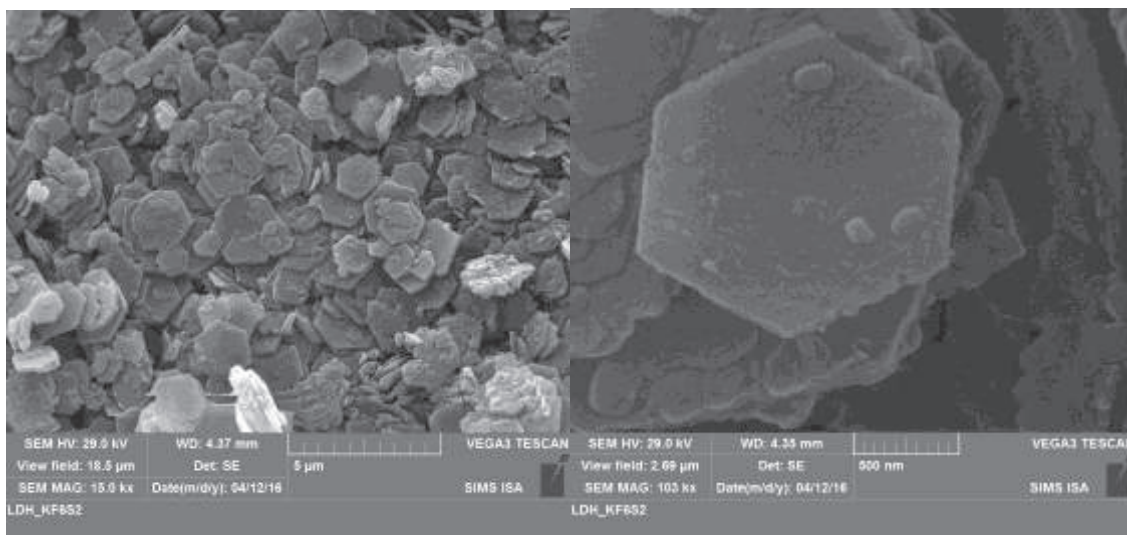


Figure 129: SEM images of intercalated LDH product $[\text{Mg}_{0.67}\text{Al}_{0.33}(\text{OH})_2][\text{Mn}_4(\text{thiaSO}_2)_2\text{F}]$.

To have retained their overall morphology despite the intercalation of bulky guest compounds into thin materials indicates an interesting structural rigidity on the part of the hydroxide layers. This property could prove useful, for example in the elaboration of materials by surface deposition. Layer by layer deposition methods such as immersion coating or spin coating require the material to be able to form a suspension during the processing, then regain their desired morphology once deposited, as these samples have been demonstrated to do.^{43, 44} Deeper structural insight was then sought by a study of the infra-red spectroscopic characteristics of these materials.

4.3.3: IR spectroscopy characterisation

The IR absorption spectrum of the LDH-nitrate material shows two important features: a broad peak at $3\,422\text{ cm}^{-1}$ corresponding to the O-H stretch and a finer peak for arising from the N=O stretch at $1\,352\text{ cm}^{-1}$. When the nitrate anion is exchanged with the luminescent complex, the O-H peak is retained, and the nitrate peak appears to have diminished or disappeared entirely. The organic ligand in the intercalated complex results in a complicated absorption pattern in the lower energy region (known as the fingerprint region), typical of the complex **2**.

The solid state IR absorption spectra for free ligand thiaSO₂, MgAl-NO₃ LDH and MgAl-[Mn₄(thiaSO₂)₂F] LDH are shown in figure 130. It can be seen on the figure that the IR spectrum of the intercalated material is essentially a combination of the two previous curves, except with the

absence of the nitrate peak at 1352 cm^{-1} as stated above. It is generally impossible to fully assign all peaks in the fingerprint region; however the general form of the trace for free thiaSO₂ and the intercalated material is similar enough to take as strong evidence that the insertion has been successful. It is possible that this same effect would be observed in the case that the luminescent complex is simply adsorbed on the surface, rather than the interior, of the LDH. However, were that the case it would have been observed in the SEM analysis previously.

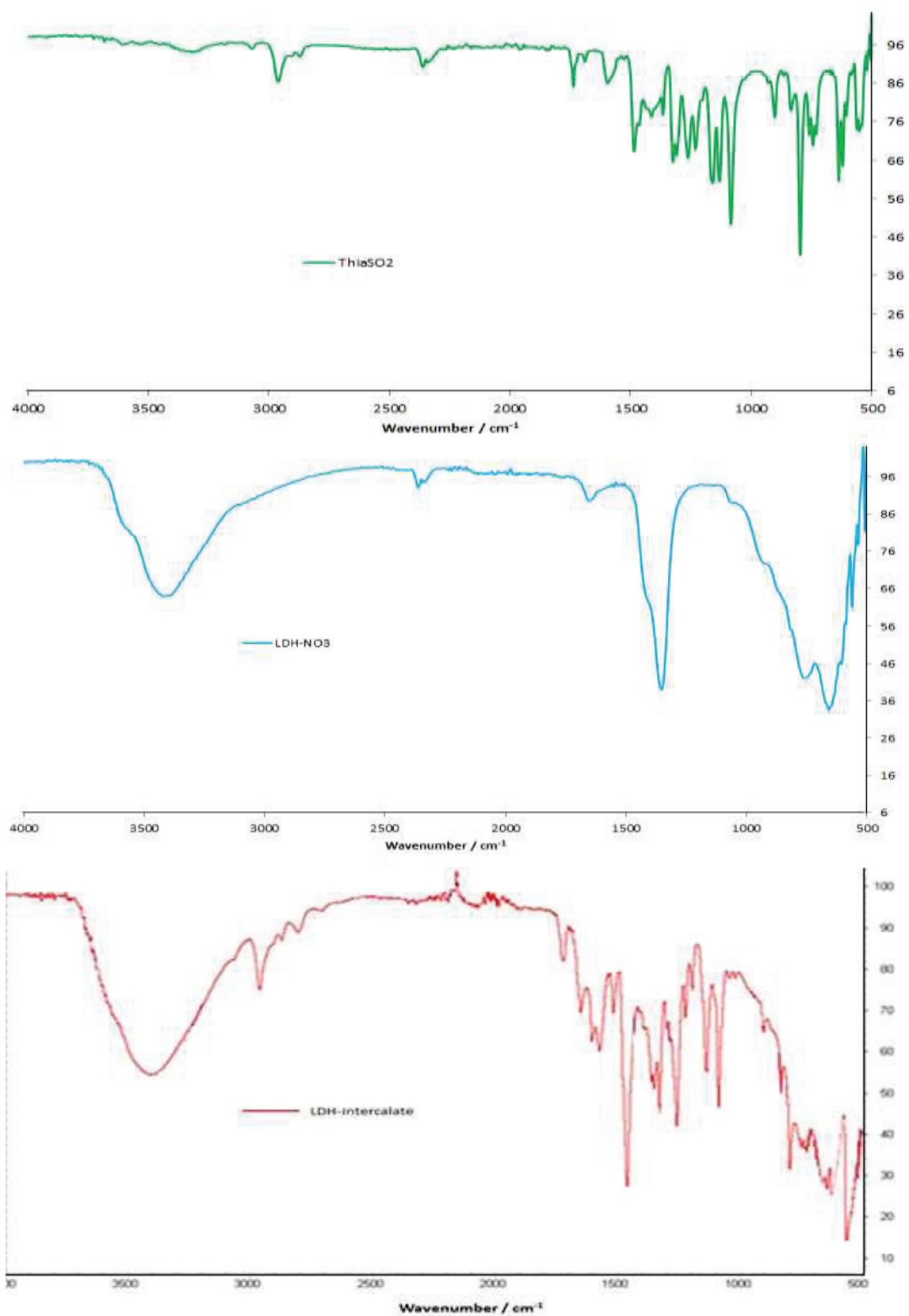


Figure 130: Comparison of infra-red absorption spectra of a) free thiaSO₂ (green spectrum), b) MgAl-NO₃ LDH (blue spectrum) and c) MgAl-[Mn₄(thiaSO₂)₂F] LDH (red spectrum).

4.3.4 Luminescence spectroscopy characterisation

Luminescence spectra, measured on the solid state material, were taken for both varying temperature (between 5 to 293 K, under a He atmosphere) and varying O₂ pressure (from 0.2 mbar to ambient pressure). Measurements were also taken of the response to pressure (ambient pressure – 7.5 GPa) in a diamond anvil cell. Figure 131 shows the evolution of the luminescence spectrum with respect to temperature.

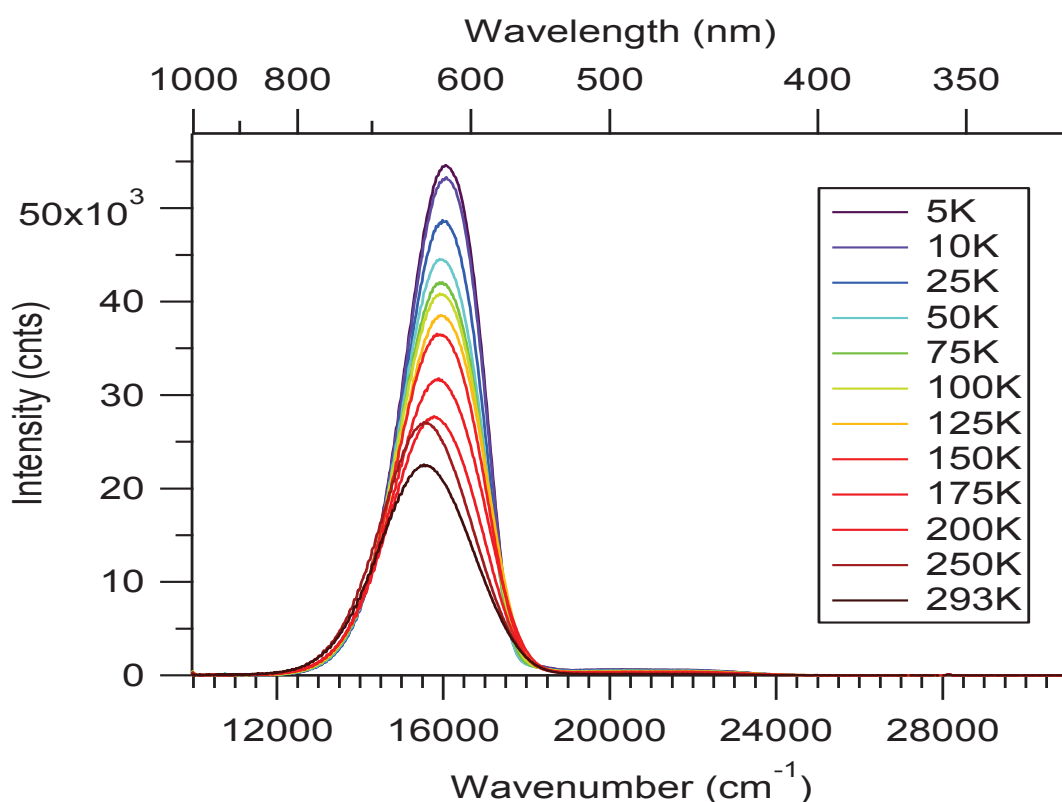


Figure 131: Plot of response of luminescence of hybrid material $[\text{Mg}_{0.67}\text{Al}_{0.33}(\text{OH})_2][\text{Mn}_4(\text{thiaSO}_2)_2\text{F}]$ to varying temperature between 5 and 293 K measured under He atmosphere with $\lambda_{\text{exc}} = 355 \text{ nm}$. A cutoff filter at 395 nm is used.

For this material the expected emission peak corresponding to the manganese-centred ${}^4\text{T}_1 - {}^6\text{A}_1$ transition. As with the un-intercalated complex, the luminescence intensity falls with increasing T, such that the intensity at 293 K is approximately 50 % of its low temperature maximum value, with the peak breadth (FWHM) increasing accordingly. There is a slight redshift of the peak maxima as the temperature increases, from about 620 nm at 5 K to 640 nm at room temperature. The luminescence lifetime actually increases from 1.6 ms at 5 K to a maximum at 80 K of about 1.8 ms before descending steadily to a value at 293 K of 1.2 ms. This is comparable to the behaviour of the free

complex, as seen in a previous chapter (§2.4.1). These data are plotted in figure 132 below. In figure 133 then the contrasting behaviour can be observed when an alternative excitation wavelength (405 nm) is used over the same range of temperature.

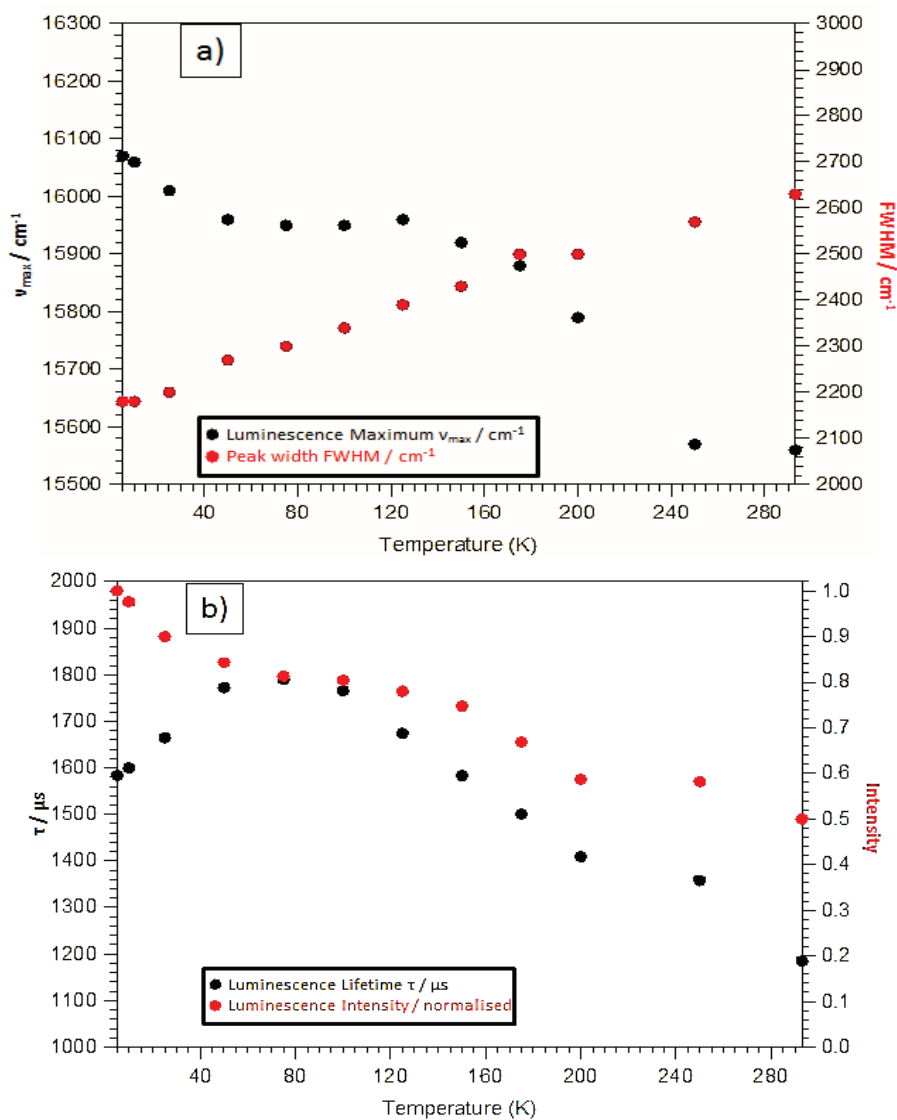


Figure 132: Plot of a) peak position (black) and width (red), and b) peak height (red) and the derived luminescence lifetime (black) for luminescence of hybrid LDH-intercalate material over the temperature range from 5 – 293 K under He atmosphere with excitation at 355 nm.

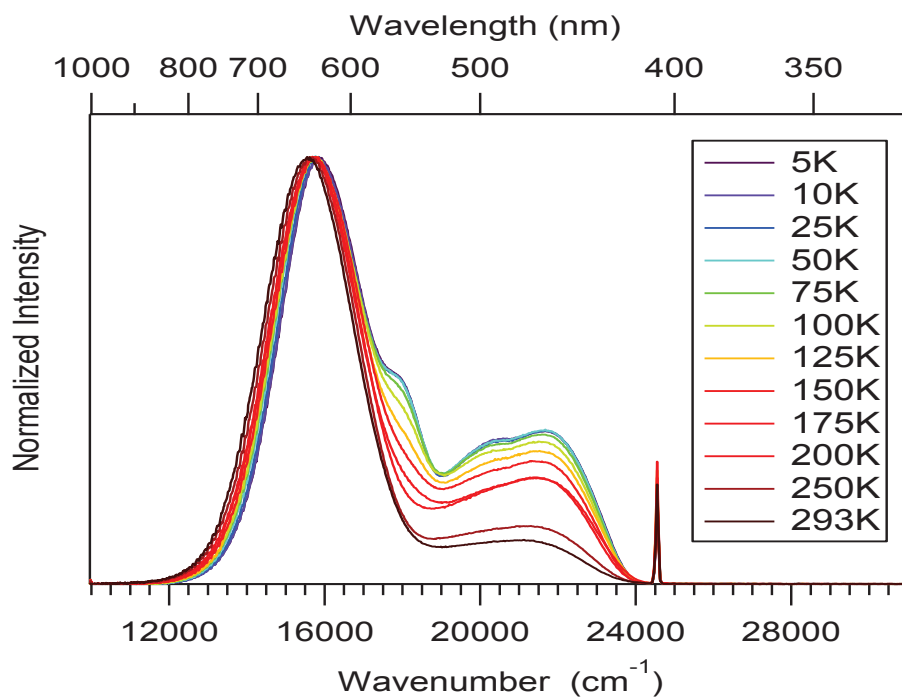


Figure 133: Plot of response of luminescence of hybrid material $[\text{Mg}_{0.67}\text{Al}_{0.33}(\text{OH})_2][\text{Mn}_4(\text{thiaSO}_2)_2\text{F}]$ to varying temperature between 5 and 293 K measured under He atmosphere with $\lambda_{\text{exc}} = 405 \text{ nm}$. A cutoff filter at 435 nm is used.

Here a noticeable change can be observed in the shape of the spectrum; a large shoulder on the expected peak is observed at low temperature, an extra broad emission peak is seen in the region approximately between 415 and 540nm, and almost no decrease in intensity of the main peak centred at 630 nm with increasing temperature is observed. However, the overall intensity of luminescence becomes less as the shoulder and higher energy peak both decrease with temperature. A fine peak is observed at the wavelength of excitation, 405 nm, for all of the temperatures measured, due to the excitation LASER used to take the measurement. There are a number of possible explanations for this unusual emission pattern, none of which can be confirmed at this time. It bears noting that the new broad emission is in accordance with the very weak absorption noticed in the excitation spectrum of the free complex (§2.4.1): it could be that some manganese ions have been liberated from the luminescent complex and have become incorporated into the positively charged hydroxide layers, wherein this emission is excited by the one wavelength examined but not by the other. Another possibility which is perhaps more likely is that this peak represents fluorescence of the thiaSO₂ ligand alone, as this region corresponds well to the known emission of this compound. However, why this effect would be observed only for the longer wavelength

excitation is not yet known. Further characterisation must be carried out to determine the source of these extra features on the luminescence diagram.

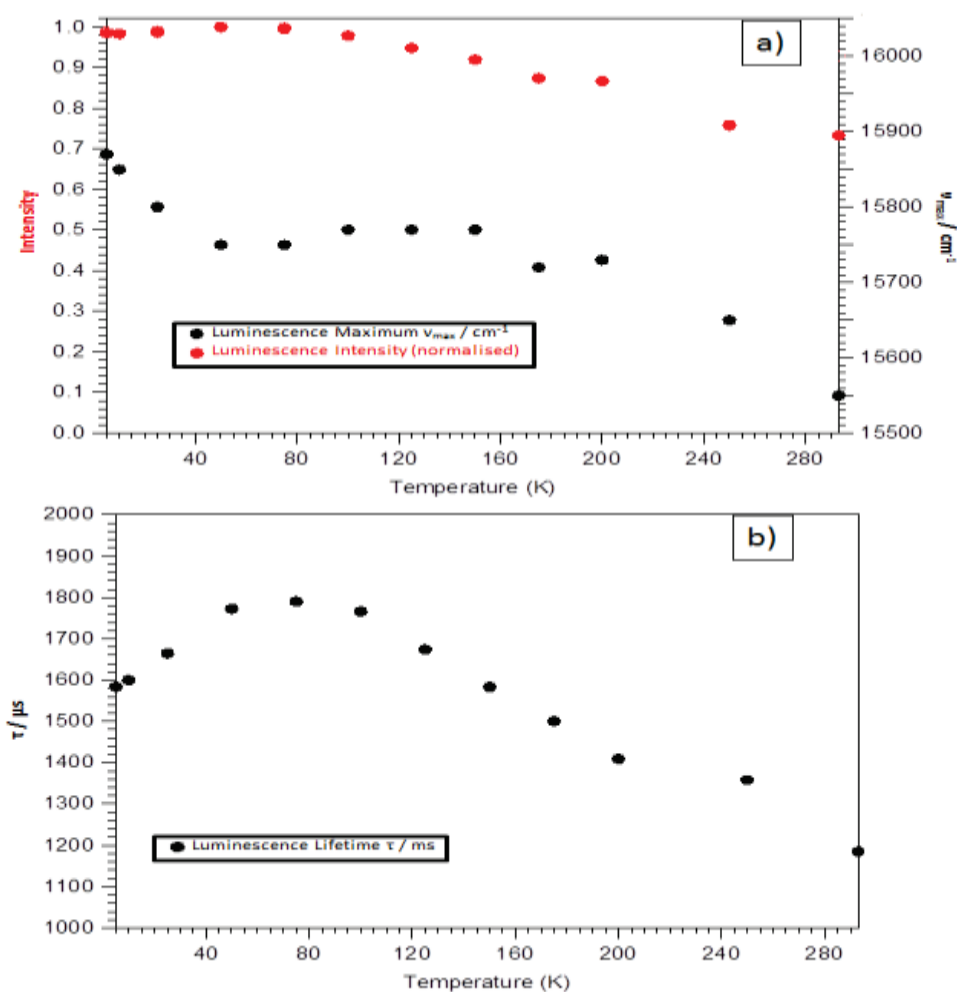


Figure 134: Plot of a) peak position (black) and intensity (red), and b) the derived luminescence lifetime for luminescence of hybrid LDH-intercalate material over the temperature range from 5 – 293 K under He atmosphere with excitation at 405 nm.

Figure 134 plots the important data from this experiment; the evolution of the position of luminescence maxima, the intensity and lifetime with temperature. Due to the complicated shoulder structure of the peak, the peak width is not shown this time. It can be seen that the luminescence intensity at room temperature is about 75 % of its original 5 K value, which is to say that the overall loss of intensity with temperature is less than when the excitation wavelength is 355 nm. There is again a redshift with increasing temperature, from about 630 nm at 5 K to 640 nm at 293 K, though between 50 K and 200 K the peak position remains quite steadily centred around 635 nm. The plot of luminescence lifetime is identical to that obtained for $\lambda_{exc} = 355$ nm.

Figure 135 illustrates the response of the luminescent material to oxygen pressure.

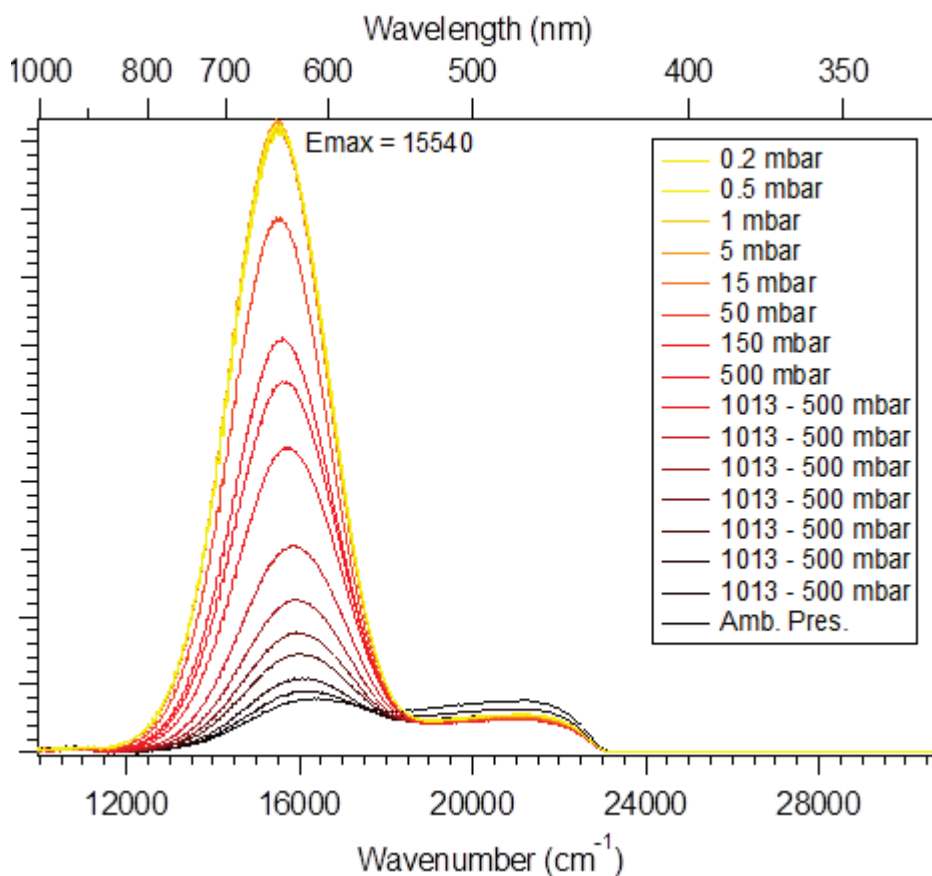


Figure 135: Evolution of solid state emission spectra of hybrid material $[Mg_{0.67}Al_{0.33}(OH)_2]-[Mn_4(thiaSO_2)_2F]$ with varying O_2 pressure between the range of 0.2 mbar and ambient pressure with excitation at 405 nm.

About 15 mbar of oxygen pressure is tolerated before the quenching effect is observing, until at ambient pressure the intensity of emission has been reduced to approximately 20 % of its value in oxygen free conditions. It is clear that molecular oxygen can penetrate the LDH structure to interact with the luminescent centres, similar to what is observed for free complex **3** in the solid state. The quenching is assumed to be due to an energy transfer process exciting molecular oxygen to its singlet state.

Finally we will consider the response of the solid state luminescence of the hybrid material with response to external pressure in a diamond anvil cell (DAC). This data is plotted in figure 136 below. The results for this experiment are not yet finalised, and presented very large uncertainties in reproduction. In fact, different results were obtained for every measurement made, with the calculated rate of change in the luminescence maxima falling between -100 and $-300 \text{ cm}^{-1} \text{ GPa}^{-1}$. It is

unclear if this is due to deformation of the material under pressure, a phase transition induced by the increased pressures, or if there is another explanation entirely.

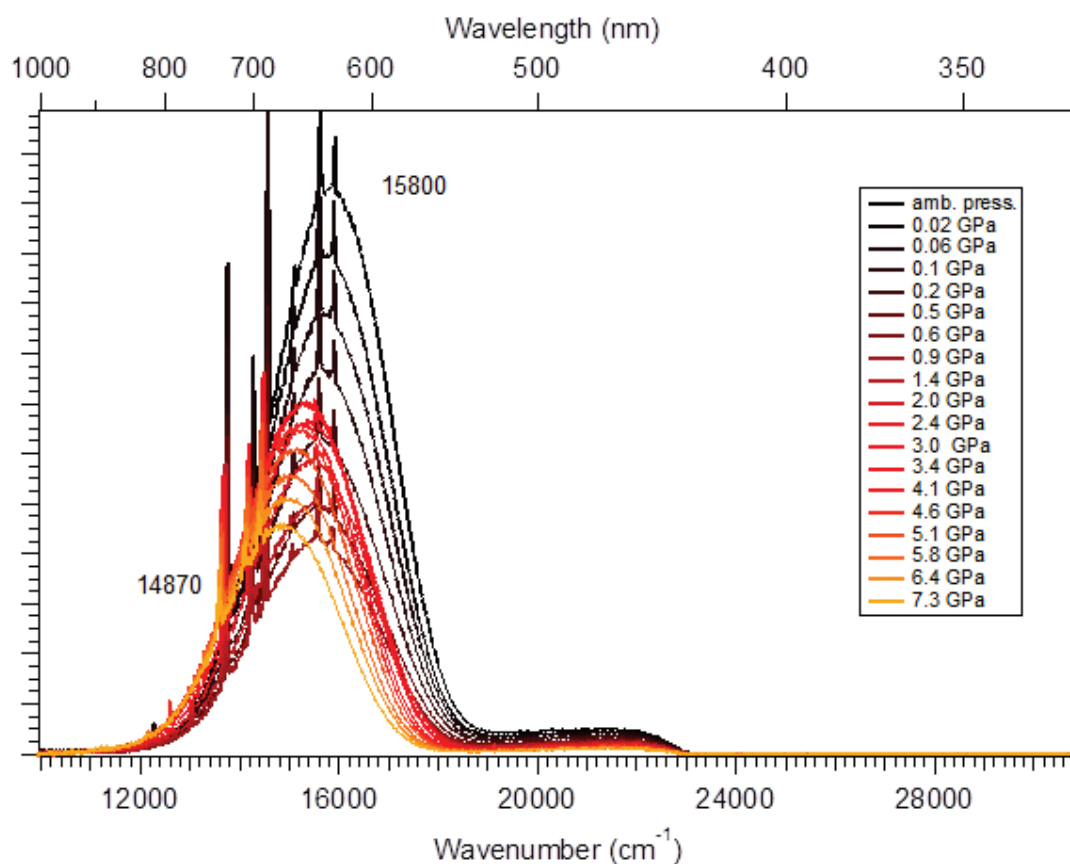


Figure 136: Evolution of solid state emission spectra of hybrid material $[\text{Mg}_{0.67}\text{Al}_{0.33}(\text{OH})_2]\text{-}[\text{Mn}_4(\text{thiaSO}_2)_2\text{F}]$ with varying pressure in a DAC under He atmosphere with excitation at 405 nm using BaFCl:Sm^{2+} as an internal standard.

The luminescence undergoes a bathochromic shift with increasing pressure as is expected for manganese centred emission. The results shown provide a value of $-130 \text{ cm}^{-1} \text{ GPa}^{-1}$ for this shift; however as stated above values between -100 and $-300 \text{ cm}^{-1} \text{ GPa}^{-1}$ were obtained on repeat analysis of the same sample.

Furthermore, the intensity of emission under ambient pressure and temperature was observed to increase significantly during the first few seconds of irradiation with 405 nm light. This is indicative of a phase transition which is induced by the LASER itself. It is hoped that the further investigation of the structural properties outlined above will help to elucidate this mysterious transition.

The luminescence properties of the hybrid material have thus been well characterised, and it can be stated with reasonable security that the intercalation procedure for synthesising these materials is successful. There remain however uncertainties pertaining to the response of the material under the action of pressure, and the aforementioned LASER-induced phase transition. Otherwise, the luminescence behaviour of the LDH-intercalate is more or less analogous to that of the pure tetramanganese cluster in solution. This fact calls to mind the solution state response to the presence of molecular oxygen, namely the creation of singlet oxygen, raising the question of whether the intercalated LDH is similarly capable of acting as a photosensitiser for the generation of singlet oxygen. With that in mind, studies were carried out on the applicability of these products to photo-oxygenation reactions of type II ($^1\text{O}_2$ mediated).

4.4 Oxygenation catalysis tests

The stated goal of this activity was to obtain a material with appropriate optical properties for some tangible, practical application. One such application would be a heterogeneous photocatalyst for oxidation reactions. It was seen in a previous chapter (**§2.4.2**) that the manganese complex in question can produce singlet oxygen ($^1\text{O}_2$) when irradiated in solution, accompanied by oxidative degradation of the manganese complex resulting in disruption of its luminescent properties, finally resulting in the superoxide ion. $^1\text{O}_2$ can act as an oxidant for molecules such as triphenylphosphine (as can superoxide) so it logically follows that illumination of the LDH-intercalate material in suspension could catalyse oxidation reactions by such production of $^1\text{O}_2$.^{45, 46} The hope is that the immobilisation of the metal complex within the inorganic layers will then offer some degree of protection against photo-oxidation and subsequent deterioration.

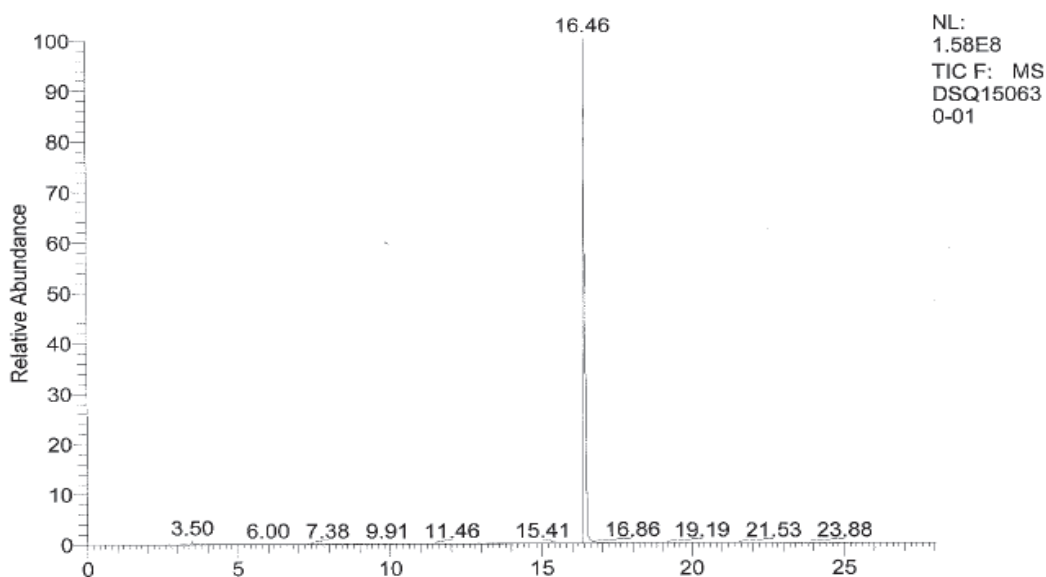
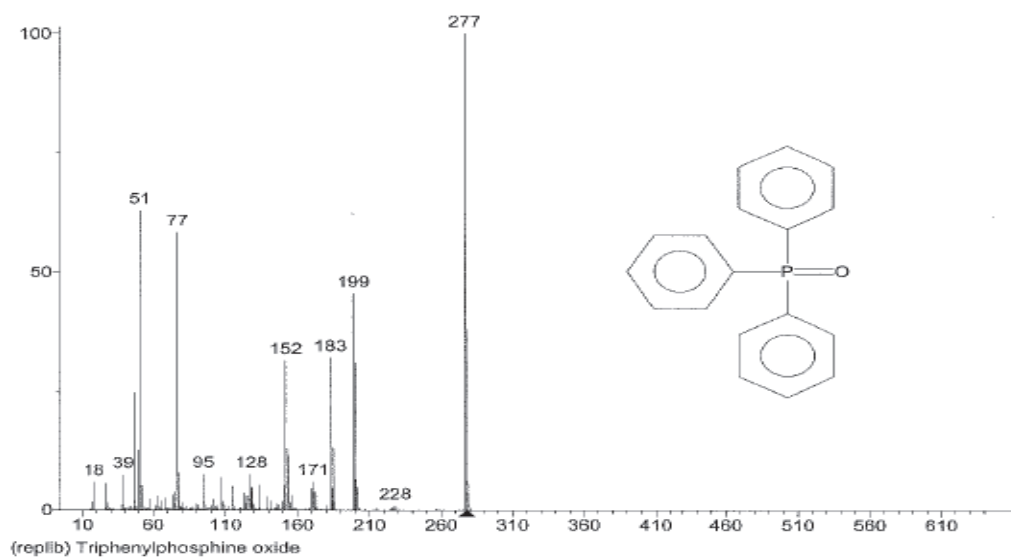


Figure 137: GC-MS analysis of supernatant solution of photocatalysed reaction of triphenylphosphine after centrifugation to remove the suspended hybrid catalyst.

To test this, a simple experimental set up was used. Triphenylphosphine is well known to readily undergo oxidation facilitated by singlet oxygen or radicals, so this molecule was chosen as a proof of concept to test if this hybrid material could catalyse the formation of its corresponding oxide. The hybrid material $[\text{Mg}_{0.67}\text{Al}_{0.33}(\text{OH})_2] \cdot [\text{Mn}_4(\text{thiaSO}_2)_2\text{F}]$ was suspended in a THF or DMF solution of triphenylphosphine, which was irradiated at 400 nm for 10 minutes with stirring. After the catalyst was recovered by centrifugation the reaction solution was analysed by GC-MS, showing only one product peak corresponding to triphenylphosphine oxide. These results are shown in figure 137. This is a promising result, demonstrating that the material is capable of photocatalysis, and the fact

that the recovered catalyst is luminescent is a good sign that the degradation has been minimised. It is worth noting that the crystalline tetramanganese cluster, whether in suspension or in the solid state, does not demonstrate any such oxidation product of triphenylphosphine when treated under the same conditions. Further experimentation should be carried out to reveal the scope of substrates to which this method is applicable, and to the capacity of the catalyst, thus recovered by centrifugation, for multiple turnovers (that is to say, the number of cycles of reaction catalysis and recovery which are possible before degradation of the catalytic efficiency is observed).

4.5 Conclusion

The combination of the title family of manganese clusters and the layered double hydroxide materials has been shown to be feasible, and offers a massive scope for the exploitation of these compounds. A reliable and reproducible method for the synthesis of a first prototype for this type of material has been presented, with a commentary upon the potential for valorisation in the long run. Although only the simplest magnesium aluminium LDH was discussed in this thesis, other LDH samples featuring variations of the metal ions involved have been successfully synthesised and intercalation results are expected shortly. It has been seen that one potential benefit to encapsulation within an appropriate inorganic LDH would be protection of the photoactive species from photodriven reactions such as oxidation.

In order to fully characterise and comprehend these systems, the future direction of study should focus on clarifying the mechanisms of insertion in order to gain a better grasp on how the arrangements of photoactive centres form within the material, and thus attempt to improve the yields of, and spatial control over, the pure product. Tests shall be carried out on the potential polarisation of the emitted light, if any is present, induced by the highly ordered arrangement of emitting materials which is possible. One method which has been envisioned to this end includes the elaboration of the material in a 'layer by layer' fashion by a series of alternating surface deposition experiments. However, for the moment the current method of suspension phase swelling of the

layers followed by reconstruction of the layers around the intended substrate provides a dependable method for generating samples for study.

References

1. Schweitzer, C.; Schmidt, R., Physical mechanisms of generation and deactivation of singlet oxygen. *Chemical Reviews* **2003**, *103* (5), 1685-1757.
2. DeRosa, M. C.; Crutchley, R. J., Photosensitized singlet oxygen and its applications. *Coordination Chemistry Reviews* **2002**, *233*, 351-371.
3. Legrini, O.; Oliveros, E.; Braun, A. M., PHOTOCHEMICAL PROCESSES FOR WATER-TREATMENT. *Chemical Reviews* **1993**, *93* (2), 671-698.
4. Castano, A. P.; Mroz, P.; Hamblin, M. R., Photodynamic therapy and anti-tumour immunity. *Nature Reviews Cancer* **2006**, *6* (7), 535-545.
5. Clennan, E. L.; Pace, A., Advances in singlet oxygen chemistry. *Tetrahedron* **2005**, *61* (28), 6665-6691.
6. Wight, A. P.; Davis, M. E., Design and preparation of organic-inorganic hybrid catalysts. *Chemical Reviews* **2002**, *102* (10), 3589-3613.
7. Mallat, T.; Baiker, A., Oxidation of alcohols with molecular oxygen on solid catalysts. *Chemical Reviews* **2004**, *104* (6), 3037-3058.
8. Maldotti, A.; Molinari, A.; Amadelli, R., Photocatalysis with organized systems for the oxofunctionalization of hydrocarbons by O₂. *Chemical Reviews* **2002**, *102* (10), 3811-3836.
9. Ma, R. Z.; Sasaki, T., Nanosheets of Oxides and Hydroxides: Ultimate 2D Charge-Bearing Functional Crystallites. *Advanced Materials* **2010**, *22* (45), 5082-5104.
10. Yan, D. P.; Lu, J.; Wei, M.; Evans, D. G.; Duan, X., Recent advances in photofunctional guest/layered double hydroxide host composite systems and their applications: experimental and theoretical perspectives. *Journal of Materials Chemistry* **2011**, *21* (35), 13128-13139.
11. Kappaun, S.; Slugovc, C.; List, E. J. W., Phosphorescent organic light-emitting devices: Working principle and iridium based emitter materials. *International Journal of Molecular Sciences* **2008**, *9* (8), 1527-1547.
12. Richards, B. S., Enhancing the performance of silicon solar cells via the application of passive luminescence conversion layers. *Solar Energy Materials and Solar Cells* **2006**, *90* (15), 2329-2337.
13. Alexandrov, S. E.; Hitchman, M. L., Chemical vapor deposition enhanced by atmospheric pressure non-thermal non-equilibrium plasmas. *Chemical Vapor Deposition* **2005**, *11* (11-12), 457-468.
14. Agrawal, A.; Cronin, J. P.; Zhang, R., REVIEW OF SOLID-STATE ELECTROCHROMIC COATINGS PRODUCED USING SOL-GEL TECHNIQUES. *Solar Energy Materials and Solar Cells* **1993**, *31* (1), 9-21.
15. Ponraj, J. S.; Attolini, G.; Bosi, M., Review on Atomic Layer Deposition and Applications of Oxide Thin Films. *Critical Reviews in Solid State and Materials Sciences* **2013**, *38* (3), 203-233.
16. Weill, A.; Dechenaux, E., THE SPIN-COATING PROCESS MECHANISM RELATED TO POLYMER-SOLUTION PROPERTIES. *Polymer Engineering and Science* **1988**, *28* (15), 945-948.
17. Itaya, K.; Chang, H. C.; Uchida, I., ANION-EXCHANGED HYDROTALCITE-LIKE-CLAY-MODIFIED ELECTRODES. *Inorganic Chemistry* **1987**, *26* (4), 624-626.
18. Li, H. J.; Zhu, G.; Yang, Z. P.; Wang, Z. L.; Liu, Z. H., Preparation and capacitance property of MnO₂-pillared Ni²⁺-Fe³⁺ layered double hydroxides nanocomposite. *Journal of Colloid and Interface Science* **2010**, *345* (2), 228-233.
19. Downs, R. T.; Hall-Wallace, M., The American mineralogist crystal structure database. *American Mineralogist* **2003**, *88* (1), 247-250.
20. Allmann, R., CRYSTAL STRUCTURE OF PYROAURITE. *Acta Crystallographica Section B-Structural Crystallography and Crystal Chemistry* **1968**, *B 24*, 972-&.
21. Allmann, R., DOUBLE LAYER STRUCTURES WITH LAYER IONS (ME(II)(1-X)ME(III)(X)(OH)₂)(X⁺) OF BRUCITE TYPE. *Chimia* **1970**, *24* (3), 99-&.
22. Gao, X. R.; Hu, M.; Lei, L. X.; O'Hare, D.; Markland, C.; Sun, Y. M.; Faulkner, S., Enhanced luminescence of europium-doped layered double hydroxides intercalated by sensitizer anions. *Chemical Communications* **2011**, *47* (7), 2104-2106.

23. Iyi, N.; Matsumoto, T.; Kaneko, Y.; Kitamura, K., Deintercalation of carbonate ions from a hydrotalcite-like compound: Enhanced decarbonation using acid-salt mixed solution. *Chemistry of Materials* **2004**, *16* (15), 2926-2932.
24. Iwasaki, T.; Yoshii, H.; Nakamura, H.; Watano, S., Simple and rapid synthesis of Ni-Fe layered double hydroxide by a new mechanochemical method. *Applied Clay Science* **2012**, *58*, 120-124.
25. Posati, T.; Bellezza, F.; Cipiciani, A.; Costantino, F.; Nocchetti, M.; Tarpani, L.; Latterini, L., Synthesis and Characterization of Luminescent Nanoclays. *Crystal Growth & Design* **2010**, *10* (7), 2847-2850.
26. Chen, Y. F.; Zhou, S. H.; Li, F.; Wei, J. C.; Dai, Y. F.; Chen, Y. W., Fluorescence of Mg-Al-Eu Ternary Layered Double Hydroxide Sensitivity to Phenylalanine. *Journal of Fluorescence* **2011**, *21* (4), 1677-1682.
27. Song, F.; Hu, X. L., Ultrathin Cobalt-Manganese Layered Double Hydroxide Is an Efficient Oxygen Evolution Catalyst. *Journal of the American Chemical Society* **2014**, *136* (47), 16481-16484.
28. Jagadale, A. D.; Guan, G. Q.; Li, X. M.; Du, X.; Ma, X. L.; Hao, X. G.; Abudula, A., Ultrathin nanoflakes of cobalt-manganese layered double hydroxide with high reversibility for asymmetric supercapacitor. *Journal of Power Sources* **2016**, *306*, 526-534.
29. Wang, Q.; O'Hare, D., Recent Advances in the Synthesis and Application of Layered Double Hydroxide (LDH) Nanosheets. *Chemical Reviews* **2012**, *112* (7), 4124-4155.
30. Vialat, P.; Leroux, F.; Taviot-Gueho, C.; Villemure, G.; Mousty, C., Insights into the electrochemistry of $(\text{Co}_x\text{Ni}_{1-x})_2\text{Al-NO}_3$ Layered Double Hydroxides. *Electrochimica Acta* **2013**, *107*, 599-610.
31. Cao, T. C.; Xu, K. L.; Chen, G. M.; Guo, C. Y., Poly(ethylene terephthalate) nanocomposites with a strong UV-shielding function using UV-absorber intercalated layered double hydroxides. *Rsc Advances* **2013**, *3* (18), 6282-6285.
32. Rueff, J. M.; Nierengarten, J. F.; Gilliot, P.; Demessence, A.; Cregut, O.; Drillon, M.; Rabu, P., Influence of magnetic ordering on the luminescence in a layered organic-inorganic OPV-Ni(II) compound. *Chemistry of Materials* **2004**, *16* (15), 2933-2937.
33. Agu, U. A.; Oliva, M. I.; Marchetti, S. G.; Heredia, A. C.; Casuscelli, S. G.; Crivello, M. E., Synthesis and characterization of a mixture of CoFe_2O_4 and MgFe_2O_4 from layered double hydroxides: Band gap energy and magnetic responses. *Journal of Magnetism and Magnetic Materials* **2014**, *369*, 249-259.
34. Ma, J. F.; Ding, J. F.; Yu, L. M.; Li, L. Y.; Kong, Y.; Komarneni, S., Synthesis of $\text{Fe}_2\text{O}_3\text{-NiO-Cr}_2\text{O}_3$ composites from NiFe-layered double hydroxide for degrading methylene blue under visible light. *Applied Clay Science* **2015**, *107*, 85-89.
35. Wang, J.; Zhou, J. D.; Li, Z. S.; Song, Y. C.; Liu, Q.; Jiang, Z. H.; Zhang, M. L., Magnetic, Luminescent Eu-Doped Mg-Al Layered Double Hydroxide and Its Intercalation for Ibuprofen. *Chemistry-a European Journal* **2010**, *16* (48), 14404-14411.
36. Anandan, S.; Chen, C. Y.; Wu, J. J., Sonochemical synthesis and characterization of turbostratic $\text{MnNi}(\text{OH})_2$ layered double hydroxide nanoparticles for supercapacitor applications. *Rsc Advances* **2014**, *4* (98), 55519-55523.
37. Okamoto, K.; Iyi, N.; Sasaki, T., Factors affecting the crystal size of the MgAl-LDH (layered double hydroxide) prepared by using ammonia-releasing reagents. *Applied Clay Science* **2007**, *37* (1-2), 23-31.
38. Hahn, T.; Paufler, P., International tables for crystallography, Vol. A. space-group symmetry D. REIDEL Publ. Co., Dordrecht, Holland/Boston, U. S. A., 1983, 854 Seiten, Preis: Dfl. 385,-, US \$ 165.00, ISBN 90-277-1445-2. *Crystal Research and Technology* **1984**, *19* (10), 1306-1306.
39. Xue, X. Y.; Gu, Q. Y.; Pan, G. H.; Liang, J.; Huang, G. L.; Sun, G. B.; Ma, S. L.; Yang, X. J., Nanocage Structure Derived from Sulfonated beta-Cyclodextrin Intercalated Layered Double Hydroxides and Selective Adsorption for Phenol Compounds. *Inorganic Chemistry* **2014**, *53* (3), 1521-1529.
40. Xu, K. L.; Chen, G. M.; Shen, J. Q., Facile synthesis of submicron-scale layered double hydroxides and their direct decarbonation. *Rsc Advances* **2014**, *4* (17), 8686-8691.

41. Huang, G. L.; Ma, S. L.; Zhao, X. H.; Yang, X. J.; Ooi, K. T., Topotactic intercalation of a bulky organic anion (thiacalix 4 arene) into LDH through an osmotic swelling/restoration reaction in formamide. *Chemical Communications* **2009**, (3), 331-333.
42. Yang, Y. M.; Zhao, X. F.; Zhu, Y.; Zhang, F. Z., Transformation Mechanism of Magnesium and Aluminum Precursor Solution into Crystallites of Layered Double Hydroxide. *Chemistry of Materials* **2012**, 24 (1), 81-87.
43. Aradi, T.; Hornok, V.; Dekany, I., Layered double hydroxides for ultrathin hybrid film preparation using layer-by-layer and spin coating methods. *Colloids and Surfaces a-Physicochemical and Engineering Aspects* **2008**, 319 (1-3), 116-121.
44. Halma, M.; Khenifi, A.; Sancelme, M.; Besse-Hoggan, P.; Bussiere, P. O.; Prevot, V.; Mousty, C., Thin bacteria/Layered Double Hydroxide films using a layer-by-layer approach. *Journal of Colloid and Interface Science* **2016**, 474, 151-158.
45. Tsuji, S.; Kondo, M.; Ishiguro, K.; Sawaki, Y., PHOSPHADIOXIRANE INTERMEDIATES IN THE REACTION OF SINGLET OXYGEN WITH PHOSPHITES AND PHOSPHINES. *Journal of Organic Chemistry* **1993**, 58 (19), 5055-5059.
46. Chemtob, A.; De Paz-Simon, H.; Dietlin, C.; Croutxe-Barghorn, C.; Salmi, H.; Allonas, X.; Chany, A. C.; Vidal, L.; Rigolet, S., A highly reactive photobase catalytic system for sol-gel polymerization. *Thin Solid Films* **2014**, 550, 177-183.

GENERAL CONCLUSION

The objective of this doctoral work was to synthesise and characterise systems containing the macrocyclic ligand *para-tert*-butylsulfonylcalix[4]arene (thiaSO₂) and manganese(II) ions, with particular attention paid to their optical properties.

Previous work in our laboratory revealed the uniquely powerful synergistic relationship between these species, manifesting as strong luminescent behaviour and a susceptibility to photo-oxidation of their polynuclear cluster compounds. The preparation of these complexes was described, and they were isolated in their crystalline form which was characterised by X-ray diffraction experiments. Preliminary investigation of their activity under illumination was made.

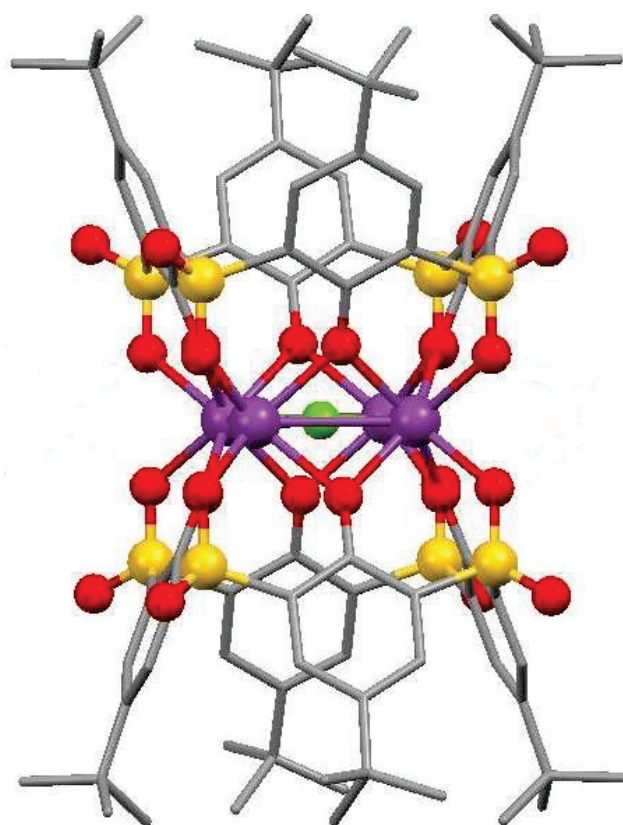


Figure I: Structure solved by single crystal X-ray diffraction analysis of the tetranuclear anionic aggregate cluster $[\text{Mn}_4(\text{thiaSO}_2)_2\text{F}]^-$ which was discovered to display intense luminescence. Colour key: C = grey, O = red, S = yellow, Mn = purple, F = green. H atoms omitted for clarity.

To continue this study, we undertook the thorough characterisation of the structural and physico-chemical aspects of this photoactivity. This involved, firstly, documenting the observed changes in the luminescence behaviour as a response to external stimuli such as pressure and

temperature conditions and the presence of oxygen, and secondly, exploring the factors governing the photo-oxidation reaction concerning these components. A preliminary study was made as to the possibility of immobilisation of these systems within an inorganic host matrix.

An initial chapter compiles the instances of the thiacalixarene family of molecules in the literature, documenting both their inherent properties as compounds and the properties of their metal complexes. The syntheses and potential functionalisations of these molecules is explored, as is the preparation of metal compounds with explanation of their various binding modes. In this way the immense versatility of these compounds in directing the functionality of metal complexes, for instance augmenting the luminescent properties of metal ions, is well shown.

The second chapter dealt with the luminescence of these complexes in the solid state, demonstrating the previously theorised antenna effect mechanism by which the energy transfer occurs. That the emitted light arises from a transition centred on Mn^{2+} ions was proven by UV-visible absorption and emission spectroscopy experiments under varying pressure and temperature conditions, which demonstrate the expected response for transition metal based emission. The effect of variations including substitution of the cation, chemical modification of the macrocycle ligand, and changing the number of manganese ions and their coordination environment, by investigating the effect of the same conditions on related compounds. Specifically, these modifications were the complexation of the cation by a crown ether, the substitution of *tert*-butyl groups with bromine ions, and the use of a dinuclear complex with a 6-coordinate octahedral manganese(II) environment. The principal observed differences are in response to oxygen presence, the position of the emission wavelength maximum, and the intensity of emission respectively. All these complexes were observed to undergo photo-oxidation, which led to the next study.

The third part then considers the photoreactivity of systems containing thiaSO₂ ligands and Mn^{2+} ions, both in complex form or in mixed solution. The reaction was shown to produce both singlet oxygen and the radical superoxide anion, meaning that these materials can be of interest as

photosensitisers for oxygen. The important roles played by the oxidant (it was demonstrated that nitrogen based anions can also act in this capacity), the (ligating) solvent, the wavelength of applied excitation, and the nature of the starting material were clarified. Then, the solution-state photoactivity of thiaSO₂ itself was assessed by both empirical and theoretical methods, which seem to imply that the photoexcitation of the molecule leads to delocalisation of an electron around all the volume of the macrocycle, with concentration to some extent around the carbon-sulfur bonds. These data were then collated to allow the postulation of electronic mechanisms for the observed transformations, involving biradical transition species wherein one of the unpaired electrons, situated on an oxygen atom, is oxidising, and the other, delocalised free electron acts as a reductant.

The fourth chapter is concerned with the transition towards more practical applications utilising all of these optical properties, by the insertion of relevant compounds into the interlayer space of LDH materials. The resulting product is therefore a hybrid material, containing distinct inorganic and organic domains in the double hydroxide layers and the intercalated manganese(II) complexes respectively. The intercalation was achieved by a process of osmotic layer swelling in formamide suspension, followed by reconstitution of the layered structure with the addition of a solution of the relevant complex of thiaSO₂. The microcrystalline product was observed to luminesce in a manner consistent with the pure Mn²⁺-complex, and the response of this complex to temperature and partial pressure of oxygen also correlated well with what was expected. The reasons for discrepancies in the response to applied pressure are as yet unknown. Perhaps most importantly, the hybrid material was observed to act as a catalyst for the photo-oxidation of triphenylphosphine, with no oxidative degradation observed in the recovered catalyst.

The versatile nature of these species means that there remains vast scope for potential further study. In particular, elaboration upon the LDH-luminescent complex material (via novel preparation techniques, alternative constitution of the hydroxide layers, etc...) and determination of the electrochemistry involved in photodriven redox reactions are of interest. The modification of the

macrocyclic with highly conjugated systems and the subsequent effect upon the luminescence of its manganese(II) complexes should be thoroughly examined. With such wide prospects of avenues of research available to us, it seems certain that these groups will be of continued interest looking to the future.

EXPERIMENTAL SECTION

6.1: Materials

Unless otherwise specified, chemical products and solvents were used as purchased with no further purification. Suppliers were Sigma Aldrich, Alfa Aesar, and Thermo-Fischer.

Apparatus and analytic procedures utilised in this thesis were as follows:

Thin Layer Chromatography Thin Layer Chromatography (TLC) analysis was carried out on Polygram – SII G/UV plates with a 0.2 mm coating layer of silica gel and a fluorescent indicator.

Silica gel column chromatography Column chromatography was carried out on silica gel of 60° pore size. The conditions of elution are specified in each case.

Infra-red spectroscopy IR spectroscopy measurements were carried out using a NICOLET 380 spectrometer, upon samples in the solid state.

Ultra-violet / visible spectroscopy UV/visible spectra were measured on a UVMC, Safas spectrometer. Quartz cuvettes with path length of 2 mm, 5 mm and 1 cm were used.

Mass spectrometry All mass spectra were carried out at the “centre commun de spectrométrie de masse” of the University of Lyon 1 (ICBMS UMR-5246) under the direction of Christian Duchamp. Standard mass spectra were carried out on a Bruker micro TOF-QII mass spectrometer with ESI source. The GC-MS analysis was performed on Focus GC (Thermo Electron Corporation, Bremen, Germany) equipped with a DB-5MS capillary column (30 m, 0,25 mm i.d, 0,25 µm film thickness), a split/splitless inlet used in the split mode (split flow 50 mL min⁻¹, split ratio 42) and a DSQ mass spectrometer as a detector (Thermo Electron corporation, Bremen, Germany). Helium is used as the carrier gas at a constant flow of 1.2 mL min⁻¹ and the injection port temperature is 220° C. For GC-MS detection an electron ionization system was used with an energy electron of 70 eV for the ionization and the mass analyser is a simple quadrupole.

Single crystal X-ray diffraction Molecular structures were solved by Mr. Erwann Jeanneau of the “Centre de Diffractometrie Henri Longchambon” of the University of Lyon 1. Measurements were made on a Gemini κ-geometry diffractometer (Agilent Technologies UK Ltd) equipped with an Atlas CDD using radiation from an Mo source ($\lambda = 0.71073 \text{ \AA}$).

Structures were solved using a direct method with SIR97 and refinement was carried out using CRYSTALS software.

Powder X-ray diffraction Powder X-ray diffraction experiments were carried out on an X'Pert Pro MPD Diffractometer (PANalytical B.V.) equipped with an X'Celerate detector using as the X-ray source Cu-K α ($\lambda = 1.5418 \text{ \AA}$). Results were processed using the X'Pert Highscore software.

NMR Nuclear Magnetic Resonance spectroscopy for both proton (^1H) and carbon (^{12}C) were carried out on a Bruker 300 MHz spectrometer, at the "centre commun de RMN (CCRMN)" of the University of Lyon 1. Unless otherwise specified measurements were made using deuterated chloroform (CDCl_3) as solvent.

EPR Electronic Paramagnetic Resonance experiments were carried out by Lhoussain Krouz of the DCM (Grenoble, France; platform dedicated to EPR spectroscopy, part of the national EPR platform, the Réseau National de RPE Interdisciplinaire (a CNRS TGE-Très Grand Instrument, FR 3443) and with C. Duboc (CNRS Director of Research) and F. Molton (engineer)), on Bruker E500-ELEXYS spectrometers with an ER 413VT temperature controller. Frequencies employed were 9.5 GHz in perpendicular mode and 9.38 GHz in parallel mode.

DFT calculations DFT calculations were made by Dr. Christophe Gourlaouen (CR) of the "Laboratoire de Chimie Quantique (LCQ)" of the "Institut de Chimie de Strasbourg", using ADF.

DFT: Functional B3LYP, Base TZP. NO relativistic effect (light elements). Inclusion of solvent across a PCM, model of dichloromethane. Eventual dispersive interaction taken into account by the Grimme approximation. All structures optimised according to the data X. Spectra calculated by TD-DFT on the optimised structures. Nature of the transitions given as the difference in electronic density between the excited state and the fundamental ground state. Convention: **loss of density in red, gain of density in green.**

Luminescence spectroscopy The following luminescence spectra were measured in the laboratory of the group of Professor Andreas Hauser at the University of Geneva.

Variable pressure luminescence spectra were measured in a Diamond Anvil Cell (DAC) with BaFCl:Sm^{2+} as an internal standard using a Fluorolog spectrometer; $\lambda_{\text{exc}} = 405 \text{ nm}$ with a cut-off filter of 435 nm, integration time = 100 ms, x binning = 2,

10 accumulations, slits = 0.05 mm.

Variable temperature and partial O₂ pressure luminescence measurements were carried out on a Fluorolog spectrometer (integration time = 0.3 s, increment = 2 nm, slits aperture = 5/3 nm) or using a CCD camera detector (integration time = 0.1 s, slits aperture = 0.05 mm, 10 accumulations, binning = 2), with either Continuous Wave (Power = 1.2 mW) or Pulsed LASER (Delay = 480 μs) excitation source, under vacuum 10⁻⁹ mbar conditions or He atmosphere; the He gas is compressed at low temperature. λ_{exc} = 300 nm, 350 nm (cut-off = 375 nm), 355 nm (cut-off = 395 nm) and 405 nm (cut-off = 435 nm). Luminescence lifetime measurements were made on a PM detector R928 (Hamamatsu) 185-900 nm and SR430 Multi-channel Scaler with YAG excitation of 355 nm. A cryostat Janis 3-300 K was used.

The solid state luminescence spectra of complexes **2** and **4** were carried out at the laboratory of the “Institut de Lumière et Matière” at the University of Lyon 1 (UMR-5306) using a CCD detector and a CW excitation source λ_{exc} = 320 nm. Collection time of 1 s with increment 2 nm was used.

¹O₂ Luminescence detection Measurements of singlet oxygen luminescence were carried out by Céline Frochot, Philippe Arnoux, and Slava Panfilov of the “Laboratoire Réactions et Génie des Procédés (UMR 7274 CNRS – UL) at ENSIC - Université de Lorraine (Nancy, France).

Fluorescence spectra were measured on a Fluorolog FL3-222 spectrofluorimeter (Horiba Jobin Yvon, Longjumeau, France) equipped with a 450 W xenon arc lamp, a thermostat compartment (25° C) a, R928 UV-visible photomultiplier (HAMAMTSU, Japan), and an InGaAs infra-red detector cooled in liquid nitrogen (DSS-16A020L Electro-Optical System Inc., Phoenixville PA, USA). The excitation beam is separated by a double grating SPEX monochromator (1 200 grooves mm⁻¹ blazed at 330 nm). Fluorescence was measured by the UV-visible detector *via* the SPEX double grating emission monochromator (1 200 grooves mm⁻¹ blazed at 500 nm). Production of singlet oxygen was measured by the infra-red detector *via* the SPEC double grating emission monochromator (600 grooves mm⁻¹ blazed at 1 μm). All spectra were measured using quartz cuvettes on 4 faces. The absorption values at the excitation wavelength for the references and the samples were adjusted to approximately 0.2.

Diodes used for reaction irradiation Illumination for photoreactions was realised using LZ4-00UA00 (LED ENGIN) lamps with emission wavelengths of 360 nm, 400 nm, and 550 nm. The operating power of these apparatus is approximately 6 W.

Autoclaves Solvothermal syntheses were carried out in 20 ml capacity steel autoclaves with a (solvothermal Teflon internal reaction vessel. Recommended usage for these vessels suggests bombs) washing with concentrated HCl, water, and acetone followed by high temperature drying after each usage.

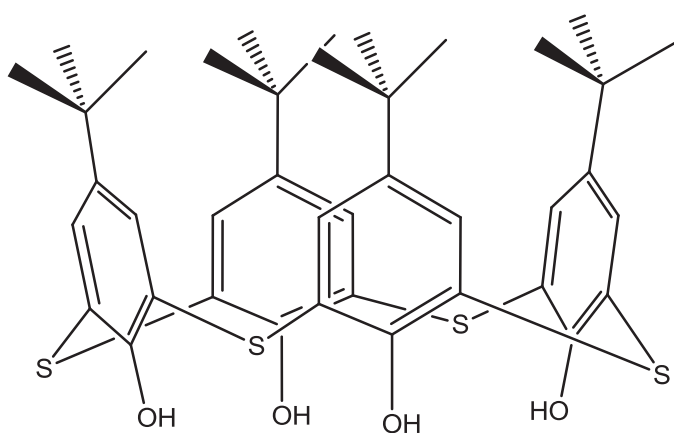
Reaction oven Heating of solvothermal reactions was carried out using a programmable Memmert oven (Model 100-800).

Centrifuges Centrifugation of products was carried out in an Eppendorf Centrifuge 5810 using Eppendorf tubes with a capacity of 50 cm³ or in a Heraeus Pico 21 (Thermo) centrifuge with tubes of 1.5 cm³ capacity.

6.2: Syntheses

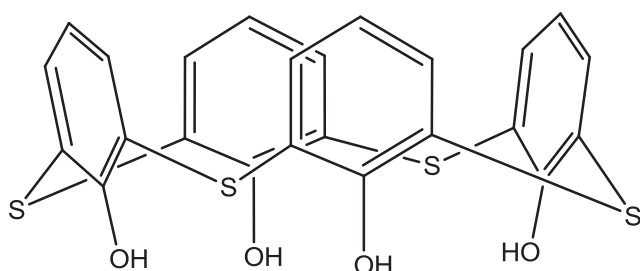
6.2.1: Ligand syntheses

thiaS (para-tert-butylthiacalix[4]arene)



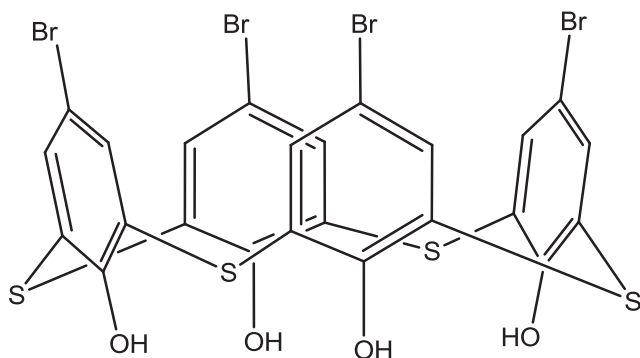
The synthesis of this molecule as well as its physico-chemical characterisations are as described in the literature.¹

H₄thiaS (thiacalix[4]arene)



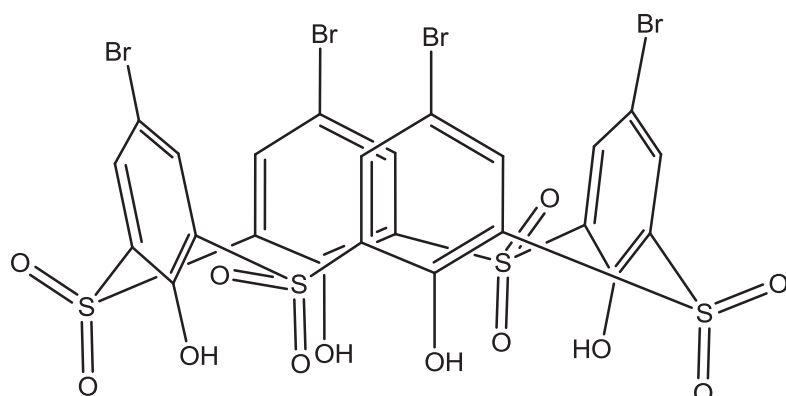
ThiaS (5.5152 g, 7.66 mmol) and phenol (0.8931 g, 9.49 mmol) were dissolved in toluene (50 cm³) under inert atmosphere. This mixture was stirred for 30 min before anhydrous AlCl₃ (5.0082 g, 37.56 mmol) was added. The mixture, while still under inert atmosphere, was then stirred under at room temperature for 16 hours. The deep red solution was decanted from the remaining thick red paste which had formed, which was then further washed and decanted with toluene (2 x 20 cm³). To the paste was then slowly added methanol, causing a white solid to precipitate. This precipitate was collected by filtration under vacuum and washed with diethyl ether before drying in the oven overnight. The product H₄thiaS was collected as a white powder (2.8239 g, 5.69 mmol = 74 % yield).
m/z (-) 495.5

Br₂thiaS (para-bromothiacalix[4]arene) and Br₄thiaSO₂ (para-bromosulfonylcalix[4]arene)



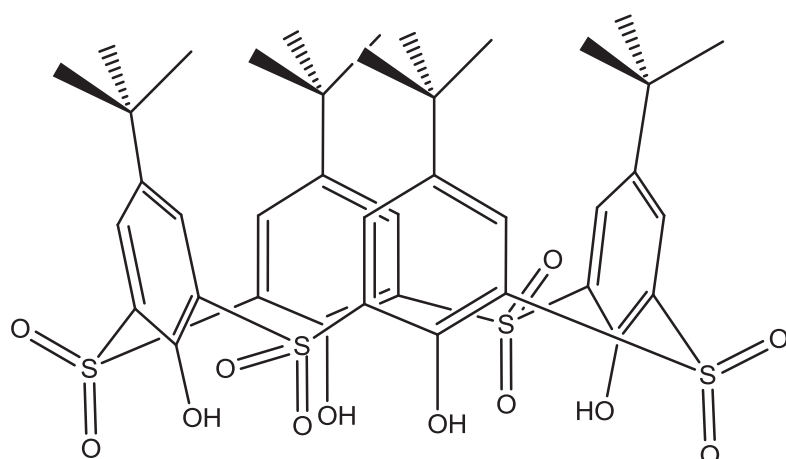
To a suspension of H₄thiaS (1.0004 g, 2.02 mmol) in acetone (50 cm³) was added a stoichiometric amount of N-bromosuccinimide (1.4302 g, 8.03 mmol). The reaction mixture was stirred at room temperature under a reflux condenser for 16 h. The pale brown solid was recovered by vacuum filtration with repeated washing steps (acetone 20 cm³, DCM 2 x 20 cm³, methanol 2 x 15

cm³) before drying overnight. The product Br₄thiaS was recovered as an off-white powder (1.0242 g, 1.26 mmol = 62 % yield). m/z (-) 810.7



To a suspension of Br₄thiaS (0.1479 g, 0.18 mmol) in chloroform (5 cm³) was added trifluoroacetic acid (5cm³, 65.30 mmol) and H₂O₂ (30 % aq. solution, 5 cm³, 48.95 mmol). This mixture was reacted at 70° C for 4 h under a reflux condenser before being allowed to cool to room temperature. The chloroform was removed under reduced pressure then the mixture was filtered under vacuum before being washed on the filter with methanol (2 x 20 cm³) and deionised water (3 x 20 cm³). After overnight drying the product Br₄thiaSO₂ was obtained as a white powder (0.1162 g, 0.12 mmol = 67 % yield). m/z (-) 938.7

thiaSO₂ (para-tert-butylsulfonylcalix[4]arene)



Two methods were used for the oxidation of thiaS:

Method 1. To a solution of thiaS (10.0270 g, 13.93 mmol) in chloroform (250 cm³) was added a solution of sodium perborate (25.6000 g, 166.39 mmol) and H₂O₂ (30 % aq. solution, 52 cm³, 509.07 mmol) in acetic acid (250 cm³). This mixture was heated to 90° C under a reflux condenser for 4 days before being allowed to cool to room temperature. The chloroform was removed under reduced pressure and to the remaining slurry was added methanol (30 cm³). The mixture was then subjected to vacuum filtration and the collected white solid was washed on the filter with methanol (3 x 35 cm³) and deionised water (3 x 35 cm³) and dried overnight. The product thiaSO₂ was recovered as a white powder (8.4615 g, 9.97 mmol = 71 % yield). m/z (-) 847.2

The synthesis and characterisation of thiaSO₂ by this method is described in the literature.²

Method 2. This method is related to that used for the oxidation of Br₄thiaS. To a solution of thiaS (1.0062 g, 1.40 mmol) in chloroform (5 cm³) is added trifluoroacetic acid (5 cm³, 65.30 mmol) and H₂O₂ (30 % aq. solution, 5 cm³, 48.95 mmol). This reaction mixture is stirred at ambient temperature under a reflux condenser for 16h before the chloroform solvent is removed under reduced pressure. The remaining slurry is subjected to vacuum filtration and washed with CH₃OH (2 x 20 cm³) and deionised H₂O (2 x 30 cm³) before overnight drying. The product is recovered as a white powder (0.7629 g, 0.90 mmol = 64 % yield). m/z (+) 849.2

6.2.2 Manganese complex syntheses

General procedure for solvothermal synthesis of Mn cluster complexes

In a Teflon lined 20 cm³ autoclave is placed MnCl₂·4H₂O, the appropriate calixarene ligand, and the cation source (potassium salt and crown ether if appropriate) in a 10:1 v:v solvent mixture of methanol and deionised water (11 cm³). In the case of complex **4** the use of pure tetraglyme (tetraethyleneglycol dimethylether) in place of this solvent mixture was in some experiments found to give larger crystal size in the product; for all solvothermal reactions reducing the volume of solvent to 5.5 cm³ was found for some experiments to have the same effect. The reaction vessel is placed in the reaction oven which is programmed with the appropriate heating profile; particularly the rate of

cooling is considered important for the crystallinity of the product. Typically this involves a plateau temperature of 150-170° C which is maintained for at least 24-72 h, with the heating and cooling steps each taking between 6-24 h. Products are recovered as crystalline solids by decanting off the supernatant solution followed by subsequent washing / decanting steps with methanol. The crystals are stored under methanol to prevent cracking.

Synthesis of complex 1 [K(HOMe)₂][Mn₄(thiaSO₂)₂(OH)]

This complex is synthesised by the solvothermal method. The quantities of reactant are thiaSO₂ (0.0500 g, 0.06 mmol), MnCl₂.4H₂O (0.0500 g, 0.25 mmol), KOH (0.0200 g, 0.36 mmol) or KSCN (0.0200 g, 0.21 mmol). The product is obtained as pale yellow block crystals (35 % yield).

The synthesis and characterisation of this complex is reported in the literature.³

Synthesis of complex 2 [K(HOMe)₂][Mn₄(thiaSO₂)₂F]

This complex is synthesised by the same method as that of complex **1** above, with KF (0.0200 g, 0.36 mmol) in place of the potassium salt. The product is obtained as pale yellow block crystals (35 % yield).

The synthesis and characterisation of this complex is reported in the literature.³

Synthesis of complex 3 [K(18-crown-6)][Mn₄(thiaSO₂)₂F]

This complex is synthesised by the solvothermal method using the same reagents in the same quantities as for complex **2** above, with the addition of 18-crown-6 (0.0200 g, 0.08 mmol). The product is obtained as pale yellow, thin platelet crystals (60 % yield). m/z (-) 1927.0

The synthesis and characterisation of this complex is reported in the literature.⁴

Synthesis of complex 4 K[Mn₄(Br₄thiaSO₂)F]

This synthesis is identical to that of complex **2** using Br₄thiaSO₂ in place of thiaSO₂. Quantities were as follows: Br₄thiaSO₂ (0.0506 g, 0.05 mmol), MnCl₂.4H₂O (0.0540 g, 0.27 mmol), KF (0.0202 g,

0.34 mmol), tetraglyme (5 cm³). After 1 h drying at 150° C the product is recovered as bright yellow microcrystals (0.0549 g, 0.026 mmol = 47 % yield).

Synthesis of complex 5 [Mn₂(thiaSO₂)(H₂O)₂(Me₂NCHO)₄]

This complex is not synthesised by a solvothermal method but rather by a conventional solution state reaction under inert atmosphere. A solution of thiaSO₂ (1 g, 1.18 mmol) and triethylamine (0.2 cm³, mmol) in CHCl₃ (50 cm³) is placed on a Schlenk apparatus under N₂ flow. To this solution is added a solution of manganese(II) nitrate in the minimum of methanol, and the reaction is heated to reflux under N₂ atmosphere for an hour then allowed to cool to room temperature. The solvent is evaporated under reduced pressure and the remaining solid is recrystallised from DMF before being washed with methanol and dried under vacuum. The product is obtained as colourless or white block crystals, and is stored under nitrogen in order to prevent oxidative degradation (yield = 80 %).

The synthesis and characterisation of this species is previously reported in the PhD thesis of Dr. Meriem Lamouchi.⁵

General procedure for the photo-oxidation of Mn²⁺/sulfonylcalixarene systems

A solution of known concentration is prepared of the appropriate manganese – sulfonylcalixarene complex or of the calixarene proligand without complexation to manganese, with addition of base as appropriate. In the latter case a solution of known concentration of manganese(II) nitrate tetrahydrate is added immediately before illumination, and the dilution effect of mixing the solutions is taken into account when manipulating the results. The reaction mixture is placed in a quartz cuvette which is stood on a mark in front of the diode and external light sources are blocked. The lamp is then switched on with ventilation for a timed period, after which the UV-visible spectrum of the solution is measured (in cases where the reaction is not followed by spectroscopy, this step is omitted and illumination is continuous). Reaction is deemed complete when the LMCT peak at approximately 540 nm has ceased to grow with additional illumination.

6.2.3: LDHs and intercalate material syntheses

Synthesis of hydrotalcite $[Mg_2Al(OH)_6](CO_3)_{0.5} \cdot \frac{3}{2} H_2O$

The LDH hydrotalcite is synthesised by a hydrothermal method (solvothetical reaction of aqueous solution). Four Teflon lined autoclaves each containing 12 cm³ of an aqueous solution of Mg(NO₃)₂·6H₂O (0.250 mol dm⁻³), Al(NO₃)₃·9H₂O (0.125 mol dm⁻³) and hexamethylenetetramine (0.325 mol dm⁻³) are heated to 150° for 36 h. The resulting suspensions are collected together and centrifuged (8 500 rpm, 30 min) followed by subsequent washing in deionised water (3 x 25 cm³) and ethanol (1 x 20 cm³) with recovery by centrifugation each time. The product is dried overnight and recovered as a white microcrystalline powder (1.1428 g, 4.05 mmol with respect to formula unit shown, yield = 67 %).

P-XRD (2θ in °): 11.45 (003), 22.90 (006).

Anion substitution of hydrotalcite $[Mg_2Al(OH)_6](NO_3) \cdot \frac{3}{2} H_2O$

On a Schlenk line under Ar flow, MgAl-CO₃ LDH (0.3120 g, 1.11 mmol) is suspended in 150 cm³ of a solution of NaNO₃ (1.0 mol dm⁻³) and HNO₃ (5 mmol dm⁻³). This mixture is agitated under Ar atmosphere at room temperature for 16 h, then is centrifuged (8 500 rpm, 30 min). The supernatant solution is decanted off and the solid material is washed with deionised water (3 x 50 cm³) and 96% ethanol (1 x 40 cm³). The product is dried under vacuum and recovered as a white microcrystalline powder (0.2650 g, 1.00 mmol = 89 % yield).

IR (ν_{mzx} in cm⁻¹): 3422.7, 2362.7, 2342.7, 1651.7, 1352.7, 763.7, 657.7.

P-XRD (2θ in °): 9.90 (003), 19.88 (006).

Intercalation of luminescent material $[Mg_2Al(OH)_6][Mn_4(thiaSO_2)_2F] \cdot xH_2O / DMF$

Variations of temperature, agitation, order of addition and so on were attempted for this reaction, to optimise the conditions. The following is a generalised synthesis derived from this optimisation.

Under inert atmosphere (Ar, N₂ or vacuum) the nitrated form of MgAl LDH (0.0298 g, 0.11 mmol) is added to formamide (25 cm³) and allowed to form a homogenous dispersion such that the suspension becomes translucent and demonstrates Tyndall light scattering. 3 cm³ of this suspension is added dropwise to a solution of complex **2** or **3** (0.1498 g, 76 μmol) in DMF (10 cm³) with stirring. This mixture is agitated under inert atmosphere overnight with heating to 90° C under a reflux condenser, then allowed to stand until it reached room temperature. The suspension is then centrifuged (13 000 rpm, 5 min) and the collected liquid and solid phases are separated.

The supernatant liquid is added to a fresh solution of luminescent complex under inert conditions and the intercalation process is repeated as above. This may be repeated several times in order to obtain the maximum yield of luminescent intercalate product. In each case the collected solid material is washed with DMF (3 x 24 cm³), degassed H₂O (3 x 24 cm³) and ethanol (1 x 24 cm³). The product is dried at 50° C under reduced pressure, and collected as a pale yellow luminescent powder (0.0346 g).

IR (ν_{\max} in cm⁻¹): 3393.7, 2960.7, 2802.7, 1722.7, 1647.7, 1605.7, 1564.7, 1517.7, 1458.7, 1362.7, 1331.7, 1258.7, 1221.7, 1194.7, 1138.7, 1086.7, 906.7, 836.7, 797.7, 749.7, 738.7, 648.7, 628.7, 562.7.

P-XRD (2 θ in °): 3.21 (003), 6.53 (006).

References

1. Kumagai, H.; Hasegawa, M.; Miyanari, S.; Sugawa, Y.; Sato, Y.; Hori, T.; Ueda, S.; Kamiyama, H.; Miyano, S., Facile synthesis of p-tert-butylthiacalix 4 arene by the reaction of p-tert-butylphenol with elemental sulfur in the presence of a base. *Tetrahedron Letters* **1997**, *38* (22), 3971-3972.
2. Morohashi, N.; Iki, N.; Sugawara, A.; Miyano, S., Selective oxidation of thiacalix 4 arenes to the sulfinyl and sulfonyl counterparts and their complexation abilities toward metal ions as studied by solvent extraction. *Tetrahedron* **2001**, *57* (26), 5557-5563.
3. Lamouchi, M.; Jeanneau, E.; Pillonnet, A.; Brioude, A.; Martini, M.; Stephan, O.; Meganem, F.; Novitchi, G.; Luneau, D.; Desroches, C., Tetranuclear manganese(II) complexes of sulfonylcalix 4 arene macrocycles: synthesis, structure, spectroscopic and magnetic properties. *Dalton Transactions* **2012**, *41* (9), 2707-2713.
4. Suffren, Y.; O'Toole, N.; Hauser, A.; Jeanneau, E.; Brioude, A.; Desroches, C., Discrete polynuclear manganese(II) complexes with thiacalixarene ligands: synthesis, structures and photophysical properties. *Dalton Transactions* **2015**, *44* (17), 7991-8000.
5. Lamouchi, M. Matériaux moléculaires à propriétés optique et magnétique à base de complexes métalliques polynucléaires : Thiacalixarènes / métaux de transition. Université Claude Bernard Lyon 1, Lyon, 2012.

ANNEXE 1: CRYSTALLOGRAPHIC DATA

[Mn₄(Br₄thiaS)₂(DMF)₂(H₂O)₂]

Crystal data

C ₅₄ H ₃₄ Br ₈ Mn ₄ N ₂ O ₁₂ S ₈	$F(000) = 1952$
$M_r = 2018.34$	$D_x = 1.533 \text{ Mg m}^{-3}$
Monoclinic, $P2_1/n$	Mo $K\alpha$ radiation, $\lambda = 0.71073 \text{ \AA}$
Hall symbol: -P 2yn	Cell parameters from 2911 reflections
$a = 11.1243 (9) \text{ \AA}$	$\theta = 3.4\text{--}24.9^\circ$
$b = 18.5376 (12) \text{ \AA}$	$\mu = 4.46 \text{ mm}^{-1}$
$c = 21.216 (2) \text{ \AA}$	$T = 150 \text{ K}$
$\beta = 92.064 (9)^\circ$	Needle, light yellow
$V = 4372.3 (4) \text{ \AA}^3$	$0.16 \times 0.04 \times 0.03 \text{ mm}$
$Z = 2$	

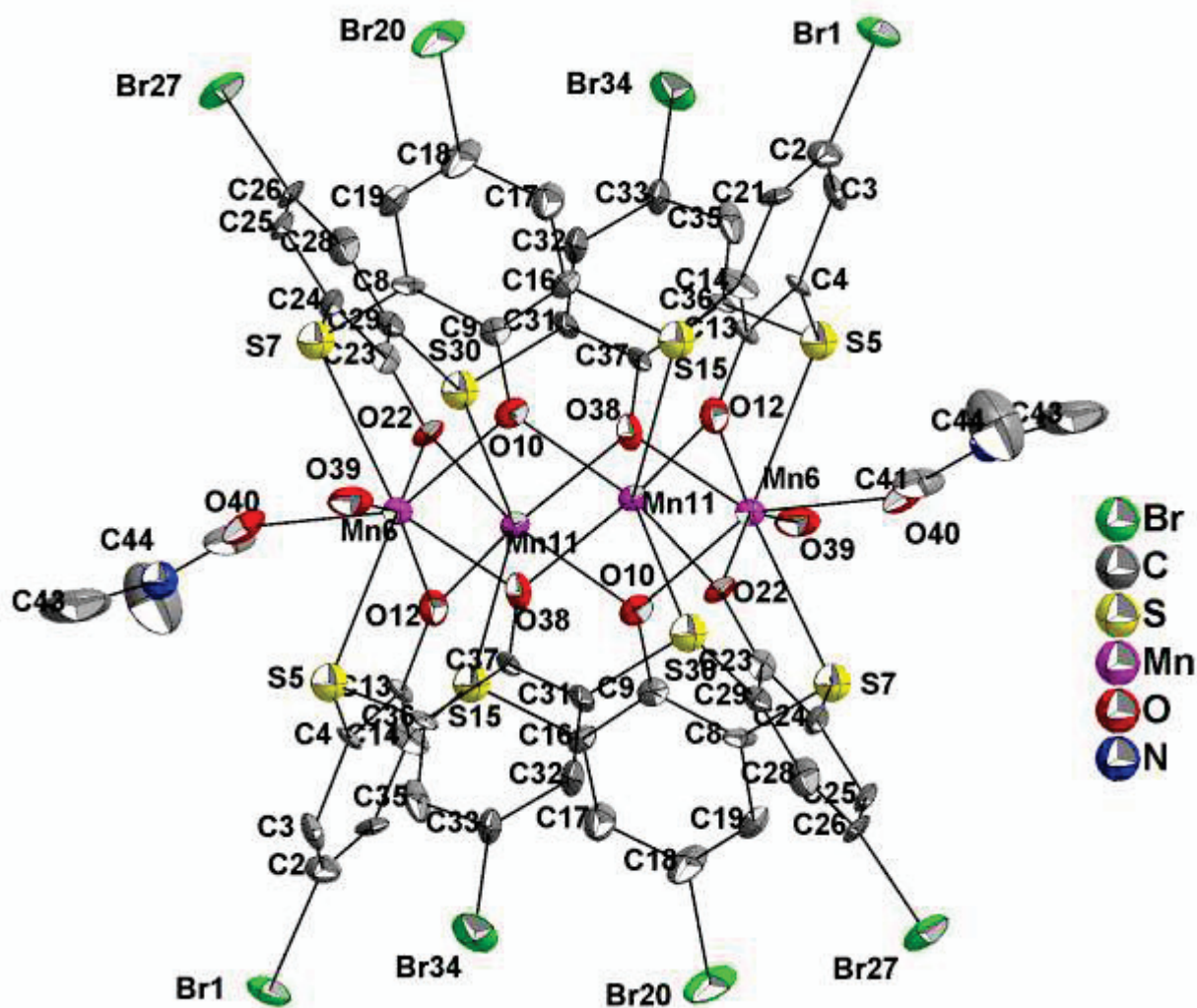
Data collection

Xcalibur, Eos, Nova diffractometer	10118 independent reflections
Radiation source: micro-focus sealed X-ray tube, Mova (Mo) X-ray Source	5696 reflections with $I > 2.0\sigma(I)$
Mirror monochromator	$R_{\text{int}} = 0.108$
Detector resolution: $15.9897 \text{ pixels mm}^{-1}$	$\theta_{\text{max}} = 29.3^\circ$, $\theta_{\text{min}} = 2.9^\circ$
ω scans	$h = -15 \rightarrow 15$
Absorption correction: gaussian <i>CrysAlis PRO</i> 1.171.38.43 (Rigaku Oxford Diffraction, 2015) Numerical absorption correction based on gaussian integration over a multifaceted crystal model Empirical absorption correction using spherical harmonics, implemented in SCALE3 ABSPACK scaling algorithm.	$k = 0 \rightarrow 23$
$T_{\text{min}} = 0.640$, $T_{\text{max}} = 0.875$	$l = 0 \rightarrow 28$
10118 measured reflections	

Refinement

Refinement on F^2	Primary atom site location: structure-invariant direct methods
Least-squares matrix: full	Hydrogen site location: difference Fourier map
$R[F^2 > 2\sigma(F^2)] = 0.114$	H-atom parameters constrained
$wR(F^2) = 0.263$	Method, part 1, Chebychev polynomial, (Watkin, 1994, Prince, 1982) [weight] = $1.0/[A_0*T_0(x) + A_1*T_1(x) \dots + A_{n-1}*T_{n-1}(x)]$ where A_i are the Chebychev coefficients listed below and $x = F/F_{\text{max}}$ Method = Robust Weighting (Prince, 1982) $W = [\text{weight}] * [1 - (\Delta F/6*\sigma F)^2]^2$ A_i are: 42.4 43.0 12.4

$S = 1.04$	$(\Delta/\sigma)_{\max} = 0.001$
10093 reflections	$\Delta\rho_{\max} = 4.94 \text{ e } \text{\AA}^{-3}$
397 parameters	$\Delta\rho_{\min} = -2.81 \text{ e } \text{\AA}^{-3}$
35 restraints	



Fractional atomic coordinates and isotropic or equivalent isotropic displacement parameters (\AA^2)

	x	y	z	$U_{\text{iso}}^*/U_{\text{eq}}$
Br1	0.27441 (18)	1.36862 (9)	0.31245 (10)	0.0341
C2	0.3110 (15)	1.2750 (8)	0.3472 (8)	0.0235
C3	0.3994 (14)	1.2376 (9)	0.3206 (8)	0.0245

C4	0.4256 (14)	1.1658 (7)	0.3442 (7)	0.0162
S5	0.5347 (3)	1.1120 (2)	0.30573 (18)	0.0173
Mn6	0.4945 (2)	0.98768 (12)	0.36977 (11)	0.0161
S7	0.4465 (3)	0.8539 (2)	0.32350 (18)	0.0175
C8	0.5574 (13)	0.8084 (8)	0.3687 (8)	0.0196
C9	0.3797 (13)	1.1553 (8)	0.5817 (7)	0.0158
O10	0.4011 (9)	1.0891 (6)	0.5665 (5)	0.0177
Mn11	0.3162 (2)	1.02182 (12)	0.49725 (11)	0.0157
O12	0.3899 (10)	1.0738 (6)	0.4179 (5)	0.0250
C13	0.3684 (14)	1.1377 (8)	0.3968 (7)	0.0168
C14	0.2770 (13)	1.1833 (8)	0.4222 (8)	0.0211
S15	0.1982 (3)	1.1512 (2)	0.48769 (18)	0.0178
C16	0.2834 (13)	1.1949 (8)	0.5497 (7)	0.0178
C17	0.2473 (16)	1.2633 (10)	0.5691 (8)	0.0303
C18	0.3187 (17)	1.2963 (10)	0.6171 (10)	0.0370
C19	0.5876 (18)	0.7393 (9)	0.3533 (8)	0.0314
H191	0.5427	0.7158	0.3216	0.0390*
Br20	0.2807 (2)	1.39410 (11)	0.63981 (14)	0.0628
H171	0.1808	1.2862	0.5502	0.0370*
C21	0.2527 (13)	1.2504 (7)	0.3979 (7)	0.0148
H211	0.1947	1.2791	0.4163	0.0200*
O22	0.3441 (9)	0.9423 (5)	0.4284 (5)	0.0172
C23	0.2808 (13)	0.8864 (8)	0.4129 (7)	0.0185
C24	0.3135 (14)	0.8373 (8)	0.3662 (7)	0.0183
C25	0.2421 (13)	0.7799 (8)	0.3474 (7)	0.0180
C26	0.1340 (14)	0.7653 (8)	0.3792 (7)	0.0185
Br27	0.03517 (18)	0.68841 (10)	0.35224 (10)	0.0371
C28	0.0986 (15)	0.8121 (9)	0.4251 (7)	0.0254
C29	0.1719 (13)	0.8695 (8)	0.4414 (7)	0.0153
S30	0.1227 (3)	0.9298 (2)	0.50281 (18)	0.0159
C31	0.1740 (13)	0.8824 (8)	0.5721 (6)	0.0147
C32	0.1107 (14)	0.8268 (8)	0.5954 (6)	0.0175
C33	0.1509 (13)	0.7919 (8)	0.6490 (7)	0.0174
Br34	0.05223 (18)	0.71905 (11)	0.68478 (10)	0.0400
C35	0.7413 (15)	1.1924 (10)	0.3218 (8)	0.0291
C36	0.6733 (13)	1.1362 (8)	0.3451 (7)	0.0177
C37	0.2915 (13)	0.9043 (8)	0.5993 (7)	0.0141
O38	0.3553 (10)	0.9546 (6)	0.5760 (5)	0.0222
H351	0.7144	1.2190	0.2867	0.0339*
H321	0.0391	0.8127	0.5752	0.0211*

H281	0.0261	0.8053	0.4449	0.0311*
H251	0.2645	0.7509	0.3138	0.0221*
O39	0.6531 (12)	0.9633 (7)	0.2991 (6)	0.0380
H392	0.7130	0.9308	0.3201	0.1010*
H391	0.6927	1.0093	0.2877	0.1010*
H31	0.4422	1.2574	0.2876	0.0300*
O40	0.3335 (9)	1.0027 (6)	0.2912 (6)	0.0277
C41	0.2282 (15)	1.0207 (9)	0.3039 (11)	0.0358
N42	0.1526 (13)	1.0531 (8)	0.2677 (10)	0.0401
C43	0.175 (3)	1.0652 (13)	0.1997 (15)	0.0902
H432	0.1066	1.0483	0.1751	0.1220*
H431	0.1863	1.1157	0.1919	0.1220*
H433	0.2453	1.0391	0.1886	0.1219*
C44	0.044 (2)	1.0759 (18)	0.2871 (14)	0.0821
H442	0.0279	1.1229	0.2702	0.1220*
H443	0.0452	1.0778	0.3324	0.1220*
H441	-0.0171	1.0430	0.2722	0.1220*
H411	0.2026	1.0097	0.3441	0.0420*

Atomic displacement parameters (\AA^2)

	U^{11}	U^{22}	U^{33}	U^{12}	U^{13}	U^{23}
Br1	0.0443 (11)	0.0184 (8)	0.0399 (11)	0.0070 (8)	0.0048 (9)	0.0097 (8)
C2	0.028 (9)	0.017 (7)	0.026 (9)	0.004 (7)	0.005 (7)	0.000 (6)
C3	0.019 (8)	0.036 (10)	0.018 (8)	-0.009 (7)	-0.008 (6)	0.015 (7)
C4	0.026 (6)	0.011 (5)	0.012 (5)	0.005 (5)	0.000 (5)	0.007 (4)
S5	0.0172 (18)	0.0189 (18)	0.0160 (18)	0.0024 (15)	0.0025 (14)	0.0004 (15)
Mn6	0.0133 (11)	0.0154 (11)	0.0198 (12)	0.0005 (9)	0.0018 (9)	0.0005 (9)
S7	0.0183 (18)	0.0174 (18)	0.0169 (18)	0.0043 (15)	0.0026 (14)	-0.0031 (15)
C8	0.012 (7)	0.009 (7)	0.037 (9)	-0.002 (6)	-0.008 (6)	0.004 (6)
C9	0.013 (5)	0.017 (5)	0.018 (6)	0.001 (5)	0.006 (5)	-0.002 (5)
O10	0.014 (5)	0.020 (5)	0.020 (6)	-0.001 (4)	0.008 (4)	-0.005 (4)
Mn11	0.0144 (11)	0.0156 (11)	0.0174 (12)	-0.0008 (9)	0.0025 (9)	-0.0011 (9)
O12	0.026 (6)	0.029 (6)	0.021 (6)	0.005 (5)	-0.003 (5)	-0.001 (5)
C13	0.022 (6)	0.013 (5)	0.014 (6)	0.004 (5)	-0.004 (5)	0.006 (4)
C14	0.016 (7)	0.019 (7)	0.029 (9)	0.014 (6)	0.010 (6)	0.007 (7)
S15	0.0144 (17)	0.0209 (18)	0.0182 (19)	-0.0005 (15)	0.0016 (14)	-0.0013 (15)
C16	0.015 (6)	0.018 (5)	0.020 (6)	-0.004 (5)	0.001 (5)	-0.004 (5)
C17	0.031 (10)	0.030 (9)	0.029 (10)	0.008 (8)	-0.007 (8)	-0.007 (8)
C18	0.036 (10)	0.027 (10)	0.047 (12)	0.016 (8)	-0.011 (9)	-0.022 (9)
C19	0.050 (12)	0.021 (9)	0.022 (9)	-0.001 (8)	-0.006 (8)	-0.011 (7)

Br20	0.0687 (16)	0.0210 (10)	0.096 (2)	0.0236 (10)	-0.0392 (15)	-0.0260 (11)
C21	0.011 (7)	0.009 (6)	0.024 (8)	-0.008 (5)	0.005 (6)	-0.001 (6)
O22	0.011 (5)	0.017 (5)	0.024 (6)	-0.011 (4)	0.001 (4)	-0.004 (4)
C23	0.012 (7)	0.019 (7)	0.024 (8)	0.011 (6)	-0.006 (6)	-0.003 (6)
C24	0.021 (6)	0.020 (6)	0.014 (6)	-0.006 (5)	-0.001 (5)	-0.004 (5)
C25	0.019 (6)	0.019 (6)	0.016 (6)	-0.007 (5)	-0.004 (5)	-0.007 (5)
C26	0.026 (8)	0.020 (7)	0.010 (7)	-0.020 (6)	0.006 (6)	-0.005 (6)
Br27	0.0392 (11)	0.0289 (10)	0.0436 (12)	-0.0173 (8)	0.0071 (9)	-0.0149 (8)
C28	0.029 (9)	0.031 (9)	0.017 (8)	0.011 (7)	0.006 (7)	-0.005 (7)
C29	0.015 (7)	0.016 (7)	0.015 (7)	0.001 (6)	0.005 (6)	0.003 (6)
S30	0.0149 (17)	0.0169 (17)	0.0159 (18)	0.0031 (14)	0.0019 (14)	-0.0008 (14)
C31	0.018 (6)	0.018 (5)	0.009 (5)	-0.003 (5)	0.006 (4)	0.006 (4)
C32	0.019 (6)	0.028 (6)	0.006 (5)	0.000 (5)	0.007 (5)	-0.004 (5)
C33	0.018 (6)	0.027 (6)	0.008 (5)	-0.001 (5)	0.006 (5)	-0.003 (5)
Br34	0.0314 (10)	0.0417 (11)	0.0467 (12)	-0.0183 (9)	0.0008 (9)	0.0215 (9)
C35	0.031 (9)	0.037 (10)	0.019 (8)	0.019 (8)	-0.005 (7)	0.000 (7)
C36	0.021 (8)	0.008 (6)	0.023 (8)	0.004 (6)	-0.009 (6)	0.006 (6)
C37	0.019 (6)	0.015 (5)	0.009 (5)	-0.004 (5)	0.004 (4)	0.006 (4)
O38	0.020 (6)	0.031 (6)	0.015 (5)	-0.001 (5)	0.000 (4)	0.003 (5)
O39	0.045 (8)	0.022 (6)	0.047 (8)	-0.010 (6)	0.003 (7)	0.003 (6)
O40	0.013 (5)	0.027 (6)	0.043 (7)	-0.007 (5)	0.005 (5)	-0.014 (5)
C41	0.016 (8)	0.017 (8)	0.074 (15)	0.009 (7)	-0.005 (9)	-0.005 (9)
N42	0.017 (7)	0.019 (7)	0.085 (14)	0.009 (6)	0.000 (8)	0.006 (8)
C43	0.11 (3)	0.031 (14)	0.13 (3)	-0.031 (15)	-0.01 (2)	0.004 (16)
C44	0.060 (17)	0.11 (3)	0.07 (2)	0.034 (18)	0.012 (15)	0.015 (19)

Geometric parameters (Å, °) for (1)

Br1—C2	1.923 (16)	C18—Br20	1.927 (17)
C2—C3	1.34 (2)	C19—H191	0.931
C2—C21	1.36 (2)	C21—H211	0.933
C3—C4	1.45 (2)	O22—C23	1.289 (18)
C3—H31	0.936	C23—C24	1.40 (2)
C4—S5	1.791 (15)	C23—C29	1.41 (2)
C4—C13	1.40 (2)	C24—C25	1.378 (19)
S5—Mn6	2.721 (4)	C25—C26	1.43 (2)
S5—C36	1.783 (15)	C25—H251	0.934
Mn6—O10 ⁱ	2.257 (11)	C26—Br27	1.876 (14)
Mn6—O38 ⁱ	2.263 (11)	C26—C28	1.37 (2)
Mn6—Mn11 ⁱ	3.464 (3)	C28—C29	1.38 (2)
Mn6—S7	2.714 (4)	C28—H281	0.931

Mn6—Mn11	3.469 (3)	C29—S30	1.817 (15)
Mn6—O12	2.243 (12)	S30—C31	1.789 (14)
Mn6—O22	2.281 (10)	C31—C32	1.35 (2)
Mn6—O39	2.399 (14)	C31—C37	1.47 (2)
Mn6—O40	2.417 (12)	C32—C33	1.37 (2)
S7—C8	1.751 (15)	C32—H321	0.928
S7—C24	1.789 (16)	C33—C35 ⁱ	1.36 (2)
C8—C9 ⁱ	1.41 (2)	C33—Br34	1.914 (15)
C8—C19	1.37 (2)	C35—C36	1.39 (2)
C9—O10	1.292 (17)	C35—H351	0.933
C9—C16	1.45 (2)	C36—C37 ⁱ	1.440 (19)
O10—Mn11	2.123 (11)	C37—O38	1.282 (17)
Mn11—O12	2.128 (12)	O39—H392	0.993
Mn11—S15	2.738 (4)	O39—H391	0.993
Mn11—O22	2.106 (10)	O40—C41	1.257 (19)
Mn11—S30	2.751 (4)	C41—N42	1.27 (2)
Mn11—O38	2.118 (11)	C41—H411	0.931
O12—C13	1.286 (17)	N42—C43	1.49 (3)
C13—C14	1.44 (2)	N42—C44	1.36 (3)
C14—S15	1.772 (16)	C43—H432	0.957
C14—C21	1.37 (2)	C43—H431	0.960
S15—C16	1.787 (15)	C43—H433	0.959
C16—C17	1.40 (2)	C44—H442	0.957
C17—C18	1.41 (2)	C44—H443	0.961
C17—H171	0.931	C44—H441	0.958
C18—C19 ⁱ	1.37 (2)		
Br1—C2—C3	116.9 (12)	S30—Mn11—O38	75.0 (3)
Br1—C2—C21	120.5 (12)	Mn6—O12—Mn11	105.0 (5)
C3—C2—C21	122.6 (15)	Mn6—O12—C13	126.1 (10)
C2—C3—C4	118.0 (15)	Mn11—O12—C13	128.4 (10)
C2—C3—H31	120.8	C4—C13—O12	122.4 (14)
C4—C3—H31	121.2	C4—C13—C14	115.1 (13)
C3—C4—S5	119.0 (12)	O12—C13—C14	122.3 (14)
C3—C4—C13	121.7 (14)	C13—C14—S15	118.2 (11)
S5—C4—C13	119.3 (11)	C13—C14—C21	121.6 (14)
C4—S5—Mn6	96.7 (5)	S15—C14—C21	120.2 (11)
C4—S5—C36	103.6 (7)	C14—S15—Mn11	95.9 (5)
Mn6—S5—C36	97.7 (5)	C14—S15—C16	99.3 (8)
O10 ⁱ —Mn6—O38 ⁱ	68.9 (4)	Mn11—S15—C16	95.9 (5)

O10 ⁱ —Mn6—S5	138.0 (3)	S15—C16—C9	118.6 (11)
O38 ⁱ —Mn6—S5	73.8 (3)	S15—C16—C17	118.5 (12)
O10 ⁱ —Mn6—Mn11 ⁱ	36.4 (3)	C9—C16—C17	122.6 (14)
O38 ⁱ —Mn6—Mn11 ⁱ	36.3 (3)	C16—C17—C18	116.5 (16)
S5—Mn6—Mn11 ⁱ	110.09 (11)	C16—C17—H171	121.3
O10 ⁱ —Mn6—S7	74.4 (3)	C18—C17—H171	122.1
O38 ⁱ —Mn6—S7	138.4 (3)	C17—C18—C19 ⁱ	121.5 (16)
S5—Mn6—S7	128.87 (14)	C17—C18—Br20	117.8 (13)
Mn11 ⁱ —Mn6—S7	110.74 (11)	C19 ⁱ —C18—Br20	120.7 (13)
O10 ⁱ —Mn6—Mn11	86.8 (3)	C8—C19—C18 ⁱ	122.2 (16)
O38 ⁱ —Mn6—Mn11	87.1 (3)	C8—C19—H191	118.7
S5—Mn6—Mn11	110.11 (11)	C18 ⁱ —C19—H191	119.1
Mn11 ⁱ —Mn6—Mn11	73.87 (8)	C14—C21—C2	120.7 (14)
S7—Mn6—Mn11	109.76 (11)	C14—C21—H211	119.4
O10 ⁱ —Mn6—O12	116.1 (4)	C2—C21—H211	119.9
O38 ⁱ —Mn6—O12	79.5 (4)	Mn6—O22—Mn11	104.5 (4)
S5—Mn6—O12	73.9 (3)	Mn6—O22—C23	124.2 (10)
Mn11 ⁱ —Mn6—O12	88.6 (3)	Mn11—O22—C23	130.3 (9)
S7—Mn6—O12	135.8 (3)	O22—C23—C24	123.3 (14)
O10 ⁱ —Mn6—O22	79.2 (4)	O22—C23—C29	122.7 (14)
O38 ⁱ —Mn6—O22	116.1 (4)	C24—C23—C29	114.0 (14)
S5—Mn6—O22	136.2 (3)	S7—C24—C23	119.1 (11)
Mn11 ⁱ —Mn6—O22	88.5 (3)	S7—C24—C25	117.6 (12)
S7—Mn6—O22	73.8 (3)	C23—C24—C25	123.0 (14)
O10 ⁱ —Mn6—O39	83.2 (4)	C24—C25—C26	119.7 (14)
O38 ⁱ —Mn6—O39	82.0 (4)	C24—C25—H251	120.0
S5—Mn6—O39	73.1 (3)	C26—C25—H251	120.3
Mn11 ⁱ —Mn6—O39	93.4 (3)	C25—C26—Br27	119.7 (11)
S7—Mn6—O39	75.0 (3)	C25—C26—C28	119.0 (14)
O10 ⁱ —Mn6—O40	147.0 (4)	Br27—C26—C28	121.0 (12)
O38 ⁱ —Mn6—O40	144.2 (4)	C26—C28—C29	118.9 (15)
S5—Mn6—O40	71.9 (3)	C26—C28—H281	120.7
Mn11 ⁱ —Mn6—O40	168.7 (3)	C29—C28—H281	120.4
S7—Mn6—O40	74.0 (3)	C23—C29—C28	125.1 (14)
Mn11—Mn6—O12	36.3 (3)	C23—C29—S30	117.2 (11)
Mn11—Mn6—O22	36.0 (3)	C28—C29—S30	117.7 (11)
O12—Mn6—O22	67.1 (4)	C29—S30—Mn11	95.4 (5)
Mn11—Mn6—O39	167.3 (3)	C29—S30—C31	101.1 (7)
O12—Mn6—O39	145.5 (4)	Mn11—S30—C31	96.5 (5)
O22—Mn6—O39	147.3 (4)	S30—C31—C32	121.3 (12)

Mn11—Mn6—O40	95.0 (3)	S30—C31—C37	116.2 (10)
O12—Mn6—O40	81.3 (4)	C32—C31—C37	122.4 (13)
O22—Mn6—O40	83.0 (4)	C31—C32—C33	120.3 (14)
O39—Mn6—O40	97.7 (4)	C31—C32—H321	119.7
Mn6—S7—C8	96.7 (5)	C33—C32—H321	120.0
Mn6—S7—C24	97.4 (5)	C32—C33—C35 ⁱ	122.1 (15)
C8—S7—C24	102.7 (7)	C32—C33—Br34	119.2 (11)
C9 ⁱ —C8—S7	119.9 (11)	C35 ⁱ —C33—Br34	118.6 (12)
C9 ⁱ —C8—C19	120.3 (14)	C33 ⁱ —C35—C36	118.8 (15)
S7—C8—C19	119.6 (13)	C33 ⁱ —C35—H351	120.1
C8 ⁱ —C9—O10	123.1 (14)	C36—C35—H351	121.1
C8 ⁱ —C9—C16	116.5 (13)	S5—C36—C37 ⁱ	117.2 (11)
O10—C9—C16	120.3 (14)	S5—C36—C35	119.7 (11)
Mn6 ⁱ —O10—C9	123.0 (10)	C37 ⁱ —C36—C35	123.1 (14)
Mn6 ⁱ —O10—Mn11	104.5 (4)	C31—C37—C36 ⁱ	113.0 (12)
C9—O10—Mn11	130.5 (10)	C31—C37—O38	123.2 (13)
O10—Mn11—Mn6 ⁱ	39.1 (3)	C36 ⁱ —C37—O38	123.9 (13)
O10—Mn11—Mn6	113.2 (3)	Mn6 ⁱ —O38—Mn11	104.5 (5)
Mn6 ⁱ —Mn11—Mn6	106.13 (8)	Mn6 ⁱ —O38—C37	123.9 (9)
O10—Mn11—O12	96.1 (4)	Mn11—O38—C37	129.2 (10)
Mn6 ⁱ —Mn11—O12	115.3 (3)	Mn6—O39—H392	109.3
Mn6—Mn11—O12	38.7 (3)	Mn6—O39—H391	109.5
O10—Mn11—S15	74.7 (3)	H392—O39—H391	109.5
Mn6 ⁱ —Mn11—S15	112.37 (11)	Mn6—O40—C41	123.8 (13)
Mn6—Mn11—S15	112.83 (11)	O40—C41—N42	127 (2)
O12—Mn11—S15	75.1 (3)	O40—C41—H411	117.1
O10—Mn11—O22	144.9 (4)	N42—C41—H411	116.1
Mn6 ⁱ —Mn11—O22	115.4 (3)	C41—N42—C43	122 (2)
Mn6—Mn11—O22	39.5 (3)	C41—N42—C44	123 (2)
O12—Mn11—O22	72.4 (4)	C43—N42—C44	115 (2)
S15—Mn11—O22	130.1 (3)	N42—C43—H432	108.9
O10—Mn11—S30	131.6 (3)	N42—C43—H431	110.0
Mn6 ⁱ —Mn11—S30	112.78 (11)	H432—C43—H431	109.5
Mn6—Mn11—S30	112.98 (11)	N42—C43—H433	109.1
O12—Mn11—S30	129.7 (3)	H432—C43—H433	109.9
S15—Mn11—S30	99.94 (13)	H431—C43—H433	109.5
O10—Mn11—O38	74.1 (4)	N42—C44—H442	109.0
Mn6 ⁱ —Mn11—O38	39.2 (3)	N42—C44—H443	109.5
Mn6—Mn11—O38	113.6 (3)	H442—C44—H443	109.7
O12—Mn11—O38	144.7 (4)	N42—C44—H441	109.3

S15—Mn11—O38	131.2 (3)	H442—C44—H441	109.6
O22—Mn11—S30	74.4 (3)	H443—C44—H441	109.7
O22—Mn11—O38	96.0 (4)		

Symmetry code: (i) $-x+1, -y+2, -z+1$.

Document origin: *publCIF* [Westrip, S. P. (2010). *J. Apply. Cryst.*, **43**, 920-925].

[Na(dibenzo-18-crown-6)][Mn₄(thiaSO₂)₂F]*Crystal data*

C ₁₀₀ H ₁₁₂ FMn ₄ NaO ₃₀ S ₈	Z = 1
M _r = 2312.13	F(000) = 1200
Triclinic, <i>P</i> 1	D _x = 1.418 Mg m ⁻³
Hall symbol: -P 1	Mo Kα radiation, λ = 0.71073 Å
a = 13.6532 (5) Å	Cell parameters from 9800 reflections
b = 13.8382 (6) Å	θ = 3.2–29.0°
c = 16.6618 (6) Å	μ = 0.69 mm ⁻¹
α = 111.685 (4)°	T = 293 K
β = 92.792 (3)°	Block, colorless
γ = 109.343 (4)°	0.40 × 0.23 × 0.20 mm
V = 2707.0 (2) Å ³	

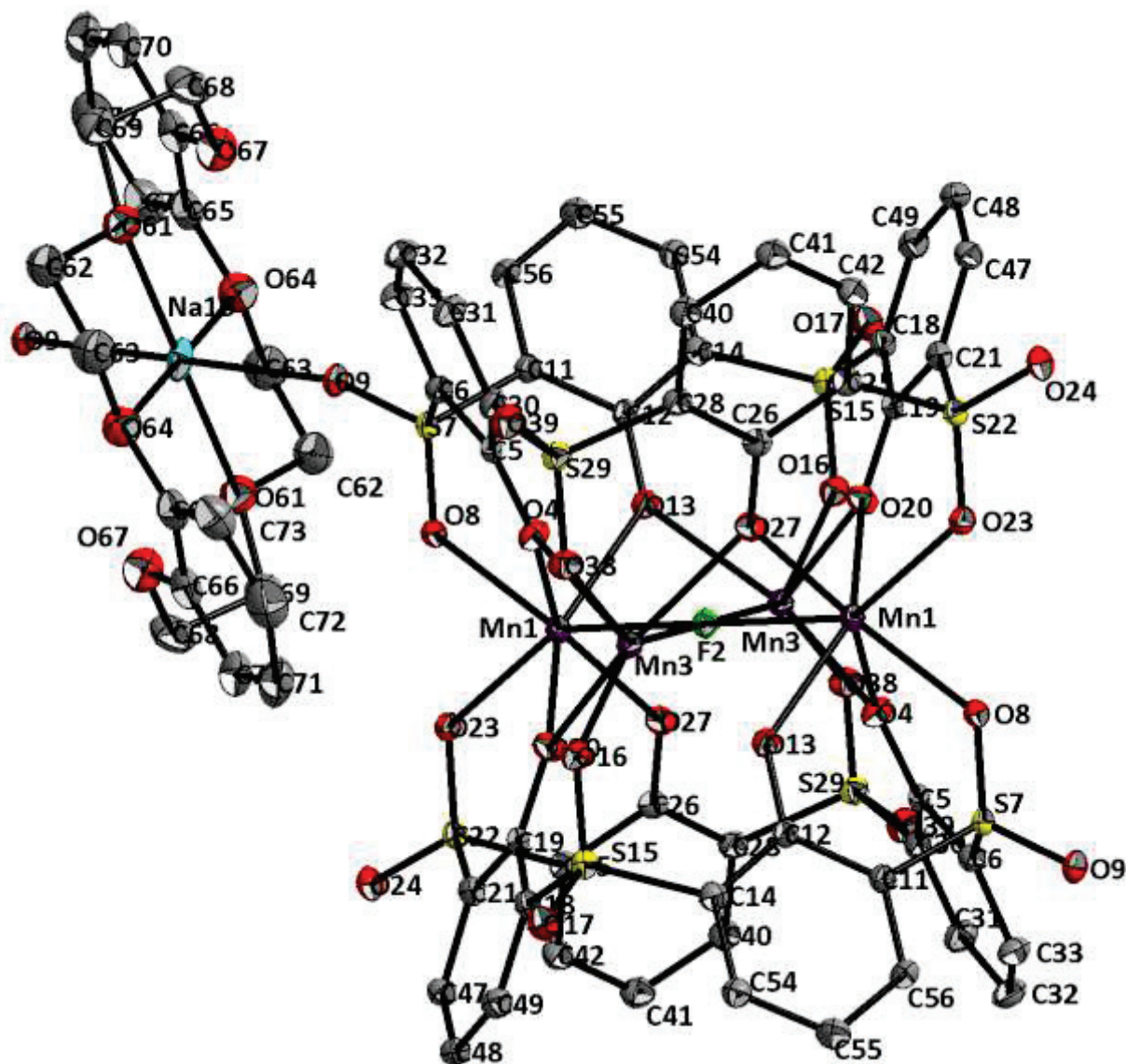
Data collection

Xcalibur, Onyx diffractometer	12499 independent reflections
Radiation source: fine-focus sealed X-ray tube, Enhance (Mo) X-ray Source	9351 reflections with <i>I</i> > 2.0σ(<i>I</i>)
Graphite monochromator	R _{int} = 0.000
Detector resolution: 8.2634 pixels mm ⁻¹	θ _{max} = 29.4°, θ _{min} = 2.8°
ω scans	h = -18→18
Absorption correction: analytical <i>CrysAlis PRO</i> 1.171.38.43 (Rigaku Oxford Diffraction, 2015) Analytical numeric absorption correction using a multifaceted crystal model based on expressions derived by R.C. Clark & J.S. Reid. (Clark, R. C. & Reid, J. S. (1995). <i>Acta Cryst.</i> A51, 887-897) Empirical absorption correction using spherical harmonics, implemented in SCALE3 ABSPACK scaling algorithm.	k = -17→17
T _{min} = 0.842, T _{max} = 0.906	l = 0→21
12499 measured reflections	

Refinement

Refinement on <i>F</i> ²	Primary atom site location: structure-invariant direct methods
Least-squares matrix: full	Hydrogen site location: difference Fourier map
R[<i>F</i> ² > 2σ(<i>F</i> ²)] = 0.049	H-atom parameters not refined
wR(<i>F</i> ²) = 0.075	Method, part 1, Chebychev polynomial, (Watkin, 1994, Prince, 1982) [weight] = 1.0/[A ₀ *T ₀ (x) + A ₁ *T ₁ (x) ... + A _{n-1}]*T _{n-1} (x)]

	where A_i are the Chebychev coefficients listed below and $x = F/F_{\max}$ Method = Robust Weighting (Prince, 1982) $W = [\text{weight}] * [1 - (\Delta F/6 * \sigma F)^2]^2$ A_i are: 0.919E+05 0.145E+06 0.747E+05 0.241E+05
$S = 1.06$	$(\Delta/\sigma)_{\max} = 0.001$
12464 reflections	$\Delta_{\max} = 1.28 \text{ e } \text{Å}^{-3}$
652 parameters	$\Delta_{\min} = -0.79 \text{ e } \text{Å}^{-3}$
0 restraints	



Fractional atomic coordinates and isotropic or equivalent isotropic displacement parameters (Å^2)

	x	y	z	$U_{\text{iso}}^*/U_{\text{eq}}$
Mn1	0.56652 (3)	1.06861 (4)	0.40693 (3)	0.0231
F2	0.5000	1.0000	0.5000	0.0225

Mn3	0.40707 (4)	1.10887 (4)	0.53180 (3)	0.0235
O4	0.52991 (17)	0.88238 (16)	0.33970 (13)	0.0273
C5	0.4829 (2)	0.8028 (2)	0.26234 (18)	0.0223
C6	0.4424 (2)	0.8210 (2)	0.19057 (19)	0.0250
S7	0.44981 (6)	0.95459 (6)	0.20086 (4)	0.0223
O8	0.53837 (15)	1.04087 (16)	0.26891 (12)	0.0265
O9	0.45107 (16)	0.95438 (17)	0.11422 (13)	0.0294
Na10	0.5000	1.0000	0.0000	0.0411
C11	0.3314 (2)	0.9670 (2)	0.22950 (18)	0.0245
C12	0.3163 (2)	1.0042 (2)	0.31869 (18)	0.0220
O13	0.39292 (15)	1.04291 (18)	0.38609 (13)	0.0271
C14	0.2109 (2)	0.9975 (2)	0.32560 (19)	0.0248
S15	0.16804 (6)	1.03015 (6)	0.42732 (5)	0.0236
O16	0.25568 (16)	1.11707 (16)	0.49698 (13)	0.0276
O17	0.07586 (17)	1.05501 (18)	0.41668 (14)	0.0317
C18	0.8701 (2)	1.0948 (2)	0.55599 (19)	0.0247
C19	0.8005 (2)	1.1224 (2)	0.51061 (18)	0.0212
O20	0.70168 (15)	1.05672 (17)	0.47391 (13)	0.0272
C21	0.8499 (2)	1.2301 (2)	0.50770 (18)	0.0240
S22	0.78184 (6)	1.29020 (6)	0.46017 (5)	0.0239
O23	0.69329 (16)	1.20341 (16)	0.39178 (12)	0.0271
O24	0.85864 (17)	1.36657 (18)	0.43301 (14)	0.0321
C25	0.7336 (2)	1.3698 (2)	0.54567 (18)	0.0250
C26	0.6333 (2)	1.3222 (2)	0.56727 (18)	0.0225
O27	0.56818 (16)	1.21824 (16)	0.52305 (13)	0.0283
C28	0.6124 (2)	1.4004 (2)	0.64037 (19)	0.0254
S29	0.49868 (6)	1.36304 (6)	0.68567 (5)	0.0253
C30	0.4659 (2)	0.6873 (2)	0.23903 (19)	0.0264
C31	0.4121 (3)	0.6033 (2)	0.1571 (2)	0.0329
C32	0.3702 (3)	0.6232 (3)	0.0897 (2)	0.0358
C33	0.3886 (3)	0.7354 (3)	0.1094 (2)	0.0321
C34	0.3063 (3)	0.5294 (3)	0.0010 (2)	0.0482
C35	0.2694 (6)	0.4180 (4)	0.0046 (4)	0.1343
C36	0.2081 (7)	0.5445 (5)	-0.0228 (5)	0.1748
C37	0.3658 (7)	0.5331 (7)	-0.0689 (4)	0.1995
O38	0.41146 (16)	1.27468 (17)	0.61677 (13)	0.0290
O39	0.48150 (17)	1.46347 (17)	0.73552 (14)	0.0332
C40	0.6825 (3)	1.5106 (3)	0.6867 (2)	0.0312
C41	0.7788 (3)	1.5541 (2)	0.6650 (2)	0.0334
C42	0.8021 (2)	1.4805 (3)	0.5935 (2)	0.0316

C43	0.8576 (3)	1.6753 (3)	0.7190 (2)	0.0458
C44	0.9044 (6)	1.7313 (5)	0.6634 (4)	0.1481
C45	0.9536 (6)	1.6686 (5)	0.7655 (5)	0.1625
C46	0.8181 (6)	1.7373 (5)	0.7906 (6)	0.2151
C47	0.9541 (2)	1.3003 (2)	0.5491 (2)	0.0296
C48	1.0192 (2)	1.2716 (3)	0.59478 (19)	0.0290
C49	0.9741 (2)	1.1660 (3)	0.5957 (2)	0.0292
C50	1.1317 (3)	1.3537 (3)	0.6441 (2)	0.0365
C51	1.1997 (3)	1.3809 (4)	0.5788 (3)	0.0569
C52	1.1850 (3)	1.3050 (3)	0.6927 (3)	0.0471
C53	1.1255 (3)	1.4615 (3)	0.7097 (3)	0.0615
C54	0.1319 (2)	0.9597 (3)	0.2527 (2)	0.0298
C55	0.1492 (2)	0.9248 (3)	0.1671 (2)	0.0303
C56	0.2509 (2)	0.9292 (3)	0.15796 (19)	0.0292
C57	0.0638 (3)	0.8798 (3)	0.0854 (2)	0.0388
C58	0.1019 (3)	0.9454 (4)	0.0287 (3)	0.0564
C59	-0.0390 (3)	0.8895 (4)	0.1085 (3)	0.0647
C60	0.0457 (4)	0.7570 (4)	0.0310 (3)	0.0727
O61	0.5574 (2)	1.2037 (2)	0.11346 (16)	0.0453
C62	0.4654 (3)	1.2259 (3)	0.1344 (3)	0.0553
C63	0.4030 (3)	1.2109 (4)	0.0524 (3)	0.0582
O64	0.3702 (2)	1.0967 (2)	-0.00775 (17)	0.0485
C65	0.3167 (3)	1.0681 (3)	-0.0908 (3)	0.0447
C66	0.7290 (3)	1.0473 (3)	0.1437 (3)	0.0444
O67	0.7148 (2)	1.1136 (2)	0.10295 (18)	0.0567
C68	0.7338 (3)	1.2284 (3)	0.1565 (3)	0.0553
C69	0.6371 (3)	1.2413 (3)	0.1888 (2)	0.0467
C70	0.7834 (3)	1.0848 (4)	0.2273 (3)	0.0562
C71	0.7914 (4)	1.0087 (5)	0.2611 (3)	0.0638
C72	0.2560 (4)	1.1030 (5)	-0.2110 (3)	0.0645
C73	0.3101 (3)	1.1425 (4)	-0.1251 (3)	0.0564
H311	0.4032	0.5297	0.1464	0.0402*
H331	0.3621	0.7526	0.0653	0.0378*
H351	0.2263	0.3607	-0.0503	0.2101*
H352	0.3326	0.4012	0.0161	0.2098*
H353	0.2333	0.4198	0.0520	0.2100*
H361	0.1563	0.4822	-0.0704	0.2143*
H362	0.1662	0.5479	0.0301	0.2138*
H363	0.2157	0.6121	-0.0263	0.2139*
H372	0.3145	0.5300	-0.1192	0.3959*

H371	0.3873	0.4643	-0.0875	0.3959*
H373	0.4297	0.6094	-0.0413	0.3959*
H401	0.6628	1.5577	0.7341	0.0377*
H421	0.8662	1.5069	0.5769	0.0397*
H441	0.9406	1.8107	0.6987	0.2072*
H442	0.8475	1.7204	0.6192	0.2069*
H443	0.9522	1.6999	0.6352	0.2071*
H451	1.0051	1.7443	0.7986	0.2288*
H452	0.9853	1.6274	0.7214	0.2289*
H453	0.9324	1.6331	0.8040	0.2290*
H461	0.8762	1.8011	0.8351	0.2918*
H462	0.7674	1.7595	0.7724	0.2918*
H463	0.7857	1.6885	0.8224	0.2918*
H471	0.9827	1.3690	0.5445	0.0353*
H491	1.0156	1.1420	0.6230	0.0361*
H511	1.2707	1.4293	0.6093	0.0822*
H513	1.1707	1.4147	0.5484	0.0817*
H512	1.2018	1.3113	0.5352	0.0825*
H521	1.2569	1.3565	0.7186	0.0694*
H522	1.1834	1.2332	0.6530	0.0700*
H523	1.1467	1.2957	0.7396	0.0702*
H531	1.1944	1.5117	0.7468	0.0920*
H532	1.1010	1.4994	0.6802	0.0920*
H533	1.0777	1.4458	0.7481	0.0921*
H541	0.0644	0.9563	0.2625	0.0363*
H561	0.2653	0.9066	0.1011	0.0365*
H581	0.0487	0.9163	-0.0235	0.0828*
H583	0.1669	0.9385	0.0126	0.0830*
H582	0.1147	1.0249	0.0627	0.0834*
H591	-0.0910	0.8621	0.0560	0.0687*
H593	-0.0649	0.8449	0.1413	0.0683*
H592	-0.0270	0.9669	0.1442	0.0674*
H601	-0.0113	0.7256	-0.0180	0.1058*
H602	0.0288	0.7148	0.0660	0.1059*
H603	0.1081	0.7501	0.0085	0.1058*
H621	0.4860	1.3023	0.1789	0.0656*
H622	0.4242	1.1745	0.1583	0.0659*
H632	0.4474	1.2578	0.0269	0.0726*
H631	0.3427	1.2299	0.0650	0.0720*
H681	0.7553	1.2721	0.1211	0.0670*

H682	0.7914	1.2570	0.2064	0.0668*
H692	0.6527	1.3190	0.2267	0.0570*
H691	0.6143	1.1954	0.2220	0.0573*
H701	0.8162	1.1620	0.2614	0.0670*
H711	0.8294	1.0369	0.3183	0.0781*
H721	0.2524	1.1545	-0.2336	0.0780*
H731	0.3411	1.2186	-0.0908	0.0687*

Atomic displacement parameters (\AA^2)

	U^{11}	U^{22}	U^{33}	U^{12}	U^{13}	U^{23}
Mn1	0.0238 (2)	0.0239 (2)	0.0204 (2)	0.00546 (18)	0.00550 (17)	0.01071 (18)
F2	0.0255 (12)	0.0241 (11)	0.0199 (11)	0.0081 (10)	0.0091 (9)	0.0117 (9)
Mn3	0.0249 (2)	0.0233 (2)	0.0215 (2)	0.00699 (18)	0.00623 (18)	0.00980 (18)
O4	0.0369 (12)	0.0233 (10)	0.0193 (10)	0.0097 (9)	0.0052 (9)	0.0076 (8)
C5	0.0206 (14)	0.0248 (14)	0.0191 (13)	0.0055 (11)	0.0089 (11)	0.0087 (11)
C6	0.0244 (15)	0.0256 (15)	0.0238 (15)	0.0066 (12)	0.0066 (12)	0.0112 (12)
S7	0.0226 (4)	0.0250 (3)	0.0179 (3)	0.0046 (3)	0.0060 (3)	0.0109 (3)
O8	0.0249 (11)	0.0280 (11)	0.0200 (10)	0.0008 (9)	0.0043 (8)	0.0110 (9)
O9	0.0322 (12)	0.0356 (12)	0.0208 (10)	0.0078 (10)	0.0083 (9)	0.0160 (9)
Na10	0.0574 (13)	0.0447 (11)	0.0341 (10)	0.0206 (10)	0.0236 (9)	0.0266 (9)
C11	0.0238 (15)	0.0258 (14)	0.0204 (14)	0.0044 (12)	0.0039 (11)	0.0103 (12)
C12	0.0255 (15)	0.0188 (13)	0.0220 (14)	0.0054 (11)	0.0043 (11)	0.0112 (11)
O13	0.0227 (10)	0.0383 (12)	0.0216 (10)	0.0108 (9)	0.0059 (8)	0.0138 (9)
C14	0.0274 (15)	0.0229 (14)	0.0249 (15)	0.0082 (12)	0.0059 (12)	0.0116 (12)
S15	0.0236 (4)	0.0244 (4)	0.0239 (4)	0.0090 (3)	0.0073 (3)	0.0108 (3)
O16	0.0273 (11)	0.0247 (10)	0.0256 (11)	0.0088 (9)	0.0048 (9)	0.0058 (9)
O17	0.0314 (12)	0.0329 (12)	0.0368 (13)	0.0168 (10)	0.0103 (10)	0.0159 (10)
C18	0.0247 (15)	0.0246 (14)	0.0235 (14)	0.0062 (12)	0.0077 (12)	0.0110 (12)
C19	0.0196 (14)	0.0248 (14)	0.0184 (13)	0.0076 (11)	0.0088 (11)	0.0081 (11)
O20	0.0207 (10)	0.0280 (11)	0.0334 (12)	0.0039 (9)	0.0039 (9)	0.0178 (9)
C21	0.0249 (15)	0.0244 (14)	0.0233 (14)	0.0082 (12)	0.0079 (12)	0.0110 (12)
S22	0.0257 (4)	0.0229 (3)	0.0218 (3)	0.0046 (3)	0.0063 (3)	0.0114 (3)
O23	0.0294 (11)	0.0268 (11)	0.0195 (10)	0.0031 (9)	0.0048 (8)	0.0103 (8)
O24	0.0322 (12)	0.0325 (12)	0.0328 (12)	0.0030 (10)	0.0118 (9)	0.0223 (10)
C25	0.0278 (15)	0.0224 (14)	0.0221 (14)	0.0049 (12)	0.0036 (12)	0.0104 (12)
C26	0.0256 (15)	0.0190 (13)	0.0223 (14)	0.0054 (11)	0.0017 (11)	0.0108 (11)
O27	0.0287 (11)	0.0190 (10)	0.0296 (11)	0.0028 (9)	0.0110 (9)	0.0066 (9)
C28	0.0279 (15)	0.0196 (13)	0.0249 (15)	0.0054 (12)	0.0056 (12)	0.0079 (12)
S29	0.0270 (4)	0.0227 (3)	0.0250 (4)	0.0091 (3)	0.0066 (3)	0.0085 (3)
C30	0.0289 (16)	0.0260 (15)	0.0225 (14)	0.0079 (12)	0.0078 (12)	0.0100 (12)

C31	0.0391 (18)	0.0231 (15)	0.0299 (17)	0.0066 (14)	0.0061 (14)	0.0084 (13)
C32	0.0425 (19)	0.0270 (16)	0.0268 (16)	0.0062 (14)	0.0021 (14)	0.0059 (13)
C33	0.0363 (18)	0.0306 (16)	0.0237 (15)	0.0068 (14)	0.0025 (13)	0.0107 (13)
C34	0.065 (3)	0.0286 (18)	0.0292 (18)	0.0018 (17)	-0.0106 (17)	0.0044 (14)
C35	0.209 (8)	0.039 (3)	0.076 (4)	-0.029 (4)	-0.069 (4)	0.018 (3)
C36	0.191 (8)	0.084 (5)	0.160 (7)	0.061 (5)	-0.130 (6)	-0.033 (4)
C37	0.150 (7)	0.196 (8)	0.051 (4)	-0.072 (6)	0.036 (4)	-0.045 (4)
O38	0.0280 (11)	0.0259 (11)	0.0294 (11)	0.0092 (9)	0.0038 (9)	0.0086 (9)
O39	0.0364 (12)	0.0266 (11)	0.0356 (12)	0.0154 (10)	0.0093 (10)	0.0084 (10)
C40	0.0355 (17)	0.0242 (15)	0.0272 (16)	0.0076 (13)	0.0061 (13)	0.0066 (12)
C41	0.0365 (18)	0.0221 (15)	0.0312 (17)	0.0030 (13)	0.0063 (14)	0.0070 (13)
C42	0.0319 (17)	0.0254 (15)	0.0321 (17)	0.0040 (13)	0.0070 (13)	0.0118 (13)
C43	0.045 (2)	0.0248 (17)	0.041 (2)	-0.0051 (15)	0.0112 (17)	0.0012 (15)
C44	0.210 (8)	0.059 (3)	0.077 (4)	-0.061 (4)	0.005 (5)	0.024 (3)
C45	0.152 (7)	0.077 (4)	0.165 (7)	-0.038 (4)	-0.094 (6)	0.037 (5)
C46	0.132 (6)	0.065 (4)	0.241 (9)	-0.055 (4)	0.114 (6)	-0.085 (5)
C47	0.0282 (16)	0.0262 (15)	0.0285 (16)	0.0035 (13)	0.0069 (13)	0.0107 (13)
C48	0.0267 (16)	0.0286 (15)	0.0243 (15)	0.0042 (13)	0.0039 (12)	0.0086 (12)
C49	0.0299 (16)	0.0307 (16)	0.0267 (16)	0.0109 (13)	0.0043 (13)	0.0119 (13)
C50	0.0264 (16)	0.0335 (17)	0.0392 (19)	0.0018 (14)	-0.0032 (14)	0.0135 (15)
C51	0.036 (2)	0.066 (3)	0.067 (3)	0.0034 (19)	0.0069 (19)	0.040 (2)
C52	0.0268 (18)	0.051 (2)	0.052 (2)	0.0019 (16)	-0.0081 (16)	0.0225 (19)
C53	0.048 (2)	0.042 (2)	0.062 (3)	0.0075 (19)	-0.009 (2)	-0.001 (2)
C54	0.0247 (15)	0.0327 (16)	0.0307 (16)	0.0078 (13)	0.0058 (13)	0.0143 (13)
C55	0.0264 (16)	0.0347 (17)	0.0272 (16)	0.0081 (13)	0.0032 (13)	0.0129 (13)
C56	0.0300 (16)	0.0328 (16)	0.0202 (15)	0.0079 (13)	0.0045 (12)	0.0095 (13)
C57	0.0280 (17)	0.054 (2)	0.0279 (17)	0.0123 (16)	-0.0007 (13)	0.0134 (16)
C58	0.050 (2)	0.087 (3)	0.040 (2)	0.025 (2)	0.0032 (18)	0.035 (2)
C59	0.031 (2)	0.111 (4)	0.044 (2)	0.022 (2)	0.0016 (17)	0.028 (2)
C60	0.073 (3)	0.054 (3)	0.060 (3)	0.015 (2)	-0.021 (2)	0.002 (2)
O61	0.0485 (15)	0.0429 (14)	0.0423 (15)	0.0153 (12)	0.0120 (12)	0.0164 (12)
C62	0.058 (3)	0.046 (2)	0.058 (3)	0.024 (2)	0.017 (2)	0.013 (2)
C63	0.059 (3)	0.049 (2)	0.065 (3)	0.029 (2)	0.011 (2)	0.014 (2)
O64	0.0502 (16)	0.0427 (15)	0.0511 (16)	0.0153 (13)	0.0102 (13)	0.0194 (13)
C65	0.0326 (19)	0.055 (2)	0.055 (2)	0.0190 (17)	0.0171 (17)	0.029 (2)
C66	0.040 (2)	0.055 (2)	0.047 (2)	0.0235 (18)	0.0243 (17)	0.0244 (19)
O67	0.071 (2)	0.0502 (17)	0.0535 (17)	0.0240 (15)	0.0208 (15)	0.0243 (14)
C68	0.049 (2)	0.039 (2)	0.068 (3)	0.0053 (18)	0.008 (2)	0.021 (2)
C69	0.052 (2)	0.0328 (19)	0.045 (2)	0.0038 (17)	0.0078 (18)	0.0157 (17)
C70	0.054 (3)	0.069 (3)	0.047 (2)	0.027 (2)	0.025 (2)	0.019 (2)

C71	0.064 (3)	0.097 (4)	0.046 (3)	0.043 (3)	0.024 (2)	0.032 (3)
C72	0.063 (3)	0.090 (4)	0.073 (3)	0.043 (3)	0.026 (3)	0.052 (3)
C73	0.049 (2)	0.057 (3)	0.072 (3)	0.023 (2)	0.016 (2)	0.032 (2)

Geometric parameters (Å, °) for (1)

Mn1—Mn3 ⁱ	3.0996 (6)	C40—H401	0.937
Mn1—F2	2.1875 (4)	C41—C42	1.384 (4)
Mn1—Mn3	3.1251 (6)	C41—C43	1.540 (4)
Mn1—O4	2.259 (2)	C42—H421	0.928
Mn1—O8	2.1789 (19)	C43—C44	1.457 (6)
Mn1—O13	2.266 (2)	C43—C45	1.537 (8)
Mn1—O20	2.194 (2)	C43—C46	1.436 (7)
Mn1—O23	2.1887 (19)	C44—H441	0.966
Mn1—O27	2.244 (2)	C44—H442	0.978
F2—Mn3 ⁱ	2.2140 (5)	C44—H443	0.950
F2—Mn3	2.2140 (5)	C45—H451	0.971
Mn3—O4 ⁱ	2.213 (2)	C45—H452	0.968
Mn3—O20 ⁱ	2.2440 (19)	C45—H453	0.945
Mn3—O13	2.228 (2)	C46—H461	0.977
Mn3—O16	2.170 (2)	C46—H462	0.925
Mn3—O27	2.2670 (19)	C46—H463	1.011
Mn3—O38	2.185 (2)	C47—C48	1.385 (4)
O4—C5	1.300 (3)	C47—H471	0.933
C5—C6	1.432 (4)	C48—C49	1.391 (4)
C5—C30	1.430 (4)	C48—C50	1.535 (4)
C6—S7	1.759 (3)	C49—H491	0.922
C6—C33	1.384 (4)	C50—C51	1.535 (5)
S7—O8	1.443 (2)	C50—C52	1.521 (5)
S7—O9	1.443 (2)	C50—C53	1.521 (5)
S7—C11	1.752 (3)	C51—H511	0.957
O9—Na10	2.2802 (19)	C51—H513	0.955
Na10—O61 ⁱⁱ	2.566 (2)	C51—H512	0.979
Na10—O64 ⁱⁱ	2.573 (3)	C52—H521	0.963
Na10—O61	2.566 (2)	C52—H522	0.962
Na10—O64	2.573 (3)	C52—H523	0.984
C11—C12	1.432 (4)	C53—H531	0.971
C11—C56	1.390 (4)	C53—H532	0.959
C12—O13	1.309 (3)	C53—H533	0.966
C12—C14	1.423 (4)	C54—C55	1.388 (4)
C14—S15	1.768 (3)	C54—H541	0.932

C14—C54	1.393 (4)	C55—C56	1.388 (4)
S15—C18 ⁱ	1.764 (3)	C55—C57	1.528 (4)
S15—O16	1.451 (2)	C56—H561	0.935
S15—O17	1.430 (2)	C57—C58	1.535 (5)
C18—C19	1.416 (4)	C57—C59	1.507 (5)
C18—C49	1.387 (4)	C57—C60	1.528 (6)
C19—O20	1.310 (3)	C58—H581	0.965
C19—C21	1.439 (4)	C58—H583	0.963
C21—S22	1.763 (3)	C58—H582	0.982
C21—C47	1.391 (4)	C59—H591	0.964
S22—O23	1.447 (2)	C59—H593	0.963
S22—O24	1.4446 (19)	C59—H592	0.966
S22—C25	1.758 (3)	C60—H601	0.956
C25—C26	1.436 (4)	C60—H602	0.953
C25—C42	1.391 (4)	C60—H603	0.965
C26—O27	1.307 (3)	O61—C62	1.420 (5)
C26—C28	1.415 (4)	O61—C69	1.428 (4)
C28—S29	1.766 (3)	C62—C63	1.483 (6)
C28—C40	1.388 (4)	C62—H621	0.975
S29—C30 ⁱ	1.762 (3)	C62—H622	0.971
S29—O38	1.448 (2)	C63—O64	1.421 (5)
S29—O39	1.435 (2)	C63—H632	0.968
C30—C31	1.386 (4)	C63—H631	0.955
C31—C32	1.391 (4)	O64—C65	1.381 (4)
C31—H311	0.930	C65—C66 ⁱⁱ	1.401 (5)
C32—C33	1.392 (4)	C65—C73	1.374 (5)
C32—C34	1.529 (4)	C66—O67	1.379 (4)
C33—H331	0.943	C66—C70	1.368 (6)
C34—C35	1.480 (6)	O67—C68	1.430 (5)
C34—C36	1.482 (8)	C68—C69	1.490 (6)
C34—C37	1.458 (7)	C68—H681	0.982
C35—H351	0.956	C68—H682	0.975
C35—H352	0.992	C69—H692	0.967
C35—H353	0.947	C69—H691	0.975
C36—H361	0.953	C70—C71	1.394 (6)
C36—H362	1.069	C70—H701	0.936
C36—H363	0.931	C71—C72 ⁱⁱ	1.354 (7)
C37—H372	1.046	C71—H711	0.936
C37—H371	1.032	C72—C73	1.395 (6)
C37—H373	1.038	C72—H721	0.933

C40—C41	1.381 (4)	C73—H731	0.922
Mn3 ⁱ —Mn1—F2	45.583 (12)	C32—C33—H331	117.8
Mn3 ⁱ —Mn1—Mn3	90.690 (17)	C6—C33—H331	119.4
F2—Mn1—Mn3	45.108 (12)	C32—C34—C35	111.9 (3)
Mn3 ⁱ —Mn1—O4	45.52 (5)	C32—C34—C36	110.1 (4)
F2—Mn1—O4	74.71 (5)	C35—C34—C36	104.7 (5)
Mn3—Mn1—O4	109.01 (5)	C32—C34—C37	110.7 (4)
Mn3 ⁱ —Mn1—O8	123.15 (6)	C35—C34—C37	112.7 (6)
F2—Mn1—O8	141.86 (5)	C36—C34—C37	106.5 (6)
Mn3—Mn1—O8	123.96 (6)	C34—C35—H351	110.9
O4—Mn1—O8	78.99 (7)	C34—C35—H352	107.9
Mn3 ⁱ —Mn1—O13	108.93 (5)	H351—C35—H352	108.1
F2—Mn1—O13	74.26 (5)	C34—C35—H353	110.1
Mn3—Mn1—O13	45.45 (5)	H351—C35—H353	111.8
O4—Mn1—O13	92.32 (8)	H352—C35—H353	107.8
O8—Mn1—O13	79.78 (7)	C34—C36—H361	116.0
Mn3 ⁱ —Mn1—O20	46.36 (5)	C34—C36—H362	107.4
F2—Mn1—O20	76.29 (5)	H361—C36—H362	100.5
Mn3—Mn1—O20	110.65 (6)	C34—C36—H363	117.0
O4—Mn1—O20	79.28 (8)	H361—C36—H363	111.6
O8—Mn1—O20	125.16 (8)	H362—C36—H363	101.8
Mn3 ⁱ —Mn1—O23	126.59 (6)	C34—C37—H372	106.0
F2—Mn1—O23	145.13 (5)	C34—C37—H371	106.5
Mn3—Mn1—O23	123.87 (6)	H372—C37—H371	112.9
O4—Mn1—O23	127.10 (8)	C34—C37—H373	105.6
O8—Mn1—O23	72.99 (7)	H372—C37—H373	111.6
Mn3 ⁱ —Mn1—O27	110.11 (6)	H371—C37—H373	113.7
F2—Mn1—O27	75.61 (5)	Mn3—O38—S29	126.35 (13)
Mn3—Mn1—O27	46.46 (5)	C28—C40—C41	122.9 (3)
O4—Mn1—O27	150.32 (7)	C28—C40—H401	118.4
O8—Mn1—O27	126.58 (8)	C41—C40—H401	118.7
O13—Mn1—O20	150.54 (7)	C40—C41—C42	115.6 (3)
O13—Mn1—O23	124.42 (8)	C40—C41—C43	122.4 (3)
O20—Mn1—O23	81.58 (7)	C42—C41—C43	121.9 (3)
O13—Mn1—O27	79.69 (8)	C25—C42—C41	122.8 (3)
O20—Mn1—O27	93.67 (8)	C25—C42—H421	119.2
O23—Mn1—O27	79.33 (7)	C41—C42—H421	118.1
Mn1—F2—Mn1 ⁱ	179.995	C41—C43—C44	112.5 (3)
Mn1—F2—Mn3 ⁱ	89.531 (17)	C41—C43—C45	107.4 (4)

Mn1 ⁱ —F2—Mn3 ⁱ	90.469 (17)	C44—C43—C45	102.6 (5)
Mn1—F2—Mn3	90.469 (17)	C41—C43—C46	112.9 (3)
Mn1 ⁱ —F2—Mn3	89.531 (17)	C44—C43—C46	116.6 (6)
Mn3 ⁱ —F2—Mn3	179.995	C45—C43—C46	103.4 (6)
O4 ⁱ —Mn3—O20 ⁱ	79.21 (7)	C43—C44—H441	109.8
O4 ⁱ —Mn3—F2	75.12 (5)	C43—C44—H442	108.4
O20 ⁱ —Mn3—F2	74.75 (5)	H441—C44—H442	108.7
O4 ⁱ —Mn3—Mn1 ⁱ	46.75 (5)	C43—C44—H443	109.9
O20 ⁱ —Mn3—Mn1 ⁱ	45.04 (5)	H441—C44—H443	110.3
F2—Mn3—Mn1 ⁱ	44.887 (12)	H442—C44—H443	109.7
O4 ⁱ —Mn3—Mn1	108.40 (6)	C43—C45—H451	108.5
O20 ⁱ —Mn3—Mn1	109.16 (6)	C43—C45—H452	108.7
F2—Mn3—Mn1	44.423 (12)	H451—C45—H452	108.7
Mn1 ⁱ —Mn3—Mn1	89.310 (17)	C43—C45—H453	110.1
O4 ⁱ —Mn3—O13	149.62 (8)	H451—C45—H453	109.9
O20 ⁱ —Mn3—O13	92.87 (8)	H452—C45—H453	110.7
F2—Mn3—O13	74.50 (5)	C43—C46—H461	110.7
Mn1 ⁱ —Mn3—O13	108.24 (6)	C43—C46—H462	113.1
Mn1—Mn3—O13	46.45 (5)	H461—C46—H462	111.4
O4 ⁱ —Mn3—O16	125.37 (8)	C43—C46—H463	108.8
O20 ⁱ —Mn3—O16	80.39 (8)	H461—C46—H463	104.0
F2—Mn3—O16	143.93 (6)	H462—C46—H463	108.4
Mn1 ⁱ —Mn3—O16	124.06 (6)	C21—C47—C48	123.0 (3)
Mn1—Mn3—O16	126.14 (6)	C21—C47—H471	119.0
O4 ⁱ —Mn3—O27	91.94 (8)	C48—C47—H471	117.9
O20 ⁱ —Mn3—O27	149.36 (8)	C47—C48—C49	115.5 (3)
F2—Mn3—O27	74.63 (5)	C47—C48—C50	121.6 (3)
Mn1 ⁱ —Mn3—O27	108.89 (6)	C49—C48—C50	122.9 (3)
Mn1—Mn3—O27	45.84 (5)	C48—C49—C18	122.8 (3)
O4 ⁱ —Mn3—O38	80.96 (8)	C48—C49—H491	118.4
O20 ⁱ —Mn3—O38	126.64 (8)	C18—C49—H491	118.7
F2—Mn3—O38	144.02 (6)	C48—C50—C51	110.0 (3)
Mn1 ⁱ —Mn3—O38	126.23 (6)	C48—C50—C52	111.6 (3)
Mn1—Mn3—O38	124.08 (6)	C51—C50—C52	108.0 (3)
O13—Mn3—O16	81.16 (7)	C48—C50—C53	108.7 (3)
O13—Mn3—O27	80.00 (7)	C51—C50—C53	109.0 (3)
O16—Mn3—O27	126.97 (8)	C52—C50—C53	109.4 (3)
O13—Mn3—O38	125.42 (8)	C50—C51—H511	109.9
O16—Mn3—O38	72.05 (8)	C50—C51—H513	110.9
O27—Mn3—O38	79.80 (7)	H511—C51—H513	110.5

Mn3 ⁱ —O4—Mn1	87.73 (7)	C50—C51—H512	109.3
Mn3 ⁱ —O4—C5	135.63 (18)	H511—C51—H512	108.0
Mn1—O4—C5	136.31 (18)	H513—C51—H512	108.2
O4—C5—C6	123.7 (3)	C50—C52—H521	108.8
O4—C5—C30	124.0 (3)	C50—C52—H522	110.4
C6—C5—C30	112.3 (2)	H521—C52—H522	110.4
C5—C6—S7	122.3 (2)	C50—C52—H523	108.7
C5—C6—C33	123.4 (3)	H521—C52—H523	109.4
S7—C6—C33	114.2 (2)	H522—C52—H523	109.2
C6—S7—O8	110.22 (13)	C50—C53—H531	110.6
C6—S7—O9	106.74 (13)	C50—C53—H532	111.2
O8—S7—O9	115.68 (12)	H531—C53—H532	109.0
C6—S7—C11	106.85 (13)	C50—C53—H533	110.7
O8—S7—C11	109.88 (13)	H531—C53—H533	107.2
O9—S7—C11	107.06 (13)	H532—C53—H533	108.1
Mn1—O8—S7	127.01 (11)	C14—C54—C55	122.7 (3)
S7—O9—Na10	162.40 (13)	C14—C54—H541	117.9
O9 ⁱⁱ —Na10—O9	179.995	C55—C54—H541	119.3
O9 ⁱⁱ —Na10—O61 ⁱⁱ	84.80 (8)	C54—C55—C56	115.7 (3)
O9—Na10—O61 ⁱⁱ	95.20 (8)	C54—C55—C57	124.2 (3)
O9 ⁱⁱ —Na10—O64 ⁱⁱ	97.76 (8)	C56—C55—C57	120.0 (3)
O9—Na10—O64 ⁱⁱ	82.24 (8)	C11—C56—C55	122.8 (3)
O61 ⁱⁱ —Na10—O64 ⁱⁱ	64.80 (8)	C11—C56—H561	119.4
O9 ⁱⁱ —Na10—O61	95.20 (8)	C55—C56—H561	117.9
O9—Na10—O61	84.80 (8)	C55—C57—C58	109.7 (3)
O61 ⁱⁱ —Na10—O61	179.996	C55—C57—C59	112.4 (3)
O64 ⁱⁱ —Na10—O61	115.20 (8)	C58—C57—C59	108.4 (3)
O9 ⁱⁱ —Na10—O64	82.24 (8)	C55—C57—C60	108.5 (3)
O9—Na10—O64	97.76 (8)	C58—C57—C60	108.0 (3)
O61 ⁱⁱ —Na10—O64	115.20 (8)	C59—C57—C60	109.8 (4)
O64 ⁱⁱ —Na10—O64	179.996	C57—C58—H581	110.0
O61—Na10—O64	64.80 (8)	C57—C58—H583	109.1
S7—C11—C12	122.7 (2)	H581—C58—H583	110.2
S7—C11—C56	114.2 (2)	C57—C58—H582	109.3
C12—C11—C56	122.9 (3)	H581—C58—H582	109.0
C11—C12—O13	122.8 (3)	H583—C58—H582	109.2
C11—C12—C14	112.9 (2)	C57—C59—H591	110.8
O13—C12—C14	124.3 (3)	C57—C59—H593	108.4
Mn3—O13—Mn1	88.11 (7)	H591—C59—H593	109.0
Mn3—O13—C12	135.31 (18)	C57—C59—H592	109.7

Mn1—O13—C12	136.57 (18)	H591—C59—H592	109.6
C12—C14—S15	122.5 (2)	H593—C59—H592	109.4
C12—C14—C54	123.0 (3)	C57—C60—H601	109.7
S15—C14—C54	114.4 (2)	C57—C60—H602	110.4
C14—S15—C18 ⁱ	105.32 (13)	H601—C60—H602	108.9
C14—S15—O16	109.39 (13)	C57—C60—H603	111.0
C18 ⁱ —S15—O16	109.54 (13)	H601—C60—H603	108.2
C14—S15—O17	107.51 (13)	H602—C60—H603	108.4
C18 ⁱ —S15—O17	108.18 (13)	Na10—O61—C62	108.5 (2)
O16—S15—O17	116.33 (13)	Na10—O61—C69	118.0 (2)
Mn3—O16—S15	126.48 (12)	C62—O61—C69	113.7 (3)
S15 ⁱ —C18—C19	123.6 (2)	O61—C62—C63	107.8 (3)
S15 ⁱ —C18—C49	113.0 (2)	O61—C62—H621	109.4
C19—C18—C49	123.3 (3)	C63—C62—H621	110.9
C18—C19—O20	124.0 (3)	O61—C62—H622	109.9
C18—C19—C21	112.9 (2)	C63—C62—H622	110.6
O20—C19—C21	123.1 (3)	H621—C62—H622	108.4
Mn1—O20—Mn3 ⁱ	88.59 (7)	C62—C63—O64	108.1 (3)
Mn1—O20—C19	136.18 (18)	C62—C63—H632	109.2
Mn3 ⁱ —O20—C19	134.84 (18)	O64—C63—H632	108.9
C19—C21—S22	123.4 (2)	C62—C63—H631	109.8
C19—C21—C47	122.4 (3)	O64—C63—H631	110.1
S22—C21—C47	113.9 (2)	H632—C63—H631	110.7
C21—S22—O23	110.45 (13)	C63—O64—Na10	115.8 (2)
C21—S22—O24	107.52 (13)	C63—O64—C65	116.5 (3)
O23—S22—O24	115.66 (12)	Na10—O64—C65	116.3 (2)
C21—S22—C25	105.81 (13)	C66 ⁱⁱ —C65—O64	115.1 (3)
O23—S22—C25	108.97 (13)	C66 ⁱⁱ —C65—C73	119.3 (4)
O24—S22—C25	107.96 (13)	O64—C65—C73	125.5 (4)
Mn1—O23—S22	125.84 (11)	C65 ⁱⁱ —C66—O67	114.1 (3)
S22—C25—C26	122.4 (2)	C65 ⁱⁱ —C66—C70	119.8 (4)
S22—C25—C42	114.9 (2)	O67—C66—C70	126.1 (4)
C26—C25—C42	122.7 (3)	C66—O67—C68	118.3 (3)
C25—C26—O27	123.3 (3)	O67—C68—C69	111.3 (3)
C25—C26—C28	112.7 (2)	O67—C68—H681	108.5
O27—C26—C28	124.0 (3)	C69—C68—H681	109.0
Mn1—O27—Mn3	87.70 (7)	O67—C68—H682	109.4
Mn1—O27—C26	136.47 (18)	C69—C68—H682	109.9
Mn3—O27—C26	135.82 (18)	H681—C68—H682	108.6
C26—C28—S29	122.5 (2)	C68—C69—O61	107.5 (3)

C26—C28—C40	123.3 (3)	C68—C69—H692	109.8
S29—C28—C40	114.0 (2)	O61—C69—H692	110.9
C28—S29—C30 ⁱ	104.73 (14)	C68—C69—H691	108.9
C28—S29—O38	109.67 (13)	O61—C69—H691	110.4
C30 ⁱ —S29—O38	110.01 (13)	H692—C69—H691	109.3
C28—S29—O39	108.16 (13)	C66—C70—C71	120.4 (4)
C30 ⁱ —S29—O39	107.31 (14)	C66—C70—H701	119.4
O38—S29—O39	116.31 (13)	C71—C70—H701	120.2
C5—C30—S29 ⁱ	123.2 (2)	C70—C71—C72 ⁱⁱ	119.7 (4)
C5—C30—C31	123.0 (3)	C70—C71—H711	118.4
S29 ⁱ —C30—C31	113.6 (2)	C72 ⁱⁱ —C71—H711	121.8
C30—C31—C32	123.3 (3)	C71 ⁱⁱ —C72—C73	120.6 (4)
C30—C31—H311	118.6	C71 ⁱⁱ —C72—H721	120.3
C32—C31—H311	118.1	C73—C72—H721	119.1
C31—C32—C33	115.1 (3)	C72—C73—C65	120.1 (4)
C31—C32—C34	122.9 (3)	C72—C73—H731	120.3
C33—C32—C34	122.0 (3)	C65—C73—H731	119.6
C32—C33—C6	122.9 (3)		

Symmetry codes: (i) $-x+1, -y+2, -z+1$; (ii) $-x+1, -y+2, -z$.

Hydrogen-bond geometry (Å, °) for (1)

$D-H\cdots A$	$D-H$	$H\cdots A$	$D\cdots A$	$D-H\cdots A$
C69—H691 \cdots O8	0.975	2.471	3.424 (6)	165.6 (2)

Document origin: *publCIF* [Westrip, S. P. (2010). *J. Apply. Cryst.*, **43**, 920-925].

[(thiaSO₂)₂Al₄(DMF)₄(OH)₄]**Crystal data**

C ₉₂ H ₁₂₀ Al ₄ N ₄ O ₃₂ S ₈	$F(000) = 2272$
$M_r = 2158.33$	$D_x = 1.157 \text{ Mg m}^{-3}$
Monoclinic, $P2_1/n$	Mo $K\alpha$ radiation, $\lambda = 0.7107 \text{ \AA}$
Hall symbol: $-P 2yn$	Cell parameters from 12609 reflections
$a = 13.9483 (4) \text{ \AA}$	$\theta = 3.1\text{--}24.7^\circ$
$b = 22.9112 (7) \text{ \AA}$	$\mu = 0.24 \text{ mm}^{-1}$
$c = 20.0188 (6) \text{ \AA}$	$T = 293 \text{ K}$
$\beta = 104.424 (3)^\circ$	Plate, colorless
$V = 6195.8 (3) \text{ \AA}^3$	$0.28 \times 0.12 \times 0.08 \text{ mm}$
$Z = 2$	

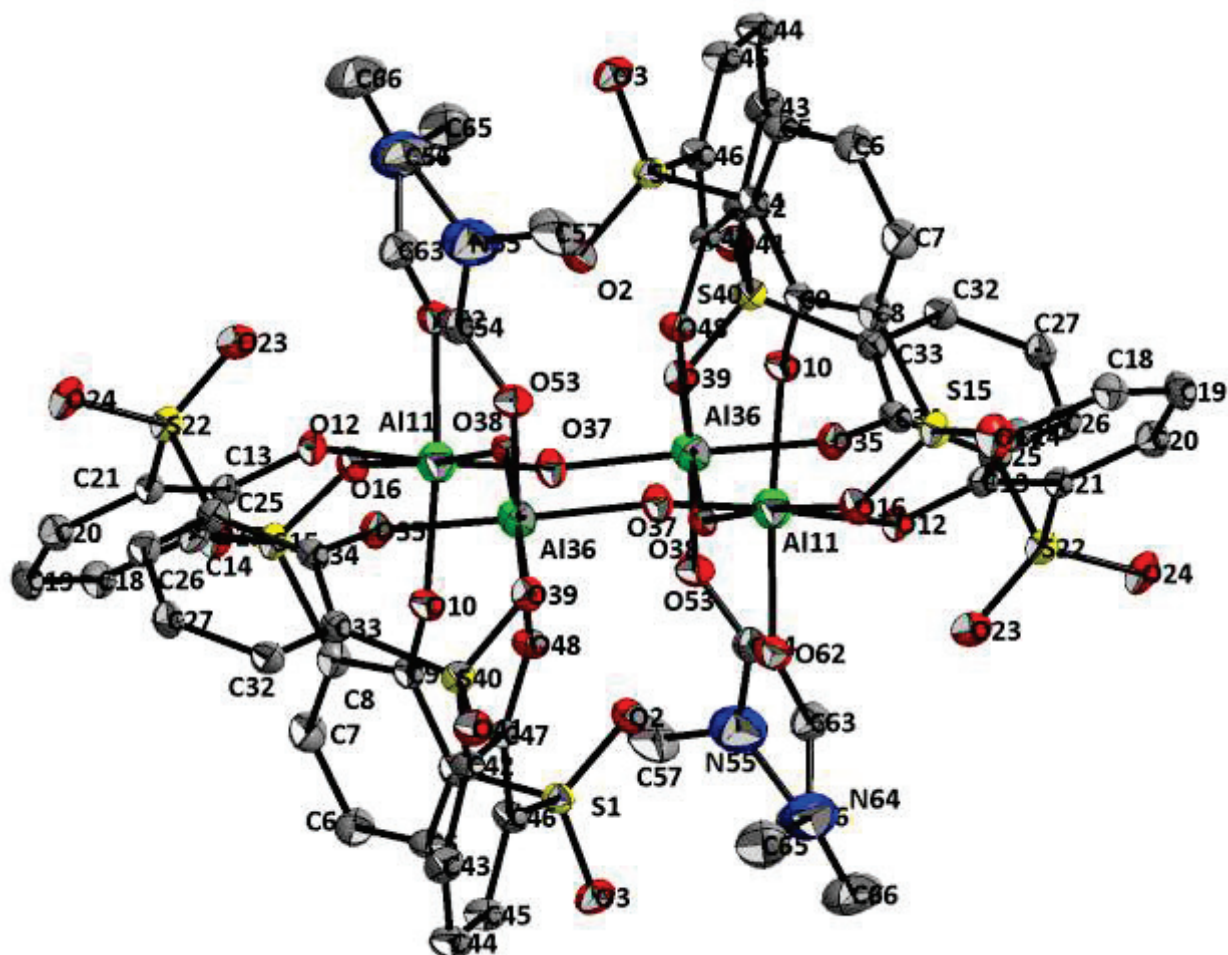
Data collection

Xcalibur, Onyx diffractometer	15054 independent reflections
Radiation source: Enhance (Mo) X-ray Source	8316 reflections with $I > 2.0\sigma(I)$
Graphite monochromator	$R_{\text{int}} = 0.087$
Detector resolution: $8.2634 \text{ pixels mm}^{-1}$	$\theta_{\text{max}} = 29.3^\circ$, $\theta_{\text{min}} = 2.8^\circ$
ω scans	$h = -18 \rightarrow 18$
Absorption correction: multi-scan <i>CrysAlis PRO</i> , Agilent Technologies, Version 1.171.36.24 (release 03-12-2012 CrysAlis171.NET) (compiled Dec 3 2012, 18:21:49) Empirical absorption correction using spherical harmonics, implemented in SCALE3 ABSPACK scaling algorithm.	$k = 0 \rightarrow 30$
$T_{\text{min}} = 0.958$, $T_{\text{max}} = 1.000$	$l = 0 \rightarrow 27$
15054 measured reflections	

Refinement

Refinement on F^2	Primary atom site location: structure-invariant direct methods
Least-squares matrix: full	Hydrogen site location: difference Fourier map
$R[F^2 > 2\sigma(F^2)] = 0.078$	H atoms treated by a mixture of independent and constrained refinement
$wR(F^2) = 0.209$	Method, part 1, Chebychev polynomial, (Watkin, 1994, Prince, 1982) [weight] = $1.0/[A_0*T_0(x) + A_1*T_1(x) \dots + A_{n-1}*T_{n-1}(x)]$ where A_i are the Chebychev coefficients listed below and $x = F/F_{\text{max}}$ Method = Robust Weighting (Prince, 1982) $W = [\text{weight}] * [1 - (\Delta F/6*\sigma F)^2]$ A_i are: 85.8 119. 58.9

	14.6
$S = 1.00$	$(\Delta/\sigma)_{\max} = 0.001$
15012 reflections	$\Delta_{\max} = 1.17 \text{ e } \text{Å}^{-3}$
637 parameters	$\Delta_{\min} = -1.18 \text{ e } \text{Å}^{-3}$
2 restraints	



Fractional atomic coordinates and isotropic or equivalent isotropic displacement parameters (Å^2)

	x	y	z	$U_{\text{iso}}^*/U_{\text{eq}}$
S1	1.11365 (9)	0.56871 (6)	0.33607 (6)	0.0336

O2	1.1380 (3)	0.55237 (16)	0.40741 (18)	0.0381
O3	1.1914 (3)	0.59542 (18)	0.3105 (2)	0.0457
C4	1.0762 (4)	0.5061 (2)	0.2844 (3)	0.0346
C5	1.1219 (4)	0.4963 (3)	0.2311 (3)	0.0423
C6	1.1066 (4)	0.4464 (3)	0.1906 (3)	0.0505
C7	1.0425 (4)	0.4054 (3)	0.2059 (3)	0.0494
C8	0.9960 (4)	0.4144 (2)	0.2587 (3)	0.0365
C9	1.0094 (4)	0.4655 (2)	0.3005 (2)	0.0314
O10	0.9601 (3)	0.47385 (15)	0.34679 (17)	0.0345
Al11	0.92089 (11)	0.42631 (7)	0.41207 (8)	0.0317
O12	0.7917 (2)	0.42479 (16)	0.36067 (17)	0.0351
C13	0.7504 (4)	0.4184 (2)	0.2961 (2)	0.0317
C14	0.7960 (4)	0.3898 (2)	0.2487 (3)	0.0345
S15	0.91571 (10)	0.36138 (6)	0.27587 (7)	0.0359
O16	0.9395 (3)	0.35447 (16)	0.35084 (18)	0.0390
O17	0.9229 (3)	0.31038 (17)	0.2365 (2)	0.0481
C18	0.7501 (4)	0.3824 (2)	0.1794 (3)	0.0423
C19	0.6551 (5)	0.4027 (3)	0.1513 (3)	0.0463
C20	0.6073 (4)	0.4289 (3)	0.1968 (3)	0.0456
C21	0.6521 (4)	0.4363 (2)	0.2660 (3)	0.0333
S22	0.57547 (10)	0.46684 (6)	0.31557 (7)	0.0365
O23	0.6043 (3)	0.44674 (17)	0.3856 (2)	0.0439
O24	0.4752 (3)	0.45465 (18)	0.2781 (2)	0.0472
C25	0.5888 (4)	0.5440 (2)	0.3116 (3)	0.0343
C26	0.5091 (4)	0.5739 (3)	0.2708 (3)	0.0412
C27	0.5075 (4)	0.6337 (3)	0.2625 (3)	0.0409
C28	0.4199 (5)	0.6667 (3)	0.2170 (3)	0.0523
C29	0.4555 (6)	0.6975 (4)	0.1591 (4)	0.0769
C30	0.3349 (5)	0.6256 (3)	0.1840 (4)	0.0782
C31	0.3805 (6)	0.7118 (4)	0.2596 (4)	0.0789
C32	0.5920 (4)	0.6636 (2)	0.2977 (3)	0.0381
C33	0.6723 (4)	0.6345 (2)	0.3385 (3)	0.0335
C34	0.6764 (4)	0.5726 (2)	0.3470 (2)	0.0331
O35	0.7539 (3)	0.54570 (15)	0.38206 (18)	0.0355
Al36	0.85791 (11)	0.56248 (7)	0.45947 (7)	0.0295
O37	0.9489 (3)	0.58564 (17)	0.54039 (18)	0.0379
O38	0.8967 (3)	0.48539 (15)	0.46753 (16)	0.0312
O39	0.8121 (3)	0.64840 (15)	0.44967 (18)	0.0350
S40	0.77633 (9)	0.67443 (5)	0.38134 (7)	0.0329
O41	0.7495 (3)	0.73484 (16)	0.3794 (2)	0.0423

C42	0.8697 (4)	0.6645 (2)	0.3376 (3)	0.0326
C43	0.8710 (4)	0.7049 (2)	0.2858 (3)	0.0427
C44	0.9437 (5)	0.7028 (2)	0.2492 (3)	0.0456
C45	1.0139 (4)	0.6589 (2)	0.2671 (3)	0.0422
C46	1.0144 (4)	0.6185 (2)	0.3184 (3)	0.0337
C47	0.9406 (3)	0.6192 (2)	0.3578 (2)	0.0288
O48	0.9437 (3)	0.58274 (15)	0.40702 (18)	0.0348
C49	0.9514 (6)	0.7498 (3)	0.1958 (4)	0.0644
C50	1.0330 (10)	0.7917 (5)	0.2306 (7)	0.1516
C51	0.9805 (9)	0.7215 (4)	0.1345 (5)	0.1319
C52	0.8557 (8)	0.7818 (4)	0.1692 (5)	0.1100
O53	0.7660 (3)	0.55845 (17)	0.51730 (19)	0.0406
C54	0.7076 (4)	0.5175 (3)	0.5181 (3)	0.0414
N55	0.6574 (4)	0.5134 (3)	0.5660 (3)	0.0541
C56	0.5937 (6)	0.4634 (4)	0.5665 (4)	0.0784
C57	0.6738 (6)	0.5546 (4)	0.6234 (4)	0.0808
C58	0.6034 (6)	0.3959 (4)	0.0739 (3)	0.0650
C59	0.5664 (15)	0.3376 (5)	0.0608 (6)	0.2580
C60	0.5194 (13)	0.4335 (7)	0.0523 (5)	0.2483
C61	0.6702 (11)	0.4088 (13)	0.0329 (5)	0.3267
O62	0.8876 (3)	0.36533 (17)	0.46872 (19)	0.0440
C63	0.8094 (5)	0.3556 (3)	0.4836 (3)	0.0514
N64	0.7960 (5)	0.3099 (3)	0.5206 (3)	0.0633
C65	0.8731 (7)	0.2687 (4)	0.5443 (5)	0.0952
C66	0.7033 (7)	0.3019 (5)	0.5389 (5)	0.1140
C67	1.1588 (6)	0.4355 (4)	0.1327 (4)	0.0764
C68	1.0872 (12)	0.4194 (10)	0.0702 (6)	0.2342
C69	1.2296 (14)	0.4770 (7)	0.1279 (9)	0.2843
C70	1.2206 (15)	0.3793 (8)	0.1494 (10)	0.2491
H51	1.1646	0.5250	0.2226	0.0498*
H71	1.0302	0.3710	0.1803	0.0589*
H181	0.7839	0.3634	0.1512	0.0510*
H201	0.5428	0.4419	0.1802	0.0547*
H261	0.4549	0.5524	0.2475	0.0487*
H291	0.4027	0.7202	0.1312	0.1149*
H292	0.5097	0.7230	0.1786	0.1149*
H293	0.4763	0.6690	0.1304	0.1150*
H301	0.2799	0.6482	0.1582	0.1148*
H302	0.3148	0.6042	0.2194	0.1150*
H303	0.3568	0.5989	0.1538	0.1149*

H313	0.3286	0.7341	0.2300	0.1168*
H312	0.4328	0.7376	0.2816	0.1169*
H311	0.3550	0.6923	0.2937	0.1170*
H321	0.5946	0.7040	0.2941	0.0458*
H431	0.8226	0.7337	0.2759	0.0510*
H451	1.0636	0.6566	0.2436	0.0511*
H501	1.0399	0.8215	0.1986	0.2249*
H503	1.0155	0.8093	0.2693	0.2250*
H502	1.0945	0.7712	0.2459	0.2250*
H512	0.9835	0.7510	0.1015	0.1949*
H511	1.0440	0.7030	0.1500	0.1950*
H513	0.9319	0.6931	0.1139	0.1949*
H522	0.8647	0.8117	0.1380	0.1649*
H523	0.8345	0.7989	0.2068	0.1649*
H521	0.8065	0.7547	0.1451	0.1649*
H541	0.6981	0.4889	0.4837	0.0489*
H562	0.5296	0.4766	0.5691	0.1169*
H563	0.6220	0.4396	0.6058	0.1169*
H561	0.5879	0.4407	0.5250	0.1168*
H573	0.6859	0.5333	0.6660	0.1211*
H571	0.7302	0.5789	0.6232	0.1210*
H572	0.6162	0.5787	0.6185	0.1211*
H631	0.7564	0.3815	0.4685	0.0599*
H652	0.8487	0.2304	0.5306	0.1440*
H653	0.8949	0.2703	0.5934	0.1440*
H651	0.9271	0.2774	0.5243	0.1440*
H663	0.6751	0.2647	0.5219	0.1709*
H661	0.7155	0.3028	0.5882	0.1710*
H662	0.6586	0.3328	0.5191	0.1710*
H681	1.1174	0.3933	0.0443	0.3440*
H683	1.0658	0.4540	0.0435	0.3440*
H682	1.0311	0.4008	0.0807	0.3440*
H702	1.2806	0.3835	0.1346	0.3680*
H703	1.2367	0.3720	0.1982	0.3680*
H701	1.1835	0.3471	0.1257	0.3680*
H381	0.921 (4)	0.479 (3)	0.5081 (12)	0.0469*
H371	0.932 (5)	0.612 (2)	0.561 (3)	0.0573*
H591	0.5429	0.3315	0.0120	0.3470*
H592	0.6187	0.3105	0.0791	0.3470*
H593	0.5129	0.3321	0.0824	0.3470*

H601	0.5227	0.4525	0.0104	0.3360*
H602	0.5186	0.4622	0.0870	0.3360*
H603	0.4607	0.4104	0.0446	0.3359*
H611	0.6563	0.3854	-0.0080	0.4570*
H612	0.6602	0.4490	0.0206	0.4569*
H613	0.7370	0.4026	0.0587	0.4570*
H691	1.2584	0.4674	0.0910	0.3127*
H692	1.2795	0.4773	0.1700	0.3127*
H693	1.2000	0.5146	0.1200	0.3127*

Atomic displacement parameters (\AA^2)

	U^{11}	U^{22}	U^{33}	U^{12}	U^{13}	U^{23}
S1	0.0340 (6)	0.0351 (7)	0.0332 (6)	-0.0005 (5)	0.0115 (5)	0.0007 (5)
O2	0.0375 (19)	0.044 (2)	0.0334 (19)	0.0039 (16)	0.0094 (15)	0.0025 (16)
O3	0.039 (2)	0.050 (2)	0.053 (2)	-0.0065 (18)	0.0223 (18)	-0.0014 (19)
C4	0.039 (3)	0.035 (3)	0.031 (3)	0.004 (2)	0.011 (2)	-0.001 (2)
C5	0.043 (3)	0.050 (3)	0.039 (3)	-0.009 (3)	0.019 (2)	-0.001 (3)
C6	0.047 (3)	0.068 (4)	0.043 (3)	-0.010 (3)	0.023 (3)	-0.013 (3)
C7	0.054 (4)	0.057 (4)	0.041 (3)	-0.006 (3)	0.019 (3)	-0.019 (3)
C8	0.038 (3)	0.036 (3)	0.037 (3)	0.001 (2)	0.012 (2)	-0.007 (2)
C9	0.034 (3)	0.033 (3)	0.028 (2)	0.003 (2)	0.010 (2)	0.000 (2)
O10	0.043 (2)	0.0334 (18)	0.0308 (18)	-0.0003 (15)	0.0169 (15)	-0.0029 (15)
Al11	0.0350 (8)	0.0309 (8)	0.0292 (7)	-0.0004 (6)	0.0080 (6)	-0.0005 (6)
O12	0.0304 (17)	0.043 (2)	0.0305 (18)	-0.0023 (15)	0.0042 (14)	-0.0055 (16)
C13	0.037 (3)	0.028 (2)	0.031 (2)	-0.005 (2)	0.009 (2)	-0.002 (2)
C14	0.031 (2)	0.036 (3)	0.037 (3)	-0.002 (2)	0.007 (2)	-0.003 (2)
S15	0.0382 (7)	0.0325 (6)	0.0371 (7)	-0.0004 (5)	0.0096 (5)	-0.0072 (5)
O16	0.041 (2)	0.040 (2)	0.0340 (19)	0.0009 (16)	0.0074 (16)	-0.0038 (16)
O17	0.055 (2)	0.042 (2)	0.049 (2)	-0.0001 (19)	0.017 (2)	-0.0164 (19)
C18	0.053 (3)	0.039 (3)	0.037 (3)	-0.002 (3)	0.015 (3)	-0.006 (2)
C19	0.053 (4)	0.049 (3)	0.033 (3)	-0.003 (3)	0.004 (3)	-0.003 (3)
C20	0.043 (3)	0.048 (3)	0.042 (3)	0.000 (3)	0.004 (2)	0.001 (3)
C21	0.032 (2)	0.032 (3)	0.036 (3)	-0.002 (2)	0.009 (2)	-0.001 (2)
S22	0.0324 (6)	0.0369 (7)	0.0408 (7)	-0.0031 (5)	0.0104 (5)	-0.0019 (6)
O23	0.045 (2)	0.043 (2)	0.047 (2)	-0.0019 (18)	0.0178 (18)	0.0034 (18)
O24	0.0323 (19)	0.048 (2)	0.061 (3)	-0.0058 (17)	0.0110 (18)	-0.006 (2)
C25	0.034 (3)	0.031 (3)	0.039 (3)	0.000 (2)	0.010 (2)	0.000 (2)
C26	0.034 (3)	0.047 (3)	0.042 (3)	-0.002 (2)	0.007 (2)	-0.002 (3)
C27	0.035 (3)	0.047 (3)	0.039 (3)	0.001 (2)	0.005 (2)	0.006 (2)
C28	0.043 (3)	0.050 (4)	0.056 (4)	0.002 (3)	-0.001 (3)	0.009 (3)

C29	0.075 (5)	0.080 (5)	0.062 (5)	-0.006 (4)	-0.011 (4)	0.021 (4)
C30	0.051 (4)	0.072 (5)	0.091 (6)	-0.004 (4)	-0.022 (4)	0.019 (4)
C31	0.058 (5)	0.083 (6)	0.088 (6)	0.025 (4)	0.003 (4)	0.003 (5)
C32	0.040 (3)	0.035 (3)	0.039 (3)	0.003 (2)	0.009 (2)	0.004 (2)
C33	0.033 (3)	0.036 (3)	0.032 (3)	0.002 (2)	0.010 (2)	0.000 (2)
C34	0.036 (3)	0.038 (3)	0.026 (2)	0.004 (2)	0.010 (2)	0.002 (2)
O35	0.0332 (18)	0.0342 (19)	0.0367 (19)	0.0034 (15)	0.0043 (15)	0.0004 (15)
Al36	0.0297 (7)	0.0326 (8)	0.0267 (7)	0.0021 (6)	0.0081 (6)	0.0013 (6)
O37	0.0353 (19)	0.044 (2)	0.0332 (19)	0.0037 (16)	0.0071 (15)	-0.0086 (16)
O38	0.0350 (19)	0.0340 (18)	0.0238 (16)	0.0004 (14)	0.0057 (14)	0.0002 (14)
O39	0.0358 (19)	0.0342 (19)	0.0353 (19)	0.0020 (15)	0.0095 (15)	-0.0038 (15)
S40	0.0321 (6)	0.0310 (6)	0.0357 (6)	0.0013 (5)	0.0086 (5)	0.0006 (5)
O41	0.046 (2)	0.033 (2)	0.047 (2)	0.0041 (16)	0.0094 (18)	0.0018 (17)
C42	0.035 (3)	0.031 (2)	0.033 (3)	0.001 (2)	0.011 (2)	0.003 (2)
C43	0.044 (3)	0.035 (3)	0.050 (3)	0.003 (2)	0.014 (3)	0.004 (2)
C44	0.059 (4)	0.037 (3)	0.045 (3)	0.003 (3)	0.021 (3)	0.008 (3)
C45	0.052 (3)	0.037 (3)	0.043 (3)	0.003 (2)	0.022 (3)	0.007 (2)
C46	0.036 (3)	0.032 (3)	0.034 (3)	0.003 (2)	0.010 (2)	0.001 (2)
C47	0.030 (2)	0.027 (2)	0.028 (2)	-0.0029 (18)	0.0056 (19)	0.0007 (19)
O48	0.0359 (19)	0.0362 (19)	0.0355 (19)	0.0039 (15)	0.0150 (15)	0.0068 (15)
C49	0.083 (5)	0.055 (4)	0.067 (4)	0.020 (4)	0.041 (4)	0.031 (4)
C50	0.190 (13)	0.097 (8)	0.158 (12)	-0.055 (8)	0.024 (10)	0.066 (8)
C51	0.226 (13)	0.113 (8)	0.098 (7)	0.076 (8)	0.118 (8)	0.065 (6)
C52	0.149 (9)	0.099 (7)	0.103 (7)	0.062 (7)	0.069 (7)	0.072 (6)
O53	0.041 (2)	0.044 (2)	0.042 (2)	0.0001 (17)	0.0197 (17)	-0.0004 (17)
C54	0.037 (3)	0.045 (3)	0.041 (3)	0.003 (2)	0.008 (2)	0.005 (2)
N55	0.044 (3)	0.069 (4)	0.056 (3)	0.003 (3)	0.025 (2)	0.009 (3)
C56	0.060 (5)	0.094 (6)	0.088 (6)	-0.012 (4)	0.033 (4)	0.026 (5)
C57	0.084 (6)	0.111 (7)	0.062 (5)	0.000 (5)	0.047 (4)	-0.011 (5)
C58	0.066 (4)	0.086 (5)	0.035 (3)	0.008 (4)	-0.004 (3)	-0.005 (3)
C59	0.45 (3)	0.103 (10)	0.101 (9)	-0.070 (14)	-0.154 (14)	-0.001 (7)
C60	0.36 (2)	0.259 (18)	0.060 (6)	0.223 (18)	-0.082 (10)	-0.047 (9)
C61	0.152 (13)	0.79 (5)	0.030 (5)	-0.15 (2)	0.013 (7)	-0.027 (14)
O62	0.053 (2)	0.039 (2)	0.039 (2)	-0.0024 (18)	0.0122 (18)	0.0053 (17)
C63	0.050 (4)	0.052 (4)	0.054 (4)	-0.003 (3)	0.018 (3)	-0.004 (3)
N64	0.081 (4)	0.054 (3)	0.058 (3)	-0.022 (3)	0.023 (3)	0.003 (3)
C65	0.113 (8)	0.063 (5)	0.100 (7)	-0.010 (5)	0.009 (6)	0.026 (5)
C66	0.110 (8)	0.141 (10)	0.107 (8)	-0.048 (7)	0.057 (6)	0.007 (7)
C67	0.078 (5)	0.107 (7)	0.059 (4)	-0.024 (5)	0.046 (4)	-0.035 (4)
C68	0.215 (16)	0.45 (3)	0.079 (8)	-0.159 (19)	0.106 (10)	-0.108 (13)

C69	0.41 (3)	0.27 (2)	0.30 (2)	-0.24 (2)	0.33 (2)	-0.210 (17)
C70	0.31 (2)	0.25 (2)	0.28 (2)	0.107 (19)	0.26 (2)	0.029 (17)

Geometric parameters (Å, °) for (1)

S1—O2	1.433 (4)	S40—O41	1.432 (4)
S1—O3	1.445 (4)	S40—C42	1.755 (5)
S1—C4	1.771 (5)	C42—C43	1.393 (7)
S1—C46	1.760 (5)	C42—C47	1.421 (7)
C4—C5	1.390 (7)	C43—C44	1.392 (8)
C4—C9	1.409 (7)	C43—H431	0.930
C5—C6	1.387 (8)	C44—C45	1.387 (8)
C5—H51	0.931	C44—C49	1.540 (8)
C6—C7	1.383 (8)	C45—C46	1.383 (7)
C6—C67	1.535 (8)	C45—H451	0.931
C7—C8	1.387 (7)	C46—C47	1.443 (7)
C7—H71	0.932	C47—O48	1.285 (6)
C8—C9	1.425 (7)	C49—C50	1.520 (13)
C8—S15	1.742 (5)	C49—C51	1.528 (11)
C9—O10	1.298 (6)	C49—C52	1.501 (11)
O10—Al11	1.884 (4)	C50—H501	0.957
Al11—O37 ⁱ	1.848 (4)	C50—H503	0.957
Al11—O12	1.840 (4)	C50—H502	0.959
Al11—O16	2.107 (4)	C51—H512	0.953
Al11—O38	1.834 (4)	C51—H511	0.961
Al11—O62	1.928 (4)	C51—H513	0.955
O12—C13	1.286 (6)	C52—H522	0.956
C13—C14	1.426 (7)	C52—H523	0.958
C13—C21	1.415 (7)	C52—H521	0.962
C14—S15	1.747 (5)	O53—C54	1.245 (6)
C14—C18	1.386 (7)	C54—N55	1.325 (7)
S15—O16	1.463 (4)	C54—H541	0.936
S15—O17	1.427 (4)	N55—C56	1.451 (9)
C18—C19	1.385 (8)	N55—C57	1.460 (9)
C18—H181	0.929	C56—H562	0.958
C19—C20	1.391 (8)	C56—H563	0.958
C19—C58	1.545 (8)	C56—H561	0.967
C20—C21	1.380 (7)	C57—H573	0.961
C20—H201	0.928	C57—H571	0.964
C21—S22	1.773 (5)	C57—H572	0.959
S22—O23	1.434 (4)	C58—C59	1.433 (13)

S22—O24	1.440 (4)	C58—C60	1.432 (13)
S22—C25	1.782 (5)	C58—C61	1.418 (14)
C25—C26	1.385 (7)	C59—H591	0.960
C25—C34	1.411 (7)	C59—H592	0.958
C26—C27	1.381 (8)	C59—H593	0.959
C26—H261	0.924	C60—H601	0.958
C27—C28	1.529 (8)	C60—H602	0.958
C27—C32	1.393 (7)	C60—H603	0.955
C28—C29	1.542 (10)	C61—H611	0.957
C28—C30	1.529 (9)	C61—H612	0.955
C28—C31	1.527 (10)	C61—H613	0.957
C29—H291	0.958	O62—C63	1.221 (7)
C29—H292	0.959	C63—N64	1.322 (8)
C29—H293	0.961	C63—H631	0.937
C30—H301	0.961	N64—C65	1.421 (10)
C30—H302	0.959	N64—C66	1.441 (10)
C30—H303	0.962	C65—H652	0.957
C31—H313	0.960	C65—H653	0.955
C31—H312	0.956	C65—H651	0.959
C31—H311	0.956	C66—H663	0.962
C32—C33	1.382 (7)	C66—H661	0.960
C32—H321	0.930	C66—H662	0.961
C33—C34	1.428 (7)	C67—C68	1.441 (14)
C33—S40	1.748 (5)	C67—C69	1.393 (13)
C34—O35	1.290 (6)	C67—C70	1.540 (18)
O35—Al36	1.880 (4)	C68—H681	0.956
Al36—O37	1.869 (4)	C68—H683	0.959
Al36—O38	1.843 (4)	C68—H682	0.959
Al36—O39	2.064 (4)	C69—H691	0.950
Al36—O48	1.837 (4)	C69—H692	0.950
Al36—O53	1.932 (4)	C69—H693	0.950
O37—H371	0.810 (19)	C70—H702	0.959
O38—H381	0.809 (19)	C70—H703	0.961
O39—S40	1.461 (4)	C70—H701	0.956
O2—S1—O3	116.8 (2)	Al36—O39—S40	120.2 (2)
O2—S1—C4	109.4 (2)	C33—S40—O39	107.1 (2)
O3—S1—C4	105.9 (2)	C33—S40—O41	108.3 (2)
O2—S1—C46	110.4 (2)	O39—S40—O41	116.5 (2)
O3—S1—C46	106.0 (2)	C33—S40—C42	108.4 (2)

C4—S1—C46	107.8 (2)	O39—S40—C42	106.9 (2)
S1—C4—C5	117.0 (4)	O41—S40—C42	109.4 (2)
S1—C4—C9	121.1 (4)	S40—C42—C43	115.7 (4)
C5—C4—C9	121.7 (5)	S40—C42—C47	120.3 (4)
C4—C5—C6	123.2 (5)	C43—C42—C47	123.9 (5)
C4—C5—H51	117.6	C42—C43—C44	121.1 (5)
C6—C5—H51	119.2	C42—C43—H431	119.2
C5—C6—C7	116.4 (5)	C44—C43—H431	119.8
C5—C6—C67	122.9 (6)	C43—C44—C45	116.7 (5)
C7—C6—C67	120.7 (6)	C43—C44—C49	121.9 (5)
C6—C7—C8	121.3 (5)	C45—C44—C49	121.3 (5)
C6—C7—H71	119.6	C44—C45—C46	123.4 (5)
C8—C7—H71	119.2	C44—C45—H451	118.5
C7—C8—C9	123.5 (5)	C46—C45—H451	118.1
C7—C8—S15	119.5 (4)	S1—C46—C45	116.2 (4)
C9—C8—S15	117.0 (4)	S1—C46—C47	122.0 (4)
C8—C9—C4	113.9 (4)	C45—C46—C47	121.8 (5)
C8—C9—O10	121.7 (5)	C46—C47—C42	113.2 (4)
C4—C9—O10	124.3 (5)	C46—C47—O48	121.3 (4)
C9—O10—A111	135.0 (3)	C42—C47—O48	125.4 (4)
O10—A111—O37 ⁱ	91.42 (18)	C47—O48—A136	134.5 (3)
O10—A111—O12	92.10 (17)	C44—C49—C50	107.3 (7)
O37 ⁱ —A111—O12	170.07 (19)	C44—C49—C51	109.8 (6)
O10—A111—O16	87.07 (15)	C50—C49—C51	108.6 (9)
O37 ⁱ —A111—O16	86.34 (16)	C44—C49—C52	112.2 (6)
O12—A111—O16	84.57 (16)	C50—C49—C52	110.6 (8)
O10—A111—O38	97.02 (16)	C51—C49—C52	108.3 (7)
O37 ⁱ —A111—O38	95.89 (16)	C49—C50—H501	109.4
O12—A111—O38	92.89 (16)	C49—C50—H503	108.9
O16—A111—O38	175.27 (17)	H501—C50—H503	109.3
O10—A111—O62	168.87 (18)	C49—C50—H502	110.1
O37 ⁱ —A111—O62	86.54 (18)	H501—C50—H502	109.5
O12—A111—O62	88.23 (17)	H503—C50—H502	109.6
O16—A111—O62	81.88 (16)	C49—C51—H512	108.7
O38—A111—O62	94.08 (17)	C49—C51—H511	109.7
A111—O12—C13	134.1 (3)	H512—C51—H511	109.9
O12—C13—C14	124.0 (5)	C49—C51—H513	109.5
O12—C13—C21	122.6 (5)	H512—C51—H513	109.3
C14—C13—C21	113.4 (4)	H511—C51—H513	109.6
C13—C14—S15	121.0 (4)	C49—C52—H522	109.3

C13—C14—C18	123.3 (5)	C49—C52—H523	110.0
S15—C14—C18	115.7 (4)	H522—C52—H523	109.7
C14—S15—C8	106.9 (3)	C49—C52—H521	108.8
C14—S15—O16	108.3 (2)	H522—C52—H521	109.3
C8—S15—O16	106.6 (2)	H523—C52—H521	109.7
C14—S15—O17	109.0 (2)	A136—O53—C54	125.3 (4)
C8—S15—O17	108.9 (2)	O53—C54—N55	121.9 (6)
O16—S15—O17	116.7 (2)	O53—C54—H541	119.5
A111—O16—S15	118.9 (2)	N55—C54—H541	118.6
C14—C18—C19	121.5 (5)	C54—N55—C56	119.7 (6)
C14—C18—H181	119.2	C54—N55—C57	121.0 (6)
C19—C18—H181	119.3	C56—N55—C57	118.8 (6)
C18—C19—C20	116.4 (5)	N55—C56—H562	109.4
C18—C19—C58	122.2 (6)	N55—C56—H563	109.0
C20—C19—C58	121.3 (6)	H562—C56—H563	109.5
C19—C20—C21	122.7 (5)	N55—C56—H561	109.9
C19—C20—H201	119.0	H562—C56—H561	109.8
C21—C20—H201	118.4	H563—C56—H561	109.2
C13—C21—C20	122.6 (5)	N55—C57—H573	109.1
C13—C21—S22	122.1 (4)	N55—C57—H571	109.9
C20—C21—S22	115.2 (4)	H573—C57—H571	109.4
C21—S22—O23	111.1 (2)	N55—C57—H572	109.3
C21—S22—O24	105.9 (2)	H573—C57—H572	109.8
O23—S22—O24	116.5 (2)	H571—C57—H572	109.3
C21—S22—C25	106.4 (2)	C19—C58—C59	109.6 (7)
O23—S22—C25	110.8 (2)	C19—C58—C60	112.6 (7)
O24—S22—C25	105.5 (2)	C59—C58—C60	106.0 (12)
S22—C25—C26	116.0 (4)	C19—C58—C61	110.5 (7)
S22—C25—C34	121.7 (4)	C59—C58—C61	110.3 (14)
C26—C25—C34	122.3 (5)	C60—C58—C61	107.8 (13)
C25—C26—C27	123.2 (5)	C58—C59—H591	109.7
C25—C26—H261	118.0	C58—C59—H592	109.2
C27—C26—H261	118.7	H591—C59—H592	109.3
C26—C27—C28	123.3 (5)	C58—C59—H593	108.9
C26—C27—C32	116.1 (5)	H591—C59—H593	109.5
C28—C27—C32	120.7 (5)	H592—C59—H593	110.3
C27—C28—C29	108.4 (5)	C58—C60—H601	108.9
C27—C28—C30	111.9 (5)	C58—C60—H602	110.5
C29—C28—C30	108.6 (6)	H601—C60—H602	109.6
C27—C28—C31	110.3 (5)	C58—C60—H603	108.6

C29—C28—C31	109.7 (6)	H601—C60—H603	109.7
C30—C28—C31	108.0 (6)	H602—C60—H603	109.5
C28—C29—H291	110.0	C58—C61—H611	111.0
C28—C29—H292	110.0	C58—C61—H612	106.0
H291—C29—H292	108.8	H611—C61—H612	109.4
C28—C29—H293	109.7	C58—C61—H613	110.5
H291—C29—H293	109.0	H611—C61—H613	109.9
H292—C29—H293	109.4	H612—C61—H613	110.0
C28—C30—H301	109.3	A111—O62—C63	129.6 (4)
C28—C30—H302	109.5	O62—C63—N64	122.8 (6)
H301—C30—H302	109.4	O62—C63—H631	119.0
C28—C30—H303	109.2	N64—C63—H631	118.2
H301—C30—H303	109.8	C63—N64—C65	120.8 (7)
H302—C30—H303	109.7	C63—N64—C66	120.3 (7)
C28—C31—H313	109.6	C65—N64—C66	118.9 (7)
C28—C31—H312	109.7	N64—C65—H652	109.2
H313—C31—H312	109.2	N64—C65—H653	109.7
C28—C31—H311	109.5	H652—C65—H653	109.3
H313—C31—H311	109.4	N64—C65—H651	109.3
H312—C31—H311	109.6	H652—C65—H651	109.4
C27—C32—C33	121.5 (5)	H653—C65—H651	110.0
C27—C32—H321	119.6	N64—C66—H663	109.7
C33—C32—H321	118.9	N64—C66—H661	108.5
C32—C33—C34	123.4 (5)	H663—C66—H661	109.6
C32—C33—S40	119.3 (4)	N64—C66—H662	109.4
C34—C33—S40	117.3 (4)	H663—C66—H662	109.9
C33—C34—C25	113.4 (4)	H661—C66—H662	109.8
C33—C34—O35	122.9 (5)	C6—C67—C68	109.9 (7)
C25—C34—O35	123.7 (5)	C6—C67—C69	114.8 (7)
C34—O35—A136	136.1 (3)	C68—C67—C69	117.7 (11)
O35—A136—O37	172.18 (18)	C6—C67—C70	108.5 (8)
O35—A136—O38	91.48 (16)	C68—C67—C70	101.8 (12)
O37—A136—O38	94.29 (17)	C69—C67—C70	102.6 (12)
O35—A136—O39	87.69 (15)	C67—C68—H681	109.0
O37—A136—O39	86.50 (16)	C67—C68—H683	108.9
O38—A136—O39	179.07 (16)	H681—C68—H683	109.6
O35—A136—O48	93.40 (17)	C67—C68—H682	110.4
O37—A136—O48	91.44 (17)	H681—C68—H682	109.5
O38—A136—O48	94.20 (16)	H683—C68—H682	109.4
O39—A136—O48	86.27 (15)	C67—C69—H691	109.8

O35—Al36—O53	89.60 (17)	C67—C69—H692	108.5
O37—Al36—O53	84.44 (17)	H691—C69—H692	109.5
O38—Al36—O53	97.24 (17)	C67—C69—H693	110.1
O39—Al36—O53	82.33 (16)	H691—C69—H693	109.5
O48—Al36—O53	168.09 (18)	H692—C69—H693	109.5
Al36—O37—Al11 ⁱ	140.6 (2)	C67—C70—H702	109.5
Al36—O37—H371	116 (5)	C67—C70—H703	110.0
Al11 ⁱ —O37—H371	103 (5)	H702—C70—H703	109.3
Al36—O38—Al11	138.5 (2)	C67—C70—H701	109.4
Al36—O38—H381	107 (4)	H702—C70—H701	109.2
Al11—O38—H381	113 (4)	H703—C70—H701	109.4

Symmetry code: (i) $-x+2, -y+1, -z+1$.

Hydrogen-bond geometry (Å, °) for (1)

$D-H\cdots A$	$D-H$	$H\cdots A$	$D\cdots A$	$D-H\cdots A$
C32— H321 \cdots O17 ⁱⁱ	0.93	2.51	3.429 (11)	169 (1)
C54— H541 \cdots O23	0.94	2.29	3.137 (11)	151 (1)
O38—H381 \cdots O2 ⁱ	0.81	2.18	2.803 (11)	134 (5)
C59— H592 \cdots O41 ⁱⁱⁱ	0.96	2.51	3.469 (11)	176 (1)

Symmetry codes: (i) $-x+2, -y+1, -z+1$; (ii) $-x+3/2, y+1/2, -z+1/2$; (iii) $-x+3/2, y-1/2, -z+1/2$.

Document origin: *publCIF* [Westrip, S. P. (2010). *J. Apply. Cryst.*, **43**, 920-925].

ANNEXE 2: CALCULATIONS OF REACTION KINETICS

$$\ln[(1 - \text{Abs}_t) / (\text{Abs}_{\text{max}})] = -k.t$$

By using the first order rate constant law approximation shown above, the rate constant k was calculated by following the growth in the UV-visible absorbance peak centred around 548 nm for various conditions in order to compare and contrast the response of the reaction. By the Beer-Lambert law the absorption intensity can here be assumed to be a direct representation for the concentration of the product (C^+)[Mn(thiaSO₂)L₂], where C^+ is a charge balancing cation and L is the ligand occupying the z-axis sites in the manganese coordination sphere. The results obtained are outlined below.

Temperature: As would be expected, increasing temperature results in an increase in the reaction rate. Measurements were made for the oxidation reaction of complex **2** (K[Mn₄(thiaSO₂)₂F]) in DMF solvent at 10° C, 20° C, 30° C, 40° C, 50° C and 60° C with illumination wavelength of 360 nm. The results are given in table 4.2 and figure 4.18. The values of k range from $-9 \times 10^{-5} \text{ s}^{-1}$ at 10° C to -10×10^{-5} at 60° C.

	A_{max}	t	$\ln((1-A)/A_{\text{max}})$	A	1-A	$(1-A)/A_{\text{max}}$
10° C	0,095590	0	2,356643835	-0,008997	1,008997	10,55546605
	0,095590	120	2,336033426	0,011586	0,988414	10,34014018
	0,095590	240	2,319936559	0,027369	0,972631	10,17502877
	0,095590	360	2,307638731	0,039257	0,960743	10,05066430
	0,095590	480	2,295703008	0,050656	0,949344	9,931415420
	0,095590	600	2,286467831	0,059383	0,940617	9,840119259
	0,095590	720	2,277555333	0,067729	0,932271	9,752808871
	0,095590	840	2,265434169	0,078961	0,921039	9,635307040
	0,095590	960	2,261654120	0,082436	0,917564	9,598953865
	0,095590	1080	2,254912570	0,088601	0,911399	9,534459672
	0,095590	1200	2,247214585	0,095590	0,904410	9,461345329

20° C	0,167781	0	1,788108179	-0,003017	1,003017	5,978132208
	0,167781	180	1,739960271	0,044132	0,955868	5,697117075
	0,167781	390	1,697598044	0,083779	0,916221	5,460814991
	0,167781	540	1,673477892	0,105614	0,894386	5,330675106
	0,167781	720	1,658518379	0,118894	0,881106	5,251524308
	0,167781	900	1,644189775	0,131429	0,868571	5,176813823

0,167781	1080	1,630430576	0,143298	0,856702	5,106072797
0,167781	1260	1,620898914	0,151425	0,848575	5,057634655
0,167781	1440	1,613786506	0,157439	0,842561	5,02179031
0,167781	1620	1,60624055	0,163773	0,836227	4,984038717
0,167781	1800	1,60143607	0,167781	0,832219	4,960150434

30° C	0,180511	0	1,714406575	-0,002446	1,002446	5,553379018
	0,180511	180	1,640719944	0,068765	0,931235	5,158882284
	0,180511	360	1,604413985	0,101968	0,898032	4,974943355
	0,180511	540	1,583747162	0,120337	0,879663	4,873182244
	0,180511	720	1,570167251	0,132202	0,867798	4,807452177
	0,180511	900	1,557953038	0,142737	0,857263	4,749090083
	0,180511	1080	1,548468862	0,150829	0,849171	4,70426179
	0,180511	1260	1,537968443	0,159699	0,840301	4,65512351
	0,180511	1440	1,527983029	0,168048	0,831952	4,608871482
	0,180511	1620	1,512889258	0,180511	0,819489	4,539828598

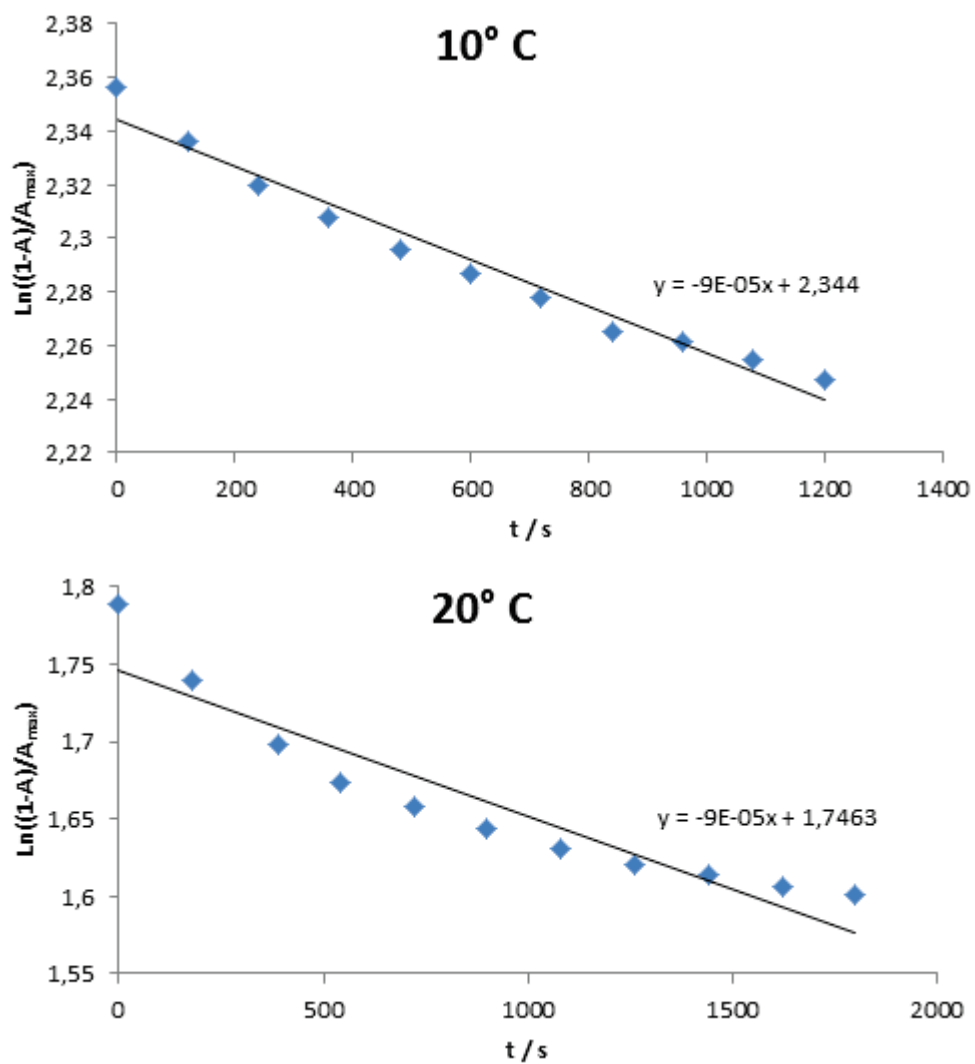
40° C	0,179770	0	1,715012456	0,001064	0,998936	5,556744729
	0,179770	120	1,659912938	0,054616	0,945384	5,258852979
	0,179770	240	1,614687501	0,096419	0,903581	5,026316961
	0,179770	360	1,585681280	0,122252	0,877748	4,882616677
	0,179770	480	1,567844960	0,137769	0,862231	4,796300829
	0,179770	600	1,551448812	0,151791	0,848209	4,718301163
	0,179770	720	1,541536714	0,160157	0,839843	4,671763921
	0,179770	840	1,536036064	0,164764	0,835236	4,646136730
	0,179770	960	1,528183572	0,171297	0,828703	4,609795850
	0,179770	1080	1,523000640	0,175581	0,824419	4,585965400
	0,179770	1200	1,517906533	0,179770	0,820230	4,562663403

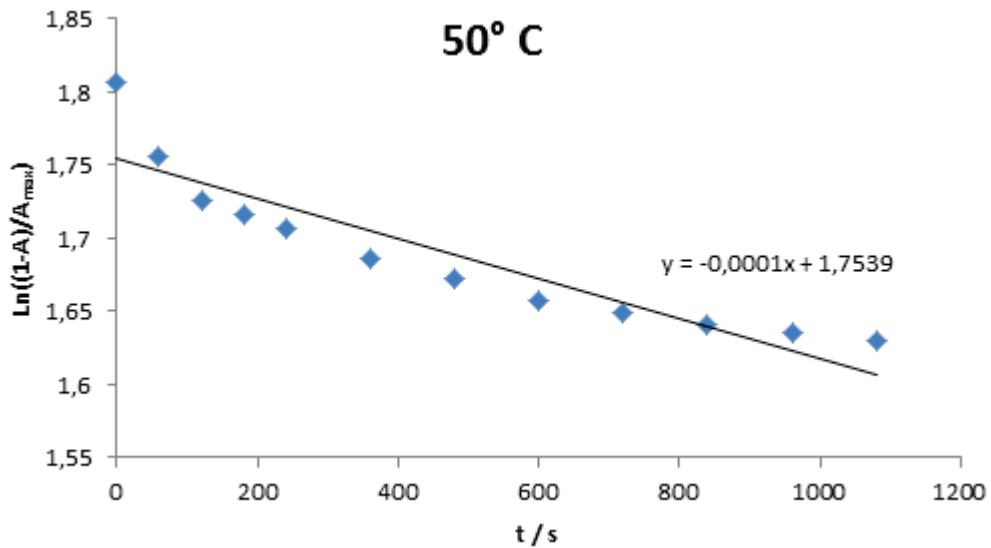
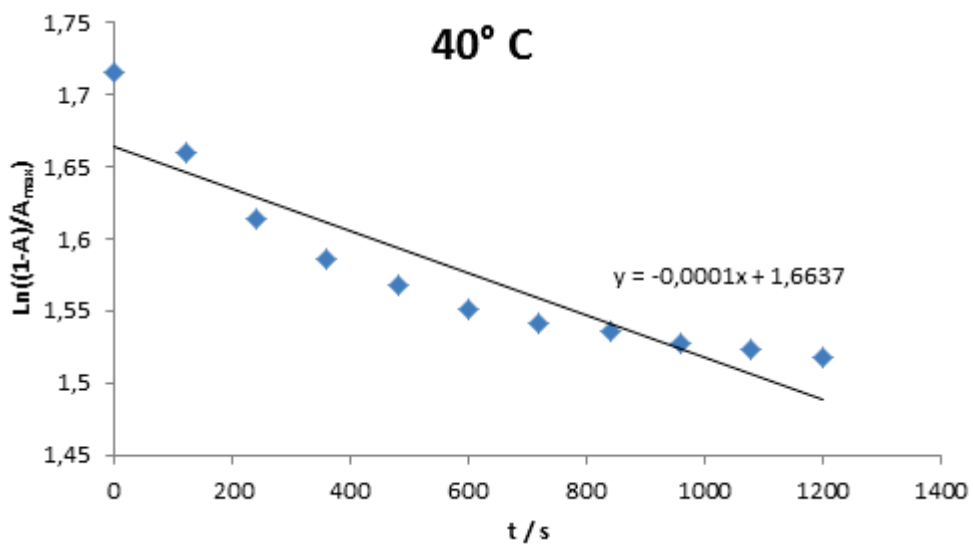
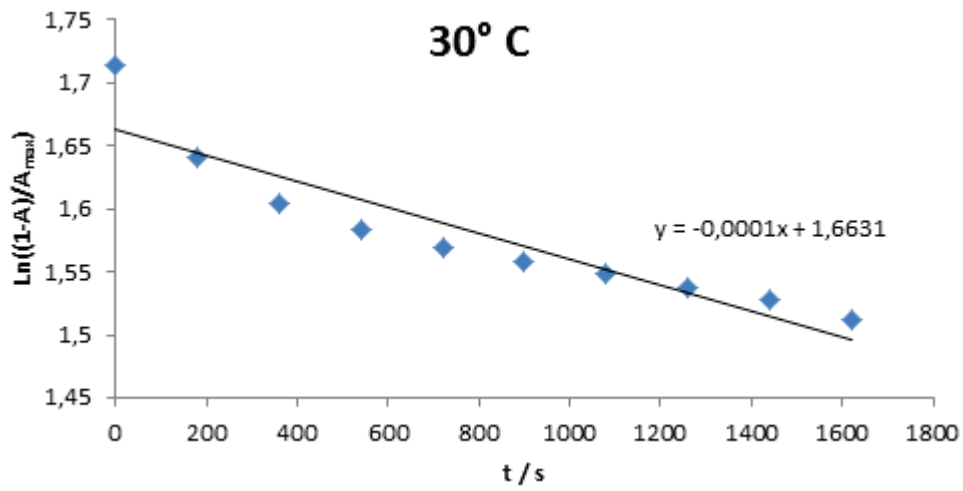
50° C	0,163930	0	1,806494113	0,001820	0,998180	6,089062405
	0,163930	60	1,755393783	0,051546	0,948454	5,785725615
	0,163930	120	1,726213778	0,078822	0,921178	5,619337522
	0,163930	180	1,716384676	0,087832	0,912168	5,564375038
	0,163930	240	1,706297442	0,096987	0,903013	5,508528030
	0,163930	360	1,686473508	0,114712	0,885288	5,400402611
	0,163930	480	1,672860243	0,126682	0,873318	5,327383639
	0,163930	600	1,656935750	0,140479	0,859521	5,243219667
	0,163930	720	1,648685607	0,147541	0,852459	5,200140304
	0,163930	840	1,640263917	0,154690	0,845310	5,156530226
	0,163930	960	1,634769202	0,159322	0,840678	5,128274263
	0,163930	1080	1,629272834	0,163930	0,836070	5,100164704

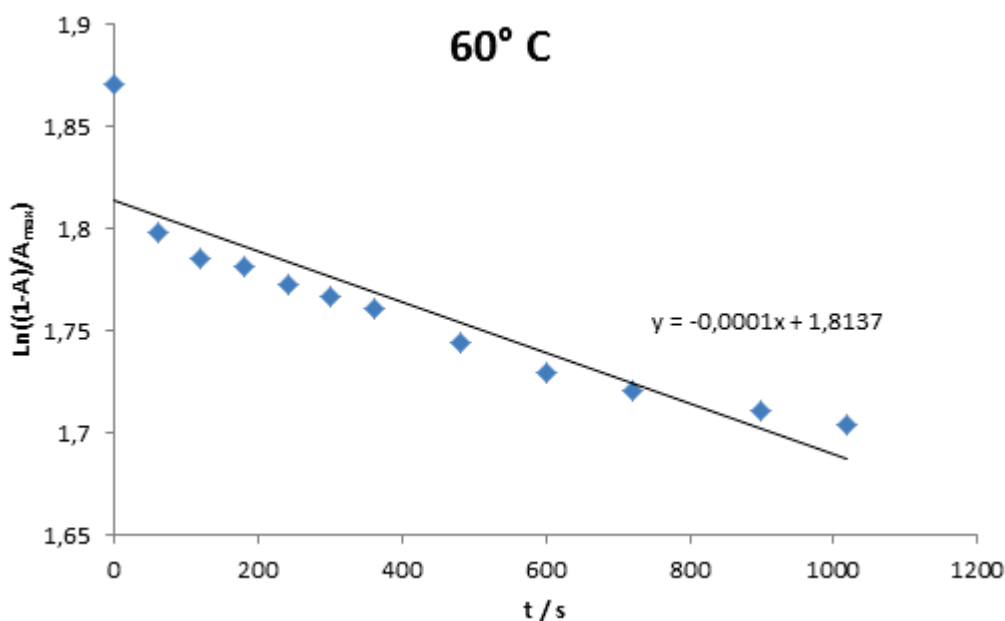
60° C	0,153891	0	1,870502211	0,001008	0,998992	6,491555712
	0,153891	60	1,798433447	0,070471	0,929529	6,040177788
	0,153891	120	1,785713151	0,082220	0,917780	5,963831543
	0,153891	180	1,781264297	0,086294	0,913706	5,937358260
	0,153891	240	1,772879732	0,093923	0,906077	5,887784211
	0,153891	300	1,767113073	0,099133	0,900867	5,853929080

0,153891	360	1,761135429	0,104502	0,895498	5,819040750
0,153891	480	1,744030695	0,119689	0,880311	5,720354017
0,153891	600	1,730026645	0,131931	0,868069	5,640804206
0,153891	720	1,721314378	0,139461	0,860539	5,591873469
0,153891	900	1,710584638	0,148645	0,851355	5,532194865
0,153891	1020	1,704403633	0,153891	0,846109	5,498105802

Measurements and calculations for the rate constant of photo-oxidation reaction of complex **2** in DMF solvent for varying temperature.







Derived plots from table 4.2 used to calculate the value of k for reaction at varying temperature.

Solvent: The reaction was carried out in the coordinating solvents dimethylformamide (DMF), dimethylsulfoxide (DMSO) and N,N-dimethylpyridylurea (DMPU). As the strength of the bonds in the Mn^{3+} complex which is formed provide some of the driving force of the reaction, it can be reasonably assumed that a ligand which forms stronger bonds to manganese will result in a faster reaction rate. In the case of DMPU the broad product peak which is observed is slightly displaced towards the red end of the spectrum with respect to the product obtained in the other two solvents; for this solvent the growth of absorption at 588 nm was used for calculations whereas for the others absorption at 548 nm was used. Reactions were carried out on freshly prepared solutions of thiaSO₂ ligand and manganese(II) chloride tetrahydrate with no addition of base, at room temperature, with an excitation wavelength of 400 nm. The k values are $-3 \times 10^{-5} s^{-1}$, $-7 \times 10^{-5} s^{-1}$, and $-20 \times 10^{-5} s^{-1}$ for DMF, DMPU, and DMSO respectively. These results indicate that the solvent DMSO favours the oxidation reaction considerably compared to the other two solvents.

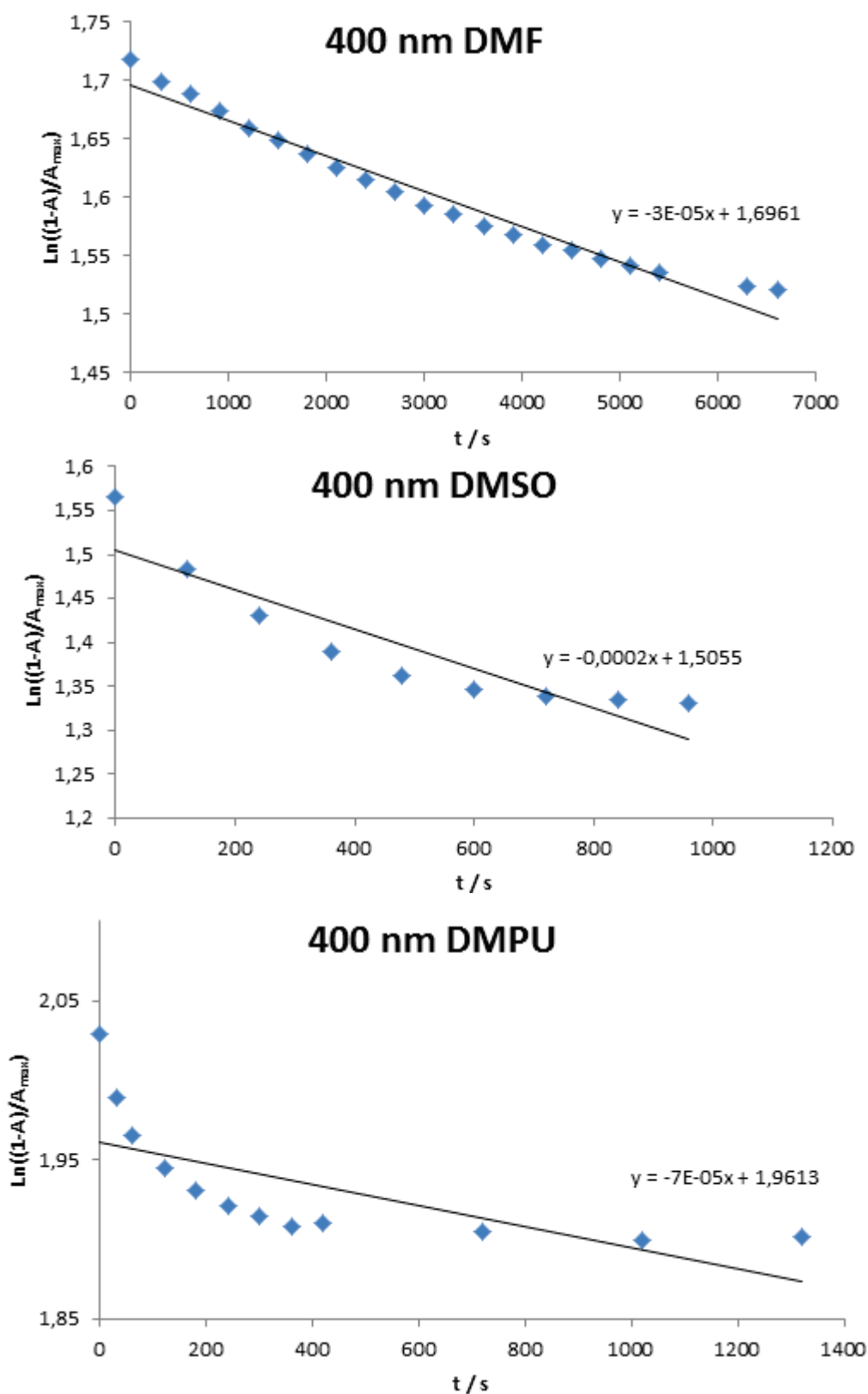
400 nm DMF	0,17932	0	1,717529805	0,001053	0,998947	5,570750613
	0,17932	300	1,699036560	0,019357	0,980643	5,468676110
	0,17932	600	1,688301456	0,029828	0,970172	5,410283292
	0,17932	900	1,673729289	0,043863	0,956137	5,332015391
	0,17932	1200	1,659881638	0,057012	0,942988	5,258688378
	0,17932	1500	1,649390825	0,066853	0,933147	5,203808833

	0,17932	1800	1,637294125	0,078073	0,921927	5,141239126
	0,17932	2100	1,625195331	0,089160	0,910840	5,079411109
	0,17932	2400	1,615011244	0,098389	0,901611	5,027944457
	0,17932	2700	1,604959911	0,107406	0,892594	4,977660049
	0,17932	3000	1,593481482	0,117593	0,882407	4,920850993
	0,17932	3300	1,58523595	0,124839	0,875161	4,880442784
	0,17932	3600	1,575759785	0,133093	0,866907	4,834413339
	0,17932	3900	1,567498808	0,140225	0,859775	4,794640865
	0,17932	4200	1,559156117	0,147368	0,852632	4,754807049
	0,17932	4500	1,554497321	0,151331	0,848669	4,732706893
	0,17932	4800	1,547344166	0,157380	0,842620	4,698973901
	0,17932	5100	1,541231434	0,162515	0,837485	4,670337943
	0,17932	5400	1,535758476	0,167086	0,832914	4,644847201
	0,17932	6300	1,523496269	0,177237	0,822763	4,588238903
	0,17932	6600	1,520961346	0,179320	0,820680	4,576622797

400 nm	0,208867	0	1,565511444	0,000546	0,999454	4,785121632
DMSO	0,208867	120	1,483600557	0,079149	0,920851	4,40879124
	0,208867	240	1,430745187	0,126557	0,873443	4,181814265
	0,208867	360	1,389352634	0,161973	0,838027	4,012251816
	0,208867	480	1,362704414	0,184010	0,815990	3,906744483
	0,208867	600	1,346940923	0,196772	0,803228	3,845643400
	0,208867	720	1,338788042	0,203294	0,796706	3,814417787
	0,208867	840	1,334094010	0,207025	0,792975	3,796554745
	0,208867	960	1,331768409	0,208867	0,791133	3,787735736

400 nm	0,130112	0	2,028854676	0,010450	0,989550	7,605370758
DMPU	0,130112	30	1,989483257	0,048653	0,951347	7,311754488
	0,130112	60	1,965441825	0,071252	0,928748	7,138065667
	0,130112	120	1,944979748	0,090063	0,909937	6,993490224
	0,130112	180	1,930406031	0,103228	0,896772	6,892308165
	0,130112	240	1,921119896	0,111517	0,888483	6,828601513
	0,130112	300	1,915023576	0,116917	0,883083	6,787098807
	0,130112	360	1,907606116	0,123443	0,876557	6,736942019
	0,130112	420	1,909857853	0,121467	0,878533	6,752128935
	0,130112	720	1,904735100	0,125956	0,874044	6,717627890
	0,130112	1020	1,899968850	0,130112	0,869888	6,685686178
	0,130112	1320	1,902002674	0,128341	0,871659	6,699297528

UV-visible spectrometry results and rate constant calculations for the effect of solvent upon the photo-oxidation of manganese(II) nitrate in the presence thiaSO₂ ligand.



Derived plots used to calculate the value of k for reaction in various solvents.

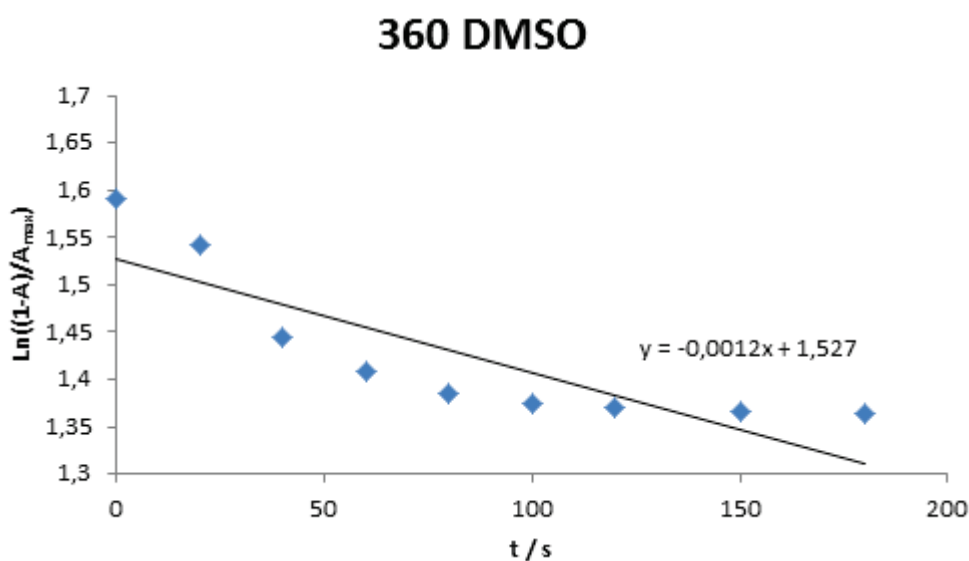
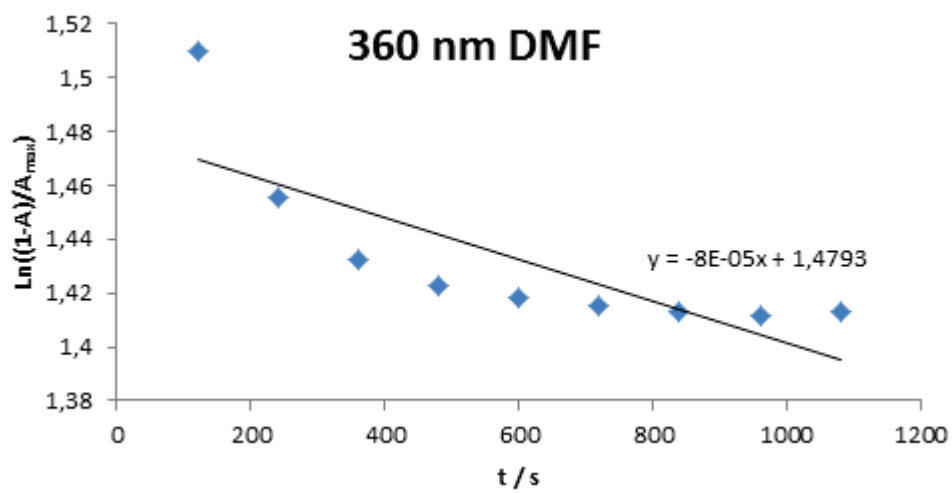
Wavelength of illumination: Measurements were carried out using both DMF and DMSO solvents to compare the effect of excitation wavelength. 360 nm and 400 nm light as the illumination

source was studied, in both cases originating from a 6W LED lamp. In all cases the reaction conditions remain as above; fresh solutions of thiaSO₂ and Mn(NO₃)₂·4H₂O without added base at room temperature. The system absorbs light of 360 nm wavelength more strongly than 400 nm light so higher rate constants should be expected for the former, and this is indeed what is observed in DMF. In DMSO however there is a discrepancy whereby the reaction takes place notably quicker with 400 nm excitation. If this result is accurate, it could indicate a synergistic absorption interaction of DMSO is occurring. The tests should be replicated to verify this hypothesis. The values of *k* which were obtained for 360 nm illumination were $-8 \times 10^{-5} \text{ s}^{-1}$ for DMF and $-12 \times 10^{-5} \text{ s}^{-1}$ for DMSO, and at 400 nm these values became $-3 \times 10^{-5} \text{ s}^{-1}$ in DMF and $-20 \times 10^{-5} \text{ s}^{-1}$ in DMSO.

	A_{max}	t	Ln((1-A)/A_{max})	A	1-A	(1-A)/A_{max}
360 nm DMF	0,195959	120	1,509875265	0,113057	0,886943	4,526166188
	0,195959	240	1,455129704	0,160308	0,839692	4,285039217
	0,195959	360	1,432533608	0,179069	0,820931	4,189299803
	0,195959	480	1,422799825	0,187021	0,812979	4,148719885
	0,195959	600	1,418212325	0,190742	0,809258	4,129731219
	0,195959	720	1,415586726	0,192864	0,807136	4,118902423
	0,195959	840	1,412933097	0,195003	0,804997	4,107986875
	0,195959	960	1,411744809	0,195959	0,804041	4,103108303
	0,195959	1080	1,413432353	0,194601	0,805399	4,110038324

360 nm DMSO	0,203723	0	1,591268013	-0,000274	1,000274	4,909970892
	0,203723	20	1,543057223	0,046806	0,953194	4,678872783
	0,203723	40	1,444494361	0,136274	0,863726	4,239707839
	0,203723	60	1,408732092	0,166617	0,833383	4,090765402
	0,203723	80	1,385342862	0,185883	0,814117	3,996195815
	0,203723	100	1,374446200	0,194706	0,805294	3,952887008
	0,203723	120	1,369456709	0,198714	0,801286	3,933213236
	0,203723	150	1,366684821	0,200932	0,799068	3,922325903
	0,203723	180	1,363185887	0,203723	0,796277	3,908625928

UV-visible spectrometry results and calculations for the rate constant of photo-oxidation reaction of the thiaSO₂ / Mn²⁺ system with 360 nm excitation wavelength.



Plots used to calculate the rate constant for photo-oxidation of the thiaSO₂ / Mn²⁺ system with 360 nm excitation.

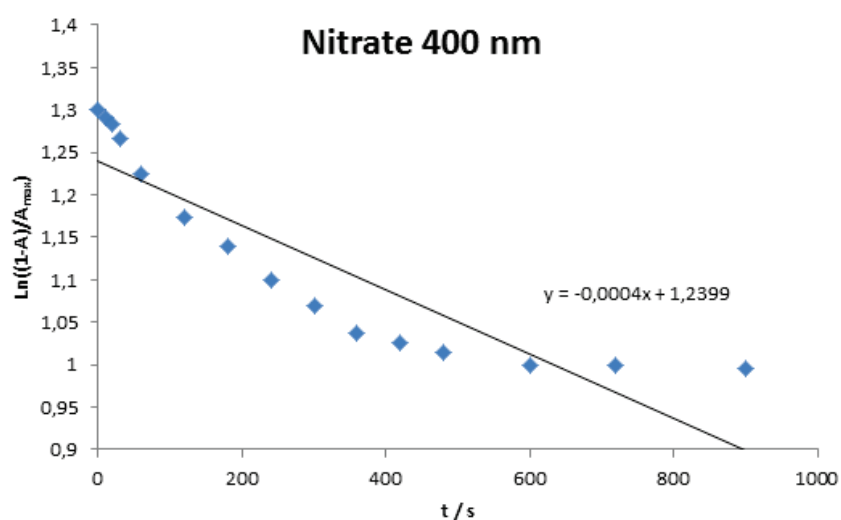
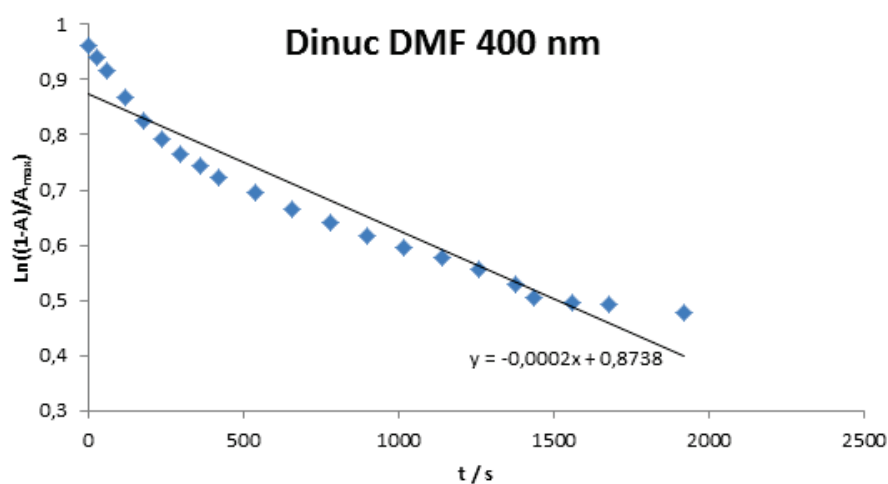
Starting material: The form of the starting reagents plays an important role in the kinetics of the oxidative transformation. Both when the reaction is carried out using the tetranuclear complex as the starting material and when the starting reagents are separate in solution, there is a transition step involving formation of the dinuclear manganese complex. Direct illumination of the dinuclear species should therefore result in faster reaction, as this transition step has been bypassed. For illumination of a DMF solution of [Mn₂(thiaSO₂)(DMF)₆] with 400 nm wavelength light at room temperature, k was calculated to be $-20 \times 10^{-5} \text{ s}^{-1}$. The same value was calculated with excitation at 360 nm, both approximately twice as large as the value of $-10 \times 10^{-5} \text{ s}^{-1}$ derived for reaction of the tetranuclear complex under the same conditions. The rate constant of the reaction thiaSO₂ + MnX₂ +

$h\nu$ (360 nm) in DMF was found to strongly depend on the nature of the manganese salt MnX_2 . When X is chloride (a large, strongly coordinating anion) the rate constant $k = 7 \times 10^{-5} s^{-1}$, slightly smaller than the value observed with the tetramanganese complex. When the starting material is the manganese nitrate salt $Mn(NO_3)_2$ the rate constant is then $40 \times 10^{-5} s^{-1}$, which corresponds to a faster reaction rate than even direct reaction of the dinuclear complex. It is possible, though not probable, that this reaction does not undergo the conformation altering transition step, with the ligand coordinating manganese during the course of reaction and remaining in the cone conformation at all times. More probably, the weakly coordinating nitrate anion allows for rapid precoordination of manganese to $thiaSO_2$, forming dinuclear complex *in situ* in a way which is not possible with the $MnCl_2$ situation.

	A_{max}	t	$\ln((1-A)/A_{max})$	A	1-A	$(1-A)/A_{max}$
Dinuclear DMF 400 nm	0,382672	0	0,962633937	-0,002059	1,002059	2,618584584
	0,382672	30	0,940586569	0,019792	0,980208	2,561483464
	0,382672	60	0,915839068	0,043752	0,956248	2,498871096
	0,382672	120	0,868326887	0,088123	0,911877	2,382920621
	0,382672	180	0,826366573	0,125594	0,874406	2,285001254
	0,382672	240	0,790840374	0,156113	0,843887	2,205248882
	0,382672	300	0,765980871	0,176833	0,823167	2,151103295
	0,382672	360	0,744457526	0,194361	0,805639	2,105299055
	0,382672	420	0,723470218	0,211093	0,788907	2,061574926
	0,382672	540	0,695264246	0,233034	0,766966	2,004238617
	0,382672	660	0,666133507	0,255054	0,744946	1,946695865
	0,382672	780	0,64186654	0,272914	0,727086	1,900024041
	0,382672	900	0,617954342	0,290094	0,709906	1,855129197
	0,382672	1020	0,596478911	0,305177	0,694823	1,815714241
	0,382672	1140	0,576357649	0,319018	0,680982	1,779544884
	0,382672	1260	0,55598956	0,332748	0,667252	1,743665594
	0,382672	1380	0,530572296	0,349494	0,650506	1,699904879
	0,382672	1440	0,503724962	0,366726	0,633274	1,654874148
	0,382672	1560	0,496848097	0,371066	0,628934	1,643532843
	0,382672	1680	0,493511504	0,373161	0,626839	1,63805818
0,382672	1920	0,478222262	0,382672	0,617328	1,613203997	
Nitrate 360 nm DMF	0,272583	0	1,299583098	0,000229	0,999771	3,667767249
	0,272583	10	1,291170896	0,008604	0,991396	3,637042662
	0,272583	20	1,282242681	0,017416	0,982584	3,604714894
	0,272583	30	1,267028568	0,032252	0,967748	3,550287435
	0,272583	60	1,224493573	0,072552	0,927448	3,402442559

0,272583	120	1,173553648	0,118613	0,881387	3,233462835
0,272583	180	1,138379663	0,149076	0,850924	3,121706049
0,272583	240	1,098598837	0,182262	0,817738	2,999959645
0,272583	300	1,0687813	0,206285	0,793715	2,911828691
0,272583	360	1,037905655	0,230417	0,769583	2,823297858
0,272583	420	1,024725067	0,240494	0,759506	2,786329302
0,272583	480	1,013943074	0,248639	0,751361	2,756448495
0,272583	600	0,998444835	0,260194	0,739806	2,714057737
0,272583	720	0,999471604	0,259434	0,740566	2,716845878
0,272583	900	0,995265983	0,262542	0,737458	2,705443846

UV-visible spectrometry results and rate constant calculations for the photo-oxidation of manganese in the presence of thiaSO₂ ligand depending on the starting reagents.



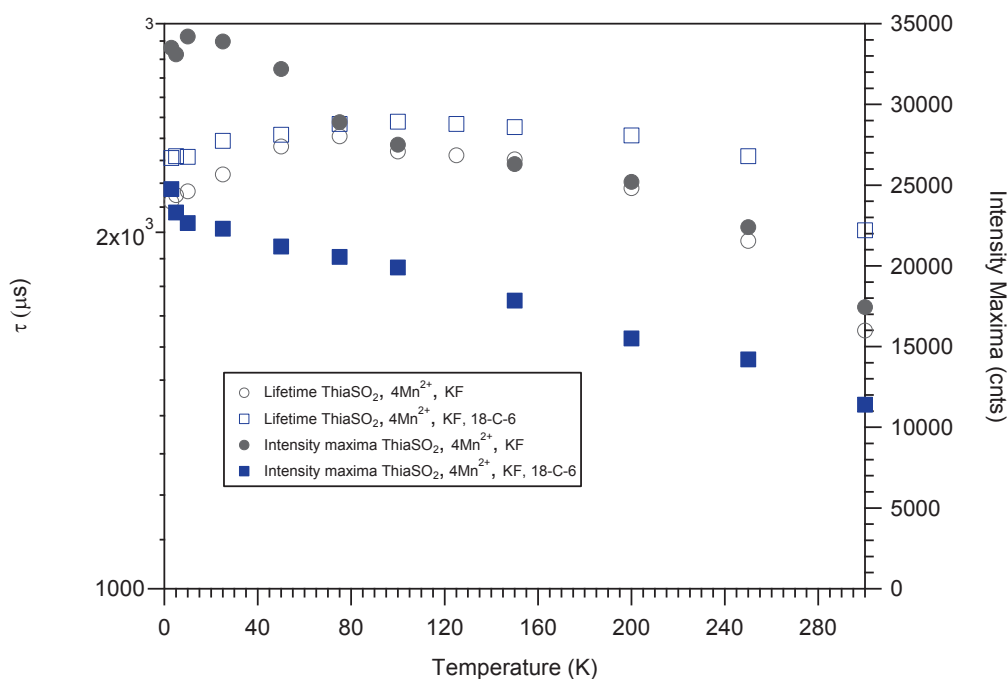
Plots derived for the calculation of rate constants for photo-oxidation of the system Mn²⁺ / thiaSO₂ with varying starting material.

ANNEXE 3: LUMINESCENCE LIFETIME DECAY CURVES

Transitions	Temperature (K)	Complex 2	Complex 2	Complex 3	Complex 3
		τ (μs)	k (s^{-1})	τ (μs)	k (s^{-1})
${}^4\text{T}_1 \rightarrow {}^6\text{A}_1$ Transition	3 (without O_2)	2122(30)	4.71E+02	2311(30)	4.33E+02
	5 (without O_2)	2150(30)	4.65E+02	2319(30)	4.31E+02
	10 (without O_2)	2166(30)	4.62E+02	2316(30)	4.32E+02
	25 (without O_2)	2238(30)	4.47E+02	2389(30)	4.19E+02
	50 (without O_2)	2363(30)	4.23E+02	2417(30)	4.14E+02
	75 (without O_2)	2410(30)	4.15E+02	2469(30)	4.05E+02
	100 (without O_2)	2340(30)	4.27E+02	2479(30)	4.03E+02
	125 (without O_2)	2323(30)	4.30E+02	2469(30)	4.05E+02
	150 (without O_2)	2305(30)	4.34E+02	2454(30)	4.07E+02
	200 (without O_2)	2179(30)	4.59E+02	2414(30)	4.14E+02
	250 (without O_2)	1967(30)	5.08E+02	2319(30)	4.31E+02
	300 (without O_2)	1652(30)	6.05E+02	2008(30)	4.98E+02
	300 (with O_2)	1684(30)	5.94E+02	528(50)	1.89E+03

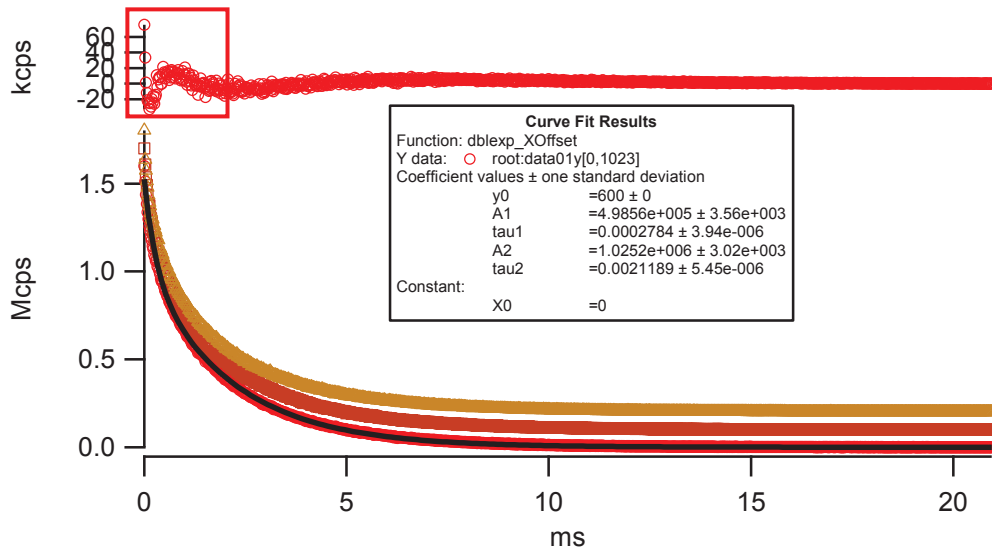
Lifetimes (μs) and rate constants (s^{-1}) of complex 2 and complex 3 obtained between 3 and 293 K (as temperature increases). Bi-exponential fit.

Conditions: Solid, alignment and optimisation on sample with CCD, wavelength scanning with PM and measurements of Lifetimes with PM And SR430 Multi-channel Scaler. Scaler: Bin width = 20.48 μs , Bins/Records = 1k, Records/scan = 1000

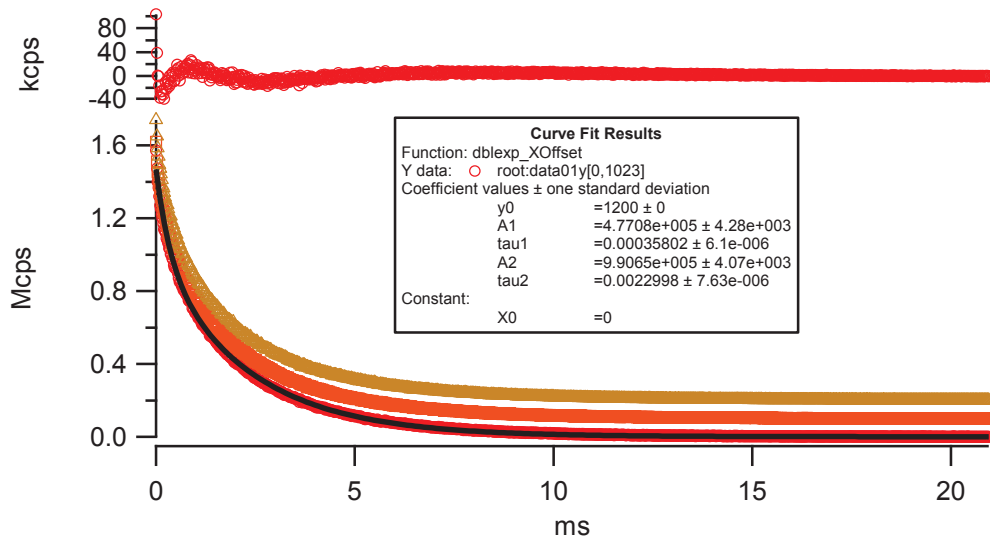


Lifetimes in μs (left axis) and luminescence intensity (right axis) of ThiaSO₂, 4Mn²⁺, KF (red circles) and ThiaSO₂, 4Mn²⁺, KF, 18-C-6 (blue squares) obtained between 3 and 293 K (as temperature increases).

a)



b)



Lifetime curves in μ s of a) Complex 2 and b) Complex 3 at 3K. Bi-exponential fit.

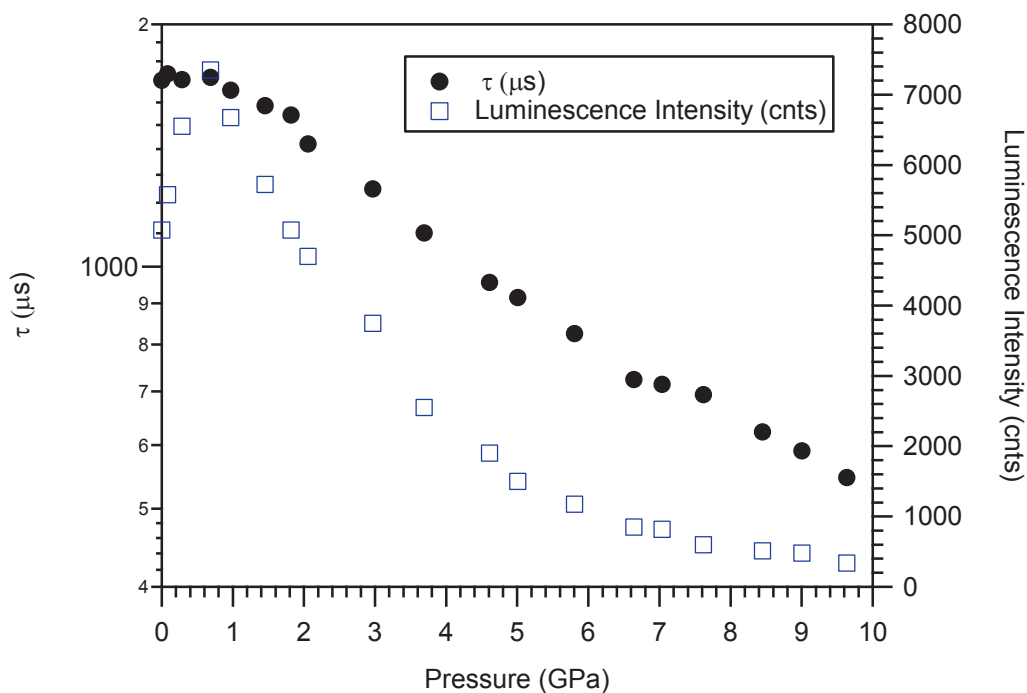
Check lifetime 3 K – 300 K, Mono-Bi-exponential fit: all the lifetime curves are bi-exponential.

$A_1 = 4.9856 \times 10^5$
$\tau_1 = 0.0002784$
$A_2 = 1.0252 \times 10^6$
$\tau_2 = 0.0021189$

Transitions	Pressure (GPa)	Complex 2 τ (μs)	Complex 2 k (s^{-1})
${}^4\text{T}_1 \rightarrow {}^6\text{A}_1$ Transition	0	1705(30)	5.87E+02
	0.0809	1736(30)	5.76E+02
	0.283	1707(30)	5.86E+02
	0.687	1719(30)	5.82E+02
	0.969	1657(30)	6.03E+02
	1.45	1585(30)	6.31E+02
	1.82	1543(30)	6.48E+02
	2.06	1421(30)	7.04E+02
	2.97	1249(30)	8.01E+02
	3.69	1101(50)	9.08E+02
	4.61	956(50)	1.05E+03
	5.01	915(50)	1.09E+03
	5.81	826(50)	1.21E+03
	6.64	724(50)	1.38E+03
	7.04	714(50)	1.40E+03
	7.62	693(50)	1.44E+03
	8.45	623(50)	1.61E+03
	9	590(50)	1.70E+03
	9.63	547(50)	1.83E+03
	0.0404	1385(50)	5.87E+02

Lifetimes (μs) and rate constants (s^{-1}) of complex 2 obtained between 0 and 9.6 GPa (at 295 K). Bi-exponential fit.

Conditions: Solid, alignment and optimisation on sample with CCD, wavelength scanning with PM and measurements of Lifetimes with PM And SR430 Multi-channel Scaler. Scaler: Bin width = 2.56-10.24 μs , Bins/Records = 2k, Records/scan = 1000

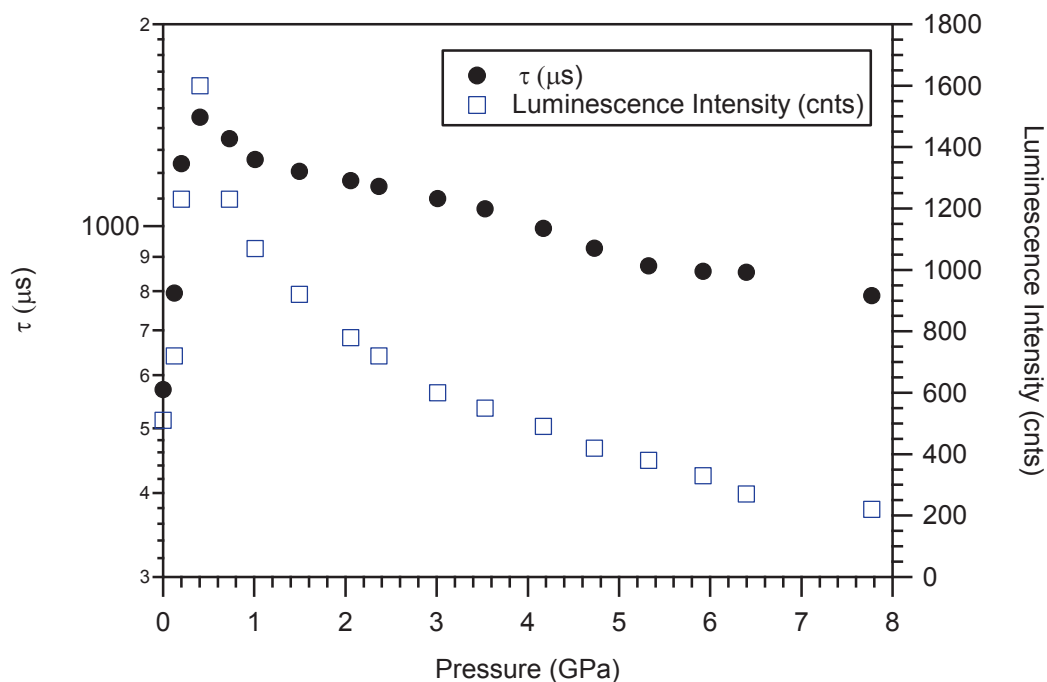


Lifetimes in μs (left axis) and luminescence intensity (right axis) of complex 2 obtained between 0 and 9.6 GPa at 295 K.

Transitions	Pressure (GPa)	Complex 3 τ (μs)	Complex 3 k (s^{-1})
${}^4\text{T}_1 \rightarrow {}^6\text{A}_1$ Transition	0	571(50)	1.75E+03
	0.121	795(50)	1.26E+03
	0.202	1239(50)	8.07E+02
	0.404	1454(50)	6.88E+02
	0.727	1351(50)	7.40E+02
	1.01	1257(50)	7.96E+02
	1.49	1207(50)	8.28E+02
	2.06	1169(100)	8.56E+02
	2.37	1147(100)	8.72E+02
	3.01	1100(100)	9.10E+02
	3.53	1061(100)	9.43E+02
	4.17	993(100)	1.01E+03
	4.73	927(100)	1.08E+03
	5.33	873(100)	1.15E+03
	5.92	857(100)	1.17E+03
	6.4	854(100)	1.17E+03
	7.77	788(100)	1.27E+03
	8.33	591(100)	1.69E+03
	10	587(100)	1.70E+03
0.242	1094(100)	9.14E+02	

Lifetimes (μs) and rate constants (s^{-1}) of complex **3** obtained between 0 and 10 GPa (at 295 K). Bi-exponential fit.

Conditions: Solid, alignment and optimisation on sample with CCD, wavelength scanning with PM and measurements of Lifetimes with PM And SR430 Multi-channel Scaler. Scaler: Bin width = 2.56-10.24 μs , Bins/Records = 2k, Records/scan = 1000

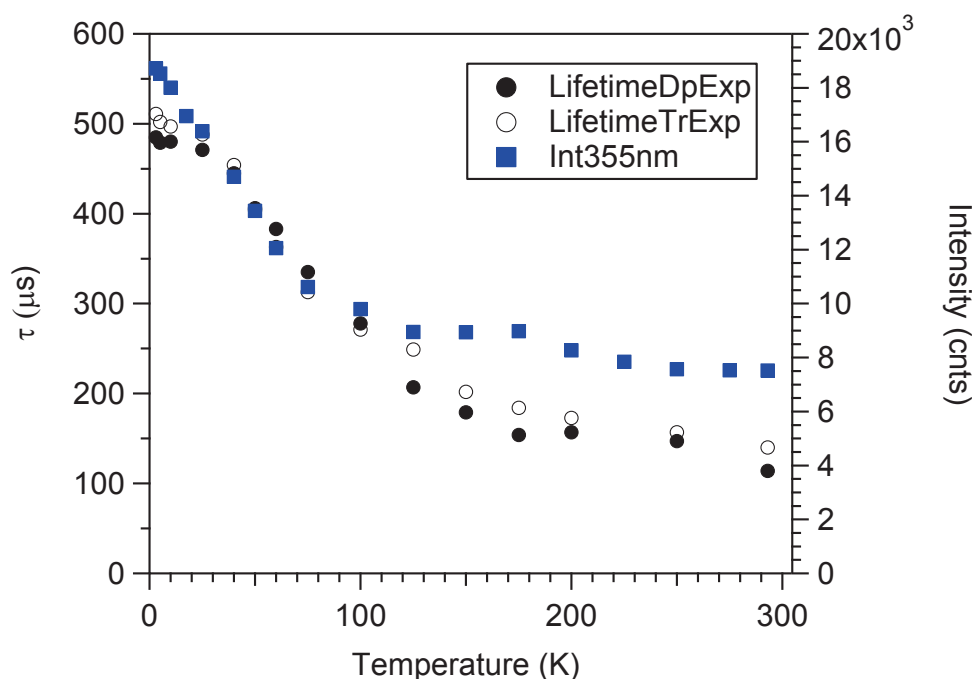


Lifetimes in μs (left axis) and Luminescence intensity (right axis) of complex **3** obtained between 0 and 10 GPa at 295 K.

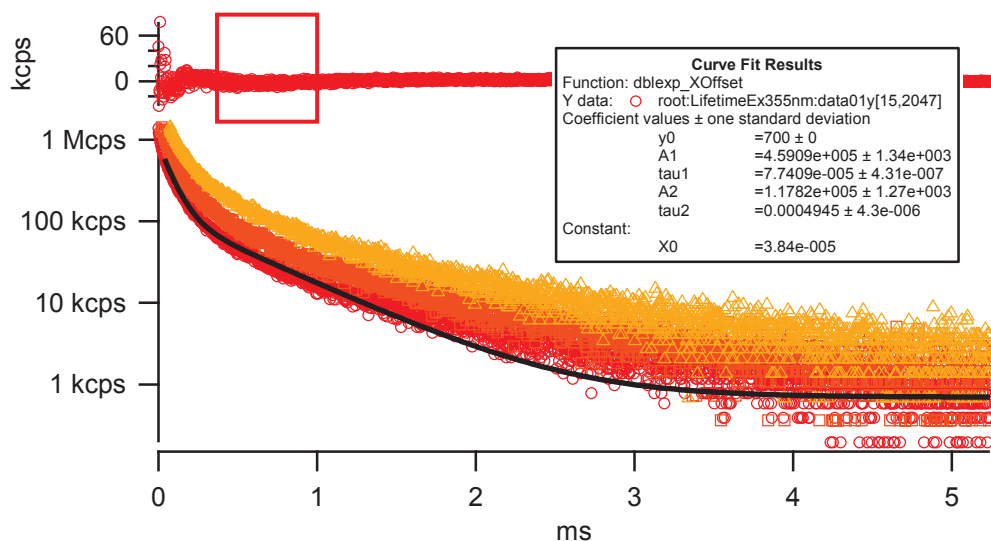
Transitions	Temperature (K)	Complex 5	Complex 5	Complex 5	Complex 5
		τ (μ s) Dp Exp	k (s^{-1}) Dp Exp	τ (μ s) Tri Exp	k (s^{-1}) Tri Exp
${}^4T_1 \rightarrow {}^6A_1$ Transition	3	485(30)	2.06E+03	511(60)	1.96E+03
	5	479(30)	2.09E+03	502(50)	1.99E+03
	10	480(30)	2.09E+03	497(50)	2.01E+03
	25	471(30)	2.12E+03	488(50)	2.05E+03
	40	445(30)	2.25E+03	454(50)	2.20E+03
	50	406(30)	2.46E+03	404(50)	2.48E+03
	60	383(40)	2.61E+03	363(70)	2.76E+03
	75	335(30)	2.98E+03	313(50)	3.20E+03
	100	278(30)	3.60E+03	271(50)	3.69E+03
	125	207(30)	4.82E+03	249(60)	4.02E+03
	150	179(30)	5.57E+03	202(50)	4.96E+03
	175	154(30)	6.51E+03	184(50)	5.42E+03
	200	157(30)	6.39E+03	173(50)	5.78E+03
	250	147(30)	6.81E+03	157(50)	6.35E+03
	293	114(30)	8.79E+03	140(50)	7.15E+03

Lifetimes (μ s) and rate constants (s^{-1}) of complex **5** obtained between 3 and 293 K (as temperature increases). Bi-exponential fit or Tri-exponential fit.

Conditions: Solid, alignment and optimisation on sample with CCD, wavelength scanning with PM and measurements of Lifetimes with PM And SR430 Multi-channel Scaler. Scaler: Bin width = 2.56 μ s, Bins/Records = 2k, Records/scan = 1000

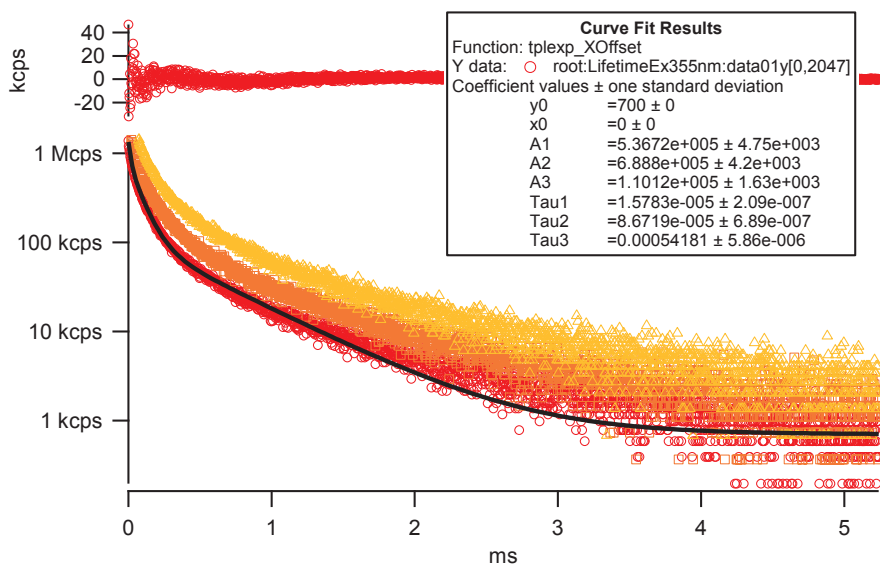


Lifetimes in μ s (left axis) and luminescence intensity (right axis) of complex **5** obtained between 3 and 293 K (as temperature increases).



Lifetime curves in μs of complex **5** at 3K. Bi-exponential fit.

$A_1 = 4.5909 \times 10^5$
$\tau_1 = 0.0000774$
$A_2 = 1.1782 \times 10^5$
$\tau_2 = 0.0004945$
$A_1\tau_1/A_2\tau_2 = 35.53/58.26 = 0.61$ (38:62) ratio 3-293 K



Lifetime curves in μs of complex **5** at 3K. Triple-exponential fit.

Check lifetime 3 K – 300 K, Mono-Bi-exponential fit: all the lifetime curves are Triple-exponential.

$A_1 = 5.3672 \times 10^5$
$\tau_1 = 0.000015783$
$A_2 = 6.888 \times 10^5$
$\tau_2 = 0.000086719$
$A_3 = 1.1012 \times 10^5$
$\tau_3 = 0.00054181$
$A_1\tau_1 = 8.47$ $A_2\tau_2 = 59.73$ and $A_3\tau_3 = 59.66$ (6.6:46.7:46.7) ratio 3-293 K

ANNEXE 4: LIST OF FIGURES

Figure 1: Structure of para- <i>tert</i> -butylthiacalix[4]arene (thiaS).	29
Figure 2: One step synthesis of para- <i>tert</i> -butylthiacalix[4]arene.	29
Figure 3: Synthesis of the para- <i>tert</i> -butylphenol thioether dimer.	30
Figure 4: Possible conformations of thiacalix[4]arene.	31
Figure 5: Summary of some of the modifications which are possible at the upper rim of thiacalix[4]arene.	33
Figure 6: Stereoselectivity of Gross formylation for tetrapropylcalix[4]arene (blue arrow) and tetrapropylthiacalix[4]arene (red arrow).	34
Figure 7: Mercuration of tetrapropylthiacalix[4]arene.	34
Figure 8: Dimerisation of tetrapropylthiacalix[4]arene.	35
Figure 9: Structure of sulfinylcalix[4]arene and sulfonylcalix[4]arene.	35
Figure 10: A representation of some stereoisomers of sulfinylcalix[4]arene.	36
Figure 11: Sulfur – oxygen bridging by Mitsunobu reaction.	36
Figure 12: Synthesis of monospirodienone derivative of para- <i>tert</i> -butylthiacalix[4]arene.	37
Figure 13: Mono-sulfilimine derivative of para- <i>tert</i> -butylthiacalix[4]arene.	37
Figure 14: Structures of thiacalix[4]aniline and mercaptothiacalix[4]arene.	37
Figure 15: Structures of N-(bromoethyl)-phthalimide (left) and N-(bromopropyl)-phthalimide (right); structurally similar molecules which show different reactivity to thiacalixarene.	39
Figure 16: Route to monofunctionalised product via disubstituted transition species.	39
Figure 17: Preparation of a thiacalixazacrown.	40
Figure 18: X-ray diffraction structure of dibenzylpara- <i>tert</i> -butylthiacalix[4]arene (methoxynaphthylpropionate).	41
Figure 19: Synthesis of tetraacetylthiacalix[4]arene in different conformations.	41
Figure 20: Representation of complexation of thiacalixarene, with direct complexation or prefunctionalisation.	43
Figure 21: Representation of the binding sites on a thiacalix[4]arene.	43
Figure 22: Octadentate binding mode.	44
Figure 23: A Co ₈ ‘coordination cage’ with two thiacalix[4]arene ligands.	45
Figure 24: Heptadentate binding mode.	46
Figure 25: A trinuclear zinc complex with para- <i>tert</i> -butylthiacalix[4]arene ligands in the heptadentate binding mode.	46
Figure 26: Hexadentate binding mode.	47
Figure 27: A dinuclear nickel cluster with para- <i>tert</i> -butylthiacalixarene demonstrating the hexadentate binding mode.	47
Figure 28: Pentadentate binding mode.	48
Figure 29: X-ray diffraction of complex demonstrating pentadentate binding, with Fe ₃ O core.	48
Figure 30: Tetradentate binding mode.	49
Figure 31: Dimer complex of tantalum illustrating tetradentate binding.	50
Figure 32: Tridentate binding mode.	50
Figure 33: Representation of a ‘mobile’ zinc complex with tridentate binding of para- <i>tert</i> -butylsulfonylcalix[4]arene.	51
Figure 34: Structure of [Ru(2,2'-bipyridine) ₂ (para- <i>tert</i> -butylthiacalix[4]arene)], with one bonding oxygen atom and one bonding sulfur atom on the ligand.	51
Figure 35: Effect of cobalt starting material on structure of the final complex product.	52
Figure 36: Cross section representation of autoclave synthesis.	54

Figure 37: Structure of ferromagnetic Cu ₁₀ SMM complex.....	55
Figure 38: Formation of an MOSC material with para- <i>tert</i> -butylsulfonylcalix[4]arene	56
Figure 39: Europium cluster compounds with sulfonylcalixarene ligands exhibiting slight conformational differences.	58
Figure 40: (Left) Chemical structure of thiacalix[4]arene- <i>N</i> -(quinolin-8-yl)-acetamide, TCAN8QA, a thiacalixarene-based fluorescent F ⁻ sensor. (Right) Emission spectra of the free ligand TCAN8QA and the same ligand in the presence of fluoride ions.....	59
Figure 41: Energy levels and transitions involved in the antenna effect luminescence of dierbium, diterbium, tetraerbium and tetra terbium complexes of thiacalixarene.....	60
Figure 42: Simulated absorption (blue curve) and emission (red curve) spectra for free thiaS.....	70
Figure 43: Structure of DPEPO.	72
Figure 44: Structure obtained by single crystal XRD of complex 1	73
Figure 45: Solvothermal synthesis of complex 1.....	73
Figure 46: Side-on view representation of the Mn ₄ -μ ₄ (OH) square at the core of complex 1 and the 7-coordinate C _{2v} environment of each Mn ²⁺ ion.....	74
Figure 47: Solid state excitation (λ _{emi} = 600 nm) and emission (λ _{exc} = 300 nm) of complex 1 and complex 2	75
Figure 48: IR spectra of complexes 1 and 2 between 3 300 cm ⁻¹ and 4 000 cm ⁻¹	75
Figure 49: Energetic configurational coordinate diagrams showing the origin of the Stoke's shift in photoluminescence	76
Figure 50: Structure obtained by single crystal XRD of derivative complex 3 with the cation [K(18-crown-6)] ⁺	77
Figure 51: Synthesis of Br ₄ thiaSO ₂ from thiaS.....	78
Figure 52: 7-coordinate C _{2v} manganese(II) centre found in complex 2	79
Figure 53: (Above) Solid state excitation spectra of complex 2 (λ _{emi} = 585 nm) at both 300 K (black curve) and 8 K (blue curve). (Below) Solid state excitation spectrum (dashed line, λ _{emi} = 602 nm) measured at 8 K magnified to highlight weak excitation peaks, and solid state emission spectrum (solid line, λ _{exc} = 350 nm) measured at 7.5 K of complex 2.	81
Figure 54: Evolution of emission spectrum of complex 2 with respect to pressure in the range from ambient pressure to 10 GPa.....	82
Figure 55: Tanabe-Sugano diagram for energy level of states in d ⁵ ions.....	83
Figure 56: Proposed mechanistic scheme (bold red arrows) of antenna effect luminescence.....	84
Figure 57: Electronic microstates involved in the photoluminescence of complex 2.....	84
Figure 58: Evolution of solid state emission spectrum of complex 2 with increasing temperature in the range from 7.5 K to ambient temperature 300 K	85
Figure 59: Evolution of the solid state emission spectrum of complex 2 at room temperature with varying oxygen pressure in the range between 0.2 mbar and ambient pressure	86
Figure 60: Occupation of the HOMO of the O ₂ molecule (a π* orbital) in its ³ Σ ground state and in the two nearest excited states	87
Figure 61: Solvothermal synthesis of complex 3.....	87
Figure 62: Zoomed in side-by-side comparison of the cation environment in a) complex 2 and b) complex 3.	88
Figure 63: View of the ab plane of the crystallographic unit cell of a) complex 2 and b) complex 3. ...	89
Figure 64: (Above): Solid state excitation spectra for complex 3 (Below): Solid state excitation spectrum and solid state emission spectrum of complex 2 and complex 3	91

Figure 65: Evolution of emission spectrum of complex 2 with respect to pressure in the range from ambient pressure to 10 GPa.....	92
Figure 66: Evolution of solid state emission spectrum of complex 2 with increasing temperature in the range from 7.5 K to ambient temperature.	93
Figure 67: Comparison of temperature dependence data for the photoluminescence of complexes 2 and 3.....	94
Figure 68: Evolution of the solid state emission spectrum of complex 3 with varying oxygen pressure in the range between 0.2 mbar and ambient pressure.	95
Figure 69: Chemical structures of complexes 4 and 5	97
Figure 70: Structure of related complex $Mn_4(Br_4thiaS)_2(DMF)_2$, with magnified view showing the two distinct coordination environments of manganese (8-coordinate and 6-coordinate).	98
Figure 71: Excitation and emission spectra for complex 2 and complex 4 in the solid state	99
Figure 72: Structure obtained by single crystal X-ray diffraction analysis of complex 5	100
Figure 73: Excitation spectrum of complex 5 measured at 8 K and 300 K under 10^{-9} mbar vacuum.	101
Figure 74: a) Emission spectra of complex 5 at various temperatures in the range between 8.5 K and 300 K under 10^{-9} mbar vacuum. b) Emission spectra of complex 5 at various temperatures in the range between 3 K and 293 K.....	102
Figure 75: Data derived from the emission spectra of complex 5 under 10^{-9} mbar vacuum at varying temperature between 8.5 K and 300 K e)-h) Data derived from the emission spectra of complex 5 measured under He atmosphere at varying temperature in the range between 3 K and 293 K	103
Figure 76: Solid state emission spectra of complex 5 measured at for various oxygen pressure in the range between 0.1 mbar to 1010 mbar	104
Figure 77: Normalised absorption, excitation and emission spectra of 2 and 3.....	105
Figure 78: Normalised solution state absorption, excitation and emission spectra of complex 5.	106
Figure 79: Normalised intensity of emission of complex 2 and complex 3 with time of exposure to N_2 -bubbling or air	107
Figure 80: Crystal structure obtained by single crystal X-ray diffraction experiments of the complex $[Na(dibenzo-18-crown-6)][Mn_4(thiaSO_2)_2F]$	108
Figure 81: Transformation of complex 2 in solution under the action of sunlight.	115
Figure 82: Types of photo-oxygenation	116
Figure 83: (Left) Structure of the Mn(III) complex obtained by photo-oxidation of tetramanganese complex. (Right) Parallel mode CW-EPR spectrum (blue curve) of this metal complex	118
Figure 84: Structures solved by single crystal XRD analysis of the Mn^{3+} oxidation product.....	119
Figure 85: Time resolved UV-vis spectra obtained for solutions containing a) tetramanganese cluster 2, and b) dimanganese cluster 5.	119
Figure 86: Structures of manganese complexes involved in the photo-oxidation reaction	120
Figure 87: Experimental and simulated EPR spectra resulting from the irradiation at 400 nm (or 360 nm) of a solution of complex 2 in the presence of DMPO	121
Figure 88: Hypothesised routes for destruction of the superoxide anion formed during the photo-oxidation reaction	122
Figure 89: UV-vis absorption spectra obtained from a solution of DMA in DMF with varying time of illumination	124
Figure 90: Oxidation by singlet oxygen of 9,10-dimethylanthracene, giving the <i>endo</i> -peroxide.....	124
Figure 91: UV-vis absorption spectra obtained from DMA with varying time of illumination in the presence of Mn^{II} cluster	125

Figure 92: Standard redox potentials for the single electron transfer transformation between molecular dioxygen and the superoxide anion.	125
Figure 93: Route of photo-oxidation of Mn ^{II} clusters derived from UV-vis absorption data.....	126
Figure 94: Mechanistic routes for the photo-oxidation of manganese(II) clusters of sulfonylcalixarene using nitrate as the oxidant.....	128
Figure 95: Rate constants k for the photo-oxidation of complex 2 under varying conditions.	129
Figure 96: Time resolved spectral changes in the UV-vis absorption profile of a solution of thiaSO ₂ and Mn(NO ₃) ₂ ·4H ₂ O (0.3 mmol dm ⁻³).....	131
Figure 97: Evolution of the UV-vis absorption spectrum of a solution of thiaSO ₂ with time of irradiation a) With 1 eq. of Mn(NO ₃) ₂ . b) With 4 eq. of Mn(NO ₃) ₂	132
Figure 98: Evolution with time of irradiation of thiaSO ₂ and 20 eq. of Mn(NO ₃) ₂	133
Figure 99: Hypothetical dynamic equilibrium established upon illumination of solutions of thiaSO ₂ and manganese(II) nitrate, with equation for calculation of the equilibrium constant K.	134
Figure 100: Modified reaction diagram for photo-oxidation reactions of sulfonylcalix[4]arene and manganese(II) nitrate taking into account a precomplexation step.....	134
Figure 101: UV-visible absorption spectra for freshly made DMF solutions of tetranuclear manganese complex 2 , dinuclear manganese complex 5, a mixture of thiaSO ₂ and manganese(II) nitrate tetrahydrate, and the pure compound thiaSO ₂	135
Figure 102: UV-vis absorption spectra for DMF solutions of thiaSO ₂ and manganese(II) nitrate, in a 1:1 molar ratio immediately after dissolution, in a 1:1 ratio after 1 night agitation, and in a 1:4 ratio after 1 night agitation.	136
Figure 103: Evolution of the UV-vis absorption spectrum with time of irradiation) for thiaSO ₂ and manganese(II) chloride.....	137
Figure 104: Proposed routes for the photoreaction of systems containing thiaSO ₂ and Mn(II) salt..	138
Figure 105: Hypothetical light-controlled switching mechanism between Mn ^{II} and Mn ^{III} systems with inset: a crystal of the mononuclear Mn ^{II} complex showing the purple colouration.....	139
Figure 106: Time resolved UV-vis absorption spectra for illuminated mixture in DMF solution of thiaSO ₂ and 1 eq. of Mn(NO ₃) ₂ ·4H ₂ O.....	140
Figure 107: UV-vis absorption spectra for fresh solutions containing the tetranuclear manganese complex 2, the dinuclear complex 5, a mixture of thiaSO ₂ and Mn(NO ₃) ₂ , and the same mixture with Et ₃ N, and the pure compound thiaSO ₂	141
Figure 108: Adaptation of figure 107 indicating the excitation wavelengths which are available to our laboratory.....	142
Figure 109: Generalised structure of the dinuclear complex formed in solution between nickel(II) or cobalt(II) ions and thiaSO ₂	143
Figure 110: Summary of the hypothesised routes of photo-oxidation of solution state mixtures of the ligand thiaSO ₂ and sources of the ion Mn ²⁺	145
Figure 111: Comparison of the UV-vis absorption profile of a solution of thiaSO ₂ in DMF immediately upon dissolution and after 40 minutes of illumination.....	147
Figure 112: Mass spectrometry results from the illumination of thiaSO ₂	147
Figure 113: Emission spectra in the range from 1 200 nm to 1 350 nm for irradiated samples of thiaSO ₂ and Rose Bengal to test for the luminescence of singlet oxygen.....	148
Figure 114: (Above) Theoretical UV-visible absorption spectra calculated by DFT methods for the molecule thiaSO ₂ in its neutral, monoanionic, and dianionic forms. (Below) The simulated spectrum	

of the monoanion, with assigned transitions shown as electronic density / molecular orbital diagrams.	149
Figure 115: Illustration of the formation of biradical forms of the molecule thiaSO ₂ by absorption due to the monoanion.....	150
Figure 116: Hypothetical reaction mechanism for the photoreaction of thiaSO ₂ with Ph ₃ P.....	151
Figure 117: Illustration of the process of photo-oxidation of Mn ²⁺ ions when in solution with the thiaSO ₂ macrocycle <i>via</i> the hypothesised charge separation transition route.....	151
Figure 118: Hypothetical representation of the assembly of ordered hybrid materials.	160
Figure 119: Representation of the structural families of a) brucite Mg(OH) ₂ and b) hydrotalcite	161
Figure 120: Powder X-Ray diffraction pattern for MgAl-CO ₃ LDH.....	166
Figure 121: Powder X-Ray diffraction pattern of MgAl-NO ₃ LDH.....	167
Figure 122: Overlay comparison of the X-ray diffractograms obtained of the intercalated hybrid material measured after treatment at 25° C and at 90° C, with the diffractograms of the nitrate and carbonate forms for comparison.	168
Figure 123: Schematic of hypothesised potential phases formed by the intercalation of luminescent aggregate into MgAl-LDH.	170
Figure 124: X-ray diffraction diagram for the intercalation product of complex 3 into MgAl LDH	173
Figure 126: Magnification of the 2θ region between 1° and 12° from the PXRD diagram of the intercalation product after a 90° C aging treatment.....	174
Figure 127: Structure of suspected contaminant tetraaluminium complex of thiaSO ₂	175
Figure 128: SEM images of MgAl-NO ₃ LDH.	176
Figure 129: SEM images of intercalated LDH product [Mg _{0.67} Al _{0.33} (OH) ₂][Mn ₄ (thiaSO ₂) ₂ F].	177
Figure 130: Comparison of infra-red absorption spectra of a) free thiaSO ₂ , b) MgAl-NO ₃ LDH and c) MgAl-[Mn ₄ (thiaSO ₂) ₂ F] LDH.....	179
Figure 131: Plot of response of luminescence of hybrid material [Mg _{0.67} Al _{0.33} (OH) ₂][Mn ₄ (thiaSO ₂) ₂ F] to varying temperature between 5 and 293 K	180
Figure 132: Plot of a) peak position and width, and b) peak height and the derived luminescence lifetime for luminescence of hybrid LDH-intercalate material.....	181
Figure 133: Plot of response of luminescence of hybrid material [Mg _{0.67} Al _{0.33} (OH) ₂][Mn ₄ (thiaSO ₂) ₂ F] to varying temperature between 5 and 293 K.	182
Figure 134: Plot of a) peak position and intensity , and b) the derived luminescence lifetime for luminescence of hybrid LDH-intercalate material over the temperature range from 5 – 293 K.....	183
Figure 135: Evolution of solid state emission spectra of hybrid material [Mg _{0.67} Al _{0.33} (OH) ₂]-[Mn ₄ (thiaSO ₂) ₂ F] with varying O ₂ pressure between the range of 0.2 mbar and ambient pressure..	184
Figure 136: Evolution of solid state emission spectra of hybrid material [Mg _{0.67} Al _{0.33} (OH) ₂]-[Mn ₄ (thiaSO ₂) ₂ F] with varying pressure in a DAC.....	185
Figure 137: GC-MS analysis of supernatant solution of photocatalysed reaction of triphenylphosphine after centrifugation to remove the suspended hybrid catalyst.	187

ANNEXE 5: PUBLICATIONS

Cite this: *Dalton Trans.*, 2015, **44**,
7991

Discrete polynuclear manganese(II) complexes with thiacalixarene ligands: synthesis, structures and photophysical properties†

Yan Suffren,^{*a} Niall O'Toole,^b Andreas Hauser,^a Erwann Jeanneau,^b Arnaud Brioude^b and Cédric Desroches^{*b}

The synthesis, crystal structure and photophysical properties of the new compound $[\text{Mn}_4(\text{ThiaSO}_2)_2\text{F}][\text{K}(18\text{-crown-6})]$, $\text{ThiaSO}_2 = p\text{-tert-butylsulphonylcalix[4]arene}$, are presented and compared to the ones of $[\text{Mn}_4(\text{ThiaSO}_2)_2\text{F}]\text{K}$. The strong orange luminescence is attributed to the Mn^{2+} centred ${}^4\text{T}_1 \rightarrow {}^6\text{A}_1$ transition. Its temperature and pressure dependence and quenching by molecular dioxygen are reported. The latter is attributed to energy transfer from the ${}^4\text{T}_1$ state exciting dioxygen to its ${}^1\Sigma^+_g$ state. In the solid state, the quenching is much more efficient in $[\text{Mn}_4(\text{ThiaSO}_2)_2\text{F}][\text{K}(18\text{-crown-6})]$ than in $[\text{Mn}_4(\text{ThiaSO}_2)_2\text{F}]\text{K}$. This is attributed to the open pore structure of the former allowing fast diffusion of dioxygen into the crystal lattice.

Received 27th February 2015,
Accepted 23rd March 2015

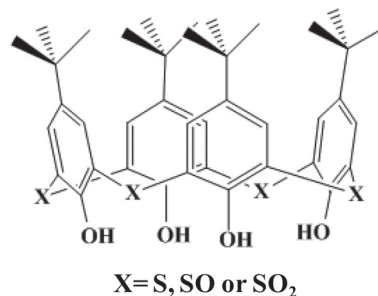
DOI: 10.1039/c5dt00827a

www.rsc.org/dalton

Introduction

The macrocycle *p-tert-butylthiacalix[4]arene* (ThiaS), a homologue of the calixarene family, consists of phenol moieties linked by sulphur atoms. Its ease of accessibility and strong multichelating power, arising from the proximity of the phenoxide groups to the bridging sulphur atoms, make this ligand a popular choice in coordination chemistry. Consequently, since the first synthesis of this molecule was described by the Myano group in 1997¹ (Scheme 1), a multitude of polynuclear metal complexes have been isolated, reinforcing: (i) its structuring role in the creation of either high-nuclearity isolable paramagnetic metal aggregates,² or the coordination-based molecular 'building bricks' leading to nano-capsule formation by supramolecular assembly,³ and (ii) its electronic properties, known as the antenna effect, for luminescence in ions such as Tb^{3+} or even Eu^{3+} .⁴

In previous work, we found that under solvothermal conditions *p-tert-butylthiacalix[4]arene* and its sulphonyl and sulphoxide derivatives give rise to tetranuclear metallic complexes comprising Mn^{2+} ions. Differences in both the optical



Scheme 1 Representation of *p-tert-butylthiacalix[4]arene* (ThiaS with $\text{X} = \text{S}$), *p-tert-butylsulphoxylcalix[4]arene* (ThiaSO with $\text{X} = \text{SO}$) and *p-tert-butylsulphonylcalix[4]arene* (ThiaSO₂ with $\text{X} = \text{SO}_2$).

and structural properties were observed between those complexes obtained with ThiaS and ThiaSO,^{2d} and those obtained with ThiaSO₂.^{2k} For ThiaS and ThiaSO neutral complexes are attained, consisting of two macrocycles and four Mn^{2+} ions in trigonal bipyramidal geometry. In both of these cases, no specific luminescence properties have been observed. For ThiaSO₂ a similar structure is obtained with the sole difference being the presence of a $\mu_4\text{-OH}^-$ group at the centre of the square formed by the four Mn^{2+} ions, which display capped trigonal bipyramidal coordination geometry. This $\mu_4\text{-OH}^-$ results in a negative charge over the aggregate, which is compensated by the presence of an alkali metal ion. In the solid state this ion interlinks the aggregates by ways of coordination to the oxygen atoms of sulphonyl groups. This family of clusters demonstrates an ambient temperature luminescence at a wavelength

^aDépartement de chimie physique, Université de Genève, 30 Quai Ernest-Ansermet, 1211 Genève 4, Switzerland. E-mail: Yan.Suffren@unige.ch

^bLaboratoire des Multimatériaux et Interfaces (UMR 5615), Université Claude Bernard de Lyon 1, Campus de la Doua, 69622 Villeurbanne, France. E-mail: cedric.desroches@univ-lyon1.fr

† Electronic supplementary information (ESI) available: Additional X-ray crystal structures; luminescence spectra; crystallographic data (in cif format). CCDC 1050380. For ESI and crystallographic data in CIF or other electronic format see DOI: 10.1039/c5dt00827a

of approximately 580 nm when excited by illumination of 360 nm. Replacing the $\mu_4\text{-OH}^-$ with $\mu_4\text{-F}^-$ considerably increases the luminescence lifetime of this system.

The strong luminescence of the Mn^{2+} ion arising from $^4\text{T}_1(^4\text{G})$ state was put to use at the start of the 20th century in luminescent mineral materials using red or green phosphors (neon discharge, fluorescent lamp).⁵ Since then, intense spectroscopic studies have been carried out, which shed light on the importance of the environment of the Mn^{2+} ion as regards its luminescence properties.⁶ However, despite the development of coordination chemistry, few studies have shown Mn(II) complexes presenting such properties at ambient temperature.⁷ For this reason, we have resolved to pursue further investigation on the $[\text{Mn}_4(\text{ThiaSO}_2)_2\text{F}]^-$ system by spectroscopic analysis, in both solution and the solid state. Moreover it has been shown that the conformation of the macrocycle, as well as the presence of sulphonyl groups, significantly modifies the electronic properties of the thiacalixarene family of complexes.⁸

Herein we report the preparation, crystal structures and photophysical behaviour of the new compound $[\text{Mn}_4(\text{ThiaSO}_2)_2\text{F}][\text{K}(18\text{C}6)]$ (**2**), 18C6 = 18-crown-6, and compare the latter to the one of $[\text{Mn}_4(\text{ThiaSO}_2)_2\text{F}]\text{K}$ (**1**). We thus will study: (i) the effect of removing the K^+ -sulphonyl interaction, and (ii) the effect of the conformation of the macrocycle.

Results and discussion

Crystal structure

The compounds of the tetranuclear complex **1** and **2** were obtained as pale-yellow coloured crystals with a relatively high

yield by solvothermal reaction of $\text{MnCl}_2 \cdot 4\text{H}_2\text{O}$, *p*-*tert*-butylsulphonylcalix[4]arene (ThiaSO_2) and KF for **1** and by adding 18C6 for **2** in a 1/10 (v/v) H_2O -MeOH mixed solvents (total 11 ml) at 170 °C during at least 2 days.

Compounds **1** and **2** are composed of squares of four manganese(II) ions sandwiched between two ThiaSO_2 macrocycles as shown in Fig. 1 and 2. In the middle of the square formed by the four manganese(II) ions, the presence of $\mu_4\text{-F}^-$ gives a negative charge to the cluster. The electroneutrality of the complex is achieved by the presence of the K^+ cation, coordinated by sulphonyl and methanol groups for **1** and coordinated by 18C6 and two methanol molecules for **2**. The originality of this type of aggregate, with a sevenfold $[\text{MnO}_6\text{F}]$ coordination polyhedron having approximately C_{2v} symmetry and a square planar relationship to the fluoride group (Scheme 2), has already been discussed in a previous article.^{2k} Both compounds crystallise in the $P\bar{1}$ space group (for details of the structure determination see Experimental section and ESI†).⁹ For both, the centre of symmetry positioned on the fluoride group requires that the macrocycles, on either side of the square formed by the manganese ions, are crystallographically equivalent. The macrocycles of **1** and **2** are in a slightly distorted cone conformation: in **1** $d(\text{O}12\text{-O}33)/d(\text{O}27\text{-O}4) = 0.98$ and in **2** $d(\text{O}4\text{-O}19)/d(\text{O}12\text{-O}30) = 0.98$.

The tetranuclear clusters in **1** are linked through the coordinated potassium ion and sulphonyl group, making **1** a one dimensional network (Fig. 3a). The coordination of K^+ by the crown ether in **2** prevents interactions between the sulphonyl groups and the potassium ion. The tetranuclear clusters in **2** stack upon each other along the *c*-axis of the network, forming columns which are isolated from one another by the inclusion of $[\text{K}18\text{C}6]^+$ groups (Fig. 3b). The shortest distance of the inter-

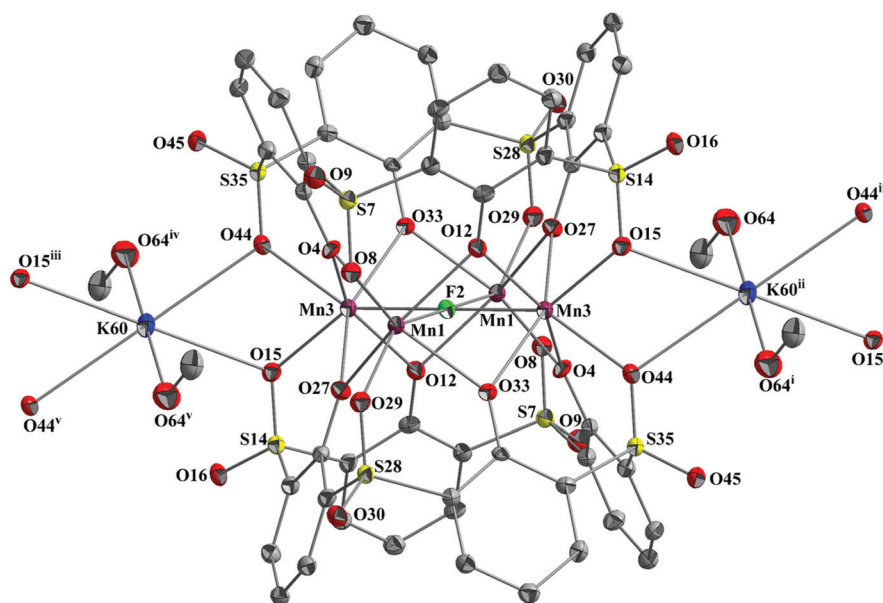


Fig. 1 ORTEP¹⁰ diagram of **1** with thermal ellipsoids at 50% probability. Hydrogen atoms and *tert*-butyl groups are omitted for clarity. Selected atom–atom distances [Å]: Mn1–Mn3ⁱ 3.0972(7); Mn1–F2 2.2018(5); F2–Mn3 2.1732(5); Mn1–O8 2.169(2) < Mn–O < Mn1–O4 2.242(2). Symmetry transformations used to generate equivalent atoms: ⁱ (1 – *x*, 1 – *y*, 1 – *z*); ⁱⁱ (–1 + *x*, *y*, *z*); ⁱⁱⁱ (–3 – *x*, 1 – *y*, 1 – *z*); ^{iv} (1 + *x*, *y*, *z*); ^v (2 – *x*, 1 – *y*, 1 – *z*).

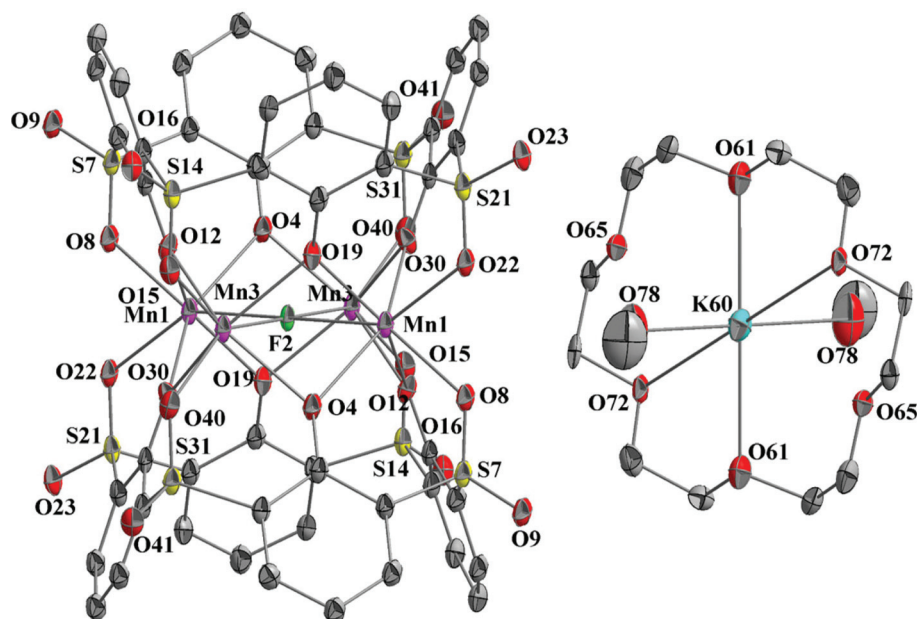
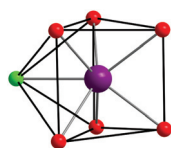


Fig. 2 ORTEP¹⁰ diagram of **2** with thermal ellipsoids at 50% probability. Hydrogen atoms and *tert*-butyl groups are omitted for clarity. Selected atom–atom distances [Å]: Mn1–F2 2.2091(4); Mn3–F2 2.1924(5); Mn1–Mn3 3.1057(7); Mn3–O15 2.177(2) < Mn–O < Mn3–O19ⁱ 2.247(2). Symmetry transformations used to generate equivalent atoms: ⁱ (–*x* + 1, –*y* + 1, –*z* + 1); ⁱⁱ (–*x*, –*y*, –*z* + 1); ⁱⁱⁱ (–*x* + 1, –*y*, –*z* + 1); ^{iv} (*x*, *y* – 1, *z*); ^v (–*x*, –*y* + 1, –*z* + 1).



Scheme 2 Representation of the sevenfold [MnO₆F] coordination polyhedron having approximately C_{2v} symmetry.

action between the K⁺ ion and the tetranuclear cluster in compound **1** is 2.72 Å (distance O15–K60) whereas for compound **2** it is 5.54 Å (distance O8–K60).

Photophysical characterisation

Absorption and luminescence in DMF solution. Fig. 4 shows the absorption, excitation and emission spectra at room temperature in dimethylformamide (DMF) solution of [Mn₄(ThiaSO₂)₂F]K (**1**) and [Mn₄(ThiaSO₂)₂F][K(18C6)] (**2**) between 11 000 and 38 000 cm^{–1} (265–910 nm). The absorption spectrum of **1** is identical to that of **2**. The absorption bands observed are mainly the signature of the ThiaSO₂ calixarene ligand. In the UV region there are two band maxima $\tilde{\nu}_{\max 1}$ and $\tilde{\nu}_{\max 2}$ at 28 490 cm^{–1} (351 nm) and 35 300 cm^{–1} (283 nm), respectively. These two bands can be attributed to $\pi \rightarrow \pi^*$ transitions of the ThiaSO₂ ligand. The molar extinction coefficient of the intense absorption band at 28 490 cm^{–1} is within experimental accuracy identical for the two compounds with a value of $\epsilon_{\max} = 72\,000\text{ M}^{-1}\text{ cm}^{-1}$.

The emission spectra of **1** and **2** in DMF (see Fig. 4) upon photoexcitation at 28 570 cm^{–1} (350 nm) show an intense and broad luminescence band between 12 000 and 18 000 cm^{–1} (555–833 nm) with a maximum $\tilde{\nu}_{\max}$ at 15 010 cm^{–1} (666 nm). As expected, in solution the influence of the cation is negligible and no difference in the emission spectra between the two compounds has been observed. The orange-red luminescence with a very large gap between the strong absorption at 28 490 cm^{–1}, a lifetime of 35 μs and a quantum efficiency of 0.4% in non-deoxygenated solution at 298 K (compared to 1.08 ms and therefore around 15% in a deoxygenated solution) originates from the lowest energy component of the ${}^4\text{T}_1(t_{2g}^4e_g^1) \rightarrow {}^6\text{A}_1(t_{2g}^3e_g^2)$ d–d transition of the manganese(II) ions in d⁵ high-spin configuration. As mentioned above, the crystal structure reveals a sevenfold coordination sphere for the Mn(II) ions in a monocapped trigonal prism geometry and close to C_{2v} symmetry, resulting in a large splitting of the ${}^4\text{T}_1$ state of octahedral parentage (see below). In essence, photoexcitation into the ligand centred $\pi \rightarrow \pi^*$ transition at 28 570 cm^{–1} is followed by fast intersystem crossing and internal conversion, thus resulting in the orange-red metal-centred d–d luminescence.

The above is further borne out by the excitation spectra of both compounds in DMF solution included in Fig. 4, which were collected at the emission maximum of 15 380 cm^{–1} (650 nm) and at very low concentrations of $c = 1.5 \times 10^{-6}\text{ M}$ in order to minimise saturation effects in the region of the strong UV absorption bands. They are indeed perfectly superimposed to the absorption spectra thus proving unambiguously that the emission is intrinsic to the complexes.

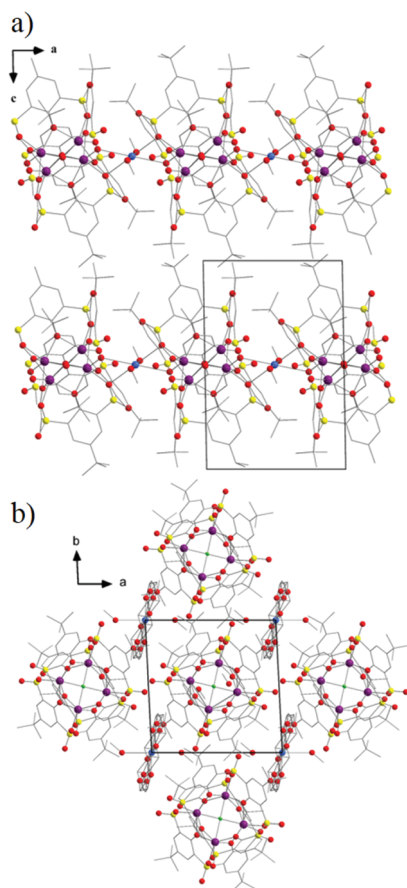


Fig. 3 (a) Projection of the crystal packing of compound **1** in the (a, c) plane, (b) projection of the crystal packing of compound **2** in the (a, b) plane.

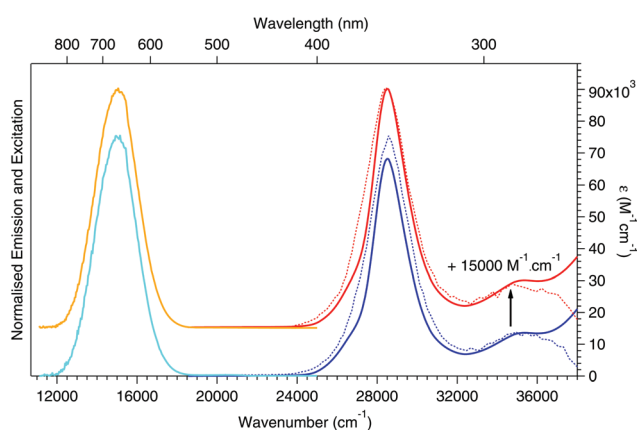


Fig. 4 Absorption (red and dark blue curves), excitation (red and blue dotted curves) and emission (orange and light blue curves) spectra in DMF solution of $[\text{Mn}_4(\text{ThiaSO}_2)_2\text{F}]\text{K}$ **1** and $[\text{Mn}_4(\text{ThiaSO}_2)_2\text{F}]\text{K}(\text{18C6})$ **2** at room temperature, $c = 1.5 \times 10^{-4}$ M for **1** and $c = 1.2 \times 10^{-4}$ M for **2** for the absorption and emission spectra, and $c = 1.5 \times 10^{-6}$ M for **1** and $c = 1.3 \times 10^{-6}$ M for **2** for the excitation spectra. The spectra of **2** are offset along the intensity/absorptivity axes for clarity.

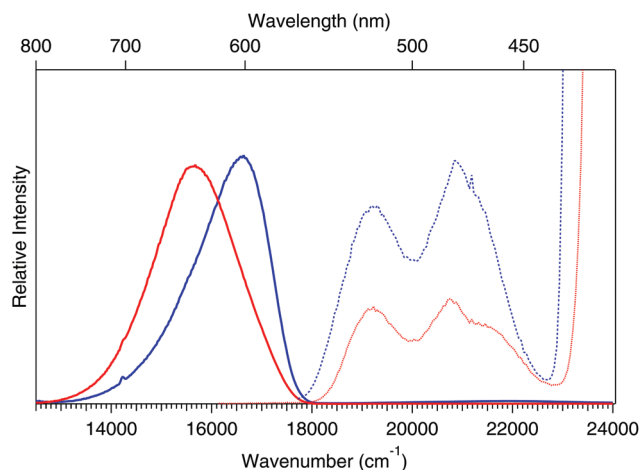


Fig. 5 Solid-state emission spectra (solid curves) at 7.5 K upon photo-excitation at $28\,570\text{ cm}^{-1}$ (350 nm) and excitation spectra at 8 K (dotted curves) of $[\text{Mn}_4(\text{ThiaSO}_2)_2\text{F}]\text{K}$ **1** (blue) and $[\text{Mn}_4(\text{ThiaSO}_2)_2\text{F}]\text{K}(\text{18C6})$ **2** (red).

Solid-state emission and excitation spectra. The low temperature solid-state emission and excitation spectra for the compounds **1** and **2** are displayed in Fig. 5. Upon excitation at $28\,570\text{ cm}^{-1}$ (350 nm), **1** presents an intense broad and asymmetric emission band centred at $16\,600\text{ cm}^{-1}$ (602 nm) with a full width at half maximum (FWHM) of approximately 1700 cm^{-1} . In contrast, **2** shows an intense symmetric emission band at $15\,660\text{ cm}^{-1}$ (639 nm) and a FWHM of about 2000 cm^{-1} . Thus there is a redshift of the luminescence band maximum by around 950 cm^{-1} and an increase by about 18% of the FWHM between compounds **1** and **2**. As in solution, the orange-red luminescence band originates from the ${}^4\text{T}_1 \rightarrow {}^6\text{A}_1$ transition of the Mn(II) in d^5 high-spin configuration.

The solid-state excitation spectra at 8 K for both compounds are included in Fig. 5. In the UV region of the strong ligand-centred $\pi\text{-}\pi^*$ absorption bands they are saturated. However, they show a broad and structured band with two maxima $\tilde{\nu}_{\text{max}1}$ and $\tilde{\nu}_{\text{max}2}$ localised at approximately $19\,200\text{ cm}^{-1}$ (521 nm) and $20\,800\text{ cm}^{-1}$ (481 nm), respectively, and an indication of a shoulder on the high-energy side. These can be attributed to the split components of the d-d ${}^6\text{A}_1 \rightarrow {}^4\text{T}_1$ transition of the manganese(II) ion, as in C_{2v} the ${}^4\text{T}_1$ excited state is split into three energy level in first order.

Temperature-dependence of the Mn²⁺ luminescence. The luminescence of **1** and **2** in the solid state between 7.5 K and room temperature and in vacuum on excitation at $28\,570\text{ cm}^{-1}$ (350 nm) is shown in Fig. 6. The luminescence intensity of **1** decreases only slightly as temperature increases up to just below room temperature and then drops more rapidly to 70% of its low-temperature value, as shown in Fig. 7. At the same time the FWHM increases by 29%, that is, from 1700 to 2200 cm^{-1} , whereas the band maximum $\tilde{\nu}_{\text{max}}$ is stable between 7.5 and 100 K with a value of $16\,600\text{ cm}^{-1}$, and shifts to slightly higher energies above 100 K.

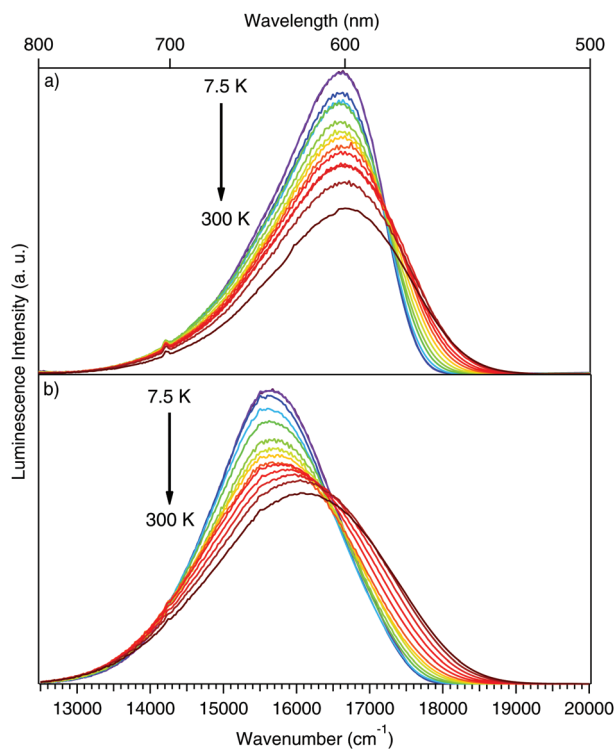


Fig. 6 Solid-state emission spectra of $[\text{Mn}_4(\text{ThiaSO}_2)_2\text{F}]\text{K}$ **1** (a) and $[\text{Mn}_4(\text{ThiaSO}_2)_2\text{F}][\text{K}(18\text{C}6)]$ **2** (b) between 7.5 and 300 K upon photoexcitation at $28\,570\text{ cm}^{-1}$ (350 nm).

For **2** the luminescence shows the same temperature dependence as for **1** with a somewhat smaller decrease to 88% between 7.5 and 300 K. The variation of the FWHM is slightly larger for **2** than for **1**, with an increase by approximately 39% from 2000 cm^{-1} to 2780 cm^{-1} in the same temperature range, and a slight redshift from $15\,660$ to $15\,630\text{ cm}^{-1}$ between 7.5 and 25 K followed by a blueshift to $16\,090\text{ cm}^{-1}$ is observed for **2**. At a given temperature, the FWHM for **2** is larger than for **1**.

Fig. 7b includes the luminescence lifetimes for **1** and **2** between 3 K and 300 K under pulsed photoexcitation at $28\,170\text{ cm}^{-1}$ (355 nm). Decay curves are close to single exponential except for a small deviation at short times. At 3 K the lifetimes calculated by the Igor fitting software¹¹ are 2.12 ms for **1** and 2.31 ms for **2**, respectively. They increase between 3 K and 75 K for **1** with a maximum value of 2.41 ms and between 3 K and 100 K for **2** with a maximum value of 2.48 ms. Then, the lifetime values decrease gradually up to room temperature reaching 1.65 ms and 2.00 ms for **1** and **2**, respectively. The luminescence quantum yield for **1** in the solid state at room temperature is around 50%. Together with the above luminescence lifetime this gives a radiative lifetime of around 3 ms, which is typical for spin-forbidden d-d transitions.

O₂ pressure-dependence of the Mn²⁺ luminescence-quenching in the solid state. As mentioned above, in solution the presence of oxygen quenches the Mn²⁺ luminescence considerably, such that in a deoxygenated solution at room tempera-

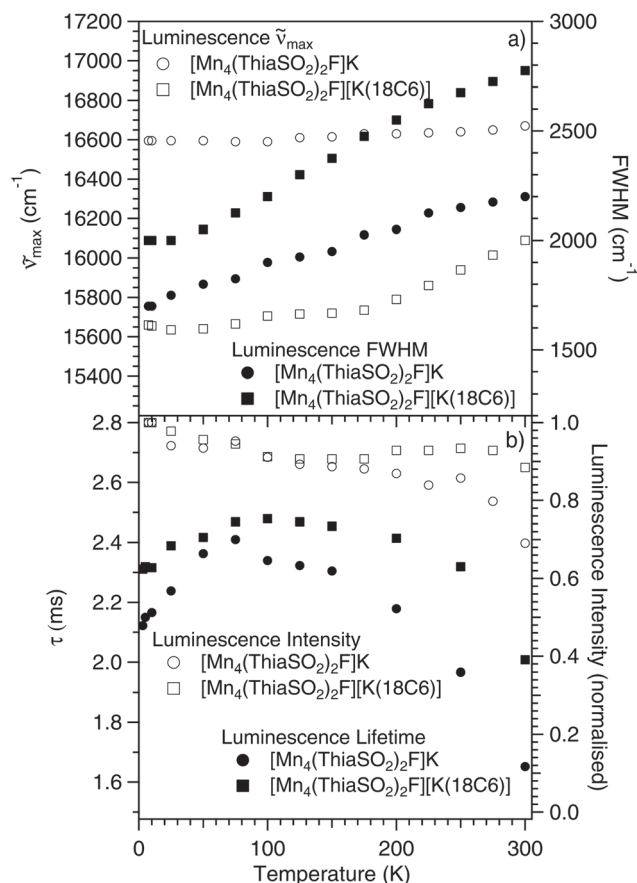


Fig. 7 (a) The energy band maxima $\tilde{\nu}_{\text{max}}$ (left axis) and FWHM (right axis) upon photoexcitation at $28\,570\text{ cm}^{-1}$ (350 nm) of **1** (circles) and **2** (squares). (b) Luminescence lifetimes (left axis) and integrated luminescence intensities (right axis) of **1** (circles) and **2** (squares) as function of temperature. The luminescence lifetimes and intensities are obtained upon photoexcitation at $28\,170\text{ cm}^{-1}$ (355 nm, pulsed laser) and $28\,570\text{ cm}^{-1}$ (350 nm, continuous laser), respectively.

ture the luminescence quantum efficiency is around 15% whereas under atmospheric conditions it is only 0.4%. What about the influence of O₂ on the solid-state luminescence? Fig. 8 shows the luminescence spectra of **1** and **2** at 298 K as a function of the air pressure between 0.1 and 1010 mbar. The behaviour observed is reversible and reproducible. The luminescence intensities increase and decrease within a few seconds by removing from or introducing the O₂ into the sample compartment.

For **1**, the luminescence intensity decreases only by approximately 15% between 0.1 and 1010 mbar. For **2**, the intensity decreases quite rapidly to less than 5% of its initial value. The difference in behaviour between the two compounds must be due to the structural differences. In **1**, the K⁺ cations bridge the $[\text{Mn}_4(\text{ThiaSO}_2)_2\text{F}]^-$ entities leading to compact structure limiting the diffusion of the dioxygen into the lattice. In contrast, for **2** the isolated $[\text{K}(18\text{C}6)]^+$ cations create a porous structure with empty spaces between the $[\text{Mn}_4(\text{ThiaSO}_2)_2\text{F}]^-$ entities connected only by weak ionic inter-

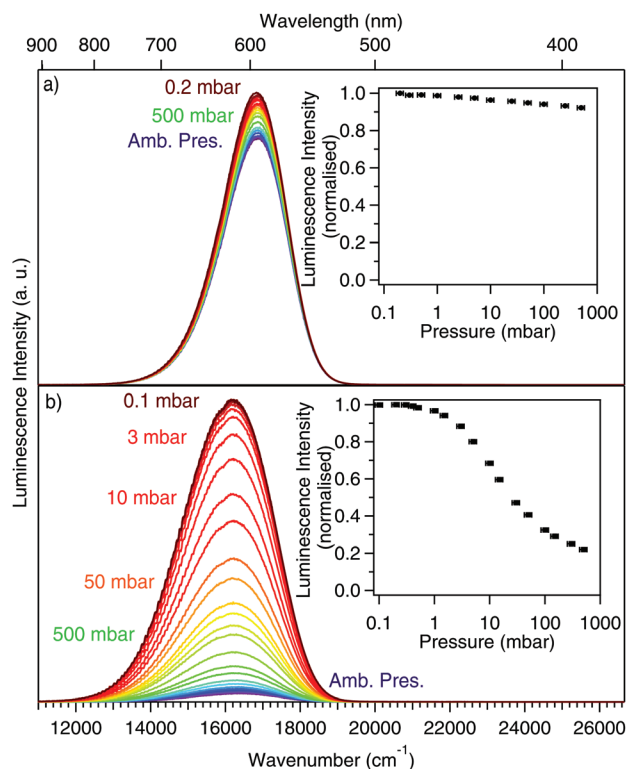


Fig. 8 Solid-state emission spectra of $[\text{Mn}_4(\text{ThiaSO}_2)_2\text{F}]\text{K}$ **1** (a) and $[\text{Mn}_4(\text{ThiaSO}_2)_2\text{F}][\text{K}(18\text{C}6)]$ **2** (b) at variable molecular oxygen pressure and upon photoexcitation at $24\,690\text{ cm}^{-1}$ (405 nm). The normalised luminescence intensities are plotted in the top and bottom insets for **1** and **2**, respectively.

actions. The dioxygen can be removed or introduced more easily into the structure.

The most probable mechanism for the quenching of the spin-forbidden Mn^{2+} centred ${}^4\text{T}_1 \rightarrow {}^6\text{A}_1$ luminescence is given by a spin-conserving energy transfer process from the excited complex to O_2 thereby exciting O_2 from its ${}^3\Sigma_g^-$ ground state to the ${}^1\Sigma_g^+$ excited state.¹²

For comparison to the solid state, the O_2 pressure-dependence of the luminescence behaviour was studied for the two compounds in DMF solution where the $[\text{Mn}_4(\text{ThiaSO}_2)_2\text{F}]^-$ tetranuclear complex is considered as totally isolated. The luminescence spectra of solutions of **1** and **2** after different times (0–900 s) of de-oxygenation by N_2 bubbling were recorded (see Fig. S1 and S2 in ESI†). The reversibility was checked as function of time (0–3600 s) of re-oxygenation of the N_2 saturated solution by exposing them to air (see Fig. S3 and S4 in ESI†). As for the solids, the luminescence behaviour is reversible, with an increase and a decrease of the luminescence intensities by bubbling N_2 (removal O_2) and by re-oxygenation (exposing to air), respectively. The maximum luminescence intensities are observed after approximately 120 s of N_2 bubbling (see Fig. S5 in ESI†).

Pressure-dependence of the Mn^{2+} luminescence. Fig. 9a and 9b show the luminescence spectra of **1** and **2**, respectively,

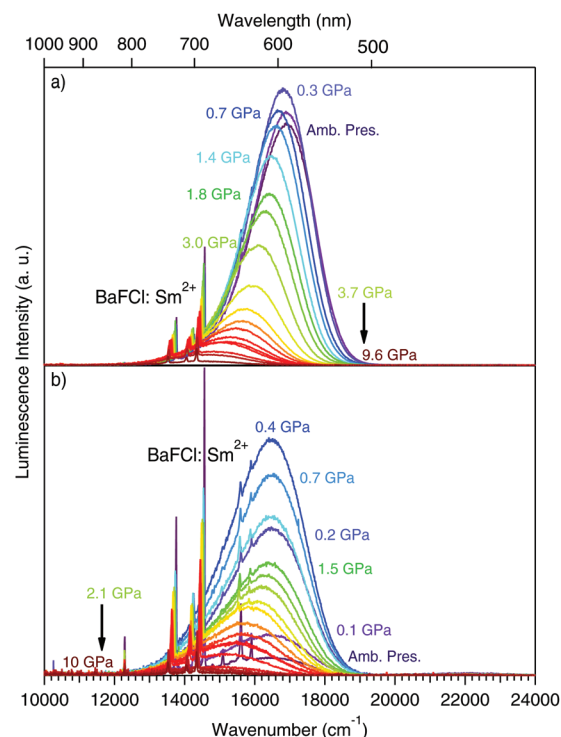


Fig. 9 Solid-state emission spectra of $[\text{Mn}_4(\text{ThiaSO}_2)_2\text{F}]\text{K}$ **1** (a) and $[\text{Mn}_4(\text{ThiaSO}_2)_2\text{F}][\text{K}(18\text{C}6)]$ **2** (b) between ambient pressure and 10 GPa upon photoexcitation at $24\,690\text{ cm}^{-1}$ (405 nm) at 298 K. The pressure in the DAC has been determined by following the shift of the ${}^5\text{D}_0 \rightarrow {}^7\text{F}_0$ emission band of the samarium(II) ion in $\text{BaFCl}:\text{Sm}^{2+}$ compound (room temperature rate of $-21\text{ cm}^{-1}\text{ GPa}^{-1}$).¹³

between ambient pressure and 10 GPa at room temperature. In addition to the broad band due the Mn^{2+} luminescence, all show a series of sharp bands corresponding to $\text{BaFCl}:\text{Sm}^{2+}$ f-f luminescence introduced into diamond anvil cell (DAC) as *in situ* pressure sensor.¹³

For **1** the luminescence intensity increases by approximately 10% between ambient pressure and 0.3 GPa, then it decreases gradually and becomes very weak at a pressure of 9.6 GPa. At the same time the luminescence band maximum shifts linearly to lower energies by $-230\text{ cm}^{-1}\text{ GPa}^{-1}$ (Fig. 10a). For **2**, the behaviour at variable pressure is very similar to **1**, except that the initial increase in intensity up to a pressure of 0.4 GPa is much larger. The luminescence band maximum is stable up to this pressure, above that pressure it likewise shifts to the red by $-190\text{ cm}^{-1}\text{ GPa}^{-1}$, that is, close to the value obtained for compound **1** (Fig. 10a). Such a redshift is expected for the spin-forbidden ${}^4\text{T}_1(t_{2g}^4e_g^1) \rightarrow {}^6\text{A}_1(t_{2g}^3e_g^2)$ d-d transition. The formal transfer of an electron from a non-bonding t_{2g} orbital to an anti-bonding e_g orbital results in an expansion of the coordination sphere during the emission process. Thus external pressure destabilises the ground state with respect to the first excited state by a work term of the form $p\Delta V$.¹⁴ The shift of around $-200\text{ cm}^{-1}\text{ GPa}^{-1}$ corresponds to $\Delta V \approx 5\text{ \AA}^3$ per complex. This is in line with ligand-field theoretical consider-

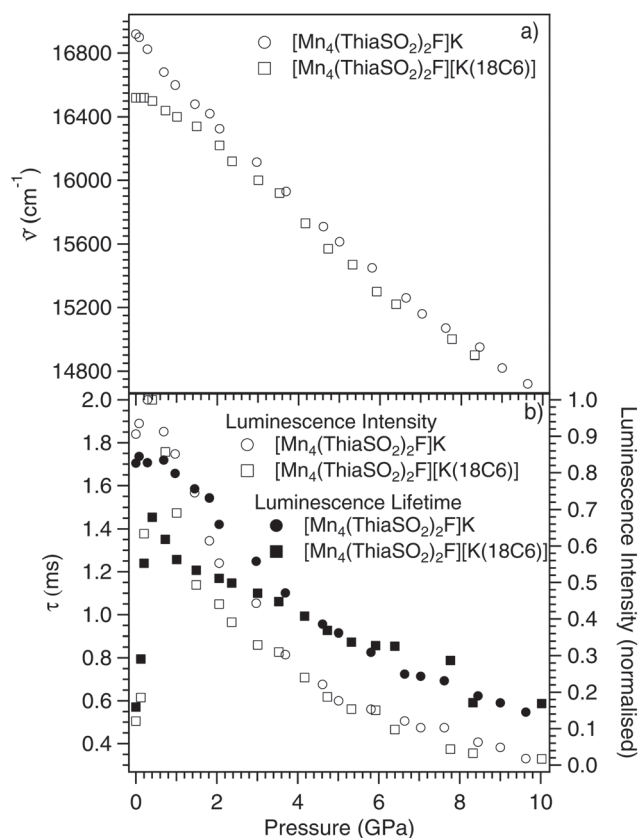


Fig. 10 (a) The energy band maxima $\tilde{\nu}_{\max}$ upon photoexcitation at $24\,690\text{ cm}^{-1}$ (405 nm) of **1** (circles) and **2** (squares). (b) Luminescence lifetimes (left axis) and integrated luminescence intensities (right axis) of **1** (circles) and **2** (squares) as function of pressure. The luminescence lifetimes and intensities at 298 K were obtained upon photoexcitation at $28\,170\text{ cm}^{-1}$ (355 nm , pulsed laser) and $24\,690\text{ cm}^{-1}$ (405 nm , continuous laser) respectively.

ations. As pressure increases, the Mn–O bond is slightly compressed and therefore the ligand-field strength increases. According to the Tanabe–Sugano diagram¹⁵ for d^5 this results in a decrease of the energy of the ${}^4\text{T}_1$ state with respect to the ${}^6\text{A}_1$ ground state.

The luminescence lifetimes between ambient pressure and 10 GPa and are plotted in Fig. 10b. For **1**, the lifetime at ambient pressure in the DAC is 1.71 ms . This value is in line with the values of 1.65 and 1.68 ms determined for **1** in the presence and absence of atmospheric O_2 , respectively. As pressure increases, the lifetime decreases continuously from 1.71 ms to 0.55 ms . Concomitantly, the luminescence intensity decreases likewise with increasing pressure.

For **2**, the luminescence lifetime of 0.57 ms at ambient pressure in the DAC is lower than the lifetime of 2.00 ms measured at room temperature and ambient pressure in a helium gas medium. Indeed, the value of 0.57 ms for the luminescence lifetime in the DAC is close to the value of 0.53 ms in the solid state under atmospheric pressure, thus indicating that oxygen also quenches the luminescence in the sample

prepared in the DAC. The luminescence lifetime for **2** then first increases from 0.57 ms at ambient pressure to 1.45 ms at 0.4 GPa , then it gradually decreases at higher pressure to 0.59 ms at 9.6 GPa , that is, above 0.4 GPa it shows the same behaviour as for compound **1**. Likewise the luminescence intensity increases up to 0.4 GPa and the decreases concomitantly with the lifetime. The strong increase of the luminescence lifetime and intensity between ambient pressure and 0.4 GPa is unusual. The only possible reason to explain this behaviour is that the O_2 that has diffused into the lattice at ambient pressure is almost quantitatively expelled from lattice upon application of a comparatively low pressure, thus reducing the quenching of the Mn^{2+} .

The decrease in luminescence lifetime and intensity with increasing pressure for **1** right from the beginning and for **2** for pressures above 0.4 GPa indicates a gradual decrease in luminescence quantum efficiency. Such a decrease is expected based on the energy gap law¹⁶ which states that the non-radiative decay rate constant increases exponentially with a decreasing zero-point energy difference. Quantitatively, according to the decrease in lifetime the quantum efficiency should decrease from the maximum value of 50% at ambient pressure and room temperature to around 15% at 10 GPa . However, the actual luminescence intensity at 10 GPa is less than 5% of its maximum value. The reason for this apparent discrepancy is not entirely clear. It seems to indicate that concomitantly with the increase in the non-radiative decay rate constant the radiative lifetime increases. This could be related to the fact that the lowest excited state of Mn^{2+} consists of a multiplet with components in thermal equilibrium having different radiative lifetimes and luminescence quantum efficiencies. Pressure would then not only shift the energy of this multiplet with respect to the ground state, but also influence the multiplet splittings and thus the observed lifetime and luminescence quantum efficiencies differently.

Conclusions

Thiacalixarene complexes have been studied since the late 1990's for their magnetic, electronic and optical properties, with various potential applications such as molecular recognition, catalysis, self-assembly, and nanomedicine.¹⁷ The new calixarene compound, $[\text{Mn}_4(\text{ThiaSO}_2)_2\text{F}][\text{K}(18\text{C}6)]$ has been characterised by single crystal X-ray diffraction. The structural studies reveal a structure very similar to that of $[\text{Mn}_4(\text{ThiaSO}_2)_2\text{F}]\text{K}$, with a square of four manganese(II) ions sandwiched between two ThiaSO₂ macrocycles. The main difference between the two structures lies in the connection of the tetranuclear clusters in the form of a one dimensional network of the clusters for **1** by K^+ coordination, and to isolated clusters by the inclusion of $[\text{K}18\text{C}6]^+$ for **2**. In both clusters, the manganese C_{2v} symmetry and the $\mu_4\text{-F}^-$ square planar geometry are rare examples in the literature. Both compounds present an intense and broad luminescence band originating from the ${}^4\text{T}_1(t_{2g}^4e_g^1) \rightarrow {}^6\text{A}_1(t_{2g}^3e_g^2)$ d–d transition of the manganese(II)

ions. This luminescence has been studied at variable temperature and ambient pressure as well as at variable pressure at room temperature. The presence of oxygen in solution and in the solid state quenches the Mn^{2+} luminescence by energy transfer from the excited complex to O_2 thereby exciting O_2 from its $^3\Sigma_g^-$ ground state to the $^1\Sigma_g^+$ excited state. The quenching is more efficient for the $[\text{K}(\text{18C6})]^+$ containing compound with its open structure, which facilitates O_2 diffusion into the lattice. This is the first compound of a calixarene complex showing such a strong O_2 pressure dependence in the solid state. Interestingly, a comparatively low hydrostatic pressure squeezes out the O_2 , thus restoring the luminescence intensity.

Experimental

All chemicals and solvents were used as received (solvents: Carlo Erba RPE; chemicals: Aldrich); all preparations and manipulations were performed under aerobic conditions. The ligands, *p*-*tert*-butylthiacalix[4]arene (ThiaS),^{1a,18} *p*-*tert*-butylsulphonylcalix-[4]arene (ThiaSO₂)^{2a,19} and compound **1**^{2k} were synthesised by the published procedures. FT-IR spectra were recorded on a Nicolet 380 spectrometer. Mass spectra were performed on a MicroTOF-QII Bruker mass spectrometer (ESI source).

Synthesis of $[\text{Mn}_4(\text{ThiaSO}_2)_2(\text{F})][\text{K}(\text{18C6})]\cdot 2\text{CH}_3\text{OH}$ (**2**)

Compound **2** was obtained in the form of pale-yellow coloured crystals from the reaction mixture of *p*-*tert*-butylsulphonylcalix-[4]arene (ThiaSO₂) (0.05 g, 0.059 mmol) with $\text{MnCl}_2\cdot 4\text{H}_2\text{O}$ (0.05 g, 0.252 mmol), KF (0.02 g, 0.357 mmol), 18-crown-6 (0.02 g, 0.075 mmol), methanol (10 mL) and water (1 mL) in a 23 mL Teflon-lined autoclave under an autogenous pressure at 170 °C for 3 days. The crystals were isolated upon filtration and were washed with methanol. Yield: 60%. IR (cm⁻¹) MS ESI (negative mode): $[(\text{Mn}_4(\text{ThiaSO}_2)_2\text{F})^-]$ calculated: 1927 *m/z*, found: 1927.03 *m/z*.

Single crystal X-ray diffraction XRD

Suitable crystals were selected and mounted on a Gemini kappa-geometry diffractometer (Agilent Technologies UK Ltd) equipped with an Atlas CCD detector and using Mo radiation ($\lambda = 0.71073$ Å). Intensities were collected at 100 K by means of the CrysAlisPro software.²⁰ Reflection indexing, unit-cell parameters refinement, Lorentz-polarisation correction, peak integration and background determination were carried out with the CrysAlisPro software.²⁰ An analytical absorption correction was applied using the modeled faces of the crystal.²¹ The structures were solved by direct methods with SIR97 and the least-square refinement on F^2 was achieved with the CRYSTALIS software.²² All non-hydrogen atoms were refined anisotropically. The hydrogen atoms were all located in a difference map, but those attached to carbon atoms were repositioned geometrically. The H atoms were initially refined with soft restraints on the bond lengths and angles to regularise their

geometry (C–H in the range 0.93–0.98 Å, N–H in the range 0.86–0.89 Å and O–H = 0.82 Å, and $U_{\text{iso}}(\text{H})$ in the range 1.2–1.5 times U_{eq} of the parent atom), after which the positions were refined with riding constraints. For the experimental details see ESI.† CCDC 1050380 contain the supplementary crystallographic data for this paper.

Spectroscopic measurements

Electronic absorption spectra in the UV-Vis were recorded at 293 K from solutions in dimethylformamide (DMF) with a double beam absorption spectrometer (Agilent, Cary 5000) and a commercial fluorimeter (Jobin Yvon Horiba FL3-22, Fluorolog@-3) equipped with a peltier-cooled photomultiplier (Hamamatsu R2658P, sensitivity: 185–1010 nm) using quartz cells of 0.2 cm and 1 cm path length, for the absorption, and excitation–emission spectra, respectively. Powder samples were mounted directly onto copper plates using conductive silver glue and cooled in an optical closed-cycle cryostat capable of reaching temperatures down to 3 K in a helium atmosphere (Sumitomo SHI-950/Janis Research CCS-500/204). The emission spectra at variable temperature (7.5–293 K) were measured on the Fluorolog@-3 spectrometer. High resolution emission spectra were recorded upon excitation with 405 and 473 nm diode lasers or with a Nd:YAG laser (Quantel Brillant B) using the third harmonic at 355 nm. The emitted light was analysed at 90° with a Spex 270M monochromator with holographic gratings (150 grooves mm⁻¹, blazed at 600). Light intensity was detected by a photomultiplier (Hamamatsu R928) or CCD camera. Appropriate filters were utilised to remove the laser light, the Rayleigh scattered light and associated harmonics from the emission spectra. The emission spectra were corrected for the instrumental response function. Luminescent lifetimes were measured using the excitation provided by the third harmonic of the Nd:YAG. The output signal of the photomultiplier was fed into a multichannel scaler (Stanford Research SR-400) and transferred to a PC for data analysis. Lifetimes were averages of 3 independent determinations. The spectra were displayed as photons versus energy (cm⁻¹) on the bottom axis and versus wavelength (nm) on the top axis. Luminescence spectra under high pressure were recorded using a diamond anvil cell (MiniDAC of D'Anvils Ltd), which could also be inserted into the closed cycle cryostat. Pressure was calibrated by using the $^5\text{D}_0 \rightarrow ^7\text{F}_0$ luminescence of Sm^{2+} doped BaFCl with a shift rate of -21 cm⁻¹ GPa⁻¹ as internal pressure sensor.¹³ The air pressure-dependent solid-state luminescence spectra have been realised in a cryostat equipped with a primary pump and an APG100 active Pirani vacuum gauge (Edwards). The degassed solutions were realised in a 1 cm corked cuvette with a Schlenk line equipped with a small Teflon-PTFE tube provided of a medical needle, and a N₂ bottle. The re-oxygenation of the solution were realised by removing the plug from the cuvette and leaving it open to ambient air. Spectra were recorded on the Fluorolog@-3 spectrometer with different times of N₂ bubbling (0–900 seconds) and O₂ re-oxygenation (0–3600 seconds).

Acknowledgements

We thank the Swiss National Science Foundation (grant number 200020_152780) for financial support.

References

- (a) H. Kumagai, M. Hasegawa, S. Miyanari, Y. Sugawa, Y. Sato, T. Hori, S. Ueda, H. Kamiyama and S. Miyano, *Tetrahedron Lett.*, 1997, **38**, 3971–3972; (b) T. Kajiwara, N. Iki and M. Yamashita, *Coord. Chem. Rev.*, 2007, **251**, 1734–1746.
- (a) G. Mislin, E. Graf, M. W. Hosseini, A. Bilyk, A. K. Hall, J. M. Harrowfield, B. W. Skelton and A. H. White, *Chem. Commun.*, 1999, 373–374; (b) T. Kajiwara, S. Yokozawa, T. Ito, N. Iki, N. Morohashi and S. Miyano, *Chem. Lett.*, 2001, 6–7; (c) H. Akdas, E. Graf, M. W. Hosseini, A. De Cian, A. Bilyk, B. W. Skelton, G. A. Koutsantonis, I. Murray, J. M. Harrowfield and A. H. White, *Chem. Commun.*, 2002, 1042–1043; (d) C. Desroches, G. Pilet, S. A. Borshch, S. Parola and D. Luneau, *Inorg. Chem.*, 2005, **44**, 9112–9120; (e) C. Desroches, G. Pilet, P. A. Szilagyi, G. Molnar, S. A. Borshch, A. Bousseksou, S. Parola and D. Luneau, *Eur. J. Inorg. Chem.*, 2006, **2006**, 357–365; (f) T. Kajiwara, T. Kobashi, R. Shinagawa, T. Ito, S. Takaishi, M. Yamashita and N. Iki, *Eur. J. Inorg. Chem.*, 2006, **2006**, 1765–1770; (g) Y. Bi, X.-T. Wang, W. Liao, X. Wang, X. Wang, H. Zhang and S. Gao, *J. Am. Chem. Soc.*, 2009, **131**, 11650–11651; (h) Y. Bi, W. Liao, G. Xu, R. Deng, M. Wang, Z. Wu, S. Gao and H. Zhang, *Inorg. Chem.*, 2010, **49**, 7735–7740; (i) Y. Bi, S. Du and W. Liao, *Chem. Commun.*, 2011, **47**, 4724–4726; (j) A. Gehin, S. Ferlay, J. M. Harrowfield, D. Fenske, N. Kyritsakas and M. W. Hosseini, *Inorg. Chem.*, 2012, **51**, 5481–5486; (k) M. Lamouchi, E. Jeanneau, A. Pillonnet, A. Brioude, M. Martini, O. Stephan, F. Meganem, G. Novitchi, D. Luneau and C. Desroches, *Dalton Trans.*, 2012, **41**, 2707–2713; (l) K. Xiong, F. Jiang, Y. Gai, Z. He, D. Yuan, L. Chen, K. Su and M. Hong, *Cryst. Growth Des.*, 2012, **12**, 3335–3341; (m) R. O. Fuller, G. A. Koutsantonis, I. Lozic, M. I. Ogden and B. W. Skelton, *Dalton Trans.*, 2015, **44**, 2132–2137.
- (a) Y. Bi, G. Xu, W. Liao, S. Du, X. Wang, R. Deng, H. Zhang and S. Gao, *Chem. Commun.*, 2010, **46**, 6362–6364; (b) K. Su, F. Jiang, J. Qian, M. Wu, K. Xiong, Y. Gai and M. Hong, *Inorg. Chem.*, 2013, **52**, 3780–3786; (c) Z. Zhang, A. Drapailo, Y. Matvieiev, L. Wojtas and M. J. Zaworotko, *Chem. Commun.*, 2013, **49**, 8353–8355; (d) F.-R. Dai, D. C. Becht and Z. Wang, *Chem. Commun.*, 2014, **50**, 5385–5387; (e) F.-R. Dai, U. Sambasivam, A. J. Hammerstrom and Z. Wang, *J. Am. Chem. Soc.*, 2014, **136**, 7480–7491; (f) K. Su, F. Jiang, J. Qian, Y. Gai, M. Wu, S. M. Bawaked, M. Mokhtar, S. A. Al-Thabaiti and M. Hong, *Cryst. Growth Des.*, 2014, **14**, 3116–3123.
- (a) T. Kajiwara, K. Katagiri, M. Hasegawa, A. Ishii, M. Ferbinteanu, S. Takaishi, T. Ito, M. Yamashita and N. Iki, *Inorg. Chem.*, 2006, **45**, 4880–4882; (b) N. Iki, S. Hirooka, M. Nakamura, T. Tanaka and H. Hoshino, *Eur. J. Inorg. Chem.*, 2012, **2012**, 3541–3545; (c) N. Iki, S. Hirooka, T. Tanaka, C. Kabuto and H. Hoshino, *Inorg. Chem.*, 2012, **51**, 1648–1656.
- C. Feldmann, T. Juestel, C. R. Ronda and P. J. Schmidt, *Adv. Funct. Mater.*, 2003, **13**, 511–516.
- (a) D. T. Palumbo and J. J. Brown, *J. Electrochem. Soc.*, 1970, **117**, 1184–1188; (b) D. T. Palumbo and J. J. Brown Jr., *J. Electrochem. Soc.*, 1971, **118**, 1159–1164; (c) T. E. Peters, R. G. Pappalardo and R. B. Hunt Jr., *J. Lumin.*, 1984, **31–32**, 290–292; (d) L. K. Singh, *Indian J. Pure Appl. Phys.*, 1984, **22**, 743–744; (e) B. T. Collins and M. Ling, *J. Electrochem. Soc.*, 1993, **140**, 1752–1755; (f) A. Morell and N. El Khiati, *J. Electrochem. Soc.*, 1993, **140**, 2019–2022; (g) C. Barthou, J. Benoit, P. Benalloul and A. Morell, *J. Electrochem. Soc.*, 1994, **141**, 524–528; (h) L. E. Shea, R. K. Datta and J. J. Brown Jr., *J. Electrochem. Soc.*, 1994, **141**, 1950–1954.
- (a) H. O. N. Reid, I. A. Kahwa, A. J. P. White and D. J. Williams, *Inorg. Chem.*, 1998, **37**, 3868–3873; (b) H. O. N. Reid, I. A. Kahwa, A. J. P. White and D. J. Williams, *Chem. Commun.*, 1999, 1565–1566; (c) Y. Wei, Y. Yu and K. Wu, *Cryst. Growth Des.*, 2008, **8**, 2087–2089; (d) J. Duan, B. Zheng, J. Bai, Q. Zhang and C. Zuo, *Inorg. Chim. Acta*, 2010, **363**, 3172–3177.
- (a) V. G. Torgov, L. N. Mazalov, G. A. Kostin, T. V. Us, T. M. Korda, N. A. Kryuchkova, E. A. Korotaev, A. D. Fedorenko and A. B. Drapailo, *J. Struct. Chem.*, 2011, **52**, 718–725; (b) N. A. Kryuchkova, S. A. Lavruchina, G. A. Kostin, L. N. Mazalov, V. G. Torgov, A. V. Kalinkin and A. B. Drapailo, *J. Struct. Chem.*, 2013, **54**, 907–916.
- Crystal data. (1): C₉₆H₁₂₆FKMn₄O₃₄S₈, *M* = 2358.31, Triclinic, *P* $\bar{1}$, *a* = 12.0143(9) Å, *b* = 12.3064(7) Å, *c* = 18.2691(8) Å, α = 101.431(4)°, β = 99.543(6)°, γ = 90.807(5)°, *V* = 2607.8(3) Å³, *R* = 0.0521, *wR*₂ = 0.1015 (*I* > 2σ(*I*)).
- L. J. Farrugia, *J. Appl. Crystallogr.*, 2012, **45**, 849–854.
- IGOR PRO v. 6.36, Wavemetrics Inc., Oregon.
- (a) R. Q. Albuquerque, Z. Popovic, C. L. De and G. Calzaferri, *ChemPhysChem*, 2006, **7**, 1050–1053; (b) M. S. Khakhalina, O. A. Rodionova and M. V. Puzyk, *Opt. Spectrosc.*, 2009, **106**, 529–531; (c) M. V. Mina and M. V. Puzyk, *Opt. Spectrosc.*, 2011, **111**, 71–73; (d) C. A. Kent, D. Liu, A. Ito, T. Zhang, M. K. Brennaman, T. J. Meyer and W. Lin, *J. Mater. Chem. A*, 2013, **1**, 14982–14989.
- M. Milos, T. Penhouet, P. Pal and A. Hauser, *Inorg. Chem.*, 2010, **49**, 3402–3408.
- (a) H. G. Drickamer, *Angew. Chem., Int. Ed. Engl.*, 1974, **13**, 39–47; (b) J. K. Grey and I. S. Butler, *Coord. Chem. Rev.*, 2001, **219–221**, 713–759.
- S. Sugano, Y. Tanabe and H. Kamimura, *Multiplets of Transition Metal Ions, Pure and Applied Physics*, Academic Press, New York, 1970, vol. 33.
- R. Englman and J. Jortner, *Mol. Phys.*, 1970, **18**, 145–164.
- R. Kumar, Y. O. Lee, V. Bhalla, M. Kumar and J. S. Kim, *Chem. Soc. Rev.*, 2014, **43**, 4824–4870.

- 18 N. Iki, H. Kumagai, N. Morohashi, K. Ejima, M. Hasegawa, S. Miyanari and S. Miyano, *Tetrahedron Lett.*, 1998, **39**, 7559–7562.
- 19 N. Morohashi, F. Narumi, N. Iki, T. Hattori and S. Miyano, *Chem. Rev.*, 2006, **106**, 5291–5316.
- 20 CrysAlisPro, Agilent Technologies, Version 1.171.134.149 (release 120-101-2011 CrysAlis2171.NET) (compiled Jan 2020 2011, 2015:2058:2025).
- 21 R. C. Clark and J. S. Reid, *Acta Crystallogr., Sect. A: Fundam. Crystallogr.*, 1995, **51**, 887–897.
- 22 (a) A. Altomare, M. C. Burla, M. Camalli, G. L. Casciarano, C. Giacovazzo, A. Guagliardi, A. G. G. Moliterni, G. Polidori and R. Spagna, *J. Appl. Crystallogr.*, 1999, **32**, 115–119; (b) P. W. Betteridge, J. R. Carruthers, R. I. Cooper, K. Prout and D. J. Watkin, *J. Appl. Crystallogr.*, 2003, **36**, 1487–1487.